Institut für Erd- & Umweltwissenschaften
Mathematisch-Naturwissenschaftliche Fakultät
Universität Potsdam

Mountain-Range Uplift & Climate - System Interactions in the southern Central Andes

DISSERTATION

von
Heiko Pingel

zur Erlangung des akademischen Grades

DOCTOR RERUM NATURALIUM
»Dr. rer. nat.«
in der Wissenschaftsdisziplin Geologie

eingereicht an der
Mathematisch-Naturwissenschaftlichen Fakultät
der Universität Potsdam

Potsdam, den 14. April 2015

Published online at the
Institutional Repository of the University of Potsdam:
URN urn:nbn:de:kobv:517-opus4-82301
http://nbn-resolving.de/urn:nbn:de:kobv:517-opus4-82301

Allgemeine Zusammenfassung

Mit einer Länge von über 7.000 km und Höhen von z.T. >6.000 m sind die Anden Südamerikas die bedeutendste topografische Barriere für atmosphärische Strömungen in der südlichen Hemisphäre. Integraler Bestandteil der Anden ist das Altiplano-Puna Plateau, das mit einer durchschnittlichen Höhe von etwa 4.000 m, nach Tibet, das zweitgrößte Gebirgsplateau der Erde ist. Diese kontinuierlichen Höhenzüge und der meridionale Verlauf der Anden sind für eine ausgeprägte Asymmetrie in der Verteilung der Niederschläge und die daraus resultierenden Erosions- und Ablagerungsprozesse im Gebirge sowie in den angrenzenden Vorländern verantwortlich. Bisher war allerdings nur ansatzweise bekannt, wann es zur Etablierung dieses Prozessgefüges kam. Daher setzt diese Studie an genau dieser Wissenslücke an und versucht auf verschiedenen Raum- und Zeitskalen zu entschlüsseln, welche Gebirgsbildungsprozesse tiefgreifende Auswirkungen auf Klima, Erosion und Sedimentation in den zentralen Anden gehabt haben. Als Untersuchungsgebiet wurde unter anderem das intermontane Humahuaca-Becken in NW-Argentinien ausgewählt, ein natürliches „Labor“, welches die Beziehungen zwischen tektonischen Deformationsprozessen, der Herkunft und Transportrichtung von Sedimenten und der Evolution der paläoökologischen Bedingungen besonders gut wiederspiegelt. Da die Gebirgsbildung der Anden in dieser Region relativ jung ist und radiometrisch datierbare vulkanische Aschen in den Sedimenten der intermontanen Becken aufgeschlossen sind, ist hier die Grundlage gegeben, die Erosions-, Sedimentations- und Deformationsgeschichte zu rekonstruieren. Des Weiteren kann damit das laterale und vertikale Wachstum des Gebirges und der direkte Impakt tektonischer und klimatischer Prozesse auf Umweltbedingungen besonders gut dokumentiert werden. Es zeigt sich, dass spätmiozäne (>6 Ma) Hebungsprozesse am Ostrand des Puna-Plateaus die anfängliche Ablagerung ostwärts transportierter Sedimente ermöglichten, welche im Zuge weiterer Hebung nach Süden abgelenkt wurden und schließlich zur Bildung eines intermontanten Beckens führten. Um die Beziehung zwischen tektonisch kontrollierter Topografie und Änderungen im Niederschlagsgeschehen näher zu untersuchen, wurde zusätzlich die Wasserstoffisotopie hydratisierter Vulkangläser aus Aschen der Becken-Sedimentabfolgen untersucht. Da heutige Isotopenverhältnisse meteorischer Wässer meist eine klare Höhenabhängigkeit aufweisen und sich diese Beziehungen auch in der Isotopie der hydratisierten Aschen erfassen lassen, kann die Auswertung dieser Daten einen wichtigen Einblick in topografische Veränderungen vermitteln. Die in diesem Kontext ausgeführten Isotopen- und Geländeuntersuchungen zeigen, dass Hebungsprozesse innerhalb der letzten 6 Millionen Jahre für die heutige Lage der intermontanen Becken verantwortlich sind und die Desertifikation der internen Gebirgsbereiche und die Ausbildung niederschlagsreicher Regionen am Ostrand des Gebirges erst nach dem Erreichen einer bestimmten Höhe der vorgelagerten Gebirgszüge erfolgte. Die heutige Verteilung und Menge der Niederschläge sowie steile Ost-West-Prozessgradienten in den Erosionsraten resultieren somit aus generell nach Osten jünger werdenden Deformationsprozessen, die sukzessive vormals humide Regionen an den Osthängen des Puna-Plateaus durch tektonische Hebungsprozesse in aride, intermontane Sedimentationsräume verwandelte, da sich feuchtebringende östliche Winde zunehmend an den orografischen Barrieren abregneten.

Abstract

Two of the most controversial issues concerning the late Cenozoic evolution of the Andean orogen are the timing of uplift of the intraorogenic Puna plateau and its eastern border, the Eastern Cordillera, and ensuing changes in climatic and surface-process conditions in the intermontane basins of the NW-Argentine Andes. The Eastern Cordillera separates the internally drained, arid Puna from semi-arid intermontane basins and the humid sectors of the Andean broken foreland and the Subandean fold-and-thrust belt to the east. With elevations between 4,000 and 6,000 m the eastern flanks of the Andes form an efficient orographic barrier with westward-increasing elevation and asymmetric rainfall distribution and amount with respect to easterly moisture-bearing winds. This is mirrored by pronounced gradients in the efficiency of surface processes that erode and re-distribute sediment from the uplifting ranges. Although the overall pattern of deformation and uplift in this sector of the southern central Andes shows an eastward migration of deformation, a well-developed deformation front does not exist and uplift and associated erosion and sedimentary processes are highly disparate in space and time. In addition, periodic deformation within intermontane basins, and continued diachronous foreland uplifts associated with the reactivation of inherited basement structures furthermore make a rigorous assessment of the spatiotemporal uplift patterns difficult.

This thesis focuses on the tectonic evolution of the Eastern Cordillera of NW Argentina, the depositional history of its intermontane sedimentary basins, and the regional topographic evolution of the eastern flank of the Puna Plateau. The intermontane basins of the Eastern Cordillera and the adjacent morphotectonic provinces of the Sierras Pampeanas and the Santa Bárbara System are akin to reverse-fault bounded, filled, and partly coalesced sedimentary basins of the Puna Plateau. In contrast to the Puna basins, however, which still form intact morphologic entities, repeated deformation, erosion, and re-filling have impacted the basins in the Eastern Cordillera. This has resulted in a rich stratigraphy of repeated basin fills, but many of these basins have retained vestiges of their early depositional history that may reach back in time when these areas were still part of a contiguous and undeformed foreland basin. Fortunately, these strata also contain abundant volcanic ashes that are not only important horizons to decipher tectono-sedimentary events through U–Pb geochronology and geochemical correlation, but they also represent terrestrial recorders of the hydrogen-isotope composition of ancient meteoric waters that can be compared to the isotopic composition of modern meteoric water. The ash horizons are thus unique recorders of past environmental conditions and lend themselves to tracking the development of rainfall barriers and tectonically forced climate and environmental change through time.

U–Pb zircon geochronology and paleocurrent reconstructions of conglomerate sequences in the Humahuaca Basin of the Eastern Cordillera at 23.5° S suggest that the basin was an integral part of a largely unrestricted depositional system until 4.2 Ma, which subsequently became progressively decoupled from the foreland by range uplifts to the east that forced easterly moisture-bearing winds to precipitate in increasingly eastward locations. Multiple cycles of severed hydrological conditions and drainage re-capture are identified together with these processes that were associated with basin filling and sediment evacuation, respectively. Moreover, systematic relationships among faults, regional unconformities and deformed landforms reveal a general pattern of intra-basin deformation that appears to be linked with basin-internal deformation during or subsequent to episodes of large-scale sediment removal. Some of these observations are supported by variations in the hydrogen stable isotope composition of volcanic glass from the Neogene to Quaternary sedimentary record, which can be related to spatiotemporal changes

in topography and associated orographic effects. δD_g values in the basin strata reveal two main trends associated with surface uplift in the catchment area between 6.0 and 3.5 Ma and the onset of semiarid conditions in the basin following the attainment of threshold elevations for effective orographic barriers to the east after 3.5 Ma. The disruption of sediment supply from western sources after 4.2 Ma and subsequent hinterland aridification, moreover, emphasize the possibility that these processes were related to lateral orogenic growth of the adjacent Puna Plateau. As a result of the hinterland aridification the regions in the orogen interior have been characterized by an inefficient fluvial system, which in turn has helped maintaining internal drainage conditions, sediment storage, and relief reduction within high-elevation basins.

The diachronous nature of basin formation and impacts on the fluvial system in the adjacent broken foreland is underscored by the results of detailed sediment provenance and paleocurrent analyses, as well as U–Pb zircon geochronology in the Lerma and Metán basins at ca. 25° S. This is particularly demonstrated by the isolated uplift of the Metán range at ~10 Ma, which is more than 50 km away from the presently active orogenic front along the eastern Puna margin and the Eastern Cordillera to the west. At about 5 Ma, Puna-sourced sediments disappear from the foreland record, documenting further range uplifts in the Eastern Cordillera and hydrological isolation of the neighboring Angastaco Basin from the foreland. Finally, during the late Pliocene and Quaternary, deformation has been accommodated across the entire foreland and is still active. To elucidate the interactions between tectonically controlled changes in elevation and their impact on atmospheric circulation processes in this region, this thesis provides additional, temporally well-constrained hydrogen stable isotope results of volcanic glass samples from the broken foreland, including the Angastaco Basin, and other intermontane basins farther south. The results suggest similar elevations of intermontane basins and the foreland sectors prior to ca. 7 Ma. In case of the Angastaco Basin the region was affected by km-scale surface uplift of the basin. A comparison with coeval isotope data collected from sedimentary sequences in the Puna plateau explains rapid shifts in the intermontane δD_g record and supports the notion of recurring phases of enhanced deep convection during the Pliocene, and thus climatic conditions during the middle to late Pliocene similar to the present day.

Combined, field-based and isotope geochemical methods used in this study of the NW-Argentine Andes have thus helped to gain insight into the systematics, rate changes, interactions, and temporal characteristics among tectonically controlled deformation patterns, the build-up of topography impacting atmospheric processes, the distribution of rainfall, and resulting surface processes in a tectonically active mountain belt. Ultimately, this information is essential for a better understanding of the style and the rates at which non-collisional mountain belts evolve, including the development orogenic plateaus and their bordering flanks. The results presented in this study emphasize the importance of stable isotope records for paleoaltimetric and paleoenvironmental studies in mountain belts and furnishes important data for a rigorous interpretation of such records.

Zusammenfassung

Zwei häufig diskutierte Aspekte der spätkänozoischen Gebirgsbildung der Anden sind der Zeitpunkt sowie die Art und Weise der Heraushebung des Puna-Plateaus und seiner Randgebiete innerhalb der Ostkordillere und die damit verbundenen klimatischen Änderungen in NW Argentinien. Die Ostkordillere trennt die Bereiche des endorheischen, ariden Plateaus von semiariden und extern entwässerten intermontanen Becken sowie dem humiden Andenvorland im Osten. Diese Unterschiede verdeutlichen die Bedeutung der östlichen Flanken der Anden als orografische Barrieren gegenüber feuchten Luftmassen aus dem Osten und spiegelt sich auch in ausgeprägten Relief- und Topografiegradienten, der Niederschlagsverteilung, und der Effizienz von Oberflächenprozessen wider. Obwohl das übergeordnete Deformationsmuster in diesem Teil der Anden eine ostwärts gerichtete Wanderung der Deformationsprozesse im Gebirge indiziert, gibt es hier keine klar definierte Deformationsfront. Hebungsvorgänge und die damit im Zusammenhang stehenden Sedimentprozesse setzen räumlich und zeitlich sehr unterschiedlich ein. Zudem gestalten periodisch wiederkehrende Deformationsereignisse innerhalb intermontaner Becken und diachrone Hebungsvorgänge, durch Reaktivierung älterer Sockelstrukturen im Vorland, eine detaillierte Auswertung der räumlich-zeitlichen Hebungsmuster zusätzlich schwierig.

Die vorliegende Arbeit konzentriert sich hauptsächlich auf die tektonische Entwicklung der Ostkordillere im Nordwesten Argentiniens, die Ablagerungsgeschichte ihrer intermontanen Sedimentbecken und die topografische Entwicklung der Ostflanke des andinen Puna-Plateaus. Im Allgemeinen sind sich die Sedimentbecken der Ostkordillere und der angrenzenden Provinzen, den Sierras Pampeanas und der Santa Bárbara Region, den durch Störungen begrenzten und mit Sedimenten verfüllten Becken der hochandinen Plateauregion sehr ähnlich. Deutliche Unterschiede zur Puna bestehen aber dennoch, denn wiederholte Deformations-, Erosions- und Sedimentationsprozesse haben in den intermontanen Becken zu einer vielfältigen Stratigrafie, Überlagerungsprozessen und einer durch tektonische Prozesse und klimatischen Wandel charakterisierten Landschaft beigetragen. Je nach Erhaltungsgrad können in einigen Fällen Spuren dieser sedimentären und tektonischen Entwicklung bis in die Zeit zurückreichen, als diese Bereiche des Gebirges noch Teil eines zusammenhängenden und unverformten Vorlandbeckens waren. Im Nordwesten Argentiniens enthalten känozoische Sedimente zahlreiche datierbare und geochemisch korrelierbare Vulkanaschen, die nicht nur als wichtige Leithorizonte zur Entschlüsselung tektonischer und sedimentärer Ereignisse dienen. Die vulkanischen Gläser dieser Aschen archivieren außerdem Wasserstoff-Isotopenverhältnisse früherer Oberflächenwasser, mit deren Hilfe – und im Vergleich mit den Isotopenverhältnissen rezenter meteorischer Wässer – die räumliche und zeitliche Entstehung orografischer Barrieren und tektonisch erzwungene Klima- und Umweltveränderungen verfolgt werden können.

Uran-Blei-Datierungen an Zirkonen aus den vulkanischen Aschelagen und die Rekonstruktion sedimentärer Paläotransportrichtungen im intermontanen Humahuaca-Becken in der Ostkordillere (23.5° S) deuten an, dass das heutige Becken bis vor etwa 4.2 Ma Bestandteil eines größtenteils uneingeschränkten Ablagerungsbereichs war, der sich bis ins Vorland erstreckt haben muss. Deformation und Hebung östlich des heutigen Beckens sorgten dabei für eine fortschreitende Entkopplung des Entwässerungsnetzes vom Vorland und eine Umlenkung der Flussläufe nach Süden. In der Folge erzwang die weitere Hebung der Gebirgsblöcke das Abregnen östlicher Luftmassen in immer östlicher gelegene Bereiche. Zudem können periodische Schwankungen der hydrologischen Verbindung des Beckens mit dem Vorland im Zusammenhang mit der Ablagerung und Erosion mächtiger Beckenfüllungen identifiziert werden. Systematische Beziehungen zwischen Verwerfungen, regionalen Diskontinuitäten und verstellten Terrassenflächen

verweisen außerdem auf ein generelles Muster beckeninterner Deformation, vermutlich als Folge umfangreicher Beckenerosion und damit verbundenen Änderungen im tektonischen Spannungsfeld der Region. Einige dieser Beobachtungen können anhand veränderter Wasserstoff-Isotopenkonzentrationen vulkanischer Gläser aus der känozoischen Stratigrafie untermauert werden. Die δD_g-Werte zeigen zwei wesentliche Trends, die einerseits in Verbindung mit Oberflächenhebung innerhalb des Einzugsgebiets zwischen 6.0 und 3.5 Ma stehen und andererseits mit dem Einsetzen semiarider Bedingungen durch Erreichen eines Schwellenwertes der Topografie der östlich gelegenen Gebirgszüge nach 3.5 Ma erklärt werden können. Tektonisch bedingte Unterbrechung der Sedimentzufuhr aus westlich gelegenen Liefergebieten um 4.2 Ma und die folgende Hinterland-Aridifizierung deuten weiterhin auf die Möglichkeit hin, dass diese Prozesse die Folge eines lateralen Wachstums des Puna-Plateaus sind. Diese Aridifizierung im Bereich der Puna resultierte in einem ineffizienten, endorheischen Entwässerungssystem, das dazu beigetragen hat, das Plateau vor Einschneidung und externer Entwässerung zu bewahren und Reliefgegensätze aufgrund fortgesetzter Beckensedimentation reduzierte.

Die diachrone Natur der Hebungen und Beckenbildungen sowie deren Auswirkungen auf das Flusssystem im angrenzenden Vorland wird sowohl durch detaillierte Analysen der Sedimentherkunft und Transportrichtungen als auch Uran-Blei-Datierungen im Lerma- und Metán-Becken (25° S) weiterhin unterstrichen. Das wird besonders deutlich am Beispiel der isolierten Hebung der Sierra de Metán vor etwa 10 Ma, die mehr als 50 km von der aktiven orogenen Front im Westen entfernt liegt. Ab 5 Ma sind typische Lithologien der Puna nicht mehr in den Vorlandsedimenten nachweisbar, welches die weitere Hebung innerhalb der Ostkordillere und die hydrologische Isolation des Angastaco-Beckens in dieser Region dokumentiert. Im Spätpliozän und Quartär ist die Deformation letztlich über das gesamte Vorland verteilt und bis heute aktiv.

Um die Beziehungen zwischen tektonisch kontrollierten Veränderungen der Topografie und deren Einfluss auf atmosphärische Prozesse besser zu verstehen, werden in dieser Arbeit weitere altersspezifische Wasserstoff-Isotopendaten vulkanischer Gläser aus dem zerbrochenen Vorland, dem Angastaco-Becken in der Übergangsregion zwischen Ostkordillere und Punarand und anderer intermontaner Becken weiter südlich vorgestellt. Die Resultate dokumentieren ähnliche Höhenlagen der untersuchten Regionen bis ca. 7 Ma, gefolgt von Hebungsprozessen im Bereich des Angastaco-Beckens. Ein Vergleich mit Isotopendaten vom benachbarten Puna-Plateau hilft abrupte δD_g-Schwankungen in den intermontanen Daten zu erklären und untermauert die Existenz wiederkehrender Phasen verstärkt konvektiver Wetterlagen im Pliozän, ähnlich heutigen Bedingungen.

In dieser Arbeit werden geländeorientierte und geochemische Methoden kombiniert, um Erkenntnisse über die Abläufe von topografiebildenden Deformations- und Hebungsprozessen zu gewinnen und Wechselwirkungen mit der daraus resultierenden Niederschlagsverteilung, Erosion und Sedimentation innerhalb tektonisch aktiver Gebirge zu erforschen. Diese Erkenntnisse sind für ein besseres Verständnis von Subduktionsgebirgen essentiell, besonders hinsichtlich des Deformationsstils und der zeitlich-räumlichen Beziehungen bei der Hebung und Sedimentbeckenbildung. Diese Arbeit weist darüberhinaus auf die Bedeutung stabiler Isotopensysteme zur Beantwortung paläoaltimetrischer Fragestellungen und zur Erforschung von Paläoumweltbedingungen hin und liefert wichtige Erkenntnisse für einen kritischen Umgang mit solchen Daten in anderen Regionen.

Contents

List of figures xii

List of tables xiii

1 Thesis organization & author contributions 1

2 Introduction 5
- 2.1 Geological setting . . . 8
- 2.2 Climatic setting . . . 10
- 2.3 Research questions . . . 11

3 Neotectonic basin & landscape evolution in the Eastern Cordillera of NW Argentina 13
- 3.1 Introduction . . . 14
- 3.2 Regional & geologic setting . . . 16
- 3.3 Methods . . . 20
- 3.4 Results . . . 20
- 3.5 Discussion . . . 31
- 3.6 Summary & conlusions . . . 37

4 Pliocene orographic barrier uplift in the southern Central Andes 39
- 4.1 Introduction . . . 40
- 4.2 Geological setting . . . 41
- 4.3 Stable isotope paleoaltimetry & hydrogen-isotope analysis . . . 42
- 4.4 Results . . . 42
- 4.5 Orographic barrier formation & plateau expansion . . . 43
- 4.6 Conclusions . . . 45

5 Neogene to Quaternary broken foreland formation & sedimentation dynamics 47
5.1 Introduction . . . 48
5.2 Geologic setting . . . 49
5.3 Methods . . . 55
5.4 Results . . . 57
5.5 Discussion . . . 70
5.6 Summary & conclusion . . . 78

6 Surface uplift & convective rainfall along the southern Central Andes 79
6.1 Introduction . . . 80
6.2 Geological setting . . . 82
6.3 Climatic conditions . . . 85
6.4 Stable isotope & paleoaltimetry . . . 87
6.5 Methods . . . 88
6.6 Results . . . 90
6.7 Discussion . . . 94
6.8 Conclusions . . . 103

7 Discussion & conclusion 105
7.1 Tectonics, climate & surface processes . . . 105
7.2 Hydrogen stable isotopes from hydrated volcanic ashes . . . 110

References 132

A U–Pb zircon geochronology 133

B Stratigraphic correlation of volcanic ashes 139
B.1 Stratigraphic correlations . . . 139

C Hydrogen-isotope analysis 141
C.1 Volcanic glass samples . . . 141
C.2 Modern stream water samples . . . 142
C.3 Stable isotope compositions of hydrated volcanic glass . . . 142
C.4 Water content of volcanic glass . . . 142
C.5 Stable isotope compositions of modern stream-water and rainfall . . . 142

D $^{40}Ar/^{39}Ar$ biotite dating of sample UQ270307-2 151
D.1 Sample preparation . . . 151

D.2 $^{40}Ar/^{39}Ar$ dating 151

E U–Pb & U–Th zircon geochronology 155

F Provenance analysis 157

G U–Pb & (U–Th)/He zircon geochronology 159

H Hydrogen stable isotope results of volcanic glass & paleoaltimetry estimates 175

List of figures

2.1 Topography, mean annual rainfall & morphotectonic provinces of the central Andes . 6
2.2 Difference between thin-skinned foreland basin & thick-skinned broken foreland . . . 9

3.1 Topography & east-draining river network of the southern Central Andes 15
3.2 Simplified geology of the Humahuaca Basin & geologic cross section 17
3.3 Geologic map of the study area, late Cenozoic stratigraphy & subsurface interpretations 19
3.4 $^{207}Pb/^{206}Pb$ vs. $^{238}U/^{206}Pb$ zircon data for Maimará samples 21
3.5 $^{207}Pb/^{206}Pb$ vs. $^{238}U/^{206}Pb$ zircon data for Tilcara & Quaternary gravel samples 22
3.6 Measured stratigraphic sections located near Incahuasi & in the Qda. de Maimará . . . 24
3.7 Palaeoflow directions in the Humahuaca Basin 26
3.8 Compilation of field images & microfossil analysis 27
3.9 Simplified structural map 29
3.10 Schematic cross section of the Andean margin in NW Argentina at ca. 23.5° S 32
3.11 Conceptual model of foreland-basin fragmentation 34

4.1 DEM with sample locations of volcanic ashes & modern stream water 41
4.2 δD of volcanic glass & conceptual basin-and-range development 44

5.1 Overview of the morphotectonic domains of the central Andes 49
5.2 Simplified geologic map & topography 50
5.3 Compilation of Neogene stratigraphy 53
5.4 $^{207}Pb/^{206}Pb$ vs. $^{238}U/^{206}Pb$ zircon results 56
5.5 $^{238}U–^{230}Th$ zircon model ages & relative probabilities 57
5.6 Paleoflow reconstruction based on clast imbrications 60
5.7 Interpretation of seismic line 2504 64
5.8 Relationship between Cretaceous extension & Quaternary compression 65
5.9 Synrift depth interval of seismic line 2447 across the Coronel Moldes anticline 67

5.10 Structural interpretation of the Sierra Vaqueros & San Lorenzo anticline 68
5.11 Structural interpretation east of the Mojotoro Range 69
5.12 Conglomerate composition & provenance signatures 70
5.13 3-km-radius relief and mean annual rainfall 72
5.14 Swath profiles of topography, 3-km-radius relief & rainfall 75
5.15 Schematic overview of the Neogene foreland fragmentation 76
5.16 Synthesis of Mio-Pliocene tectonics-climate interactions & sediment dynamics 77

6.1 Overview map of the study area 83
6.2 Satellite image of the studied Angastaco Basin & geological cross section 84
6.3 Generalized patterns of South American surface wind directions during austral summer 86
6.4 Hydrogen stable isotope compositions of volcanic glass samples 93
6.5 Conceptual model showing structural & orographic development of the Angastaco Basin 98
6.6 Oxygen stable isotope composition of published soil carbonate records 100

7.1 Spatiotemporal evolution of basin filling and climatic conditions 106

C.1 δD_g of glass & δD_{gc} from stream water samples vs. latitude 144
C.2 $\delta^{18}O$ vs. δD from stream-water 144
C.3 Systematic relationship of δD from stream waters with elevation 145
C.4 Combined dataset of modern water samples from this study and Dettinger (2013) . . . 145
C.5 δD in precipitation & rainfall amount at Purmamarca GNIP station 146

D.1 Age spectrum, $^{37}Ar_{Ca}/^{39}Ar_K$ ratios & normal isochron by $^{40}Ar/^{39}Ar$ analysis 152

G.1 Cathodo-luminescence (CL) images of mounted zircons I 173
G.2 Cathodo-luminescence (CL) images of mounted zircons II 174

List of tables

A.1 Summary of U–Pb zircon analytical data. 134

C.1 Hydrogen stable isotope analysis of volcanic glass 147
C.2 Raw data for NBS30 biotite standard & water content calculation 148
C.3 Results of modern water stable isotopes 149

D.1 $^{40}Ar/^{39}Ar$ analytical results of UQ270307-2 biotite, C08049 153

E.1 Summary of U–Pb zircon analytical data II 155
E.2 Summary of U–Th zircon analytical data 156

F.1 Conglomerate compositional data 158

G.1 Summary of U–Th–Pb zircon analytical data I 160
G.2 Summary of U–Th–Pb zircon analytical data II 167
G.3 (U–TH)/He analytical data for sample 005 172
G.4 Summary of U–Pb zircon analytical data. 172

H.1 Hydrogen stable isotope analysis of volcanic glass 176
H.2 Paleoaltimetry results 178

Chapter 1

Thesis organization & author contributions

This study constitutes a cumulative thesis that combines peer-reviewed, published articles and a manuscript that will be submitted for review to a scientific journal. The overarching goal of the research conducted as part of this thesis is to better understand interactions between climate, tectonics, and surface processes in the southern Central Andes of northwestern Argentina. The project was initially started within the framework of the *DFG-Leibniz Center for Surface Process and Climate Studies*, funded by the Leibniz awards of Deutsche Forschungsgemeinschaft (DFG) to M. Strecker and G. Haug, which had the aim to link studies of tectonics, climate, and surface processes on geologic to annual timescales. Fully financed by DFG, this center provided the platform for a pilot and feasibility study that ultimately resulted in a DFG-research proposal, titled *Neogene to Quaternary tectono-geomorphic evolution and paleohydrology of the South Central Andes, NW Argentina*, funded to M. Strecker, A. Mulch, and D. Sachse. This thesis represents an integral part of this proposal, which had three main goals: (1) Obtaining a detailed record of present-day isotopic hydrogen and oxygen signatures of meteoric waters, carbonates, and organic matter; (2) deciphering paleo-hydrologic and climatic changes through the use of compound-specific isotope compositions of lipid biomarkers extracted from sedimentary basin deposits; (3) evaluating the magnitude of elevation changes and their effects on orographic precipitation, using the isotopic signature of hydrated glass from volcanic ashes to validate the interpretation of long-term precipitation changes as a trigger for changes in basin sedimentation and erosion episodes; and (4) combining the results to analyze and understand the patterns of lateral orogenic growth during foreland-basin segmentation and ensuing changes in climatic and depositional systems.

Chapter 2 – Introduction. This chapter reviews the basic principles of the interactions among tectonics, climate, and surface processes in tectonically active mountain belts. In addition, the rationale and motivation of the dissertation and resulting research questions are laid out following a brief overview of the geological history and the climatic setting of the southern Central Andes.

Chapter 3 – Neotectonic basin & landscape evolution in the Eastern Cordillera of NW Argentina. This chapter discusses the late Cenozoic evolution of the intermontane Humahuaca Basin in northwestern Argentina as deduced from field observations of deformation patterns and regional unconformities in

basin strata, sediment provenance, and paleocurrent analyses. The study also furnishes a new U–Pb zircon geochronology of interbedded volcanic ash deposits to improve the history of tectono-sedimentary processes in this intermontane setting. As such, this study entails the development of a refined basin stratigraphy and chronology of a tectonically active, intermontane basin in the Eastern Cordillera of the Andes and evaluates the causes and consequences of multiple basin-fill and excavation cycles during the Plio-Pleistocene, with an emphasis on possible links between the reactivation of basinal fault systems and mass removal. This chapter has been published: *Pingel, H., Strecker, M.R., Alonso, R.N., Schmitt, A.K., 2013. Neotectonic basin and landscape evolution in the Eastern Cordillera of NW Argentina, Humahuaca Basin (~24 ° S). Basin Research 25, 554–573.* HP carried out all fieldwork, including detailed geological and structural mapping, fault-kinematic and clast-imbrication measurements, and clast counting of conglomeratic units. HP also sampled key volcanic ash horizons, carried out mineral separation, and finally performed isotope measurements, corrections, and data interpretation for U–Pb zircon age determination under the guidance of AS. MRS and RA supported fieldwork and logistics. All illustrations are the responsibility of HP. All authors participated in discussing the results and interpretations, and critically read the manuscript.

Chapter 4 – Pliocene orographic barrier uplift in the southern Central Andes. This chapter explores the potential for hydrogen stable isotopes in hydrated volcanic glass in reconstructing paleoenvironmental changes in northwestern Argentina. This method allows for an assessment of the spatiotemporal evolution of orographic barriers through a known relationship between topographic change and the isotopic composition of meteoric water that eventually becomes incorporated in the proxy record. In particular, applied to the well-studied Humahuaca Basin, this method enables the investigation of the timing and rates of topographic growth during Mio-Pliocene deformation and range uplift, and the subsequent development of efficient orographic effects once threshold elevations have been attained. This chapter is also published: *Pingel, H., Alonso, R.N., Mulch, A., Rohrmann, A., Sudo, M., Strecker, M.R., 2014. Pliocene orographic barrier uplift in the southern Central Andes, Geology 42(8), 691–694.* HP performed fieldwork and sample collection of volcanic ashes, sample preparation, and mineral separation. Under the guidance of AM, HP was also responsible for measuring stable hydrogen isotope ratios of volcanic glass shards and data interpretation. AR, MRS, and RA supported fieldwork, sample collection, and logistics. MS performed sample preparation, isotope measurements, corrections, and $^{40}Ar/^{39}Ar$ age interpretation of a key volcanic ash sample. All illustrations are the responsibility of HP. All authors contributed to discussing the results and critically read the manuscript.

Chapter 5 – Neogene to Quaternary broken foreland formation & sedimentation dynamics. This chapter deciphers the tectono-stratigraphic evolution across the Eastern Cordillera and the broken foreland of the Santa Bárbara System at ~25° S, deduced through extensive clast-provenance and paleocurrent analyses, U–Pb and U–Th zircon geochronology, and subsurface interpretation of industry seismic reflec-

tion data. This chapter is published: *Hain, M.P., Strecker, M.R., Bookhagen, B., Alonso, R.N., Pingel, H., Schmitt, A.K., 2011. Neogene to Quaternary broken foreland formation and sedimentation dynamics in the Andes of NW Argentina ~25 ° S, Tectonics 30, TC2006, doi: 10.1029/2010TC002703.* MH performed fieldwork, including sample collection, geological and structural mapping, clast-imbrication measurements, and clast counting of conglomeratic units. HP conducted additional clast provenance and paleocurrent measurements and collected key volcanic ashes in the field. HP performed sample preparation and isotopic measurements, corrections, and data interpretations of U–Pb zircon and U–Th ages together with AS. MRS and RA supported fieldwork and helped identifying key sampling sites. MH performed seismic reflection interpretation and is responsible for illustrations. All authors participated in discussing the results and critically read the manuscript.

Chapter 6 – Orographic barrier uplift & convective rainfall along the Central Andes of NW Argentina. This manuscript is in preparation for publication. This part of the study investigates possible feedbacks between hydrogen stable isotopes in volcanic glass from the Mio-Pliocene intermontane basin record of the Angastaco Basin at ~25° S and atmospheric processes. Although the evolution of tectono-sedimentary processes at this location is similar to other intermontane basins in northwest Argentina, recent investigations have shown that the present-day meteorological conditions are much more complex than in regions farther north, and thus affect modern stable-isotope compositions in rainfall. This raises the question as to whether or not stable isotope paleorecords can be confidently used in this region of the Andes to infer paleoenvironmental change. By comparing the hydrogen stable-isotope compositions from the Angastaco Basin and other basins to the south with published data from the intra-orogenic Puna plateau to the west, this part of the study reveals repeated episodes with conditions similar to the present-day, which render generalized regional paleoenvironmental inferences difficult.

Chapter 7 – Discussion & Conclusion. This chapter of the thesis combines the principal results of the individual studies and reviews the data in a regional context. Furthermore, additional research questions stimulated by this study and possible future efforts to solve them are discussed.

Chapter 2

Introduction

Next to rifting and the formation of ocean basins, mountain building is one of to the most significant processes in shaping Earth's surface over geological time. Mountain building and the development of pronounced topography may fundamentally impact atmospheric flow and cause asymmetries in the distribution and amount of rainfall on hemispheric scales (e.g., Bookhagen & Burbank, 2006; Bookhagen & Strecker, 2008). Consequently, this may in turn produce steep gradients in surface processes, such as the efficiency of erosion across an orogen (Lal *et al.*, 2003; Gabet *et al.*, 2008; Owen *et al.*, 2010; Bookhagen & Strecker, 2012; Burbank *et al.*, 2012; Placzek *et al.*, 2015). Importantly, together these tectono-climatic interactions and the resulting processes shaping Earth's surface control a wide variety of geological and biological processes on our planet. In orogenic settings, such as the South American Andes and the Himalaya, for example, precipitation is often focused along the windward flanks of high topography, while the orogenic interior is characterized by progressively reduced rainfall, if the transport of air masses is perpendicular or oblique with respect to the orientation of the mountain belt (Fig. 2.1). Furthermore, tectonics, climate, and surface processes are not only tightly linked, but there may be intriguing feedbacks among them, which may impact on lithospheric processes and regional stress fields (Dahlen, 1990; Whipple & Meade, 2006; Meade & Conrad, 2008; McQuarrie *et al.*, 2008). For example, it has been suggested that orographic rainout along tectonically active mountain fronts can trigger enhanced localized rock uplift as a consequence of increased erosional unloading through efficient mass wasting and removal of material by fluvial processes (e.g., Molnar & England, 1990; Willett, 1999; Zeitler *et al.*, 2001; Reiners *et al.*, 2003; Reiners & Brandon, 2006). On the leeward side of such orographic barriers, however, reduced surface-process rates may cause increased sediment trapping, loading and an increase in lithospheric stresses, which causes fault inactivity in basins and the propagation of deformation into undeformed foreland regions, thereby possibly aiding the outward growth of plateaus (e.g., Sobel *et al.*, 2003; Garcia-Castellanos, 2007). Moreover, an increasing body of evidence suggests that once intermontane sedimentary basins are re-captured and excavated by headward-incising rivers, deformation may step back into these formerly, tectonically quiescent regions (Sobel *et al.*, 2003; Hilley & Strecker, 2005; Strecker *et al.*, 2007a; Hain *et al.*, 2011; Pingel *et al.*, 2013). In this context it is interesting to note that although

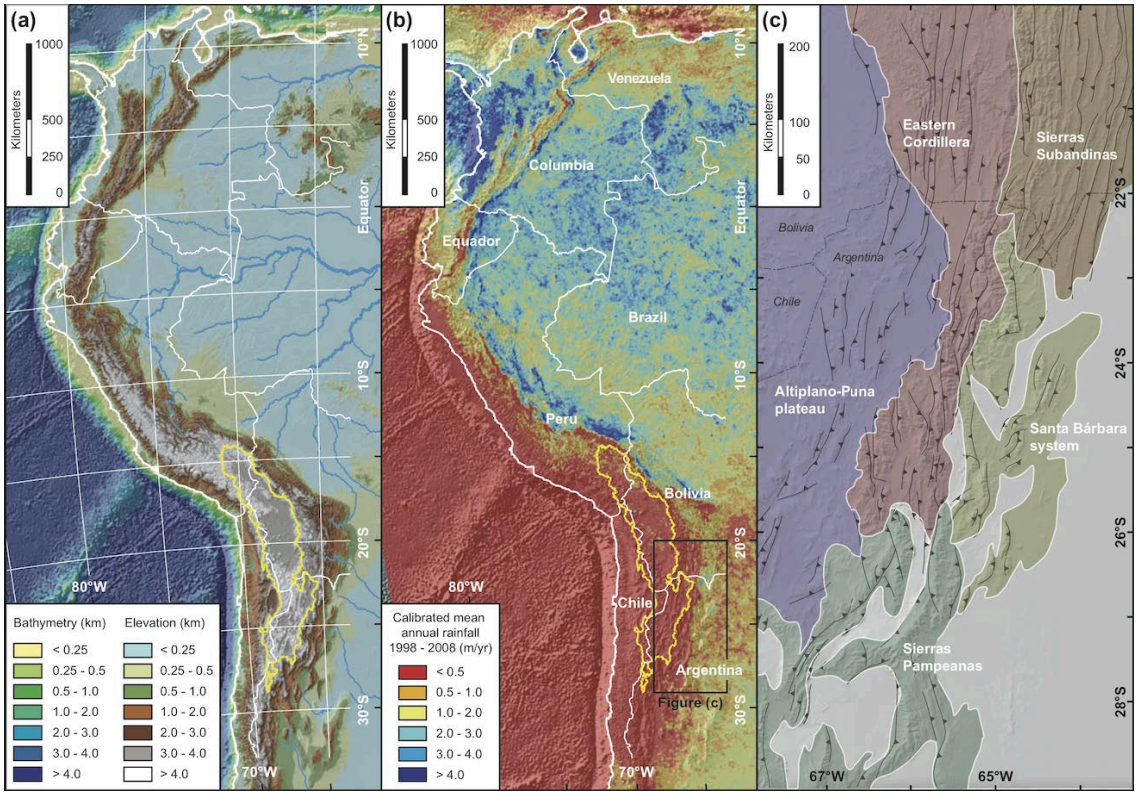

Figure 2.1 – (a) Topography of the northern and central Andes. Yellow outline delineates the internally-drained area of the Altiplano-Puna plateau. (b) Mean annual rainfall map of the Andes derived from NASA's Tropical Rainfall Measurement Mission (TRMM). Note orographic rainout along the eastern flanks of the Andes and the resulting arid interior of the orogen. Modified after Bookhagen & Strecker (2008). (c) Shaded relief map and principal morphotectonic domains of the South Central Andes of northwestern Argentina (after Jordan *et al.*, 1983).

the relationships between tectonic growth, tectonically induced climate change, and surface processes have been widely discussed in the recent past, their timing, rates, and relative roles in forcing deformation processes remain poorly understood because of the complex feedbacks that may exist (reviewed in Hilley & Coutand, 2009).

Excellent outcrop conditions, a rich archive of radiometrically datable volcanic ashes, and pronounced topographic, climatic, and surface-process gradients across the southern Central Andes of northwestern Argentina constitute an exceptional environment that lends itself to a detailed investigation of forcing factors that have been driving Cenozoic orogenic evolution. Such an attempt may not only help decipher the details of tectonic-climatic interactions, but it may also resolve yet outstanding issues regarding the spatiotemporal patterns of range uplift, thus contributing to better understand the underlying processes that shaped the characteristics of the southern Central Andes. Recent debates on the southern Central Andes, for example, focus on the onset of plateau formation, the establishment of the South American Monsoon system, but also on issues regarding plateau formation as a result of lithosphere-asthenosphere

interaction (e.g., Kay *et al.*, 1994; Allmendinger *et al.*, 1997; McQuarrie, 2002; Garzione *et al.*, 2006). Alternatively, inferred synergetic processes of foreland-directed uplift of basement ranges and superposed climatic effects of basin isolation, basin-fill thickness and the reduction of relief under increasingly arid conditions by foreland-directed uplift are currently being discussed (Masek *et al.*, 1994; Sobel *et al.*, 2003; Strecker *et al.*, 2007b, 2009).

Sedimentary basins are remarkable archives that may play a pivotal role in answering some of the outstanding research questions concerning the tectonic and climatic effects of lateral orogenic growth and thus long-term orogenic evolution and forcing of climate by tectonic processes and possible feedbacks between them. The sedimentary strata of such basins potentially record tectonic activity and its impact on climate and the environment, thus providing key proxy indicators of environmental change that track tectonically and climatically forced processes in orogenic evolution. Intermontane basins straddling the flank on the Argentine side of the Puna plateau, the southern extension of the vast Altiplano-Puna Plateau, have commonly preserved Neogene to Quaternary sedimentary strata (e.g., Strecker *et al.*, 1989; Kleinert & Strecker, 2001; Starck & Anzótegui, 2001; Hilley & Strecker, 2005; Hain *et al.*, 2011; Galli *et al.*, 2014), which hold the key to unravel the tectonic, sedimentary, and climatic history of this actively deforming region. As such, these basins may provide analogs of similar tectonic and sedimentary conditions in the orogen interior. For example, these basin sediments are distinctly deformed, contain marked regional unconformities, and record spatiotemporal variations in grain-size and composition (e.g., Strecker *et al.*, 2007a). In addition, paleo-transport directions reflect uplift, deformation, and erosion processes of the surrounding mountain ranges. Moreover, fossil content, lithologic characteristics or authigenic mineral composition furnish valuable information on the paleoenvironmental conditions, including the availability of moisture and rainfall (e.g., Kleinert & Strecker, 2001; Starck & Anzótegui, 2001). Northwest Argentina is well suited for studies attempting to characterize these issues, because in addition to many sedimentological and paleontological indicators, stable isotopes measured on hydrated volcanic glass or pedogenic carbonates and authigenic clay minerals provide a valuable resource to assess paleoenvironmental change (e.g., Latorre *et al.*, 1997; Chamberlain & Poage, 2000; Blisniuk & Stern, 2005; Mulch *et al.*, 2008, 2010; Cassel *et al.*, 2012). Volcanoes located within the volcanic arc and on the Puna plateau have been repeatedly active since the late Miocene (Francis & de Silva, 1989). This has resulted in extensive ash-fall deposits within the eastern Andean intermontane basins and foreland regions, providing unique radiometrically datable event horizons that allow spatiotemporal tracking of environmental change associated with mountain building.

During the past two decades new developments in stable-isotope geochemistry and modeling efforts applied to paleoaltimetry topics have led to significant advances in determining paleo-elevations, resulting in new insights into the topographic development of orogens (e.g., Chamberlain & Poage, 2000; Rowley *et al.*, 2001; Mulch *et al.*, 2004; Garzione *et al.*, 2004, 2006; Kent-Corson *et al.*, 2006; Mulch *et al.*, 2007;

Garzione *et al.*, 2008; Mulch *et al.*, 2008; Poulsen *et al.*, 2010; Insel *et al.*, 2012b; Chamberlain *et al.*, 2012; Hoke *et al.*, 2014a,b). One particular method to investigate the relationship between tectono-sedimentary events and paleoenvironmental change, such as surface uplift and hinterland aridification following orographic barrier formation, is to analyze hydrated volcanic glass shards for their hydrogen stable-isotope composition as a proxy for surface uplift and associated climatic shifts (e.g., Friedman *et al.*, 1993a,b; Shane & Ingraham, 2002; Mulch *et al.*, 2008; Cassel *et al.*, 2012; Dettinger, 2013; Canavan *et al.*, 2014; Carrapa *et al.*, 2014; Cassel *et al.*, 2014; Quade *et al.*, 2015, and this study). This innovative approach is possible, because rhyolitic glass incorporates significant amounts of meteoric water after deposition (e.g., Friedman *et al.*, 1993a,b; Shane & Ingraham, 2002). Rainfall and surface-water isotopic composition generally shows a negative vertical correlation with elevation at which rainfall occurs and, among other factors, is sensitive to variations in the amount of precipitation (e.g., Dansgaard, 1964). Since the glass-hydration process occurs with a systematic isotopic fractionation, the D/H-ratio of the glass (δD_g) represents a unique fingerprint of the hydrogen-isotope composition of meteoric water present at that time. This allows the reconstruction of the isotopic composition of paleo-precipitation, which is an important indicator for long-term changes in precipitation patterns and continental moisture transport (e.g., Mulch *et al.*, 2008).

2.1 Geological setting

The South American Andes are the largest active subduction orogen on Earth (e.g., James, 1971; Jordan *et al.*, 1983). In addition, the Central Andes of Bolivia, northern Chile, and northwestern Argentina host the second largest orogenic plateau, the Andean Altiplano-Puna plateau, with a north-south extent of more then 1,500 km (e.g., Allmendinger *et al.*, 1997). The Puna Plateau, the southern part of this arid and largely internally drained region, is at an average elevation of ~4.4 km (Whitman *et al.*, 1996). In comparison to the northern Altiplano, which is characterized by very low relief due to large, contiguous sedimentary basins, the Puna plateau is characterized by north-south oriented, fault-bounded mountain ranges that dissect the landscape and constitute a compressional basin-and-range topography with structural similarities to the adjacent Eastern Cordillera and its intermontane basins (Strecker et al., 2009). During the Cenozoic Andean orogeny a number of other morphotectonic provinces have formed in northwestern Argentina (Fig. 2.1c, Jordan *et al.*, 1983; Allmendinger *et al.*, 1983). These include the Eastern Cordillera and the Sierras Pampeanas provinces that delimit the eastern Puna plateau margin. To the north of the area analyzed in this thesis, the thick-skinned thrust belt of the Eastern Cordillera is characterized by high relief, external drainage, and contains a series of reverse-fault bounded intermontane basins (Marrett *et al.*, 1994; Mon & Salfity, 1995; Kley *et al.*, 1996; Kley, 1996; Marrett & Strecker, 2000; Hilley & Strecker, 2005; Coutand *et al.*, 2006; Strecker *et al.*, 2007b, 2009). The Sierras Pampeanas to the south are a Laramide-style, thick-skinned basement uplift province (Jordan & Allmendinger, 1986).

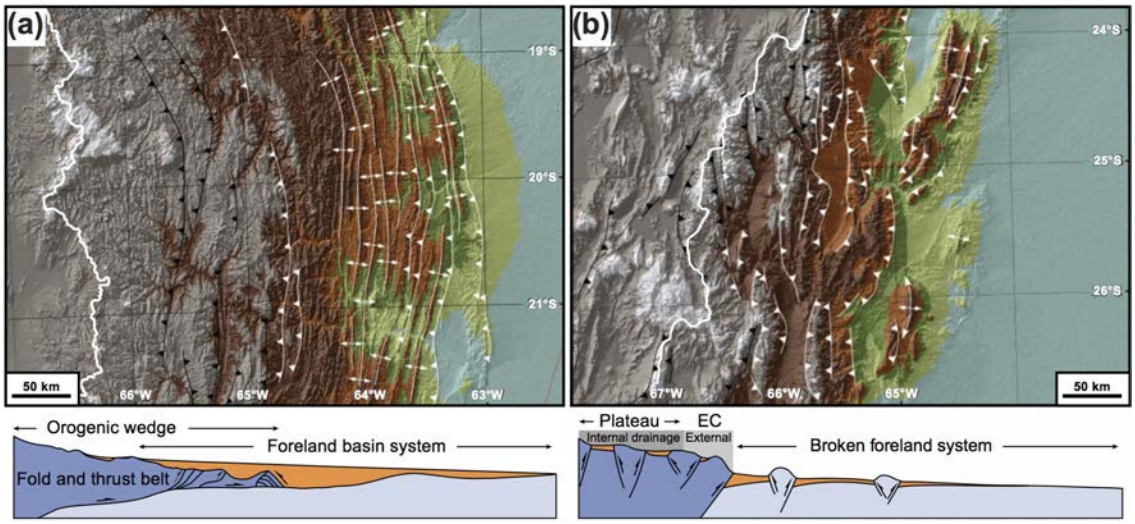

Figure 2.2 – Topographic and structural differences between (a) the thin-skinned foreland-basin system of southern Bolivia and NW Argentina as described in DeCelles & Giles (1996) and (b) the broken foreland of NW Argentina, modified after Strecker *et al.* (2011).

The basement-cored ranges are highly disparate in space and time and constitute a broken foreland with numerous, only partly connected depositional centers (e.g., Jordan *et al.*, 1983; Ramos *et al.*, 2002). In southern Bolivia and northern Argentina, the Eastern Cordillera transitions into the active, thin-skinned fold-and-thrust belt of the Sierras Subandinas (e.g., Gubbels *et al.*, 1993; Echavarría *et al.*, 2003). Here, deformation is predominantly accommodated by folding associated with shallow detachment faults (e.g., Dunn *et al.*, 1995) and extensive thrusting of thick Paleozoic and Mesozoic units (e.g., Echavarría *et al.*, 2003). This, however, is not the case in the NW-Argentine Santa Bárbara System, which is structurally transitional between the Sierras Subandinas and the Sierras Pampeanas. In the Santa Bárbara System shortening is accommodated along steeply dipping, inverted normal faults that initially formed during Cretaceous extension (e.g., Grier *et al.*, 1991; Kley, 1996; Kley & Monaldi, 2002; Kley *et al.*, 2005). As a consequence of normal-fault inversion and the lack of a thick sedimentary cover (e.g., Allmendinger & Gubbels, 1996, and references therein), the Santa Bárbara System is characterized by spatially disparate range uplifts and intervening sedimentary basins at low elevation. These characteristics thus markedly differ from the thin-skinned foreland-basin system in Bolivia to the north (e.g., DeCelles & Giles, 1996) and constitute a highly differentiated broken-foreland (Fig. 2.2). The structural, topographic, and sedimentological processes of this region are therefore similar to the Sierras Pampeanas of Argentina (e.g., Jordan & Allmendinger, 1986; Mortimer *et al.*, 2007) and other Cenozoic broken-foreland belts worldwide (e.g., Sobel & Strecker, 2003).

Cenozoic crustal shortening in the southern Central Andes commenced in Eo-Oligocene time and was marked by widespread range uplift and exhumation along reactivated, inherited structures in the realm

of the present-day Puna plateau (Kraemer *et al.*, 1999; Carrapa *et al.*, 2005; Coutand *et al.*, 2001, 2006; Deeken *et al.*, 2006; Letcher, 2007; Hongn *et al.*, 2007; Insel *et al.*, 2012a). This is also documented by regional unconformities and growth strata in middle Eocene foreland deposits, which highlight the potential for the existence of an early broken foreland similar to the Sierras Pampeanas (Hongn *et al.*, 2007; Del Papa *et al.*, 2013; Galli *et al.*, 2014). During the middle to late Miocene, deformation propagated eastward and affected the present-day Puna plateau margin in the Eastern Cordillera and the Santa Bárbara System, causing a progressive compartmentalization of the formerly contiguous foreland basin (Marrett & Strecker, 2000; Kleinert & Strecker, 2001; Sobel & Strecker, 2003; Deeken *et al.*, 2005, 2006; Coutand *et al.*, 2006; Mortimer *et al.*, 2007; Carrera & Muñoz, 2008; Siks & Horton, 2011; Hain *et al.*, 2011, and this study). This stage of deformation involved a pattern of diachronous and spatially disparate range uplifts associated with the formation of intermontane basins along the Puna margin (reviewed in Strecker et al., 2009). Deformation in the area of the Santa Bárbara System has been active since ca. 10 Ma (Sierra de Metán), but it has been more widespread since the Pliocene (e.g., Reynolds *et al.*, 2000; Hain *et al.*, 2011; González Bonorino & del Valle Abascal, 2012).

Presently, virtually all intermontane basins in northwestern Argentina are fluvially connected with the foreland base level, and most of them have experienced severed fluvial conditions associated with multiple phases of up to km-scale basin filling and subsequent re-excavation during the Plio-Pleistocene (e.g., Strecker *et al.*, 2007a, 2009). This variability in basin behavior is attributed to a range of mechanisms, entailing Pliocene range uplift, associated orographic effects, and reduced fluvial connectivity. In this setting, the hinterland fluvial system is cut off from the foreland and reduced rainfall amounts, due to the growth of orographic barriers, disable the export of locally produced sediment from the hillslopes (e.g., Hilley & Strecker, 2005; Hain *et al.*, 2011). In addition, regional climate variations can cause temporary wetter conditions in the hinterland, for example during pluvial episodes, which may lead to enhanced slope instabilities and greater sediment production, which may further reduce stream power.

2.2 Climatic setting

Due to its vast latitudinal extent and areally extensive high elevations, the Central Andes constitute a first-order topographic barrier to atmospheric circulation, resulting in extreme across-strike gradients in moisture availability (e.g., Bianchi & Yañez, 1992; Bookhagen & Strecker, 2008). For example, the eastern slopes of the Central Andes receive relatively large amounts of rainfall of more than 3,000 mm/yr (Fig. 2.1) and are characterized by a dense vegetation cover. In contrast, orogen-interior regions, such as the high-elevation Puna plateau to the west and the transitional intermontane basins along its eastern margin, receive progressively less rainfall (<200 mm/yr) and are characterized by semi-arid to arid conditions (e.g., Bianchi & Yañez, 1992; Bookhagen & Strecker, 2008). This contrast in the spatial distribution and amount of rainfall is accompanied by a strong gradient in fluvial runoff and efficiency of surface processes,

which results in very low erosion rates on the internally-drained and low-relief plateau area compared to higher rates in the externally-drained high-relief sector of the Eastern Cordillera (e.g., Strecker *et al.*, 2009; Bookhagen & Strecker, 2012).

Presently, moist air masses from the Atlantic Ocean and the Amazon Basin are transported towards the Andes via the seasonal South American Monsoon system (Seluchi *et al.*, 2003; Vera *et al.*, 2006a,b), with peak rainout along the Andes during the austral summer (~80% of annual precipitation; Bianchi & Yañez, 1992). These air masses are being deflected to the south as they impinge on the high-elevation, eastern Andean flanks. Moisture is thus transported into subtropical regions of South America that are otherwise characterized by generally arid conditions. Climate modeling suggests that a minimum of ~50% of the modern Andean topography has to be attained to achieve comparable topographic-atmospheric interactions as seen today (e.g., Ehlers & Poulsen, 2009; Poulsen *et al.*, 2010). Evidence from the geological record in northwestern Argentina and southern Bolivia, along the present-day Altiplano-Puna plateau margin, suggests that this attainment of topography may have been reached between approximately 10 and 8 Ma (e.g., Starck & Anzótegui, 2001; Uba *et al.*, 2009; Mulch *et al.*, 2010). Other interpretations, in contrast, have argued for generally high elevations on the plateau since Eo-Oligocene time, based on disparate stable-isotope records from sedimentary basins in the Puna region (e.g., Canavan *et al.*, 2014; Quade *et al.*, 2015).

2.3 Research questions

Against the background of the rich interactions between tectonics, climate and surface processes in the NW Argentine Andes this thesis mainly focuses on the development and evolution of intermontane basins within the Eastern Cordillera and the broken foreland basin of the Santa Bárbara System of NW Argentina. Due to numerous well-dated sedimentary sections and newly dated volcanic ash horizons in the course of this thesis such a focus enables analyzing spatiotemporal changes and patterns of tectonism in basins of the principal morphotectonic provinces and adjacent mountain ranges. In addition, this approach furnishes valuable insight into the different styles of sedimentation and climatic shifts that are associated with topographic growth perpendicular to the major moisture-bearing wind systems. The main aim of this study is thus to answer the following thematically linked, principal research questions that address the late Cenozoic topographic evolution of the southern Central Andes:

i) What are the tectono-sedimentary characteristics of the intermontane Humahuaca Basin of the NW-Argentine Eastern Cordillera flanking the eastern Puna margin at ca. 23° S? What are the mechanisms that caused basin-fill and excavation cycles in the basin, and how do these processes relate to repeated intra-basin deformation over time? (Chapter 3)

ii) What is the timing of range uplift and orographic barrier formation in the area of the present-day Humahuaca Basin, and are these changes reflected in the hydrogen stable-isotope composition of volcanic

glass? If so, what can we learn from the isotopic trends in terms of surface-uplift rates vs. the onset of enhanced aridity in the hinterland? What is the impact of hinterland aridification on the development and maintenance of the Puna plateau as an internally drained morphotectonic entity? (Chapter 4)

iii) What are the spatiotemporal patterns of foreland-basin fragmentation across the transition between the Eastern Cordillera and the Santa Bárbara system at ca. 25° S? What are the mechanisms for increased sediment accumulation in currently externally drained intermontane basins? (Chapter 5)

iv) In light of recent insights into the influence of convective storms on modern stable-isotope compositions of meteoric water (e.g., Rohrmann *et al.*, 2014), research on the evolution of topography in the Central Andes during the geological past faces several challenges and questions: given the regional differentiation in isotopic fractionation of meteoric waters, is paleoaltimetry based on stable isotopes a feasible tool for estimating paleoelevations south of ~25° S? Has the atmospheric circulation been constant or has it fluctuated on longer timescales involving fundamental environmental change during the Mio-Pliocene? What consequences may this have for paleoaltimetry estimates in this region? Is it possible to track atmospheric-scale changes through time to decipher the origin and mechanisms of enhanced convective rainfall in this region or surface uplift during episodes of reduced convection? (Chapter 6)

Chapter 3

Neotectonic basin & landscape evolution in the Eastern Cordillera of NW Argentina, Humahuaca Basin (~24° S)*

Heiko Pingel[1], Manfred R. Strecker[1], Ricardo N. Alonso[2] and Axel K. Schmitt[3]

[1]*DFG Leibniz Center for Surface Process & Climate Studies, Institut für Erd- & Umweltwissenschaften, Universität Potsdam, Germany*

[2]*Departamento de Geología, Universidad Nacional de Salta, Salta, Argentina*

[3]*Department of Earth & Space Sciences, University of California - Los Angeles, CA, USA*

Abstract

The intermontane Quebrada de Humahuaca Basin (Humahuaca Basin) in the Eastern Cordillera of the southern Central Andes of NW Argentina (23°- 24° S) records the evolution of a formerly contiguous foreland-basin setting to an intermontane depositional environment during the late stages of Cenozoic Andean mountain building. This basin has been and continues to be subject to shortening and surface uplift, which has resulted in the establishment of an orographic barrier for easterly sourced moisture-bearing winds along its eastern margin, followed by leeward aridification. We present new U–Pb zircon ages and palaeocurrent reconstructions suggesting that from at least 6 Ma until 4.2 Ma, the Humahuaca Basin was an integral part of a largely contiguous depositional system that became progressively decoupled from the foreland as deformation migrated eastward. The Humahuaca Basin experienced multiple cycles of severed hydrological conditions and subsequent re-captured drainage, fluvial connectivity with the foreland and sediment evacuation. Depositional and structural relationships among faults, regional unconformities and deformed landforms reveal a general pattern of intrabasin deformation that appears to be associated with different cycles of alluviation and basin excavation in which deformation is focused on basin-internal structures during or subsequent to phases of large-scale sediment removal.

* *published in Basin Research (2013) vol. 25, p. 554–573, doi: 10.1111/bre.12016*

3.1 Introduction

To understand the spatiotemporal evolution of tectonically active range fronts in mountain belts, it is essential to unravel the relationships between styles and rates of tectonic deformation, surface uplift, and the distribution of precipitation and surface processes that reflect relief and local climatic conditions. This evolution may be partially recorded by the sedimentary deposits preserved in intermontane basins in the peripheral sectors of an orogen, in the compartmentalized basins within broken forelands, or farther away in adjacent foreland basins.

Sediment accumulation within contiguous foreland basins is predominantly determined by the flexural response of the crust to the topographic load from an adjacent fold-and-thrust belt and from the sediments derived from the orogen (e.g., Beaumont, 1981; DeCelles & Giles, 1996). As a fundamental characteristic of foreland basins, protracted deformation and coeval deposition progressively extend into the previously undeformed, distal foreland regions, with the orogenic deformation front and associated sedimentary facies patterns advancing in a systematic spatiotemporal pattern (e.g., DeCelles & Giles, 1996). In contrast, broken foreland basins may develop in regions where shortening is accommodated along reactivated high-angle structures inherited from former tectonic regimes (Jordan & Allmendinger, 1986; Jordan & Alonso, 1987), often leading to highly diachronous and spatially disparate basement uplifts (reviewed in Strecker *et al.*, 2011). Isolated range uplifts promote much more subdued flexural subsidence with accommodation space that is limited to the margins of the individual ranges (Strecker *et al.*, 2011). If these tectonic characteristics are paired with arid climate conditions, headwater basins can become isolated from the downstream fluvial network, leading to sediment accumulation between uplifting ranges (Meyer *et al.*, 1998; Sobel *et al.*, 2003; Hilley & Strecker, 2005). Over geological timescales, an array of isolated to variably connected and laterally restricted depocentres may develop, forming a landscape similar to the partially coalesced basins observed in Cenozoic orogenic plateaus and their flanks, such as the southern part of the Andean Altiplano-Puna Plateau or the Tibetan Plateau and the adjacent Qilian Shan in Asia (Meyer *et al.*, 1998; Sobel *et al.*, 2003; Alonso *et al.*, 2006; Strecker *et al.*, 2009).

The dynamics of basin hydrology in these environments may depend on a type of competition between uplift of downstream ranges, which favours fragmentation of the fluvial network, and headward incision, which promotes the persistence or re-integration of rivers draining the periphery of these orogens (Sobel *et al.*, 2003; Hilley & Strecker, 2005; Garcia-Castellanos, 2007). As a result, changes in climatic conditions or tectonic rates may cause these marginal basins along the flanks of an orogenic plateau to transition between conditions in which fluvial connectivity is promoted or basins are hydrologically isolated from their downstream watersheds. These alternations in the fluvial network are expected to influence the rate and tempo of sediment removal from the interior of the orogen to the unrestricted parts of foreland basins.

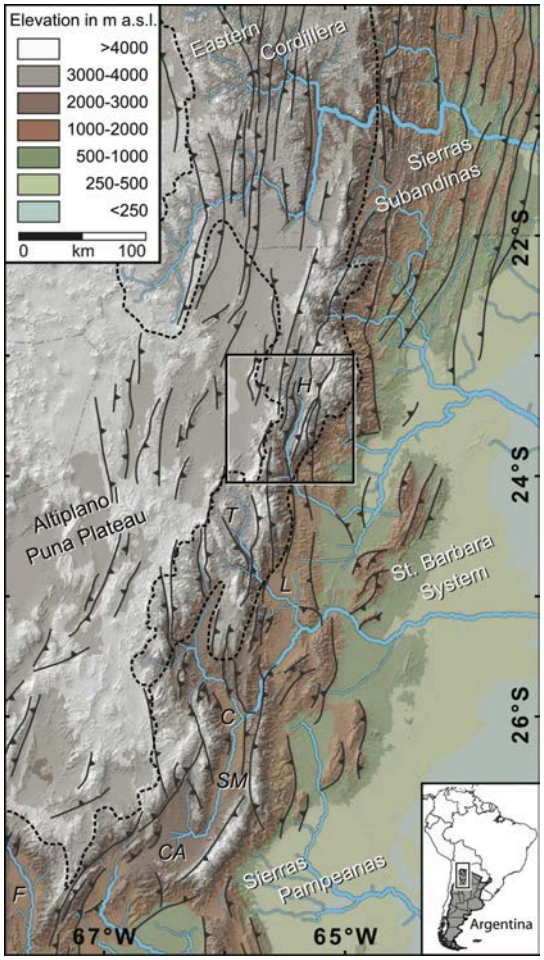

Figure 3.1 – Topography and east-draining river network of the southern Central Andes in NW Argentina and S Bolivia based on SRTM-GTOPO30. Structural information is taken from Kley *et al.* (1997), Allmendinger & Zapata (2000), Sobel *et al.* (2003), Carrapa *et al.* (2006), Mortimer *et al.* (2007), Uba *et al.* (2007), Mulch *et al.* (2010) and Hain *et al.* (2011). Dashed lines delineate morphotectonic domains. Letters relate to major intermontane basins in NW Argentina discussed in the text: H – Quebrada de Humahuaca; T – Quebrada del Toro; L – Lerma Basin; C – Calchaquí Basin; SM – Santa María Basin; CA – El Cajón-Campo Arenal Basin; F – Bolsón de Fiambalá Basin. Black box indicates location of Fig. 3.2.

The Andean broken foreland areas of the northern Sierras Pampeanas, the Santa Bárbara System and parts of the Eastern Cordillera of NW Argentina (Fig. 3.1) illustrate the complex morphology resulting from tectonic uplift, basin formation and basin excavation along the eastern flanks of the orogenic Altiplano-Puna Plateau. While field studies in this region show that rivers connecting intermontane basins with the foreland are often interrupted due to spatial and temporal changes in deformation, climate and the erodibility of exposed bedrock (e.g., Hilley & Strecker, 2005), predicting the combinations of driving factors responsible for alternating states of basin isolation and fluvial connectivity is still difficult. Deposits preserved in the intermontane basins are often deformed, faulted and frequently show syntec-

tonic growth as a result of initial foreland fragmentation and out-of-sequence deformation, demonstrating clear tectonic influence on basin sedimentation (for a summary see Hilley & Strecker, 2005; Strecker *et al.*, 2011). Moreover, regional unconformities show that large volumes of sediment have been rapidly removed from these basins once they have been re-captured (e.g., Hilley & Strecker, 2005; Strecker *et al.*, 2009). These superposed processes raise an interesting and as yet unexplored possible feedback between the re-integration of these intermontane basins with the foreland through fluvial connectivity and renewed faulting within the orogenic realm following the removal of sedimentary loads. While these relationships among tectonics, sedimentation and erosion have been suspected to exist in many intermontane basins of the NW Argentine Andes (Strecker *et al.*, 1989, 2009; Hilley & Strecker, 2005; Alonso *et al.*, 2006), the timescales for individual filling and excavation cycles have remained poorly constrained.

A rich record of frequently intercalated volcanic ashes in the sediments of the southern Humahuaca Basin of NW Argentina (~23.5° S, Fig. 3.1) provides the requisite chronology to quantify temporal associations among tectonics, climate and sedimentation on the scale of a single intermontane basin. In our study, we present new chronostratigraphic ($^{206}Pb/^{238}U$ zircon and AMS ^{14}C), structural and sedimentological data for various preserved conglomeratic basin fills within the Humahuaca Basin and document that (a) the transition between a largely continuous foreland depositional environment and a subsequent fault-bounded intermontane basin is related to more pronounced surface uplifts to the east after ~4.2 Ma; (b) the intermontane basin stage has been characterized by multiple cycles of basin filling and subsequent sediment removal; and, although speculative, (c) out-of-sequence reactivation of faults within the basin may be closely linked with sediment evacuation.

3.2 Regional & geologic setting

The Humahuaca Basin (Jujuy Province) is the northernmost intermontane sedimentary basin in an array of reverse-fault bounded basins within the Eastern Cordillera of NW Argentina along the eastern Puna Plateau margin, the southern extension of the Bolivian Altiplano (Fig. 3.1). The Humahuaca Basin is surrounded by highelevation mountain ranges exceeding 5,000 m a.s.l. that consist of smaller reverse and thrust fault-bounded blocks. The Sierra Alta separates the basin from the internally drained and arid Puna Plateau to the west, while the Tilcara ranges constitute the boundary with the humid foreland depositional system to the east. At present, the Humahuaca Basin is connected to the foreland via a narrow, fault-bounded bedrock gorge to the south, through which the Río Grande exits the basin (Figs 3.2 and 3.9). Here, the course of the Río Grande firstly follows and then obliquely crosses the trace of the west-dipping reverse fault that bounds the southern sector of the Tilcara ranges.

Basement blocks constitute the basin-bounding ranges that have been uplifted along north to northnortheast striking, bivergent thrust and reverse-fault systems (Rodríguez Fernández *et al.*, 1999; Kley *et al.*, 2005, Fig. 3.2). At the latitude of the Humahuaca Basin, the eastern margin of the neighbour-

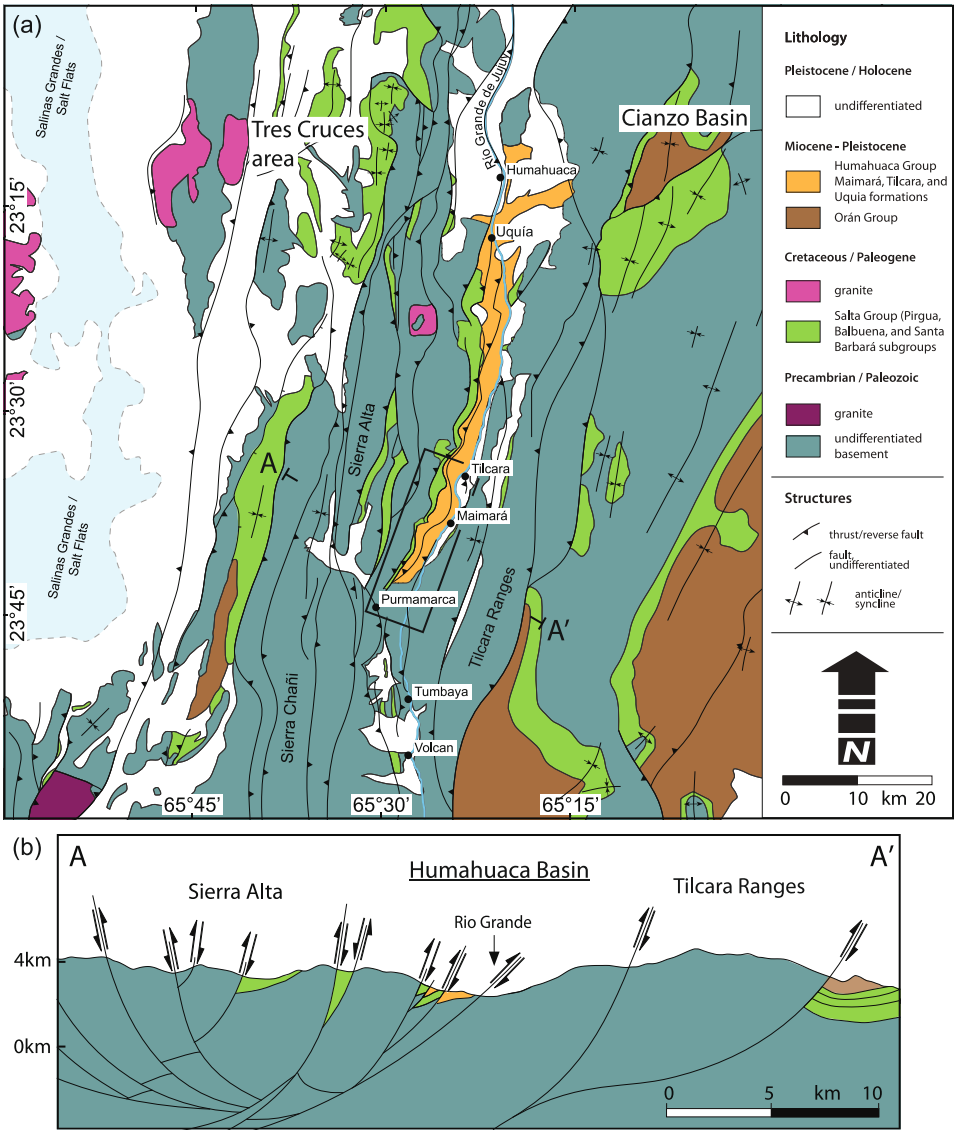

Figure 3.2 – (a) Simplified geology of the Humahuaca Basin and surroundings and (b) geological cross section after Rodríguez Fernández *et al.* (1999) and own data. Black box indicates the area mapped in detail (Fig. 3.3a).

ing Altiplano-Puna Plateau records a middle Eocene to Oligocene deformation history, influenced by pre-existing crustal heterogeneities and structures that were reactivated during Cenozoic compression (Coutand *et al.*, 2001, 2006; Deeken *et al.*, 2006; Hongn *et al.*, 2007; Insel *et al.*, 2012a). Between 10 and 8 Ma, the eastern plateau margin apparently attained sufficient elevation and relief to intercept moisture-bearing easterly winds; this topography constituted a major orographic barrier to atmospheric circulation on a hemispheric scale, resulting in the aridification of the orogen interior and the establishment of humid conditions on the eastern flanks (Allmendinger *et al.*, 1997; Kleinert & Strecker, 2001; Starck & Anzótegui, 2001; Strecker *et al.*, 2007a; Uba *et al.*, 2007; Carrapa *et al.*, 2008; Mulch *et al.*, 2010; Vezzoli

et al., 2012). During the Mio-Pliocene, deformation migrated into the present-day Eastern Cordillera, where the formerly contiguous foreland basin was partitioned by regional range uplifts. This deformation is spatially disparate, highly diachronous (reviewed in Strecker *et al.*, 2007a, 2009) and ongoing (Bevis & Isacks, 1984; Cahill *et al.*, 1992, USGS/NEIC PDE-catalogue).

The basement rocks exposed along the flanks of the Humahuaca Basin comprise tightly folded late Proterozoic to early Palaeozoic low-grade metasediments of the Puncoviscana Formation (Turner, 1960; Omarini, 1983). These units are unconformably overlain by Cambro-Ordovician sandstones and quartzites of the Mesón and Santa Victoria groups (Moya, 1988; Sánchez & Salfity, 1999; Aceñolaza, 2003). An angular unconformity separates these sediments from the late Cretaceous to Palaeogene Salta Group related to the Cretaceous Salta Rift (Salfity, 1982; Galliski & Viramonte, 1988; Marquillas *et al.*, 2005). The most prominent strata of these sequences exposed in the southern Humahuaca Basin are continental red beds of the Pirgua Subgroup, white sandstones and yellow-coloured marine carbonates of the Lecho Formation and the stromatolitic Yacoraite Formation (Balbuena Subgroup), respectively, and fluvial deposits of the Lumbrera Formation (Santa Bárbara Subgroup). For detailed reviews, see Marquillas *et al.* (2005) and Sánchez & Marquillas (2010).

These lithologies are typically overlain by early Cenozoic foreland sediments such as the Quebrada de los Colorados Formation (middle Eocene-Oligocene), the deposits of the Orán Group (Mio-Pliocene) or equivalent strata (Gebhard *et al.*, 1974; Russo & Serraiotto, 1978; Díaz & Malizzia, 1984; Vergani & Starck, 1989a; Coutand *et al.*, 2001) in the Puna and present-day foreland regions to the east of the study area. However, these sediments have mostly been removed in the highly exhumed Eastern Cordillera (Jordan & Alonso, 1987; Kley *et al.*, 2005). A regional exception to this general pattern is a *ca.* 6-km thick succession of middle Eocene to Pliocene foreland and intermontane basin deposits in the Cianzo Basin of the Eastern Cordillera, 20 km east of the town of Humahuaca (details in Siks & Horton, 2011). Strata overlying the Salta Group in the Humahuaca Basin largely consist of weakly consolidated, mainly conglomeratic deposits that reflect a complex history of deposition, erosion and deformation that spans the late Miocene and Quaternary.

Three major units have previously been described: the Maimará Formation (Salfity *et al.*, 1984), the Uquía Formation (Castellanos, 1950; Marshall *et al.*, 1982; Walther *et al.*, 1998) and thick conglomeratic fills of Quaternary age (Tchilinguirian & Pereyra, 2001; Robinson *et al.*, 2005; Strecker *et al.*, 2007a; Sancho *et al.*, 2008). In the following sections, we will refine this stratigraphic framework for the southern part of the Humahuaca Basin and focus our attention on its distinct volcanic ash-bearing conglomerates and sandstones that document sustained deposition, deformation and erosion in the basin, and which provide excellent stratigraphic markers to assess the late Cenozoic basin evolution.

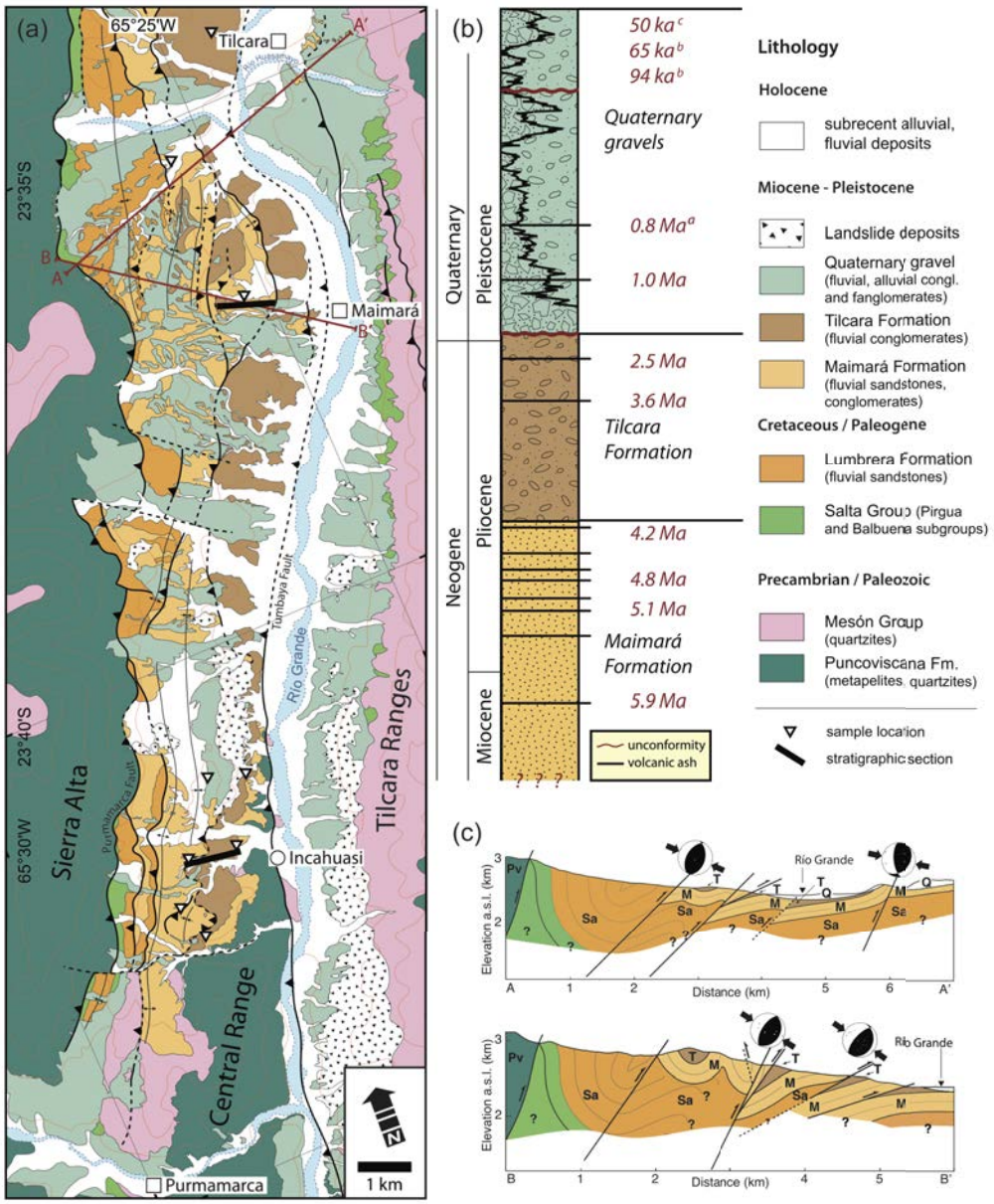

Figure 3.3 – (a) Geological map of the central study area between Tilcara and Purmamarca in the southern Humahuaca Basin. Triangles represent U–Pb zircon sample locations (see Table S1) and thick black lines show the position of measured stratigraphic sections from Fig. 3.6. Map is rotated anti-clockwise by 20°. (b) Simplified late Cenozoic chronostratigraphy of the study area. Unless otherwise indicated, values represent averaged U–Pb zircon ages from this study. [a] $^{40}Ar/^{39}Ar$–biotite (Strecker *et al.*, 2007a); [b] OSL–quartz (Robinson *et al.*, 2005; Sancho *et al.*, 2008); [c] AMS ^{14}C (this study). (c) Subsurface interpretations of severely deformed strata. Shown are pseudo-fault-plane solutions calculated from fault-kinematic indicators documenting thrust kinematics during the Pliocene. Pv, Puncoviscana Fm; Sa, Salta Group; M, Maimará Fm; T, Tilcara Fm; Q, Quaternary gravels.

3.3 Methods

We used stratigraphic and structural analysis, together with detailed geological mapping of exposed units (Fig. 3.3), regional unconformities, sediment provenance, lateral facies pinch-outs and lithological contacts to document the tectono-sedimentary history of the southern Humahuaca Basin. A similar approach is used in an ongoing chronostratigraphic study of the northern Humahuaca Basin (Streit *et al.*, 2012).

Despite apparent similarities between the various synorogenic lithologies, spatiotemporal changes in the sediment sources result in distinct differences among the conglomeratic fill units in the Humahuaca Basin. We characterized the compositional differences of the fills by counting at least 100 clasts from within a 0.25 m^2 grid in key stratigraphic units. To deduce sediment provenance and transport directions for ancient river systems, we measured ~1,600 imbricated clasts at 33 localities. Where possible, we measured the orientation of at least 50 clasts per site, applied corrections for structural dip and displayed them in unidirectional rose diagrams using OSXStereonet software (by N. Cardozo & R. Allmendinger).

To provide a chronological base for different tectonic and sedimentological events, we dated 12 volcanic ash deposits interbedded in the Mio-Pleistocene basin strata using U–Pb zircon geochronology. Samples were crushed, sieved and treated with standard heavy-liquid and magnetic separation techniques to isolate zircon crystals. About 30 crystals per sample were handpicked, mounted in epoxy, polished and cleaned, and then gold-coated for microprobe analysis. Crystals free of inclusions, or cracks were selected for U–Pb analysis using the CAMECA IMS 1270 ion microprobe at the University of California in Los Angeles, following protocols described in Schmitt *et al.* (2003) and Grove *et al.* (2003). The $^{206}Pb/^{238}U$ ages have been corrected for common Pb and initial disequilibrium. The uncertainties in U–Pb ages, estimated from the reproducibility of standard AS3 zircons (1,099.1 Ma; Paces & Miller, 1993), were 2.2% and 2.7% (1 standard deviation) for the analytical sessions in July 2009 and June 2010, respectively.

3.4 Results

3.4.1 U–Pb zircon geochronology

Most analysed samples show complex zircon age distributions. This could be due to protracted pre-eruptive crystal residences (e.g., Schmitt *et al.*, 2003), or post-eruptive reworking in which case mixing and contamination with detrital crystals during emplacement would lead to the presence of multiple age populations. We therefore systematically omitted older ages from our calculations of an average zircon crystallization age. The statistically uniform younger age population was then used as an approximation for the depositional age, while acknowledging that this is likely to overestimate the eruption age because of pre-eruptive zircon crystallization (e.g. by ~0.1 Ma for the large-volume Atana ignimbrite; Schmitt *et al.*, 2001). Most samples yielded consistent $^{206}Pb/^{238}U$ ages for the majority of crystals, as indicated by

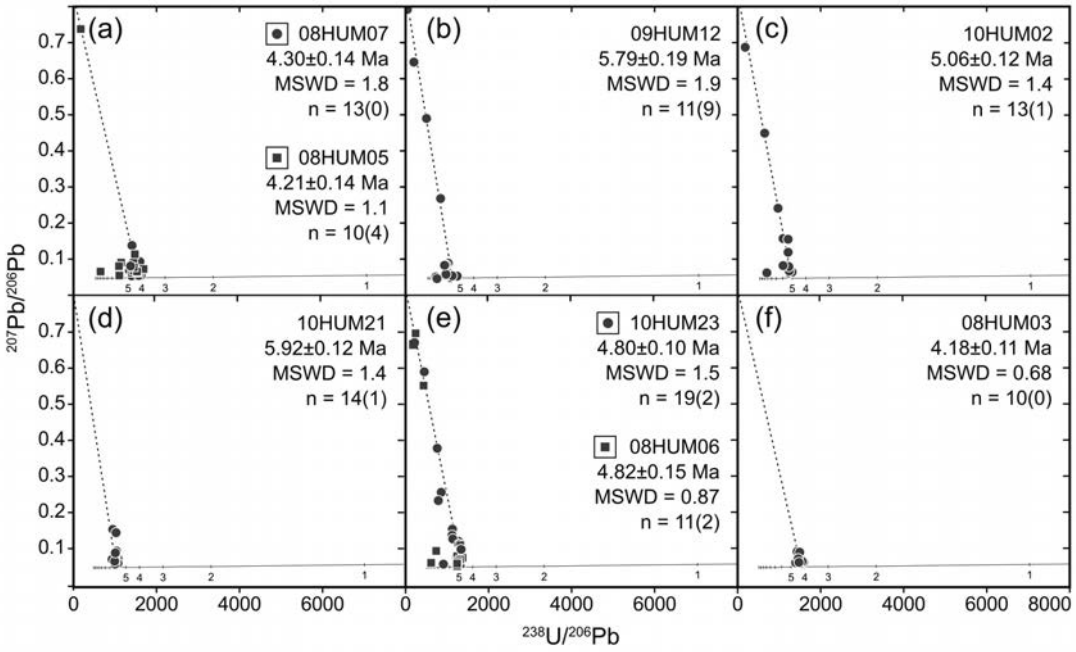

Figure 3.4 – $^{207}Pb/^{206}Pb$ vs. $^{238}U/^{206}Pb$ zircon data for Maimará samples, uncorrected for common Pb and regression lines with a fixed y-axis intercept corresponding to common Pb ($^{207}Pb/^{206}Pb = 0.83$). Concordia segment (ages in Ma) is plotted for initial disequilibrium D $^{230}Th/^{238}U = 0.2$ and D $^{231}Pa/^{235}U = 3$. Number of analyses excluded from regression is given in parentheses.

near-unity values for the mean square of weighted deviates (MSWDs), suggesting only minor reworking. In some cases, however, only a small percentage of the crystals defined a coherent young population; in these cases, we have interpreted the $^{206}Pb/^{238}U$ zircon age as the maximum age for deposition. Results are shown in Figs 3.3–3.5, and summarized in Table A.1.

3.4.2 Late Miocene to Pliocene stratigraphy

Maimará Formation

The ochre to yellow beds of the Maimará Formation unconformably overlie the older lithologies exposed in the basin, including the Proterozoic Puncoviscana Formation. The Maimará Formation generally comprises arkosic sandstones and interbedded cobble conglomerates, and is at least 250-m thick (Fig. 3.6). The matrix to clast-supported conglomerates are composed of well-rounded pebbles and cobbles, and occasionally boulders, mainly from Proterozoic (23.5% P_V) and Palaeozoic (64.5% P_Z) sources (Puncoviscana Fm. & Mesón Group). This unit also contains clasts of limestones and sandstones from the Cretaceous to Palaeogene Salta Group (12% C_R) and a minor proportion of lithic-rich, late Miocene to Pliocene ignimbrites with the nearest known exposures confined to the Puna Plateau to the west (e.g., Riller & Oncken, 2003).

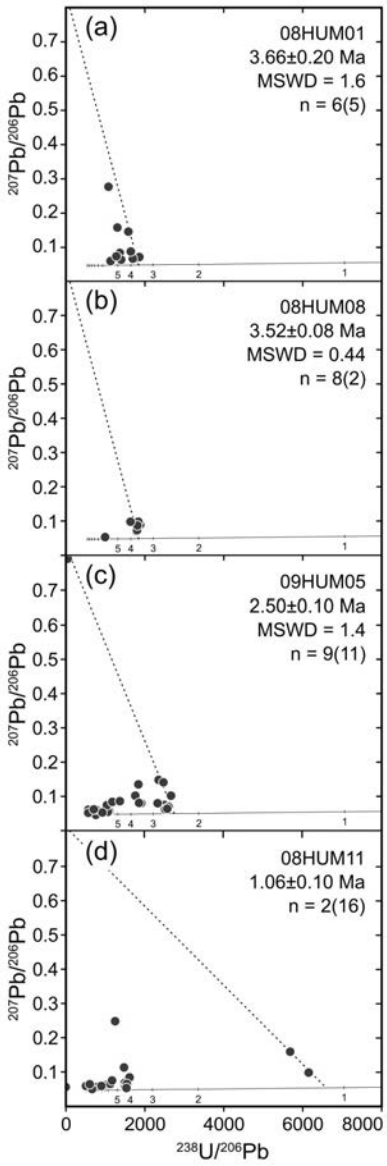

Figure 3.5 – $^{207}Pb/^{206}Pb$ vs. $^{238}U/^{206}Pb$ zircon data for Tilcara and Quaternary gravel samples, uncorrected for common Pb and regression lines with a fixed y-axis intercept corresponding to common Pb ($^{207}Pb/^{206}Pb = 0.83$). See caption of Fig. 3.4 for additional information.

The most complete section is exposed in the Quebrada de Maimará, west of the town of Maimará (Figs 3.3 and 3.6), where the succession has been thrust eastward over Pliocene conglomerates. Fossil-rich clay beds and siltstones dominate the basal 50 m of this section and contain freshwater ostracods (*Limnocythere sp.*; Fig. 3.8b) and intact calcic encrustations of charophyte oogonia. The following 200-m thick sequence of interbedded sandstones and conglomerates is intercalated with at least seven volcanic ash layers.

About 75 m of faulted strata of the Maimará Formation is also exposed at Incahuasi, located about 10 km south of the Quebrada de Maimará. This section unconformably overlies palaeo-relief developed in the Proterozoic to Palaeozoic basement and comprises several metre-thick banks of moderately consolidated fine-grained arkosic sandstones that are frequently intercalated with rhyolitic ash layers, debris-flow deposits and conglomeratic channel fills (Fig. 3.6). Further exposures of the Maimará Formation exist east of the town of Tilcara, along the Río Huasamayo, where the Maimará Formation has been thrust over late Pleistocene conglomerates (e.g., Salfity *et al.*, 1984; Marrett *et al.*, 1994, Fig. 3.8a).

The presence of ignimbrite clasts sourced in the Puna supports the notion of an eastward fluvial transport across the present-day Sierra Alta, the major mountain range that now constitutes the eastern margin of the Altiplano-Puna Plateau west of the basin. The notion of a western provenance is in agreement with our palaeocurrent estimates that demonstrate an east-southeast-directed palaeo-drainage system at that time (Fig. 3.7). We therefore conclude that the former fluvial network must have drained eastward across both ranges that now delimit the basin.

Our U–Pb zircon ages from various volcanic ashes (08HUM03; 08HUM05; 08HUM07; 09HUM12; 10HUM02; 10HUM21; 10HUM23; Figs 3.4 and 3.6; Table A.1) constrain that this depositional setting existed at least between 5.92 ± 0.12 Ma (MSWD = 1.4; n = 14) and 4.18 ± 0.11 Ma (MSWD= 0.68; n= 10).

Tilcara Formation

In the southern Humahuaca Basin, the Maimará Formation is overlain by a series of metre-thick interbedded conglomerate, fanglomerate and sandstone beds, at least 250-m thick, which also contain volcanic ash layers. The transition to subsequent lithologies is always characterized by a pronounced regional unconformity, rendering all measurements of total sediment thickness minimum estimates (Figs 3.8c, d). In contrast to the Maimará Formation, the poorly consolidated strata comprise well-rounded and well-imbricated pebble- to boulder-sized clasts with only a minor quantity of Salta Group clasts, but no ignimbrites (27.5% P_V; 71% P_Z; 1.5% C_R). Carbonate cementation of conglomerates occurs in metre-thick beds. The nearly filled pore spaces, within such beds, suggest advanced pedogenic K-horizon formation (e.g., Gile *et al.*, 1965; Machette, 1985), a common feature associated with conglomerate deposits in the semi-arid environments of the southern Central Andes (e.g., Strecker *et al.*, 1989). Clast-imbrication measurements record a change to a southerly direction of sediment transport (Figs 3.6 and 3.7). While on average, this change demonstrates a rotation of *ca.* 20° south (Fig. 3.7), palaeocurrent directions measured along continuous sections reflect a dramatic reorganization of the fluvial system by >90° (Fig. 3.6).

Two ashes sampled in the lower part of the section (08HUM01 and 08HUM08) yielded overlapping U–Pb zircon ages of 3.66 ± 0.20 (MSWD = 1.6; n = 6) and 3.52 ± 0.08 Ma (MSWD = 0.44; n = 8; Fig. 3.5; Table A.1). Because these age determinations are statistically indistinguishable, we consider them to represent the same ash horizon. A second ash layer from the upper section (09HUM05) yielded a significantly younger $^{206}Pb/^{238}U$ zircon age of 2.50 ± 0.10 Ma (MSWD = 1.4; n = 9; Fig. 3.5; Table A.1).

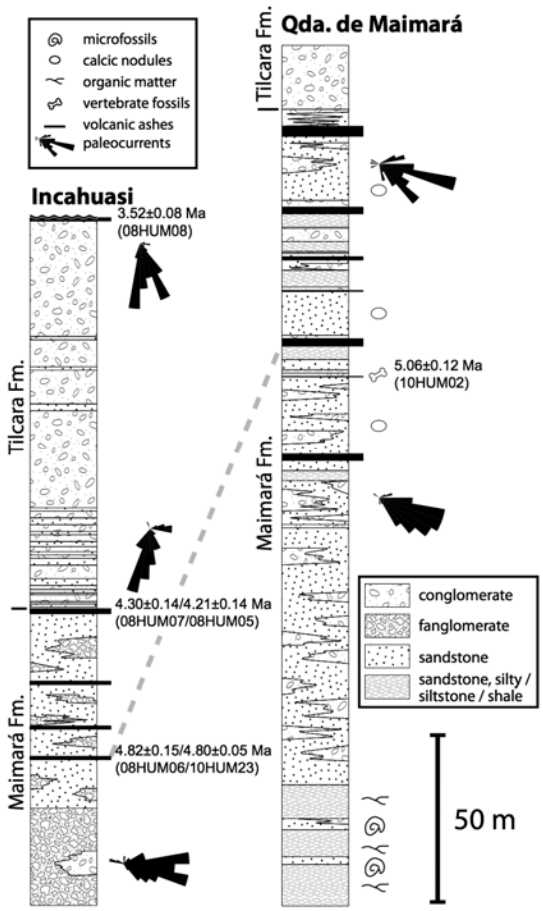

Figure 3.6 – Measured stratigraphic sections located near Incahuasi and in the Quebrada de Maimará. Detailed locations are given in Fig. 3.3a.

Previous stratigraphic and palaeontological studies have shown that in the northern Humahuaca Basin, strata of the Maimará Formation are overlain by the fossil-bearing fluvial Uquía Formation. This unit comprises mud and sandstones with occasional conglomeratic beds and interbedded volcanic ash horizons (Castellanos, 1950; Reguero *et al.*, 2007). Clast counts for the Uquía Formation at a limited number of outcrops reveal ~10% Proterozoic rocks (Puncoviscana Fm.) and ~90% Palaeozoic rocks (Mesón Group). Age determinations of a basal volcanic ash from the Uquía Formation (3.54 ± 0.04 Ma, Marshall *et al.*, 1982) and from within the upper third of the section (zircon fission-track age ~2.5 Ma, Walther *et al.*, 1998) are in good agreement with our chronology of the Tilcara Formation. Furthermore, palaeomagnetic results from the Uquía Formation (Marshall *et al.*, 1982) imply that its uppermost strata may be as young as ~1.5 Ma. As the topmost section of the Tilcara Formation is not preserved, we are unable to determine an upper depositional age limit. However, we infer that the timing of deposition was similar in both sub-basins. We consider this assumption to be valid because (a) we do not find any evidence of

other deposits between 2.5 and >1 Ma in the southern Humahuaca Basin, and (b) the oldest Quaternary sediments that cover both formations uniformly may be as old as ~1 Ma. It is therefore quite possible that the (unpreserved) top of the Tilcara Formation in the southern basin is temporally equivalent to the ~1.5 Myr old top of the Uquía Formation to the north.

Although chronostratigraphic investigations in the northern Humahuaca Basin are still ongoing (Streit *et al.*, 2012), we have sufficient evidence for lithological differences between the corresponding Plio- Pleistocene deposits in the two sub-basins to establish a new lithological unit in the southern basin: the Tilcara Formation. Our radiometric ages show that deposition of this unit took place between ~4.2 and 2.5 Ma and by correlation may have lasted until approximately 1.5 Ma.

Landslide deposits

We identified multiple voluminous landslide deposits south of Maimará village that unconformably cover older units along the eastern basin margin (Fig. 3.3a). These deposits predominantly consist of Palaeozoic and Cretaceous to Eocene rocks, and overlie previously exhumed Palaeozoic rocks that dip steeply westward. Multiple, pervasively shattered rock sheets with no stratigraphic context are located 60 m above the valley floor and appear to be sourced in the eastern basin-bounding range. In places, the landslide deposits have been subsequently covered by sub-horizontally bedded conglomerates of Pleistocene age. The depositional age of the landslide deposits can, therefore, be only crudely constrained to be older than the Pleistocene conglomerates.

To the west of the Río Grande and north of Incahuasi (Fig. 3.3a), a voluminous Quaternary landslide deposit that extends for approximately 3.5 km to the north has been preserved covering an erosional palaeo-landscape in the previously deposited and folded units. The deposit comprises two distinct source lithologies: (a) basal conglomerates whose clast composition, size and general appearance match the conglomeratic sections of the Maimará Formation; and (b) Proterozoic basement, found only in the upper section of the landslide. In both parts, the rocks are heavily sheared and fractured, with the degree of cataclasis increasing with depth, culminating at the bottom where underlying undifferentiated sediments have been injected upward into the fully disintegrated rocks. The contact between the two units comprising the landslide deposit is very sharp and resembles a thrust fault identical to the relationships that can be observed along the present-day basin-bounding Sierra Alta to the west. The landslide deposit is covered by ash-bearing fanglomerates that have been dated to ~1 Ma (see section below), which were subsequently tilted by faulting.

Quaternary gravels

The youngest deposits in the southern Humahuaca Basin constitute thick gravel fills covering palaeotopography in the previously deformed and eroded units. Two lithological units can be distinguished on the basis of clast compositions. The first unit comprises dark grey to black fanglomerates that were de-

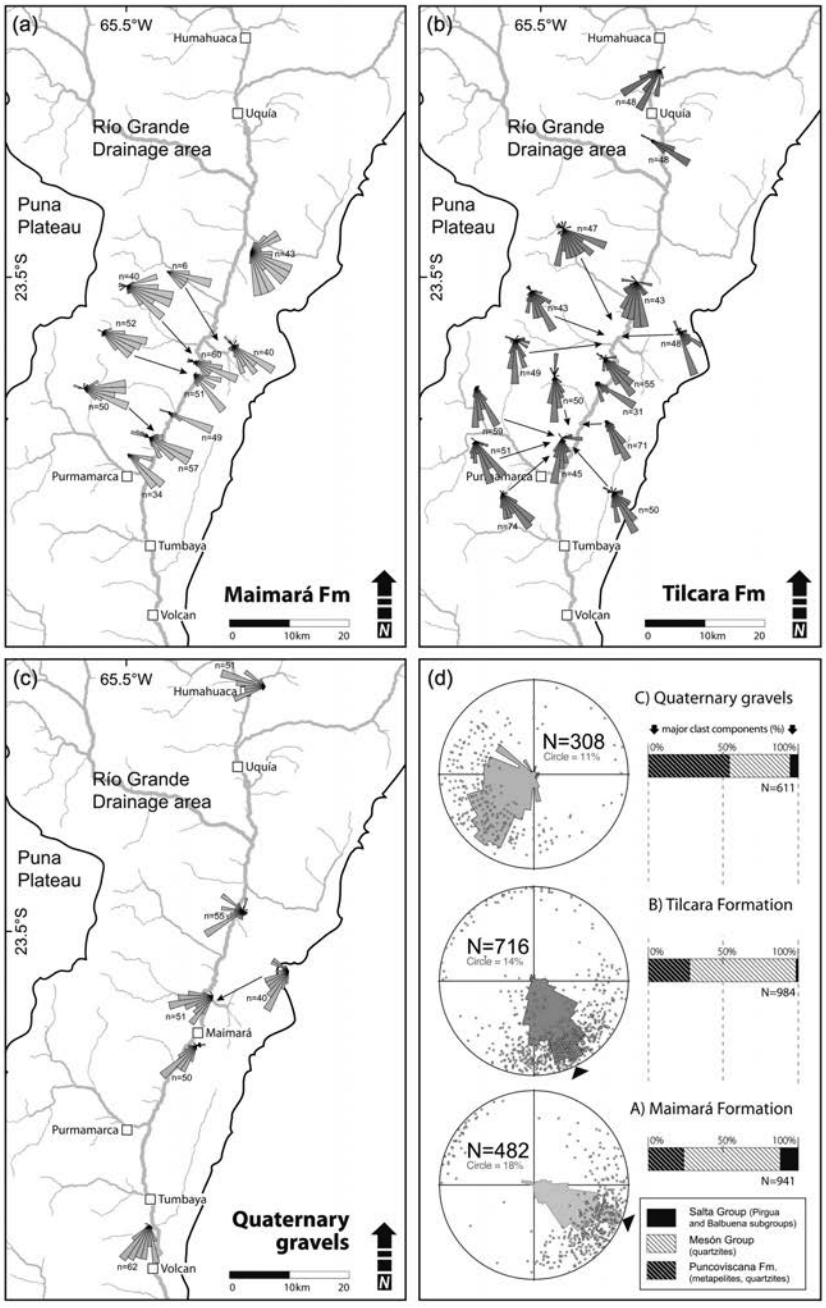

Figure 3.7 – Palaeoflow directions in the Humahuaca Basin derived from clast-imbrications measured in late Miocene to Pleistocene basin strata. Directions are presented on unidirectional rose diagrams for each site. Panels (a), (b) and (c) show the development of the fluvial network in the Maimará, Tilcara and Quaternary gravel formations respectively. Panel (b) also shows data from the Uquía Formation in the northern Humahuaca Basin. A combination of all clast imbrications for each unit is given in panel (d) highlighting a significant change in transport directions after 4.2 Ma associated with changes in the topographic boundary conditions. Palaeoflow directions in the Quaternary gravels are biased by a lack of properly distributed sample sites; locations are mainly along the eastern margins of the basin, thus more prone to reflect westerly drainages. Results of provenance analyses are shown in histogram plots depicting mean clast compositions of conglomeratic units.

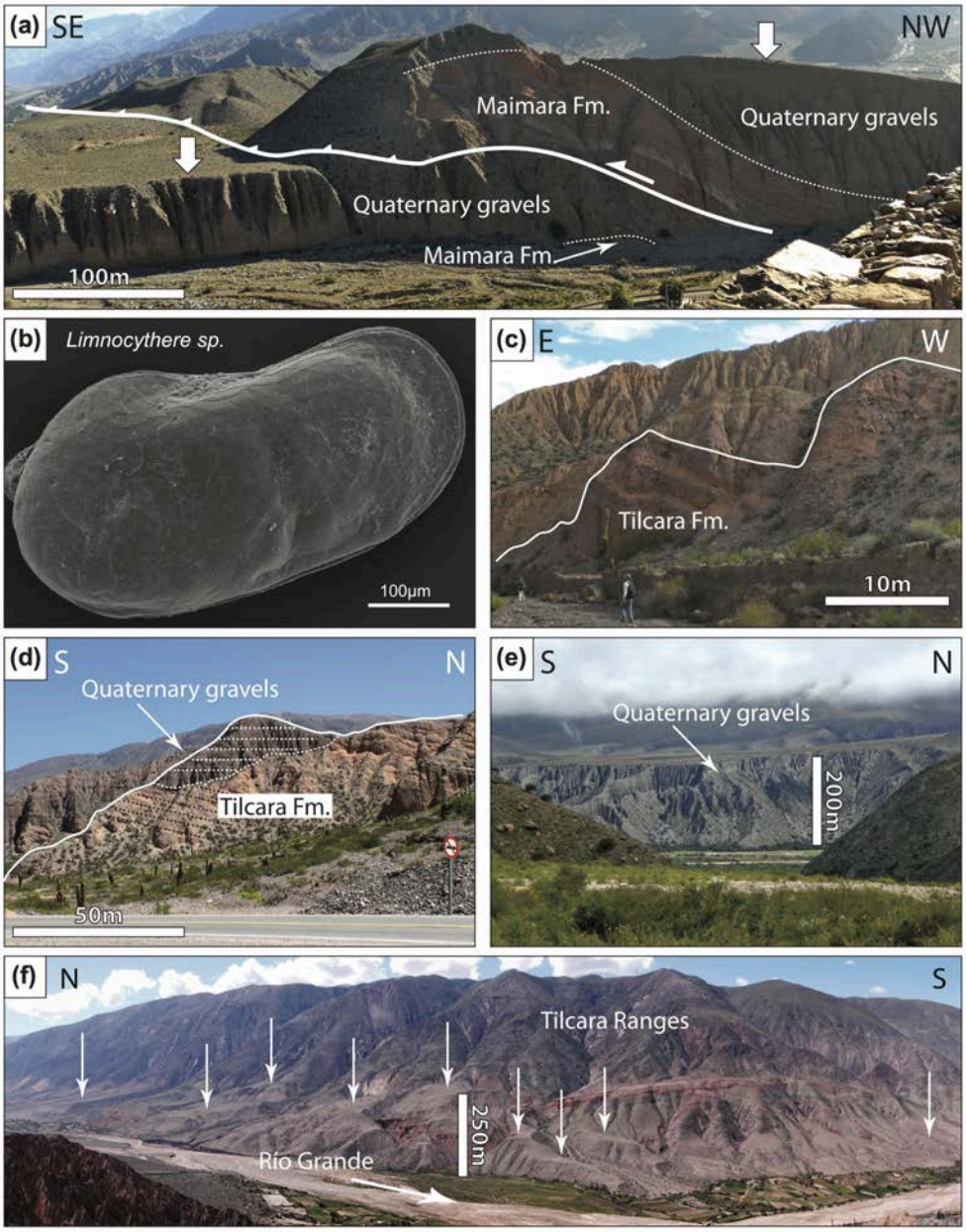

Figure 3.8 – (a) Thrust fault near Tilcara along the Río Huasamayo, juxtaposing late Miocene Maimará deposits against Quaternary gravels. Arrows and dashed lines indicate the vertical displacement (up to 20 m) of a formerly contiguous terrace surface. (b) SEM image of *Limnocythere sp.* from the lower beds of the Maimará Formation. (c) Deformed bedding-parallel erosion surfaces in the Tilcara Formation preserved below Quaternary landslide deposits. Tectono-sedimentary relationships suggest an episode of river incision and excavation prior to deformation. (d) Another example of the marked regional unconformity between the Tilcara Formation and Quaternary gravels. (e) Thick conglomeratic fill unit (Quaternary gravels) near the town of Tumbaya. (f) Panoramic view towards the east showing well developed geomorphic surfaces along the western flanks of the Tilcara ranges at successively lower elevation.

rived exclusively from source regions to the west. These sediments consist predominantly of angular to subangular clasts of the Puncoviscana Formation, together with less abundant clasts from the Mesón and Salta groups. We thus interpret these strata to be proximal alluvial-fan deposits sourced from the Sierra Alta. At several locations corresponding to more distal sectors of the inferred alluvial fans, the fanglomerates interfinger with well-stratified layers of pebble conglomerates, graded sands and unconsolidated silty clay. The layers are characterized by lateral, east-west-oriented pinch-outs. By analogy with the present-day depositional environment of the Río Grande and from the geometry of the pinch-outs, we infer that the former fluvial system also drained southward. The youngest zircons from a trachy-dacitic ash deposit in the upper part of a deformed succession 2 km north-west of Incahuasi yielded mid-Pleistocene ages (1.06 ± 0.10 Ma; n=2; 08HUM11; Fig. 3.5; Table A.1) we infer to represent a maximum depositional age.

The second unit in the Quaternary gravels comprises a group of grey alluvial-fan deposits and fluvial conglomerates (Fig. 3.8e) that are widely distributed within the Humahuaca Basin, its tributary valleys and in the basin outlet region to the north of Volcan village (Figs 3.2 and 3.9). These gravels typically consist of approximately equal proportions of Proterozoic and Palaeozoic clasts with minor contributions from Cretaceous lithologies, representing the present-day exposure of rock types in the surrounding source areas. The oldest conglomeratic fill in this unit forms an abandoned geomorphic surface to the east of the town of Tilcara, which is up to 400 m above the present-day baselevel and has an $^{40}Ar/^{39}Ar$–biotite age of ~800 ka, taken from a volcanic ash layer in the lower third of the section (Strecker *et al.*, 2007a).

Other investigators have further differentiated these gravels and document at least one additional, separate fill unit at lower elevations, corresponding to a third basin-filling episode between 93.8 ± 7.9 and 65 ± 4 ka (Tchilinguirian & Pereyra, 2001; Robinson *et al.*, 2005; Sancho *et al.*, 2008). In the south of Tilcara, this younger fill unit has been episodically downcut during the last ~65 ka, which has resulted in fluvial terrace surfaces at successively lower elevations (Fig. 3.8f). In the tributary Quebrada de Purmamarca in the south-west of the study area, even younger deposits, up to 250-m thick, constitute massive basin fills that have been dated 47.6 ± 2.8 ka (using OSL, Robinson *et al.*, 2005) and, although at the limit of the dating method, at 49.55 ± 1.7 ka BP (23° 40.9' S, 65° 34.5' W; AMS ^{14}C this study).

3.4.3 Structures

Three east-vergent, basement-involved fault systems define the structural framework of the Humahuaca Basin: (a) the basin-bounding Purmamarca Thrust Fault to the west; (b) a set of thrust-and-reverse faults within the Tilcara ranges to the east; and (c) the Tumbaya Fault in the basin centre, close to the Río Grande (Fig. 3.9).

The Purmamarca Thrust Fault juxtaposes Proterozoic basement of the Sierra Alta over Meso-Cenozoic sediments along the western basin margin and has developed a characteristic deformation pattern in the overthrust lithologies, involving steep eastward dips, or overturned strata. Moreover, multiple splays have developed from that fault extending into the basin, offsetting the Cenozoic strata (Figs 3.2 and 3.3). The

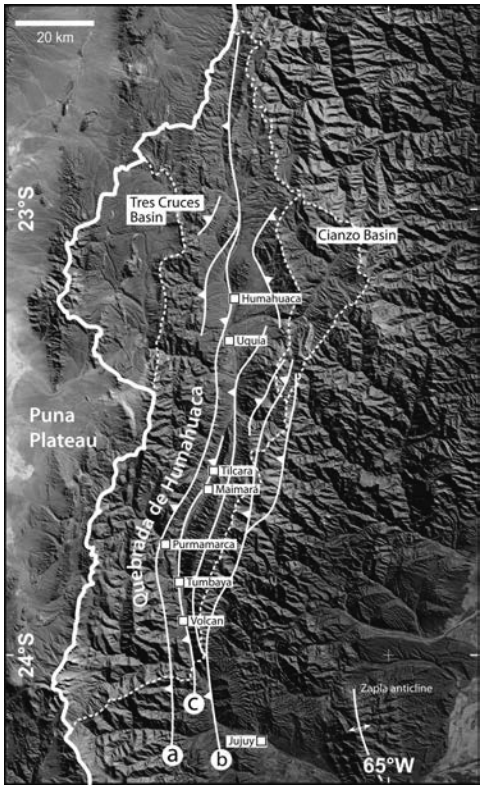

Figure 3.9 – Simplified structural map of the location and strike of major fault systems responsible for the basin geometry. Indicated are (a) the Purmamarca Thrust Fault, (b) the Tilcara Thrust System and (c) the central Tumbaya Fault. Solid thick white line represents the watershed between the internally drained Puna Plateau and the presently externally drained Eastern Cordillera; dashed lines delineate the Humahuaca Basin and adjacent sub-basins (Tres Cruces and Cianzo basins); also shown is the location of the Zapla anticline east of San Salvador de Jujuy.

Sierra Alta belongs to a set of subparallel basement ranges that have been uplifted along bivergent thrust and reverse faults. Apatite fission track thermal modelling suggests that exhumation of the eastern-most ranges constituting the Sierra Alta began between 15 and 10 Ma (Deeken *et al.*, 2004).

Present-day elevations of the eastern basin-bounding Tilcara ranges are attributed to shortening, crustal thickening and block rotation along multiple major east-verging thrust faults located within the range (Rodríguez Fernández *et al.*, 1999, Fig. 3.2). Because fault activity was mainly restricted to areas east of the Humahuaca Basin, the Proterozoic basement and overlying Palaeozoic to Mesozoic strata along the western flanks of the range were affected by westward tilting of this basement block.

At Molle Punco, near Tumbaya (Figs 3.2 and 3.9), Proterozoic rocks of the Puncoviscana Formation are thrust over the Palaeozoic successions of the Mesón Group along the Tumbaya Fault. The Tumbaya Fault can be traced into the northern Humahuaca Basin, intersecting the course of the Río Grande repeatedly. In the southern Humahuaca Basin, this fault is responsible for an uplifted central range (Fig. 3.3a) that causes the narrowing of the basin. The surface expression of the fault and associated basement expo-

sure gradually decrease northward, but the fault location can still be inferred from west-dipping Cenozoic basin strata in its hanging wall.

The sedimentary strata and landforms in the southern Humahuaca Basin attest to protracted deformation during the Plio-Pleistocene (see section below and Fig. 3.3c). The deformation includes thrusting of Precambrian to Mesozoic rocks over the conglomerates of the Maimará Formation along the Purmamarca Thrust Fault and associated folding, and the subsequent tilting of late Miocene to Pleistocene basin sediments in the hanging wall of the Tumbaya Fault until after 1 Ma.

Shortening within the basin was further accommodated by a number of mesoscale structures, mostly affecting the Maimará and Tilcara formations. Tight to open folding and the development of generally east-vergent and shallow-dipping thrust systems led to multiple stacked repetitions of the Miocene-Pliocene strata within the basin (Fig. 3.3). These thrusts are often associated with the development of drag folds, and shortening is in places accommodated by antithetic west-vergent faults. This pronounced Plio-Pleistocene strain accommodation in the southern Humahuaca Basin is mainly observed in the west of the Río Grande between the Purmamarca and Tumbaya faults.

3.4.4 Tectono-sedimentary relationships & deformation of basin sediments

The Maimará Formation rests unconformably on deformed sandstones of the Palaeogene Lumbrera Formation (upper Salta Group) and Proterozoic to Palaeozoic basement rocks. This unconformity and onlap relationships between the Maimará Formation and the underlying, irregularly shaped basement surface suggests deposition on palaeotopography that was sculpted into these rocks prior to ~6 Ma. To date, no evidence has been observed supporting an unconformable relationship between the Maimará Formation and the intermontane Tilcara Formation. The Tilcara Formation is always cut by a marked regional unconformity that in many places has been subsequently altered and obscured by continued deformation, erosion and deposition. Lateral correlation with the Uquía Formation in the northern Humahuaca Basin suggests that deformation following the initial incision occurred after ~1.5 Ma. Near the Tumbaya Fault at Incahuasi (Figs 3.3a and 3.9), this deformed unconformity resembles fluvial erosion surfaces sculpted into the Tilcara Formation that are tilted at ~20°- 30° W, parallel to bedding (Fig. 3.8c). These unconformable relationships and the vestiges of an erosional palaeotopography in the Tertiary sedimentary rocks are well preserved under a >1.06 ± 0.1 Ma conglomeratic fill unit that dips 10°- 15° W. Basal remnants of this earlier fill unit have a depositional age of about 0.8 Ma.

A subsequent conglomerate unit (~94-65 ka at Tilcara and <50 ka near Purmamarca) filled palaeotopography, covering the channel of the former trunk stream, which is now being re-excavated. This >200-m thick fill unit terminates in a smooth terrace surface that is connected with the mountain fronts. At Purmamarca, these gravels are generally not affected by fault displacement or other deformation. Near Tilcara, however, a prominent thrust fault close to the eastern margin of the basin (Fig. 3.8a) juxtaposes the Maimará Formation with young terrace-forming sections of the Quaternary strata (Salfity *et al.*, 1984;

Marrett *et al.*, 1994). Here, deformation resulted in vertical offsets between 15 and 20 m, which translates into an average vertical displacement rate of 0.27 ± 0.04 mm/a during the last 65 kyr. Horizontal displacements of ~40 m (Sancho *et al.*, 2008) suggest shortening rates of 0.62 ± 0.04 mm/a. Although these rates are only approximations, they emphasize the importance of protracted tectonic activity in the Humahuaca Basin within the interior of the orogen, which is compatible with the characteristics of regional shallow crustal seismicity (e.g., Bevis & Isacks, 1984; Cahill *et al.*, 1992). It is noteworthy that this youngest deformation followed a major phase of gradual basin evacuation.

3.5 Discussion

3.5.1 Foreland basin fragmentation & orographic barrier development

Crustal deformation corresponding to the region of the present-day interior of the Puna Plateau initiated in Eocene to Oligocene time (e.g., Kraemer *et al.*, 1999; Carrapa *et al.*, 2005; Deeken *et al.*, 2006; Hongn *et al.*, 2007; Letcher, 2007, Fig. 3.10). While individual ranges were uplifted, thick synorogenic strata buried the region that now constitutes the Eastern Cordillera and adjacent regions to the east (Reynolds *et al.*, 2001; Deeken *et al.*, 2006; Del Papa *et al.*, 2013). Today, these sediments are only rarely preserved in the uplifted Eastern Cordillera and the south-eastern flanks of the present-day Puna Plateau (Jordan & Alonso, 1987; Bossi *et al.*, 2001; Coutand *et al.*, 2001; Kley *et al.*, 2005; Mortimer *et al.*, 2007) and none appear to have been retained in the southern Humahuaca Basin. A regional exception is a *ca.* 6-km thick succession of middle Eocene to Pliocene foreland and intermontane basin deposits in the Cianzo Basin (Fig. 3.9), about 20 km east of the town of Humahuaca, where deformation and severed drainage conditions have been documented at *ca.* 10 Ma (Siks & Horton, 2011). Similarly, the Tres Cruces Basin in the Puna (Fig. 3.9) to the west has retained thick Cenozoic deposits (e.g., Boll & Hernández, 1986; Coutand *et al.*, 2001). In both cases, major reverse faults enclosing the basins have helped to preserve the Cenozoic sedimentary record. These regional relationships support the notion of widely distributed early Tertiary sediments in the area of the Eastern Cordillera and regions farther east. Their general absence in these high-elevation sectors of the orogen thus suggests their removal during regional exhumation in the realm of the Eastern Cordillera at about 15-10 Ma (Deeken *et al.*, 2004, 2006; Coutand *et al.*, 2006; Siks & Horton, 2011).

The earliest synorogenic strata recognized in the southern Humahuaca Basin belong to the Maimará Formation and were deposited on a palaeotopography of exposed Proterozoic and Palaeozoic basement. Deposition of Maimará sediments after a prolonged period of exhumation and deformation along the former orogenic flanks clearly documents that by *ca.* 6 Ma (and possibly some time earlier), new topographic conditions had evolved that would have promoted sedimentation in the study area. Our palaeocurrent and provenance data including ignimbrite clasts from currently isolated areas in the Puna interior and clasts from the Eastern Cordillera document that these sediments were sourced from the west. As the

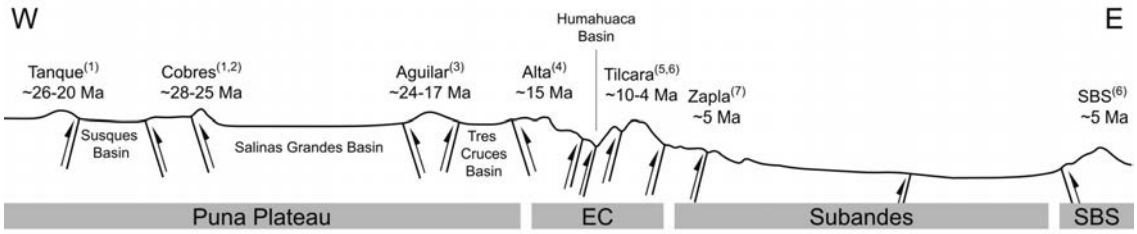

Figure 3.10 – Schematic cross section (~250 km) of the Andean margin in NW Argentina at about 23.5° S showing times of pronounced Cenozoic deformation. (1) Letcher (2007); (2) Deeken *et al.* (2005); (3) A. Deeken personal communication (2012); (4) Deeken *et al.* (2004); (5) Siks & Horton (2011); (6) this study; (7) Reynolds *et al.* (1994, 2000).

Humahuaca Basin and the Puna are not connected anymore, this observation confirms that thrusting in the Sierra Alta had not completely interrupted eastward-draining rivers at about 6 Ma and that the final disruption of the fluvial network must have occurred later.

We do not record any sedimentary evidence for uplift of the Tilcara ranges at the time when the Maimará Formation was deposited. This suggests that the Humahuaca Basin was part of an unrestricted foreland, and that surface uplift of the eastern ranges started later, coupled with the deposition of the Tilcara Formation. Alternatively, one could envision a scenario with an eastward-directed antecedent fluvial network that may have traversed the uplifting Tilcara ranges and transported sediment towards the regions farther east. In both settings, more pronounced surface uplift in Plio-Pleistocene time would have ultimately forced the full establishment of intermontane basin conditions and the formation of an efficient drainage divide, with rivers routing sediments towards the south. Although not documented in this study, a lateral correlation between the Maimará Formation and the upper sections of the Orán Group east of the ranges cannot be excluded. Sediments of the Orán Group may yield additional information to further elaborate these interpretations in future.

Nevertheless, Orán Group sediments exposed in the Zapla anticline to the south-east of the Tilcara ranges (Fig. 3.9), record a major pulse in deformation prior to 5 Ma (Reynolds *et al.*, 1994, 2000; Kley & Monaldi, 2002). This is consistent with our palaeocurrent data from the Tilcara Formation that record a distinct early Pliocene changeover of fluvial transport towards a north-south-oriented drainage system, which is also documented in the Uquía Formation of the central and northern Humahuaca Basin (Fig. 3.7). Based on the currently available data, we conclude that full intermontane basin conditions were achieved during the deposition of the Tilcara Formation, but that an antecedent drainage system traversing a proto-Tilcara range may have existed prior to that (Fig. 3.11).

Palaeo-environmental evidence from the Miocene-Pliocene palaeontological and sedimentary record prior to pronounced uplift indicates that climatic conditions during that time were relatively humid. While the Uquía Formation is well known for its fossil assemblage indicating subtropical to tropical

warm, humid conditions (Alonso *et al.*, 2006; Reguero *et al.*, 2007; Reguero & Candela, 2008), ostracods analysed in this study additionally attest to the existence of permanent freshwater bodies in the lower Maimará Formation, clearly indicating that topography and relief conditions must have been subdued. Calcic rhizoconcretions and nodules in the upper section of the Maimará Formation indicate regional wet-dry seasonality, a characteristic, which is maintained in the overlying Tilcara and Uquía formations. In stark contrast are the more arid conditions and the efficient orographic barrier to the east observed in the Humahuaca Basin today. Stratigraphic relationships and inferred palaeoclimatic indicators suggest that aridification may be a relatively young phenomenon, related to the uplift of the Tilcara ranges.

The timing of tectonic uplift and associated aridification appears to have been diachronous and basin-specific throughout the southern Central Andes, and determined by the individual behaviour of the basin-bounding faults. Although such environmental shifts are a hallmark of virtually all intermontane basins along the eastern flank of the Puna Plateau and generally took place during the Pliocene (Bossi *et al.*, 2001; Kleinert & Strecker, 2001; Starck & Anzótegui, 2001; Coutand *et al.*, 2006; Hain *et al.*, 2011), our observations demonstrate that in the Humahuaca Basin, the change to drier conditions probably occurred as late as Plio-Pleistocene time.

3.5.2 Basin-fill evolution & deformation in the Humahuaca Basin

The abrupt change in palaeoflow directions during the deposition of the Tilcara Formation at ~4.2 Ma and the associated facies change from distal to rather proximal sources (upward coarsening; Figs 3.3 and 3.6) record the tectonically induced reorganization of east-flowing river networks that formerly traversed the Tilcara ranges (Fig. 3.11). By analogy with neighbouring intermontane basins (e.g. the Toro and Lerma basins), the strata of the Tilcara Formation are interpreted as heralding the attainment of an intermontane basin stage. At that time, deposition in the Humahuaca Basin must have taken place under conditions of restricted fluvial connectivity with the foreland; otherwise, the deposition of over 250 m of sediment within the basin may not have been possible. Others have suggested that protracted internal drainage (e.g., Sobel *et al.*, 2003) or restricted external drainage (e.g., Hilley & Strecker, 2005) appear to be related to the combined effects of high uplift rates, exposure of resistant rocks and aridity. In this context, the following mechanisms for basin aggradation between 4.2 and ~1.5 Ma may be envisioned: (1) increased surface-uplift rates in the Tilcara ranges, associated with activity along a reverse fault that obliquely crosses the outlet region, and/or exposure of more resistant rock types reducing the fluvial transport efficiency within the basin; and (2) a change in global and/or regional climatic conditions towards increased aridity, reduced runoff and transport capacity.

Reduced runoff by increased aridity appears unlikely given the record of humid palaeoclimatic conditions. Moreover, the Tilcara Formation belongs to a group of spatially widespread Miocene-Pliocene conglomerates in NW Argentina commonly known as Punaschotter (Penck, 1920). These deposits are more likely related to individual range uplifts, because their diachronous deposition in various intermontane

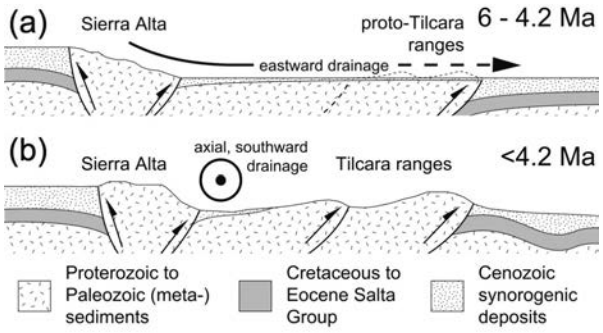

Figure 3.11 – Conceptual model of foreland-basin fragmentation. (a) The Maimará Formation is deposited into an exposed basement palaeotopography in a largely continuous depositional system since *ca.* 6 Ma. (b) Surface uplifts to the east led to re-routing of the fluvial network and deposition of the Tilcara Formation into an intermontane basin after 4.2 Ma.

basins and foreland regions excludes a coeval sedimentary response to regional climate change (McPherson, 2008; Schoenbohm *et al.*, 2008). As glaciation in the Central Andes has not been documented prior to 3.5 Ma (Clapperton, 2004) and subsequent glaciations have been minor due to limited moisture availability (Haselton *et al.*, 2002), it seems also unlikely that the style and deposition of the Tilcara conglomerates in the Humahuaca Basin results from glacial erosion at high elevation. Therefore, although a global trend towards colder and drier climates since mid-Miocene (e.g., Zachos *et al.*, 2001) may have favoured basin isolation, it is unlikely to have initiated basin filling here at 4.2 Ma. We therefore favour the first scenario as the most likely mechanism for initializing partial hydrological isolation of the Humahuaca Basin, which is consistent with the inferred tectonic forcing and severing of the fluvial system. The transition towards coarser grain sizes with the onset of deposition of the Tilcara Formation is thus best explained by erosion of more proximal sources in the uplifting Sierra Alta and Tilcara ranges.

Based on the depositional age estimates from the Tilcara and Uquía formations (i.e. ~4.2-1.5 Ma) and the unconformably overlying Quaternary gravel (<1.06 ± 0.10 Ma), it appears that fluvial connectivity with the foreland must have been re-established in the intervening time period. Although our data are currently insufficient to resolve the processes that led to basin excavation, incision rates at the valley outlet must have been sufficient to preserve external drainage, and sufficient transport capacity must have existed to allow sediment from upstream to bypass the basin while large volumes of sediment were removed. These processes, however, do not necessarily imply more availability of moisture in the Humahuaca Basin itself, but may instead represent efficient headward erosion at the location of the valley outlet, where current precipitation rates abruptly decline upstream towards the Humahuaca Basin (Strecker *et al.*, 2007a).

Although later surface processes have often altered the unconformity in the Tilcara Formation, preserved vestiges of deformed erosion surfaces suggest that fluvial incision predated an episode of deformation in the basin. These events were followed by a prolonged phase of restricted hydrological connectivity

with the foreland associated with basin filling of up to 400-m thick fluvial and alluvial gravel between >1.06 and <0.8 Ma. Whether this filling episode was linked to tectonically induced basin isolation farther downstream, regional uplift of the Tilcara ranges or the result of climatic forcing remains uncertain. It is, however, conceivable that the ongoing surface uplift of the Tilcara ranges exceeded a regional threshold elevation to form an efficient orographic barrier to cause basin-wide semi-arid conditions (i.e. reduced runoff and transport capacities) as observed today.

These 400-m thick gravels were largely removed from the basin during basin excavation, followed by the deposition of a second major fill, which reached a thickness of approximately 250 m between at least about 94 and 65 ka in the Humahuaca Basin (Robinson *et al.*, 2005; Sancho *et al.*, 2008) and until after ~50 ka in the tributary Quebrada de Purmamarca (this study). This fill unit and all previous deposits now form the substrate for gravel-covered pediments and multiple fluvial terraces that have been sculpted into these deposits. These terrace systems were formed at successively lower elevations (Fig. 3.8f), indicating renewed incision that may record recent reductions in channel gradients and/or changes in local baselevel with respect to the Andean foreland. These periods of sediment removal are episodic and have occurred some time between 65 and 50 ka and the present day. Faulting that has affected these deposits is an expression of renewed deformation within the basin during, or shortly after an episode of extensive basin excavation in the Pleistocene (Fig. 3.8a).

Although the last basin-fill episode in the Humahuaca Basin coincides to some extent with more humid phases documented in the Altiplano-Puna Plateau (e.g., Bobst *et al.*, 2001; Placzek *et al.*, 2006), a direct correlation cannot be observed. Due to limited age control on the younger Quaternary deposits and landforms in the Humahuaca Basin, we cannot entirely exclude such a possible correlation. However, aggradation during humid phases requires that sediment generation from hillslopes must increase with precipitation more rapidly than the increase in the transport capacity of rivers that would result from enhanced discharge in rivers during this time.

Interestingly, our observations point towards a systematic behaviour among erosion, deposition and tectonic processes in the Humahuaca Basin, an intriguing relationship that can also be found in other intermontane basins of the NW Argentine Andes (Strecker *et al.*, 1989; Hilley & Strecker, 2005). According to these observations, basin-internal/out-of-sequence deformation occurs during or following episodes of enhanced basin excavation. This is documented at least three times in the stratigraphic record of the southern Humahuaca Basin. First, after ~1.5 Ma, the Tilcara Formation was partly removed from the basin followed by major out-of-sequence thrusting along the basin-internal Tumbaya Fault. Here, deformation ceased prior to 1 Ma, which is documented by the onlap of ~1-Myr old gravels. Second, deformed remnants of these gravels, which lack evidence of syntectonic deposition, might also indicate that deformation occurred in association with the removal of the strata. Third, renewed, but locally limited deformation of young river terraces near Tilcara is observed right after the removal of the youngest Qua-

ternary gravels. Although this phenomenon and the associated mechanisms will require more detailed studies in the future, it is conceivable that the removal of basin fills and the resulting reduction in lithostatic stresses on formerly locked thrust and reverse faults could ultimately result in the reactivation of these faults.

3.5.3 Regional context of foreland fragmentation & basin-fill evolution

Many intermontane basins along the Puna margin record the partial or complete loss of fluvial connectivity with the foreland through the presence of thick conglomeratic fills (Strecker *et al.*, 2007a). Periodic reconnection to the foreland is documented by marked fluvial incision and excavation of these basin fills, reflected in distinct regional unconformities and complex onlap relationships. Virtually all basins in the northern Sierras Pampeanas, the Santa Bárbara System and the Eastern Cordillera of north-western Argentina exhibit similar, but diachronous, patterns of basin-fill and erosion throughout their history (reviewed in Strecker *et al.*, 2007a, 2009). The unifying characteristic in the history of these basins is that following the reorganization of fluvial systems by surface uplift, the establishment of orographic barriers results in progressive aridification, interrupted drainages and reduced fluvial transport capacity (Sobel *et al.*, 2003). While the basins in the arid interior of the orogen (the Puna Plateau) have maintained internal drainage systems, resulting in thick sediment accumulations (Alonso *et al.*, 1991; Vandervoort *et al.*, 1995), the intermontane basins along the eastern flank have alternated between restricted external and transient internal drainages, and fully integrated fluvial systems connected with the foreland.

At present, virtually all of the intermontane basins to the east of the Puna are hydrologically connected to the foreland, often via narrow, deeply incised bedrock gorges (Fig. 3.1). For example, the Toro Basin at 24.5° S was cut off from the foreland between 8 and 6 Ma and has subsequently experienced at least two cycles of basin filling and excavation (Marrett & Strecker, 2000; Hilley & Strecker, 2005). Similarly, between 5.2 and 2.4 Ma, the uplift of an orographic barrier to the east of the present-day Calchaquí Valley at ~25.5° S caused aridification associated with deposition of the conglomeratic San Felipe Formation, which was subsequently incised, deformed and finally overlain by another conglomeratic gravel after 2.4 Ma (Coutand *et al.*, 2006). After renewed sediment removal, a subsequent gravel unit with complex onlap relationships was deposited that once formed a continuous surface of coalesced alluvial fans and river gravel. River superposition, incision and removal of most of the gravels in the lower Calchaquí Basin document the on going erosion of this unit (Coutand *et al.*, 2006; Strecker *et al.*, 2007a). The Santa María Basin at ~26.5° S is a result of foreland compartmentalization related to basement uplift to the east that occurred after 6 Ma (Kleinert & Strecker, 2001; Bossi *et al.*, 2001; Sobel & Strecker, 2003), which was followed by aridification, severed fluvial connection to the foreland, deformation, erosion and finally, the deposition of thick conglomerates after 2.9 Ma (Strecker *et al.*, 1989). These units were subsequently incised, as documented by successively lower pediments and fluvial terraces. Further examples of this type of basin development are provided by the El Cajón and Fiambalá basins, at 27° S and 27.5° S, respectively

(Mortimer *et al.*, 2007; Carrapa *et al.*, 2008), emphasizing the similarities between the processes and depositional facies that control the evolution of intermontane basins within this environment.

We suggest that the tectono-sedimentary history of the Humahuaca Basin and other intermontane basins in NW Argentina can be best explained through a threshold process described in Sobel *et al.* (2003), in which active uplift of downstream topographic barriers steepens the channels that traverse these ranges, while aggradation upstream must keep pace with the associated uplift of the channel. As rates of rock uplift increase relative to the transport efficiency (related to precipitation) and bedrock erodibility, internal drainage is favoured. Conversely, low rates of rock uplift in the downstream basement ranges, a high level of erodibility of exposed rock types and pronounced rainfall gradients all promote incision, headward erosion and basin capture. All of these processes ultimately contribute to sustaining fluvial connectivity with the foreland. This, however, is only possible if the narrow outlets of the arid basins are in close proximity to steep rainfall and run-off gradients or if the structural setting is conducive to funnelling moist air into the orogen interior during protracted moist episodes. In turn, this condition would increase precipitation, run-off and erosion, which would ultimately help to achieve or re-establish external drainage conditions. Indeed, on the basis of our chronology, observations and interpretations, we are able to show that the intermontane Humahuaca Basin is the result of progressive rock uplift and associated surface processes in the Eastern Cordillera that commenced at 15-10 Ma and subsequently led to deposition of the Maimará Formation at about 6 Ma. The largely continuous depositional system finally became dismembered after 4.2 Ma when topography of the Tilcara ranges deflected the fluvial network into range-parallel drainage. Until about 1.5 Ma, the basin was characterized by restricted fluvial conditions most likely related to ongoing regional uplifts. Afterwards, the basin was rapidly excavated and internally deformed. The ensuing regional palaeotopography in the basin was subsequently refilled between >1.06 and <0.8 Ma. The reason for the initial excavation is not known, but this could have been related to headward erosion and fluvial connectivity, followed by re-established hydrological isolation. The resulting basin fill, then, was largely removed, deformed and replaced by a younger fill that periodically has been excavated some time after ~65 and 50 ka. Excavation, again, seems to have been accompanied by basin-internal deformation, recorded by offset fluvial terraces near Tilcara, while currently the basin is aggrading (Rivelli & Flores, 2009).

3.6 Summary & conlusions

In this study, we have combined new provenance and palaeocurrent data from the sedimentary record of the intermontane Humahuaca Basin of the Eastern Cordillera of the southern Central Andes with 12 new $^{206}Pb/^{238}U$ zircon age estimates from intercalated volcanic ash deposits to assess its spatiotemporal evolution. This enabled us to improve our understanding of the neotectonic basin and landscape evolution of an intermontane setting in the immediate vicinity of the intra-orogenic Puna Plateau, the world's

second largest plateau, and an important barrier to atmospheric circulation and surface-process regimes. We suggest that the coupled tectonic, erosion and sedimentary processes and associated landscape development in the Humahuaca Basin reflect an environment whose evolution is relevant for the assessment of intermontane basins worldwide, including the North American Laramide province, and the Tien Shan and Qilian Shan basement uplifts in Asia. From our analysis, we draw the following conclusions:

(1) In comparison with the previously developed chronostratigraphy for the Humahuaca Basin, our new U–Pb zircon dates extend the lower boundary of the Maimará Formation into late Miocene, older than 5.92 ± 0.12 Ma, confirms existing ages from the northern basin, and reveals Quaternary fills as old as ~1 Ma.

(2) On the basis of provenance, lithology and spatial distribution, we introduced a new stratigraphic unit, the Tilcara Formation, in the southern Humahuaca Basin that is apparently coeval with the radiometrically and palaeontologically constrained Uquía Formation from the central and northern sectors of the basin. The Tilcara Formation highlights the different depositional environments and source areas between the southern and northern parts of the basin.

(3) The sedimentary units in the Humahuaca Basin record a transition between a partially segmented foreland basin and a fault-bounded intermontane basin in the course of surface uplift to the east. This resulted in a change in fluvial connectivity and the re-arrangement of the formerly eastward-draining river network into an axial, south-directed drainage after ~4.2 Ma.

(4) Repeated hydrological disconnection from the foreland due to tectonism and ensuing aridification in the lee of rising topography repeatedly resulted in restricted fluvial connectivity and possibly transient fluvial isolation and accumulation of at least three basin-fill units during Plio-Pleistocene times. After episodic re-capture, these fills were partially evacuated by fluvial incision. This is similar to other intermontane basins along the eastern flank of the Puna where surface uplift resulted in the tectonic defeat of fluvial networks, hydrological isolation and basin aggradation, until renewed river incision exceeded rock uplift at tectonically active basin outlets.

(5) We furthermore observed that major deformation events in the Humahuaca Basin apparently followed a phase of enhanced removal of basin-fill units, a scenario that has been observed in other intermontane basins of NW Argentina. We speculate that this behaviour is related to the reduction in lithostatic stresses acting on subsurface structures during major phases of basin excavation.

Supporting information

A summary of U–Pb zircon analytical data of volcanic ash samples in the Humahuaca Basin using CAMECA IMS 1270 ion microprobe at UCLA can be found in the appendix (see Appendix A).

Chapter 4

Pliocene orographic barrier uplift in the southern Central Andes*

Heiko Pingel[1], Ricardo N. Alonso[2], Andreas Mulch[3], Alexander Rohrmann[1], Masafumi Sudo[1] and Manfred R. Strecker[1]

[1]*Institut für Erd- & Umweltwissenschaften, Universität Potsdam, Germany*

[2]*Departamento de Geología, Universidad Nacional de Salta, Argentina*

[3]*Institut für Geowissenschaften, Goethe Universität Frankfurt, Biodiversity & Climate Research Centre (BiK-F), Frankfurt/Main, Germany*

Abstract

Sedimentary basin fills along the windward flanks of orogenic plateaus are valuable archives of paleoenvironmental change with the potential to resolve the history of surface uplift and orographic barrier formation. The intermontane basins of the southern Central Andes contain thick successions of sedimentary material that are commonly interbedded with datable volcanic ashes. We relate variations in the hydrogen isotopic composition of hydrated volcanic glass (δD_g) of Neogene to Quaternary fills in the semiarid intermontane Humahuaca Basin (Eastern Cordillera, northwest Argentina) to spatiotemporal changes in topography and associated orographic effects. δD values from volcanic glass in the basin strata (-117‰ to -98‰) show two main trends that accompany observed tectono-sedimentary events in the study area. Between 6.0 and 3.5 Ma, δD_g values decrease by ~17‰; this is associated with surface uplift in the catchment area. After 3.5 Ma, δD_g values show abrupt deuterium enrichment, which we associate with (1) the attainment of threshold elevations for blocking moisture transport in the basin-bounding ranges to the east, and (2) the onset of semiarid conditions in the basin. Such orographic barriers throughout the eastern flanks of the Central Andes have impeded moisture transport into the orogen interior; this has likely helped maintain aridity and internal drainage conditions on the adjacent Andean Plateau.

* *published in Geology (2014) vol. 42, no. 8, p. 691–694, doi: 10.1130/G35538.1*

4.1 Introduction

Over the past decades, reconstructions of surface uplift of the world's orogenic plateaus have played a pivotal role in assessing the relative importance of mantle dynamics and crustal and/or lithospheric shortening and thickening in shaping the topography of our planet (e.g., Allmendinger *et al.*, 1997; Garzione *et al.*, 2006). However, deconvolving how the complex interactions among surface uplift, atmospheric circulation, and orographic rainfall affect paleoaltimetric reconstructions remains a key challenge for many approaches, including stable isotope studies, which have been among the most prominent methods applied in the Central Andes (Garzione *et al.*, 2006, 2008; Quade *et al.*, 2007). One promising method to help disentangle the complex tectono-climatic relationships is to focus on the surface-elevation history of plateau bounding margins, because it is challenging to deduce the relative roles of surface uplift and changes in atmospheric patterns from orogen interior stable isotope records alone (e.g., Mulch *et al.*, 2010).

The Andean Altiplano-Puna Plateau is the second largest Cenozoic orogenic plateau on Earth, with an average altitude of 3.7 km, low internal relief, high and deeply incised flanks, and pronounced climatic gradients across the orogen (Fig. 4.1; Isacks, 1988). The eastern, windward margin of the plateau has high precipitation and denudation rates that are in contrast to the semiarid to arid conditions and low denudation rates in the orogen interior and along the western plateau margin (Rech *et al.*, 2006; Bookhagen & Strecker, 2008, 2012). Despite extensive stable isotope studies, the timing and style of uplift of the Andean Plateau and its eastern margin (Eastern Cordillera) remain controversial (e.g., Garzione *et al.*, 2006, 2008; Ehlers & Poulsen, 2009; Mulch *et al.*, 2010). However, knowledge of the spatiotemporal development of topography along the eastern Andean flanks is crucial to understand changes in precipitation characteristics over time as well as associated changes in erosion rates and the depositional style of basin fills. In northwestern Argentina and southern Bolivia, the timing of uplift and exhumation has been inferred using low-temperature thermochronology (e.g., Deeken *et al.*, 2006), paleoenvironmental and provenance data obtained from basin fills (e.g., Starck & Anzótegui, 2001; Pingel *et al.*, 2013) or oxygen ($\delta^{18}O$) and carbon ($\delta^{13}C$) isotope data from calcic paleosols (e.g., Mulch *et al.*, 2010). Often, however, precise timing of these events and their regional correlation has been limited by poor chronological constraints.

Here we evaluate topographic growth along the plateau margin using hydrogen isotope ratios of hydrated volcanic glass (δD_g) from the intermontane Humahuaca Basin in northwestern Argentina (Fig. 4.1). The basin's deformed strata lack continuous sedimentary sections, but they contain abundant datable volcanic ash horizons that provide high-resolution chronologic constraints. We report δD_g values on 17 glass samples from dated volcanic ashes (Fig. 4.2; Table C.1) to provide insights into patterns of range uplift and the associated evolution of paleoenvironmental conditions in the southern Central Andes.

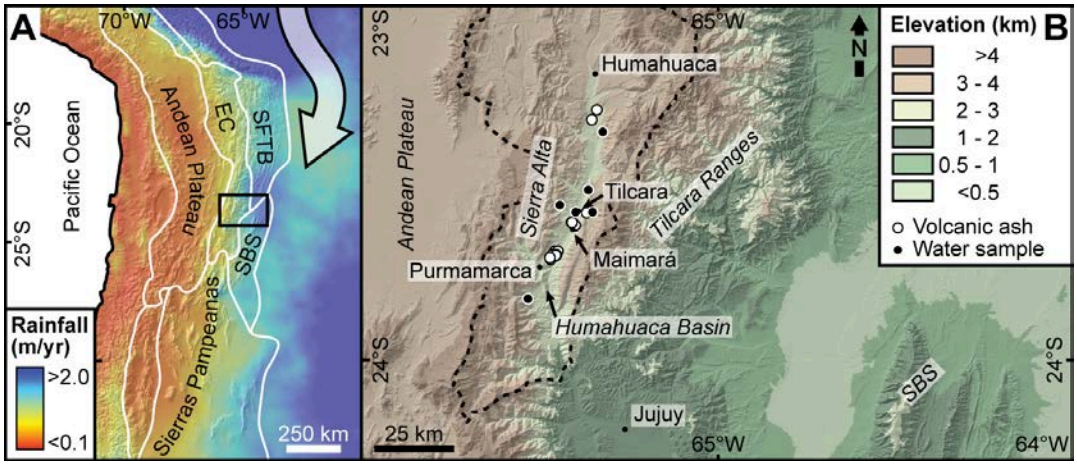

Figure 4.1 – (a) Morphotectonic map of southern Central Andes showing mean annual rainfall derived from National Aeronautics and Space Administration Tropical Rainfall Measurement Mission (after Strecker *et al.*, 2007a) and main moisture transport (white arrow) to the study area (black box). EC–Eastern Cordillera, SFTB–Subandean fold-thrust belt; SBS–Santa Bárbara System. (b) Digital elevation model with sample locations of volcanic ashes (white) and modern water (black) in Humahuaca catchment (dashed line).

4.2 Geological setting

The Humahuaca Basin is located between 23° S and 24° S in the Eastern Cordillera (Fig. 4.1). To the west, the Sierra Alta ranges separate the basin from the arid, high-elevation Andean Plateau, and to the east, the Tilcara ranges delineate the boundary with the humid sectors of the broken foreland (Santa Bárbara System, Figs. 4.1 and 4.2c). Thermochronologic and sedimentologic evidence shows that widely distributed deformation within the area that now constitutes the plateau and its present-day eastern margin started in Eocene-Oligocene time (e.g., Deeken *et al.*, 2006; Hongn *et al.*, 2007). During the Miocene-Pliocene, deformation was focused on the Eastern Cordillera and Santa Bárbara System, where the formerly contiguous Andean foreland was compartmentalized (e.g., Deeken *et al.*, 2006). While apatite fission-track thermochronology reveals that the Sierra Alta was exhumed rapidly beginning ca. 15-10 Ma (Deeken *et al.*, 2005), Pliocene drainage reorganization within the Humahuaca Basin suggests surface uplift in the Tilcara ranges and foreland fragmentation by ca. 4.2 Ma (Pingel *et al.*, 2013).

The Humahuaca Basin exposes late Miocene-Pliocene sandstones and conglomerates of the Maimará Formation, which unconformably overlie older units. Puna-derived ignimbrite clasts and paleocurrent directions both indicate fluvial connectivity between the orogen interior and the foreland across the present-day basin-bounding ranges (Fig. 4.2b; Pingel *et al.*, 2013). Interbedded freshwater deposits suggest generally humid conditions at that time (Pingel *et al.*, 2013). While in the south these sedimentary rocks are overlain by the conglomeratic Tilcara Formation (4.2-1.5 Ma; Pingel *et al.*, 2013), the northern part of the basin is characterized by sandstones of the fossiliferous Uquía Formation (3.5-1.5 Ma; Reguero

et al., 2007). Mammal fossil assemblages in the Uquía Formation suggest more humid conditions until ca. 2.5 Ma (Reguero *et al.*, 2007). Axial north-south drainage conditions and the absence of ignimbrite clasts document that the basin-bounding ranges on either side of the basin had attained sufficient elevation to interrupt fluvial connectivity between the plateau, the basin, and the foreland by ca. 4.2 Ma (Pingel *et al.*, 2013). The entire Tertiary sequence is deformed, eroded, and unconformably overlain by multiple generations of thick Quaternary fill units that were episodically deposited and subsequently partly eroded, as a consequence of fluctuations in tectonic activity, climate, and associated local drainage conditions (Strecker *et al.*, 2007a; Pingel *et al.*, 2013).

4.3 Stable isotope paleoaltimetry & hydrogen-isotope analysis

Stable isotope paleoaltimetry benefits from a systematic relationship between $\delta^{18}O$ and δD of meteoric water and elevation (e.g., Dansgaard, 1964). Various terrestrial materials incorporate meteoric water by mineral-specific isotope fractionation, preserving a signal of the original isotopic composition of meteoric water. In continental settings, rhyolitic glass may incorporate large amounts of meteoric water (3-8 wt%), saturating ~5-10 k.y. after deposition (Friedman *et al.*, 1993a; Mulch *et al.*, 2008; Dettinger, 2013; Cassel *et al.*, 2012). This hydration process occurs systematically, whereby the final δD_g represents an integrated signal of the meteoric water present during hydration that is preserved over geological time scales, allowing for reconstructions of paleoenvironmental conditions (Friedman *et al.*, 1993a; Mulch *et al.*, 2008; Dettinger, 2013; Cassel *et al.*, 2012) and to examine feedbacks between tectonic processes and climate (this study).

We analyzed 17 volcanic glass samples from ash beds in late Miocene to Pleistocene sediments of the Humahuaca Basin, from elevations between 2,350 m and 2,900 m (Fig. 4.1; Table C.1). Our age model relies on new $^{40}Ar/^{39}Ar$ biotite ages, stratigraphic correlation (Fig. B.1), and previously obtained radiometric ages. To compare ancient δD_g with modern meteoric waters, we converted δD of 6 stream waters from elevations between 2,530 m and 2,930 m into glass-hydrogen isotopic composition (Table C.3; Friedman *et al.*, 1993a). All isotope measurements were performed at the Joint BiK-F-Goethe University Stable Isotope Facility, Frankfurt. All isotopic ratios are reported relative to V-SMOW. For more details see appendices B, C and D.

4.4 Results

The δD_g values of all samples range between -98‰ and -117‰ (Fig. 4.2a; Table C.1), except for one sample (08HUM03) with an anomalously high δD_g value (-83‰), which was excluded from further interpretation. δD_g values form two distinct trends: (1) from 6.0 to 3.5 Ma, average δD_g values decrease by 17‰, showing high variability, and (2) after 3.5 Ma, δD_g values are significantly higher (-105‰ to -100‰) and relatively stable over time. Present-day stream water δD values would be in equilibrium with an average δD_{gc} value of -94‰ (Fig. 4.2a; Table C.3; for details see Appendix C).

4.5 Orographic barrier formation & plateau expansion

There are various potential causes for changes in δD.

1. Although δD of meteoric water is largely coupled to air temperatures during condensation and rainfall, global climate reconstructions show no major cooling trends (e.g., Zachos *et al.*, 2001) that would explain the initial decrease in δD_g values.

2. An alternative way to lower regional temperatures, and therefore δD values, is to increase elevations, which undoubtedly occurred over the past 6 m.y. (Pingel *et al.*, 2013). The surface uplift that could explain the initial decrease in δD_g can be quantified. However, various assumptions, combined with large uncertainties, may render these estimates insignificant (see the Appendix C).

3. Another possibility is that changing water-vapor sources influenced δD in precipitation. The present-day moisture sources in northwestern Argentina are the Atlantic Ocean and the Amazon Basin (Vera *et al.*, 2006a). A shift from the only other potential source in the past (southeast Pacific Ocean) to present-day conditions may have been related to mountain building to the west and likely occurred prior to 10 Ma (reviewed in Insel *et al.*, 2012b). It is therefore unlikely that the moisture source for this sector of the Andes has changed significantly since the late Miocene.

4. The isotopic signature of hydrated glass may be altered by burial heat (Dettinger, 2013); this is an unlikely scenario because the sediment thickness in the study area barely exceeds 1 km.

5. Rainfall amount negatively correlates with δD and $\delta^{18}O$ of precipitation during rainout (Dansgaard, 1964), which becomes relevant when threshold elevations along uplifting mountain ranges are attained (Insel *et al.*, 2012b). Because the Sierra Alta underwent deformation by ca. 15-10 Ma, it is likely that the initial decrease in δD_g is in part related to this amount effect.

6. In arid climates D-enriched δD values in hydration water may result from enhanced evaporation either during subcloud evaporation or soil-water formation (Quade *et al.*, 2007). Our data show a rapid increase in δD_g after ca. 3.5-2.6 Ma (Fig. 4.2a) that occurs ~0.7-1.6 m.y. after the inferred onset of surface uplift in the present-day Tilcara ranges by 4.2 Ma (Pingel *et al.*, 2013). We suggest that between ca. 3.5 and 2.6 Ma, the Tilcara ranges developed sufficient elevation to force enhanced precipitation along their eastern flanks, which subsequently led to increasingly dry leeward conditions.

In contrast, our modern water isotope data do not show signs of evaporation (Fig. C.2). However, considering that those samples were collected late in the rainy season (March), we do not expect a strong evaporation signal because evaporation and deuterium enrichment are commonly observed during the dry season (Fig. C.5). This may also explain why our δD_{gc} values of modern water (-94‰) are higher than those of Pleistocene glass (-104‰; Fig. 4.2a), and highlight challenges when comparing stable isotope data from different episodes in the past over which isotopic signals are integrated. Another explanation for this deviation may be related to inherent uncertainties in the empirical glass-fractionation equation, which, in northwestern Argentina, may result in precisions of ±20‰ (Dettinger, 2013).

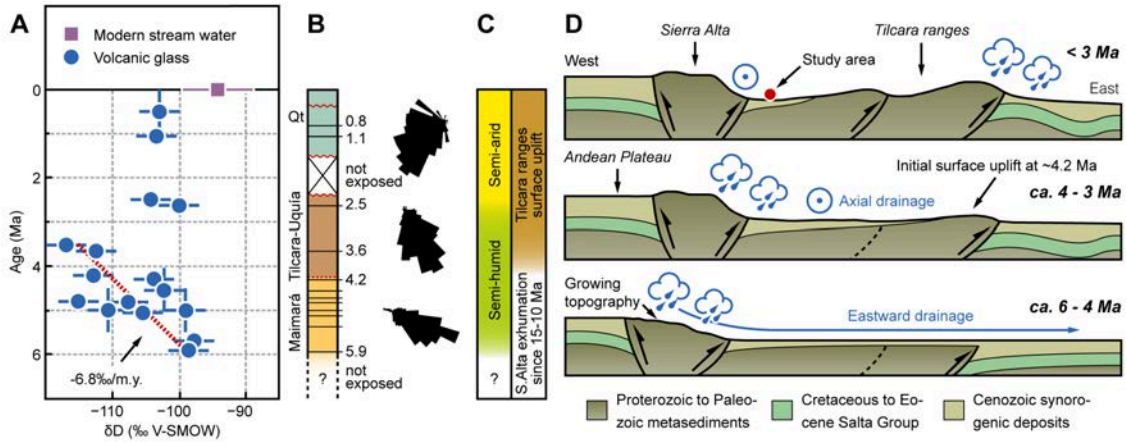

Figure 4.2 – (a) δD of volcanic glass (blue circles) and mean modern water (purple square) converted to glass composition (Friedman *et al.*, 1993a). Red line depicts mean trend between 6.0-3.5 Ma. VSMOW-Vienna standard mean ocean water. (b) Generalized stratigraphy with selected ash layers and age estimates (in Ma; Qt-Quaternary gravels) and paleocurrent estimates from each stratigraphic unit. (c) Paleoclimate estimates and uplift history as documented by Pingel *et al.* (2013). S.–Sierra. (d) Conceptual model of basin-and-range development, showing drainage reorganization and shift in orographic rainfall.

Observed trends in our data and the broad synchronicity of isotopic change with tectono-sedimentary events in the Humahuaca Basin and the adjacent ranges suggest that changes in isotopic composition are related to topographic growth in the basin catchment. It is intriguing that the temporal discrepancy between initial surface uplift and drainage reorganization recorded in the basin sediments and the isotopic response is likely related to the attainment of threshold elevations in the Tilcara ranges by 4.2 Ma; currently high enough (4-5 km) to intercept easterly moisture-bearing winds and to cause semiarid conditions in the Humahuaca Basin.

These observations have critical implications for the climatic and sedimentary development of the Central Andes and orogenic plateau margins elsewhere. Synchronous with initial surface uplift in the Tilcara ranges at 4.2 Ma, the Sierra Alta gained sufficient elevation to trap sediment sourced in the plateau interior (expansion of the internally drained area; Fig. 4.2d; Pingel *et al.*, 2013). Moreover, ongoing uplift of the Sierra Alta and the attainment of critical elevations of the Tilcara ranges between 3.5 and 2.6 Ma, associated with increased hinterland aridification and low erosion rates in the lee of the Sierra Alta (e.g., Bookhagen & Strecker, 2012), must have helped to sustain internal drainage conditions on the plateau. Similar observations from other intermontane basins along the Andean plateau margin (e.g., Strecker *et al.*, 2009) support the notion that generally eastward-migrating range uplift forces orographic precipitation toward foreland areas, while the orogen interior increasingly aridifies. In addition, oscillating sedimentary filling and excavation episodes in these marginal basins may have buffered the overall tendency of the fluvial system to incise into the plateau.

Our findings suggest that the efficiency of orographic barriers strongly depends on the development of threshold elevations at which changes in precipitation impact stream power, erosion, and sedimentation due to reduced moisture supply into the orogen interior. As a consequence, such internally-drained, moisture-starved regions are likely to trap large volumes of sediments (e.g., Sobel *et al.*, 2003), ultimately forming extensive low-relief plateaus that may expand as crustal deformation and range uplift propagate outward. Similar positive feedbacks between tectonics and climate may contribute to lateral plateau expansion in the Chinese Qilian Shan or the northern Anatolian plateau.

4.6 Conclusions

We observe a systematic relation between tectono-sedimentary events in the Humahuaca Basin and δD of volcanic glass contained in the sedimentary basin fill. Specifically, the initial decrease in δD_g can be related to topographic growth, while hydrogen isotope ratios after ca. 3.5-2.6 Ma likely reflect aridification by orographic barrier formation to the east. These results highlight the potential for isotopic studies of hydrated glass to decipher the history of topography in the Central Andes and other tectonically and volcanically active regions, particularly when threshold elevations for orographic rainfall are attained. We show that in a generally eastward-migrating deformation regime in the southern Central Andes, orographic barriers in the Eastern Cordillera may help maintain internal drainage on the plateau, and that these processes may ultimately favor lateral plateau growth.

Supporting information

Stratigraphic correlation, Methodology, paleoaltimetry estimates, and data tables of hydrogen stable isotope analyses of volcanic glass and modern stream water samples and $^{40}Ar/^{39}Ar$ dating (see Appendix B, C and D).

Chapter 5

Neogene to Quaternary broken foreland formation & sedimentation dynamics in the Andes of NW Argentina (25° S)*

Mathis P. Hain[1,2], Manfred R. Strecker[1], Bodo Bookhagen[3], Ricardo N. Alonso[4], Heiko Pingel[1] and Axel K. Schmitt[5]

[1]DFG Leibniz Center for Surface Process & Climate Studies, Institut für Erd- & Umweltwissenschaften, Universität Potsdam, Germany; [2]Department of Geosciences, Princeton University, Princeton, New Jersey, USA; [3]Geography Department, University of California - Santa Barbara, CA, USA; [4]Departamento de Geología, Universidad Nacional de Salta, Salta, Argentina; [5]Department of Earth & Space Sciences, University of California - Los Angeles, CA, USA

Abstract

The northwest Argentine Andes constitute a premier natural laboratory to assess the complex interactions between isolated uplifts, orographic precipitation gradients, and related erosion and sedimentation patterns. Here we present new stratigraphic observations and age information from intermontane basin sediments to elucidate the Neogene to Quaternary shortening history and associated sediment dynamics of the broken Salta foreland. This part of the Andean orogen, which comprises an array of basement-cored range uplifts, is located at ~25° S and lies to the east of the arid intraorogenic Altiplano/Puna plateau. In the Salta foreland, spatially and temporally disparate range uplift along steeply dipping inherited faults has resulted in foreland compartmentalization with steep basin-to-basin precipitation gradients. Sediment architecture and facies associations record a three-phase (~10, ~5, and <2 Ma), east directed, yet unsystematic evolution of shortening, foreland fragmentation, and ensuing changes in precipitation and sediment transport. The provenance signatures of these deposits reflect the trapping of sediments in the intermontane basins of the Andean hinterland, as well as the evolution of a severed fluvial network. Present-day moisture supply to the hinterland is determined by range relief and basin elevation. The conspiring effects of range uplift and low rainfall help the entrapment and long-term storage of sediments, ultimately raising basin elevation in the hinterland, which may amplify aridification in the orogen interior.

* *published in Tectonics (2011) vol. 30, TC2006, doi: 10.1029/2010TC002703*

5.1 Introduction

Broken forelands are an integral part of many orogens. For example, today such systems characterize parts of the Colombian Andes (e.g., Mora *et al.*, 2006, 2009; Parra *et al.*, 2009a,b), the Tian Shan (e.g., Sobel & Dumitru, 1997; Sobel *et al.*, 2003), the Qilian Shan (e.g., Tapponnier *et al.*, 1990), and the Salta foreland of northwest Argentina (e.g., Allmendinger *et al.*, 1983, this study, Fig. 5.1). The geologic record holds more examples, including the Cretaceous-Eocene Laramide province of North America (e.g., Jordan & Allmendinger, 1986; Talling *et al.*, 1995; Marshak *et al.*, 2000; Davis *et al.*, 2009; Ernst, 2010) and the Paleozoic Alice Springs broken foreland in Australia (Haines *et al.*, 2001). In these environments, patterns of deformation, sediment routing and accumulation are different from thin-skinned foreland fold-and-thrust belts (e.g., DeCelles & Giles, 1996) and may be characterized by highly disparate spatiotemporal patterns of deformation and sedimentation (e.g., Strecker *et al.*, 2011, Fig. 5.1).

Over recent years a conceptual framework for the interactions between tectonic forcing, climatic conditions and sediment dynamics in broken forelands has been proposed (Sobel *et al.*, 2003; Sobel & Strecker, 2003; Hilley & Strecker, 2005; Strecker *et al.*, 2007a, 2009, 2011). In summary, these models posit that reactivation of basement anisotropies and spatiotemporally disparate patterns of range uplifts lead to the formation of highly localized depocenters that may experience aridification when the frontal ranges attain laterally continuous threshold topography, which is able to block moisture-bearing winds. Ensuing basin-scale sediment storage within the intermontane basins is driven by tectonic fragmentation of the drainage system and may be enhanced by orographic shielding, which reduces precipitation, discharge, river transport capacity, and ultimately river incision rates in the hinterland. Accordingly, sediment provenance in the deposits of the foreland should change drastically when range uplift severs drainage conditions and traps sediment in the hinterland. In this study we evaluate this prediction by providing an account of the facies, provenance signatures, and distribution of syntectonic deposits of the broken Salta foreland of northwestern Argentina at approximately 25° S (Fig. 5.1).

Despite great interest in the interaction between tectonics, climate and sediment dynamics, the age of uplift of many ranges that presently compartmentalize the Salta foreland is unknown, especially in the eastern sector (cf. Reynolds *et al.*, 2000). The deformation history is only adequately resolved in the arid, well exposed western sector of the foreland, along the eastern flanks of the Puna Plateau (Salfity *et al.*, 2004; Deeken *et al.*, 2006; Coutand *et al.*, 2006; Hongn *et al.*, 2007; Mortimer *et al.*, 2007; Carrapa *et al.*, 2008; Carrera & Muñoz, 2008; Bosio *et al.*, 2009; Bywater-Reyes *et al.*, 2010).

Our study specifically examines the heavily vegetated eastern sector of the Salta foreland whereby we are trying to resolve the following questions: When was the foreland compartmentalized by range uplifts? How did deformation modify sediment dynamics? Was sediment transiently trapped in the intermontane basins or exported from the orogen? To answer these questions we first present a detailed introduction to the basement lithologies and the stratigraphic record of the region, which forms the foundation for

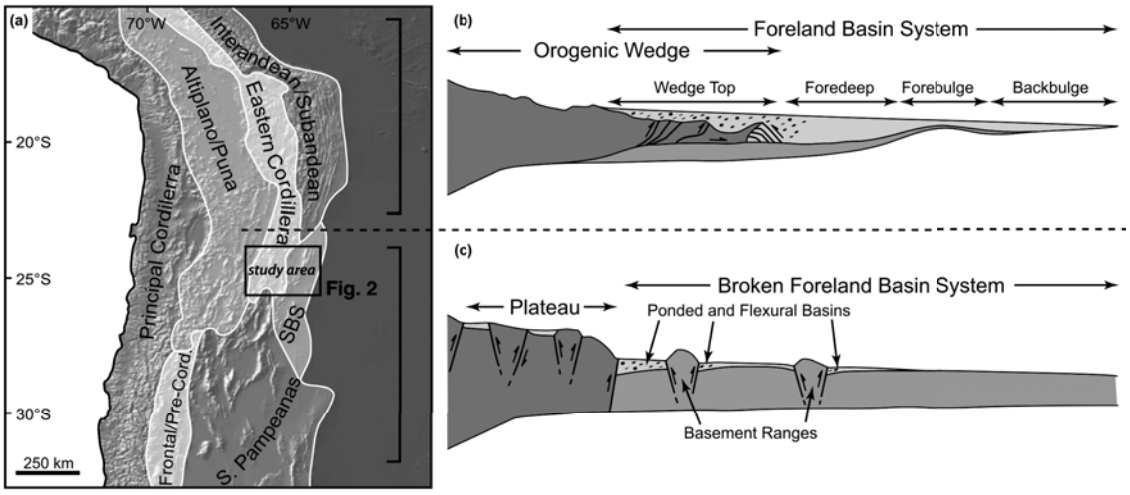

Figure 5.1 – (a) Overview of the morphotectonic domains of the central Andes and schematic representation of (b) the thin-skinned Subandean foreland fold-and-thrust belt (modified after DeCelles & Giles, 1996, with permission of John Wiley) and (c) the thick-skinned broken foreland system farther to the south (modified after Strecker *et al.*, 2011, with permission of Blackwell). Dashed line at 25.5° S represents the transition in tectonic style of the retroarc foreland of the southern central Andes.

the synthesis we are attempting to accomplish. Second, we present an account of tectonostratigraphic relationships of late Mio-Pliocene and Quaternary strata. Third, changes of the conglomerate provenance signatures and facies pertaining to three syntectonic formations allow to distinguish between sediment export from the orogen versus sediment trapping in the hinterland. Fourth, we undertake a detailed analysis of present-day geomorphic and climatological conditions. Overall, our observations agree well with and add detail to the model outlined above. Importantly, we will use observations to illustrate (1) that efficient intermontane sediment trapping does not require internal drainage conditions and (2) that intermontane sediment storage may modify precipitation patterns by raising basin elevation in the hinterland.

5.2 Geologic setting

The study area is situated at ~25° S, between the arid, internally drained orogenic Puna Plateau in the west and the undeformed Chaco Plain foreland basin in the east. Specifically, this region comprises the southern sectors of the Eastern Cordillera (EC), the Santa Bárbara System (SBS), and the Sierras Pampeanas morphotectonic provinces (Figs 5.1 and 5.2b); here, we refer to the study area as a whole as the *Salta foreland*. At this latitude the Andean orogen was, until the middle Miocene, bordered by a contiguous foreland basin (e.g., Coutand *et al.*, 2001; Hernández *et al.*, 2005; Carrapa *et al.*, 2008; Bosio *et al.*, 2009). Since that time, contractile inversion of the Cretaceous Salta Rift (e.g., Baldis *et al.*, 1976; Rolleri, 1976; Bianucci & Homovc, 1982; Salfity, 1982; Allmendinger *et al.*, 1983; Marquillas & Salfity, 1988; Grier *et al.*, 1991; Mon & Salfity, 1995; Viramonte *et al.*, 1999; Kley & Monaldi, 2002; Kley *et al.*, 2005; Carrera

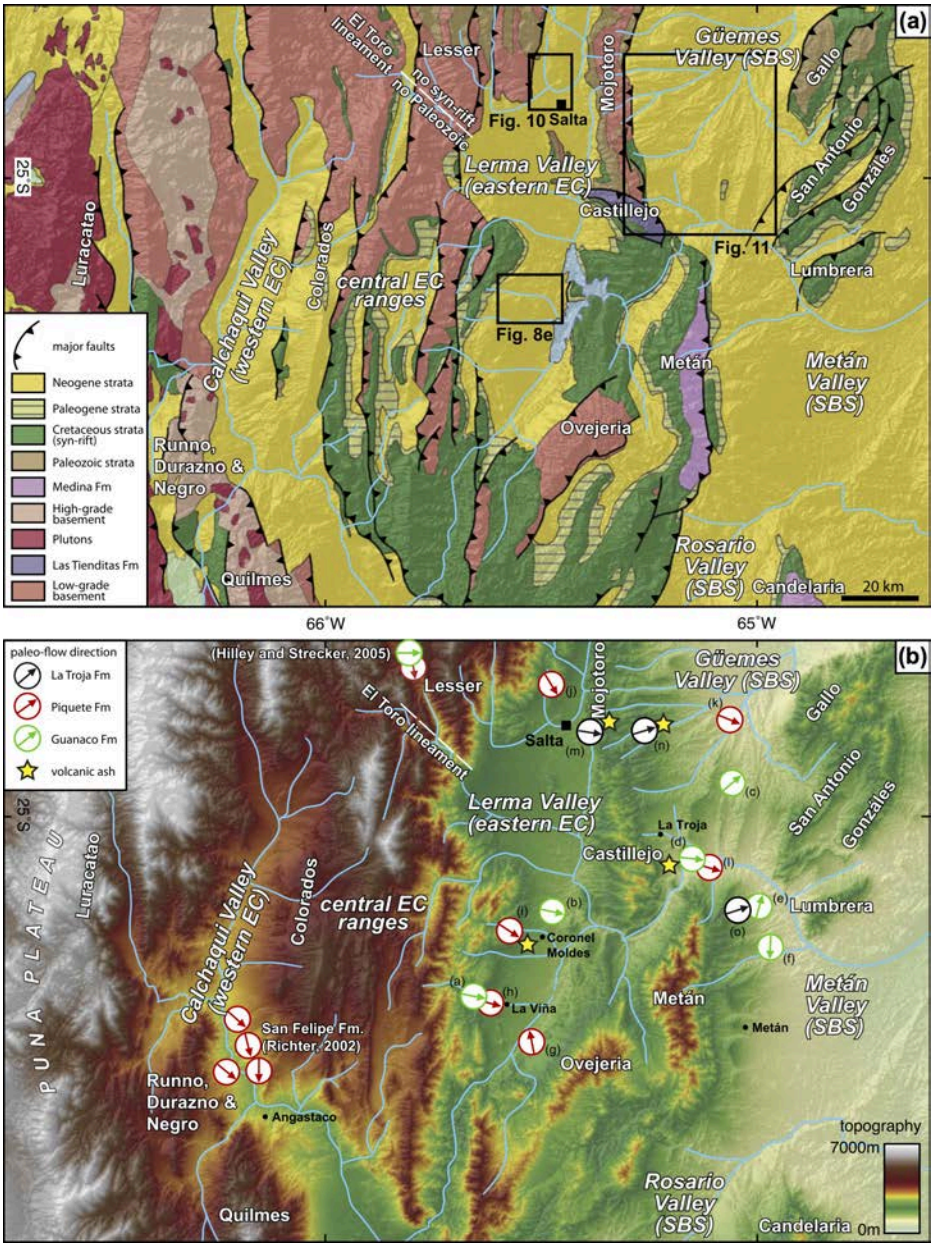

Figure 5.2 – (a) Simplified geologic map (after Salfity *et al.*, 1998). Note that the Ovejeria and Metán ranges expose hornblende-bearing subvolcanic rocks, however, their spatial extent is below the scale of the map. (b) Topography of the study area showing paleoflow directions derived from clast imbrication measurements (this study; Richter, 2002; Hilley & Strecker, 2005, and unpublished data from A. Richter).

et al., 2006; Carrera & Muñoz, 2008) has led to a patchwork of basement-cored ranges and intervening intermontane basins that have experienced episodes of internal, or reduced external, drainage conditions (e.g., Malamud *et al.*, 1996; Bookhagen *et al.*, 2001; Salfity *et al.*, 2004), but have been recaptured by rivers that are adjusted to the undeformed foreland (Fig. 5.2a).

Inversion of Cretaceous normal faults constitutes the primary mode of Neogene contractile reactivation in both the SBS (e.g., Mon & Salfity, 1995; Kley & Monaldi, 2002) and the EC (e.g., Carrera *et al.*, 2006). The Cretaceous Salta Rift was characterized by a series of subbasins distributed around the Salta-Jujuy High, a central horst area of the former rift system (Marquillas & Salfity, 1988). The inverted rift subbasins within the Salta foreland are structurally linked by an inferred detachment horizon at a depth of 10 to 16 km that dips gently toward the west (Grier *et al.*, 1991; Kley & Monaldi, 2002; Carrera *et al.*, 2006). The normal faults of the former rift generally strike NNE-SSW and many of them dip to the east, toward the present-day foreland (e.g., Grier *et al.*, 1991). However, in the vicinity of the city of Salta (i.e., the Salta-Jujuy High, see section 5.2.2 and Fig. 5.2a), reactivated Neogene contractional structures strike strictly N-S and are thought to have been guided by Paleozoic thrusts faults, extensional fault arrays, and metamorphic foliations (Mon & Hongn, 1991; Hongn & Riller, 2007; Wegmann *et al.*, 2008; Hongn *et al.*, 2008). In fact, Hongn *et al.* (2010) recently documented that these older basement fabrics have also influenced the Cretaceous Salta Rift. Although these principle structures are well described the timing when they compartmentalized the foreland sector remains largely unresolved.

In sections 5.2.1-5.2.4 we provide a detailed synopsis of the rich lithologic and stratigraphic database of the region. This information serves as a backdrop to understand the tectonic significance of the provenance signatures that we document.

5.2.1 Basement rocks

A suite of different metamorphic grades and distinct N-S oriented tectonometamorphic domains characterize the basement beneath the Salta foreland (Mon & Hongn, 1991; Mon & Salfity, 1995). Most relevant to this study is an Ordovician-Silurian orogenic belt that exposes a basement composed mainly of gneisses, mylonites and Precambrian granitoid batholiths (Mon & Hongn, 1991; Salfity *et al.*, 1998). This tectonometamorphic domain along the former western margin of Gondwana broadly coincides with the present-day boundary between the Puna Plateau and the EC (e.g., Allmendinger *et al.*, 1983; Mon & Hongn, 1991; Hongn & Riller, 2007). It has been suggested that the lithologic transition at the Puna/EC boundary is ultimately related to a Mesoproterozoic suture formed during the assembly of Rodinia (see Ramos, 2008, and references therein). Consequently, Neogene reverse faults at the Puna Plateau margin (westernmost EC) expose only amphibolites and migmatites together with plutonic and pegmatitic rocks (high-grade basement in Fig. 5.2a), whereas greenschist-facies metasedimentary rocks of the Puncoviscana Formation (low-grade basement in Fig. 5.2a) are exposed throughout the central and eastern EC and the SBS (e.g., Ruíz Huídobro, 1968; Ježek *et al.*, 1985; Mon & Hongn, 1991; Salfity *et al.*, 1998; Ramos, 2008). However, in the vicinity of Metán (i.e., Sierra Metán), recrystallization, still under greenschist metamorphic conditions, resulted in a regionally distinct lithology that has been grouped into the Medina Formation (e.g., Salfity *et al.*, 1998, Fig. 5.2a). In contrast to the Puncoviscana Formation, this unit contains macroscopic mica and chlorite and displays folds with wavelengths of up 20 cm (Durand

& Rossi, 1999). The Cumbres del Castillejo expose black carbonates of the Las Tienditas Formation dating back to the Precambrian/Phanerozoic boundary (Sial *et al.*, 2001). The basement rocks of the Sierra de Ovejeria and the Metán ranges expose light gray, hornblende-bearing volcanic rocks associated with Cretaceous rift-related magmatism (Viramonte *et al.*, 1999). With respect to the objectives of this study, the latter three units (i.e., Medina Formation, Las Tienditas Formation and light gray volcanics) provide excellent marker lithologies for provenance studies with well-defined source regions.

5.2.2 Paleozoic, Mesozoic, & Paleogene sedimentary successions

Paleozoic strata of the Salta foreland include shales, lithic sandstones, and pebbly quartz arenites (e.g., Ruíz Huídobro, 1968; Turner, 1970), limited to areas northeast of the NW-SE striking El Toro lineament (Allmendinger *et al.*, 1983, Paleozoic strata in Fig. 5.2a). During the extension that generated the Cretaceous Salta Rift this lineament constituted the southwestern limit of the Salta-Jujuy High. Consequently, the clastic and volcanic Cretaceous rift fill (Pirgua Subgroup) as well as carbonates and shales (Balbuena and Santa Bárbara subgroups; Paleogene strata in Fig. 5.2a) deposited in the basins during postrifting thermal subsidence, occur only southwest of the lineament (e.g., Grier *et al.*, 1991; Salfity *et al.*, 1998). Although the lithologic contrast across the El Toro lineament suggests a fault that was active during both the Paleozoic and the Cretaceous, in the absence of unambiguous observations concerning its Cenozoic tectonic activity, we simply note its importance as a discriminator for sediment provenance.

The upper section of the Santa Bárbara Subgroup and coeval units farther west exhibit early signs of contractional deformation. For example, growth strata preserved along the present-day Puna margin provide evidence for Eo-Oligocene tectonism giving rise to foreland-basin style sedimentation (e.g., Hongn *et al.*, 2007; Bosio *et al.*, 2009). Proximal and distal units pertaining to this early stage of Andean evolution are well documented (e.g., Vergani & Starck, 1989a,b; Salfity *et al.*, 1993; Starck & Vergani, 1996).

5.2.3 Metán Subgroup

Following the establishment of internal drainage in the Puna region during the middle Miocene (e.g., Jordan & Alonso, 1987; Alonso *et al.*, 1991; Vandervoort *et al.*, 1995) foreland-style sedimentation continued unconformably atop Paleogene strata (e.g., Hongn *et al.*, 2007). In the eastern EC and the SBS, the Neogene Metán Subgroup (Orán Group) is composed of sandstones and mudstones, with occasional beds of oolitic limestones (e.g., Russo & Serraiotto, 1978; Galli *et al.*, 1996). These horizons pertaining to the Anta Formation have been associated with the Paranense transgression between 15 and 13 Ma (e.g., Hernández *et al.*, 2005). The transition from the thinly bedded Anta Formation to the overlying sandstone-dominated Jesus Maria Formation (eastern EC and the SBS) defines an upward coarsening and thickening trend. Distinct lateral facies zonation recorded in the EC (Russo & Serraiotto, 1978) furthermore enables a correlation with coeval conglomerates and sandstones of the Angastaco Formation of the western EC (Fig. 5.3), related to deposition in a braidplain environment (Díaz & Malizzia, 1984).

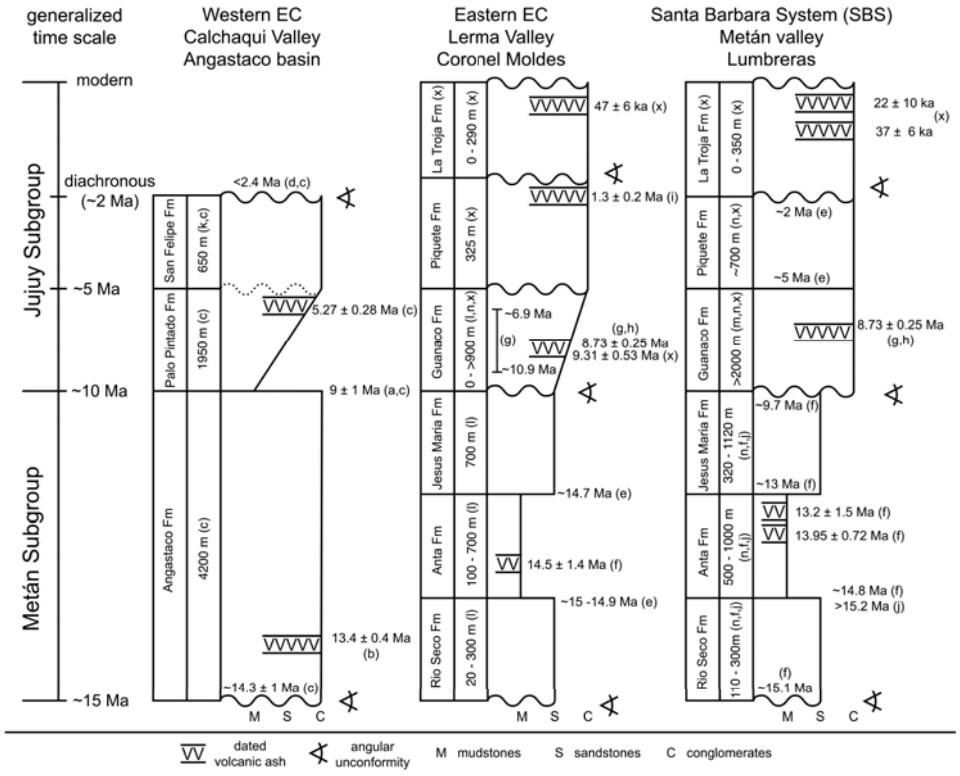

Figure 5.3 – Compilation of Neogene stratigraphy and chronologic constraints for the three principle intermontane basins east of the Puna margin. The thicknesses of the formations are not shown to scale as they have been aligned to a generic time scale that also corresponds to megasequences II to IV of Starck & Vergani (1996). Note that, especially at the Piquete/La Troja contact, diachronous onset of deformation/ syntectonic deposition is implicated. Deposits in the Calchaquí Valley equivalent to the La Troja Formation have not been investigated herein, but Carrera & Muñoz (2008) Salfity *et al.* (2004) report Quaternary strata closely associated with neotectonic compressional structures. Compilation based on the following: [a]Marshall *et al.* (1983); [b]Grier & Dallmeyer (1990); [c]Coutand *et al.* (2006); [d]unpublished data from M. Strecker; [e]Reynolds *et al.* (1994); [f]Reynolds *et al.* (2000); [g]Viramonte *et al.* (1994); [h]Viramonte *et al.* (1984); [i]Malamud *et al.* (1996); [j]Galli *et al.* (1996); [k]Grier (1990); [l]Vergani & Starck (1988); [m]Gebhard *et al.* (1974); [n]Gonzalez Villa (2002); [x]this study.

5.2.4 Jujuy Subgroup

The Jujuy Subgroup (Orán Group) is currently subdivided into the Guanaco and Piquete formations (Gebhard *et al.*, 1974; Russo & Serraiotto, 1978; Starck & Vergani, 1996). In addition to these late Miocene to early Pleistocene formations we document evidence for thick Quaternary strata exposed in both the EC and the SBS, constituting a new unit, the *La Troja Formation*.

5.2.4.1 Guanaco Formation

The well-sorted sandstones, gravelly sandstones, and intraformational conglomerates of the Guanaco Formation overlie the Metán Subgroup. The appearance of conglomerates and the meter- to decameter-scale

bedding is the continuation of the upward coarsening and thickening trend that commenced in the Metán Subgroup. Within the SBS, the Guanaco Formation is characterized by multiple sharp transitions from mudstones to conglomerates and sandstones. Mudstones are less abundant in the EC, where well-sorted sandstones dominate the formation, together with conglomeratic and gravelly sandstone channels that form sharp contacts with the well-sorted sandstones. Matrix-supported conglomerates are common in both the EC and the SBS (Gonzalez Villa, 2002), mostly associated with small-scale cut-and-fill geometries and planar cross stratification. The basal contact with the Metán Subgroup has been reported as being conformable to erosive (e.g., Gebhard *et al.*, 1974), but Cristallini *et al.* (1997) recognized an onlap relationship in the SBS, possibly related to an early uplift at the EC/SBS transition (Hain, 2008, this study). In the seismic reflection data presented below it will be shown that a low-amplitude angular unconformity also exists in the eastern EC.

The Guanaco Formation was deposited between >10.9 and <6.9 Ma (Viramonte *et al.*, 1994; Reynolds *et al.*, 2000). In the vicinity of Coronel Moldes (Fig. 5.2) we dated a volcanic ash layer at 9.31 ± 0.31 Ma (Fig. 5.4a and Table E.1; see also section 5.3.1) from within a Guanaco Formation sandstone sequence with scarce granitoid clast bearing conglomeratic channels. Farther west, along the Puna margin, the Palo Pintado Formation (Calchaquí Valley western EC) was deposited between 9 ± 1 Ma and <5.27 ± 0.28 Ma (Coutand *et al.*, 2006) in an unrestricted foreland setting with longitudinal rivers, swamps and ponds (Starck & Anzótegui, 2001). This is interesting because, we will argue below, the Palo Pintado and Guanaco Fms comprise a megafan system that delivered sediment with a Puna border provenance signature across the entire foreland sector.

5.2.4.2 Piquete Formation

The Piquete Formation erosionally to paraconformably overlies the Guanaco Formation in the SBS (Cristallini *et al.*, 1997) and the eastern part of the EC, whereas these formations are separated by an angular unconformity in the central EC (Gonzalez Villa, 2002; Carrera & Muñoz, 2008). In the eastern sector of the EC, the Piquete Formation comprises well imbricated, clast-supported, and laterally continuous conglomerate horizons interbedded with silty sandstones. In the SBS, the Piquete Formation is characterized by abundant carbonate-bearing paleosols interbedded with gravelly sandstones and conglomerates that are predominantly matrix supported. The channel facies frequency and the modal clast size of the associated conglomerates tend to decrease from the EC to the SBS.

Based on magnetostratigraphic data and an apatite fission track dated tuff near Coronel Moldes in the Lerma Valley, the Piquete Formation was deposited between ~5 Ma (Reynolds *et al.*, 1994, 2000) and <1.3 ± 0.2 Ma (Malamud *et al.*, 1996). These strata are thus coeval with the San Felipe Formation in the Calchaquí Valley to the west (Coutand *et al.*, 2006; Strecker *et al.*, 2007a, Fig. 5.3).

5.2.4.3 La Troja Formation

Only two reports have addressed the accumulation of thick Quaternary strata in the eastern EC and the SBS (Monaldi *et al.*, 1996; Carrera & Muñoz, 2008). Monaldi *et al.* (1996) attribute these deposits to the Piquete Fm. Noting both growth strata and unroofing trends in conglomerate composition they propose two Pleistocene thrust fronts, one in the central EC and one at the EC/SBS transition, as the sediment source regions. Carrera & Muñoz (2008) briefly mention Quaternary growth strata in the eastern EC, complimentary to a wealth of similar Quaternary structures they document in the western and central EC. Furthermore, Salfity *et al.* (2004) documented lake deposits ponded west of a Quaternary fault in the western EC. Below we present previously unpublished observations pertaining to the Quaternary deposits (Hain, 2008) and suggest the adoption of the name *La Troja Formation*.

5.3 Methods

5.3.1 U–Pb & U–Th zircon geochronology

It is important for our assessment of the stratigraphic record of the poorly exposed, heavily vegetated eastern sector of the Salta foreland that we assign our observations to the correct formations. For this reason we radiometrically dated zircons from five volcanic ash samples, one pertaining to the inferred megafan deposit (Guanaco Fm) and four pertaining to the sediments deposited during and after the latest stage of intrabasin deformation (La Troja Fm; sample sites marked as yellow stars in Fig. 5.2b). U–Pb and U–Th zircon ages were obtained using the CAMECA IMS 1270 ion microprobe at UCLA (Tables E.1 and E.2). Instrument setup and relative sensitivity calibrations for U–Pb and U–Th analysis are described by Grove *et al.* (2003) and Schmitt *et al.* (2006). U–Pb age uncertainties estimated from the reproducibility of AS3 zircon (1099.1 Ma, Paces & Miller, 1993) are 2.3 to 2.7%. Secular equilibrium standard AS3 yielded $(^{230}\mathrm{Th})/(^{238}\mathrm{U}) = 1.001 \pm 0.013$ (MSWD – mean square of weighted deviates = 0.3; $n = 12$) with parentheses denoting activities. U–Th zircon melt isochron ages (Reid *et al.*, 1997) were calculated using published $(^{230}\mathrm{Th})/(^{232}\mathrm{Th})$ and $(^{238}\mathrm{U})/(^{232}\mathrm{Th})$ for evolved central Andean lava (Parinacota rhyolite 91-014, Bourdon *et al.*, 2000) as representative of the melt. Because of the strong U/Th fractionation of zircon relative to the melt, uncertainties in the melt composition contribute to the overall uncertainty of the model ages only to a negligible amount.

Ash 2 yielded a $^{206}\mathrm{Pb}/^{238}\mathrm{U}$ age of 9.31 ± 0.31 Ma (2σ, MSWD = 1.9, $n = 7$, Fig. 5.4a). Three zircon crystals in Ash 2 are slightly older (~11 Ma), and were omitted from the average. Ash 3 yielded few crystals, and the ones analyzed are Paleozoic-Precambrian in age ($^{206}\mathrm{Pb}/^{238}\mathrm{U}$ age between 315 and 711 Ma; $n = 4$). Because xenocrystic zircon is rare in the other ashes, we interpret these crystals to be detrital. Initial U–Pb dating of zircon crystals in samples Ash U, Ash Q, SA150406-01, and SA150406-03 yielded very low and highly unradiogenic $^{206}\mathrm{Pb}$ intensities. Although individual age uncertainties are large, the zircon crystals have Late Pleistocene $^{206}\mathrm{Pb}/^{238}\mathrm{U}$ ages (with an overall average between ~50-120 ka, after correc-

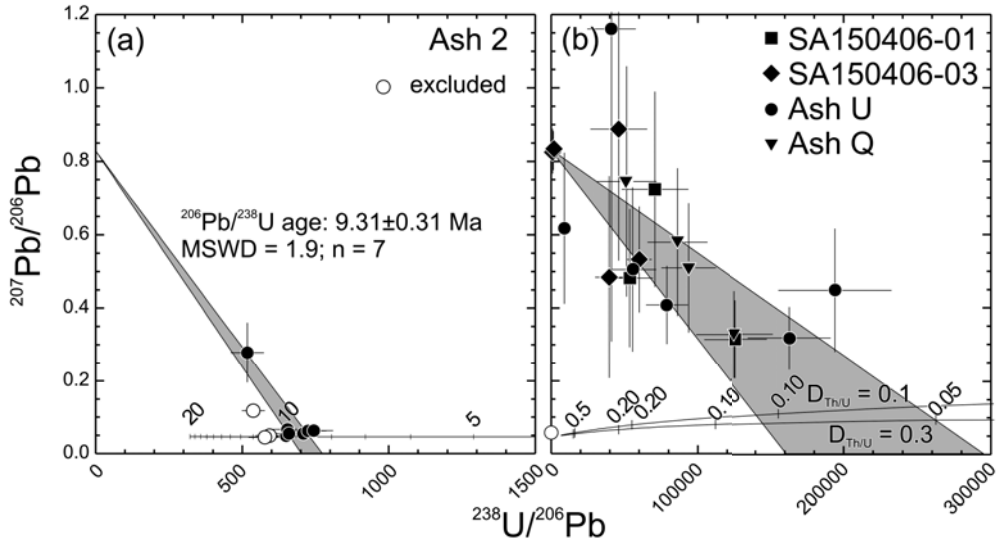

Figure 5.4 – (a and b) Shown are ^{207}Pb/^{206}Pb versus ^{238}U/^{206}Pb zircon results, uncorrected for common Pb, showing segments of concordia (ages in Ma) and regression lines with a fixed y axis intercept corresponding to common Pb (^{207}Pb/^{206}Pb = 0.83). Concordia intercept ages in Fig. 5.4b vary as a function of the fractionation between Th and U in zircon crystallizing from a melt. The ^{206}Pb deficit resulting from ^{230}Th disequilibrium was calculated from zircon mineral melt distribution coefficients ($D_{Th/U}$) between ~0.1 and 0.3, estimated from Th/U in zircon and the average for continental arc magmas. Based on model intercept ages, maximum eruption ages for ashes SA150406-01, SA150406-03, Ash U, and Ash Q of 0.10 ± 0.05 Ma are inferred.

tion for initial disequilibrium; Fig. 5.4b), with the exception of a single old zircon (~534 Ma) in Ash U. The young crystallization age of these zircons was confirmed by subsequent ^{238}U-^{230}Th dating, which indicated uranium-series disequilibrium in most crystals with (^{230}Th)/(^{238}U) ranging between 0.18 and 1.0. Zircon melt model ages (Fig. 5.5 and Table E.2) range between 22 ka and >380 ka (which represents the upper age limit resolvable by the ^{238}U-^{230}Th method). The geochronological data cannot distinguish between crystals being derived from different eruptions, or protracted crystallization within an individual magma system and a single eruption. Protracted zircon crystallization is characteristic for silicic magma systems in convergent margin settings (e.g., Schmitt *et al.*, 2010). Regardless of the causes for the heterogeneous zircon age population in these ashes, it is the youngest crystal(s) in each population which we use in order to constrain maximum depositional ages (Fig. 5.5): Ash U (22 ± 10 ka), Ash Q (47 ± 6 ka), SA150406-01 (37 ± 6 ka), and SA150406-03 (26 ± 10 ka).

5.3.2 Paleoflow reconstructions

To reconstruct paleoflow directions the orientation of individual pebbles (usually 60 or more) in clast-supported conglomerates were measured. Using Stereonet software (by R. Allmendinger; *www.geo.cornell.edu/geology/faculty/RWA/programs.html*) this raw data was then rotated so as to restore

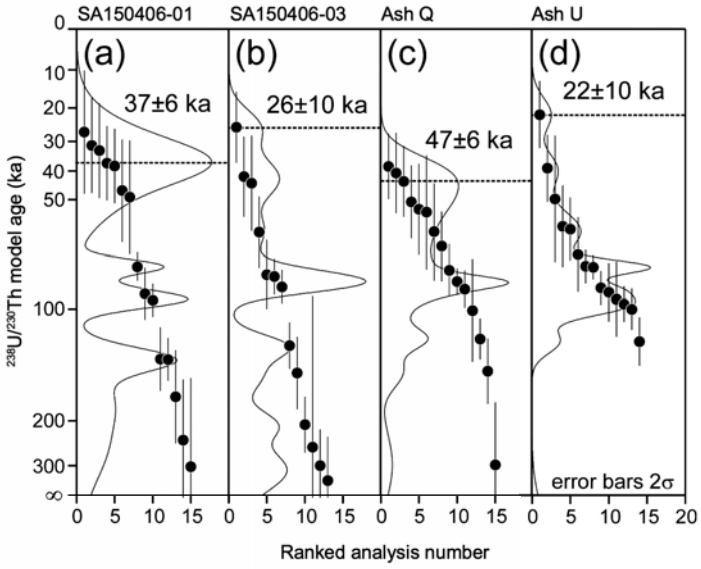

Figure 5.5 – (a-d) Shown are ^{238}U–^{230}Th zircon model ages and relative probabilities plotted for SA150406-01, SA150406-03, Ash Q, and Ash U. Dashed lines indicate maximum depositional age determined from the youngest zircon crystallization age in the population.

bedding to horizontality. According to this procedure clast orientations are assumed to point upstream (i.e., imbrication) requiring 180° rotation around the vertical to reflect transport direction. Fig. 5.6 represents the raw (i.e., unrotated) lower hemisphere projection of the data and the orientation of bedding. The central tendency of the inferred transport directions is shown in Fig. 5.2b.

5.3.3 Interpretation of seismic reflection data

Three dimensional reflector mapping and analysis was completed on the unmodified (i.e., not depth migrated) data set using Schlumberger Petrel software. We measured the vertical distance (in TWT – two-way travel time) of the Cretaceous rift sediments to assess if extensional structures (i.e., localized extensional depocenters) are present in the seismic grid. To illustrate the geometry of the inferred half-graben depocenters we flattened the first (i.e., deepest) postrift reflector, which amounts to a purely vertical distortion. This approach is a good approximation of the reflector geometries prior to shortening since the inferred extensional fault did not offset the stratigraphic interval shown. If not noted otherwise, seismic sections are displayed without modifications.

5.4 Results

5.4.1 Tectonostratigraphy

In addition to the shortening accommodated by the reactivated former extensional hanging walls now constituting the ranges in the broken foreland, the basins have also been shortened, affecting most of the

synorogenic succession (e.g., Kley & Monaldi, 2002; Salfity *et al.*, 2004). In the basins, the Neogene deposits have been folded and faulted by mild inversion of Cretaceous extensional fault systems in both the SBS (Cristallini *et al.*, 1997) and the EC (Carrera & Muñoz, 2008). Below, we present further evidence for Quaternary deformation in the eastern EC and the SBS, making a case for an episode of widespread, continued basin inversion. These intrabasin structures are of particular importance because they create accommodation space for the La Troja Fm. We will demonstrate that large volumes of Quaternary sediments are stored at moderate to high elevation despite drainage connectivity to the foreland.

5.4.1.1 Coronel Moldes anticline

A grid of eleven seismic lines from the Coronel Moldes area augmented by borehole data and detailed structural mapping have helped to decipher the deformation history of the basin interior in the Lerma Valley (eastern EC; Fig. 5.2).

A planar 255° (WSW) dipping anisotropy was imaged in the basement below the town of Coronel Moldes (Fig. 5.7). The anisotropy does not displace Neogene strata, nor is it oriented parallel to the 35° -215° (NE-SW) trending Coronel Moldes anticline (Hain & Strecker, 2008, Fig. 5.8e). We tentatively relate this subsurface structure to the N-S striking Precambrian basement structures (i.e., the thrust separating the Choromoro and Lules tectonometamorphic belts, or alternatively, the west dipping axial plane foliation of the Choromoro Belt (Mon & Hongn, 1991).

Although no normal fault was directly imaged in the investigated seismic sections, the thickness distribution of the Cretaceous rift fill, interpolated from the seismic grid, defines four distinct depocenters (DC1 to DC4 in Fig. 5.8e). Three of the depocenters are aligned within the core of the Coronel Moldes anticline (Figs 5.8e and 5.9). Toward the SW, where the DC4 is offset to the west, the anticline abruptly disappears in both surface and subsurface expression. In the area of DC4, a second subparallel anticline has developed. The overall geometry defined by the deformed fills thus resembles a SSW striking, WNW dipping, en echelon half-graben array. The absence of reflector offsets in the synextensional strata (Fig. 5.9) may be related to drape folding (e.g., Howard & John, 1997). Nonetheless, a more complex deformation mechanism involving transtension (e.g., Janecke *et al.*, 1998) of the aforementioned deep basement anisotropy resulting in fault-oblique drape folding cannot be excluded.

The early deformation episode separating the Guanaco Formation and the Metán Subgroup has no expression discernible in our field observations. However, a low amplitude angular unconformity imaged by the seismic survey (Fig. 5.7) correlates with the transition between the Metán Subgroup and the Guanaco Formation (Fig. 5.8). We suggest that this erosional truncation of Metán Subgroup strata in the eastern EC, onlap relationships in the SBS (e.g., Cristallini *et al.*, 1997), and a new isolated sediment source at the EC/SBS transition (section 5.4.2.1), reflect the uplift of the Sierra Metán at ~10 Ma.

Since the Coronel Moldes anticline involves the Piquete Formation (Fig. 5.8) with an intercalated volcanic ash dated at 1.3 ± 0.2 Ma (Malamud *et al.*, 1996), the inversion of the fault array must be younger.

During and after folding sedimentation of the La Troja Formation occurred on both sides of the anticline but at different elevations (up to 1400 m to the west and 1130 m to the east) as a result of structurally controlled sediment ponding west of the fold (Fig. 5.8c). Onlap against the anticline is imaged in the seismic reflection profiles (Fig. 5.8b) and can be locally seen in outcrop (Fig. 5.8a). The sediment-filled western syncline exhibits growth strata. Beneath the town of Coronel Moldes (i.e., the filled eastern syncline) the La Troja Formation attains an acoustic thickness of 240 ms (TWT, Fig. 5.7).

The modern topographic expression of the Coronel Moldes fold array may at first sight appear to be minor, especially when compared to the ranges that segment the foreland. Nonetheless, we argue that this Quaternary intrabasin structure absorbed shortening at a high rate. Perpendicular to the structures, the 19.5 km long top of the Piquete Formation was shortened to 16.5 km (Fig. 5.8c). Given the 1.3 ± 0.2 Ma age of the ash intercalated within this unit (Malamud *et al.*, 1996) we find that the strata were shortened at a rate in excess of 3.1 ± 0.6 mm/a.

5.4.1.2 Sierra Vaqueros & San Lorenzo anticlines

A second example of a Quaternary fold array in the Lerma Valley can be found near the northwestern limits of the city of Salta, the provincial capital (Fig. 5.10). Here, the fault-cored Sierra Vaqueros exposes Piquete Formation conglomerates, and the en echelon San Lorenzo anticline involves Quaternary strata (i.e., the La Troja Fm). The top of the Sierra Vaqueros structure is 700 m higher than the floor of the Lerma Valley. Multiple uplifted fluvial terraces attest to recent deformation and modification of the river network, unambiguously documenting that this structure is actively growing in a southwestward direction. We attribute much of the ~140 m elevation difference between San Lorenzo (1340 m; west of the fold) and Salta (1200 m; east of the fold) to differential Quaternary sediment storage (Fig. 5.10); a situation very similar to the two filled synclines in the Coronel Moldes area (Fig. 5.8c). It is interesting to note that one of the recent earthquakes located within the interior of the Lerma Valley, a magnitude 6.3 event, was registered immediately east of the Sierra Vaqueros (Fig. 5.10; USGS event ID: U.S.2010tfc3).

5.4.1.3 Santa Bárbara System inversion

Previous studies have shown that Andean contractional structures in the SBS invert Cretaceous normal faults (e.g., Grier *et al.*, 1991; Cristallini *et al.*, 1997; Kley & Monaldi, 2002). Onlap of the Guanaco Formation just east of the Sierra Metán has been documented (Cristallini *et al.*, 1997), and the Guanaco and Piquete formations are not separated by an angular unconformity (Cristallini *et al.*, 1997; Gonzalez Villa, 2002). Both units, however, have been subsequently folded and faulted (Fig. 5.11, Gonzalez Villa, 2002; Kley & Monaldi, 2002). During and after shortening the Quaternary La Troja sediments were deposited in the synclines; in Fig. 5.11, the east sloping remnant fill surface of the central syncline reaches elevations of >1250 m whereas the fill of the eastern syncline slopes south at elevations well below 1000 m. Possible onlap relationships and/or growth strata in the central syncline have been largely eroded. Along the

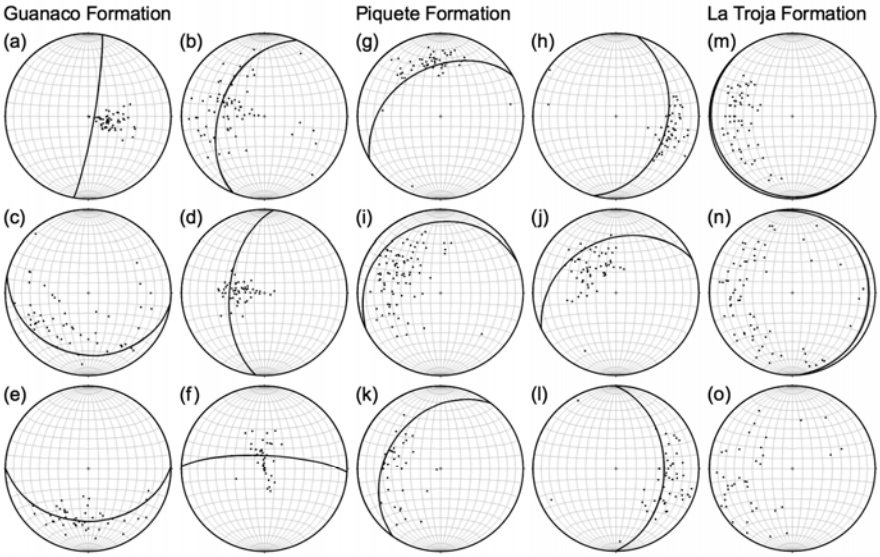

Figure 5.6 – Paleoflow reconstruction based on clast imbrications. Shown here are lower hemisphere projections of clast orientations as measured in the field and bedding orientations (great circle). The central tendency derived from these data (corrected for deformation) is shown in Fig. 5.2b as paleoflow direction; see section 5.3.2 for details on the correction. The precise locations of the stations are (a) 25°26.062' S, 65°36.617' W; (b) 25°13.888' S, 65°26.232' W; (c) 24°49.606' S, 65°0.824' W; (d) 25°7.739' S, 65°5.485' W; (e) 25°11.941' S, 64°57.335' W; (f) 25°17.334' S, 64°55.652' W; (g) 25°31.602' S, 65°30.682' W; (h) 25°26.659' S, 65°35.448' W; (i) 25°16.142' S, 65°31.955' W; (j) 24°42.654' S, 65°26.922' W; (k) 24°48.019' S, 65°1.484' W; (l) 25°7.833' S, 65°01.206' W; (m) 24°47.363' S, 65°21.440' W; (n) 24°48.103' S, 65°13.353' W; and (o) 25°13.101' S, 64°56.024' W.

eastern flank of the Mojotoro Range remnant alluvial fan conglomerates pertaining to the La Troja Formation rest unconformably on the folded and eroded Mio-Pliocene strata (Fig. 5.11). The tectonostratigraphic patterns observed in the SBS therefore resemble those that we have documented in the Coronel Moldes area. Importantly, large volumes of Quaternary sediments are stored at high elevations and thus contribute to basin average elevation and topographic load.

5.4.2 Provenance signatures

In the following we will document the conglomerate compositions in the Guanaco, Piquete and La Troja formations. The changes in clast provenance between these formations speak directly to sediment export versus sediment trapping in the hinterland. We argue that the disappearance of clasts with a hinterland provenance provides clear evidence for basin-scale trapping of sediments in the intermontane basins.

5.4.2.1 Guanaco Formation

More than 15% of high-grade metamorphic and granitoid clasts characterize the composition of conglomerates found in the Guanaco Formation in both EC and SBS (Table F.1 and Fig. 5.12a), providing a strong constraint for the sediment source areas, as these lithologies only crop out near the Puna margin (Fig.

5.2a). Specifically, in broad agreement with reconstructed paleoflow directions (Figs 5.2b and 5.6; see section 5.3.2), the presence of amphibolites and the leucosome of migmatites indicate eastward sediment transport. Fine-grained, brick red granites of the Tastil pluton (NW of the El Toro lineament outside Fig. 5.2) imply southeastward transport. Thus, our conglomerate composition data (Table F.1) identifies the source areas for the Guanaco Formation as the basement ranges to the west of the Palo Pintado Formation depocenter (i.e., ranges at the Puna margin just west of the Calchaquí Valley, western EC). This is important, because it suggests that between ~10 and ~5 Ma sediments were derived from the Puna margin and distributed across the entire foreland.

In addition to the above regional provenance pattern, farther east, in the SBS, the occurrence of hornblende-bearing volcanic, Cretaceous carbonate, and Medina Group basement clasts in Guanaco Formation conglomerates (Gonzalez Villa, 2002, Table F.1) suggests a distinct, isolated sediment source. Only the Sierra Metán at the EC/SBS transition (Fig. 5.2), immediately west of the anomalous Guanaco conglomerates, exposes Medina Group basement, along with the other two lithologies. The Ovejeria Range (Fig. 5.2) also exposes the carbonates and hornblende-bearing volcanic lithologies and can thus not be ruled out as a sediment source during the time of the deposition of the Guanaco Formation (i.e., ~10 to 5 Ma). However, the uplift of the Metán/Ovejeria ranges apparently did not significantly interfere with sediment export from the hinterland.

5.4.2.2 Piquete Formation

Throughout the eastern EC and SBS, the conglomerate composition of the Piquete Formation dramatically diverges from that of the Guanaco Formation in that plutonic and medium to high-grade metamorphic clasts are virtually absent (Table F.1 and Fig. 5.12a), although most paleoflow indicators within the Piquete Formation show paleoflows toward the E and SE (Fig. 5.2b; note that the south directed flow pertains to the age equivalent San Felipe Formation). Instead, the Piquete Formation composition of conglomerates in the eastern EC and the SBS varies systematically from N to S, displaying covariance with the location of the El Toro lineament (Figs 5.12b and 5.2). This characteristic compositional signal must originate from the ranges (herein central EC) presently separating the Calchaquí Valley in the western EC from the Lerma Valley in the eastern sector of the EC. In contrast to the Piquete Fm, the coeval San Felipe Formation in the Calchaquí Valley retains Guanaco-like conglomerate compositions characterized by plutonic and high-grade metamorphic clasts (Coutand *et al.*, 2006). The uplift of the central EC ranges must therefore have been able to intercept sediment transport from the Puna margin, causing the divergence between the Piquete and San Felipe conglomerate compositions. This scenario is also compatible with changing transport directions in the San Felipe Formation of the Calchaquí Valley; showing eastward and southward directed paleoflow directions in conglomerates (A. Richter, unpublished data, 2002, Fig. 5.2b).

Diverging from the above pattern, the Piquete Formation is anomalous at two clast count stations (32 and 34) in the SBS in that it resembles the composition of the Guanaco Formation (Fig. 5.12a and Table F.1), suggesting either limited Puna margin sourced sediment bypassing the EC into the SBS or, alternatively, reworking of the Guanaco Formation as observed in the central (e.g., Gonzalez Villa, 2002) and eastern parts of the EC.

Notably, in the southernmost Lerma Valley (eastern EC) clast imbrications indicate north directed transport (Station g in Fig. 5.2b). However, the characteristic hornblende-bearing volcanic lithology exposed today in the Ovejeria Range to the south, is absent (clast count station 39).

Overall, the change of conglomerate composition from the Guanaco Formation to the Piquete Formation suggests that between ~5 and 2 Ma coarse sediments shed from the Puna margin were trapped in the intermontane Calchaquí Valley (i.e., the San Felipe Formation, western EC) rather than being exported from the orogen interior. It appears that the uplift of the central EC ranges at ~5 Ma (1) produced the sediment that constitutes the Piquete Formation and (2) intercepted the Puna margin derived gravel.

5.4.2.3 La Troja Formation

Conglomerate compositions for the Piquete Formation and the La Troja Formation are indistinguishable in the eastern EC except for the decrease in basement clasts and the increased contribution of clasts derived from the Paleozoic and Cretaceous sedimentary cover units to the La Troja Formation conglomerates (relative to Piquete Fm). This difference indicates a shift toward less unroofed sections in the source regions and/or uplift of new sources (Fig. 5.12b, cf. Monaldi *et al.*, 1996). In contrast to the Piquete Fm, Pirgua Subgroup sandstones, which disintegrate over very short transport distances in modern rivers, frequently contribute to the La Troja Formation conglomerates in areas proximal to the present-day ranges of the central EC, south of the El Toro lineament.

North of the El Toro lineament, the lithologic contrast between the central EC ranges and the Mojotoro Range is minimal and conglomerate compositions (but not facies; see section 5.4.3.3) are similar of the Piquete and La Troja formations in both eastern EC and SBS. In the SBS, however, Ordovician fossil-bearing sandstones of the Mojotoro Formation, which are prone to abrasion in modern rivers, contribute to the La Troja Fm, but not to the Piquete Formation, suggesting amarked decrease in transport distance.

At the southern tip of the Mojotoro Range and only few kilometers downstream from the Castillejo Range, the only exposure of black carbonates in the region (Las Tienditas Formation) provides a very direct lithologic constraint (Fig. 5.2a) on the source area for the La Troja Formation in the SBS. While the Guanaco and Piquete formations as well as the base of the exposed section of the La Troja Formation infilling of the local syncline (see section 5.4.1.3 and Fig. 5.11) are devoid of Las Tienditas clasts (Table F.1 Gonzalez Villa, 2002), boulders of the Las Tienditas Formation appear toward the top of the La Troja section, attesting to Quaternary uplift of the Castillejo Range.

In summary, it appears that most of the sediment contributing to the La Troja Formation in the SBS is derived from the ranges at the EC/SBS boundary (i.e., Mojotoro, Castillejo and Metán ranges). Furthermore, there is evidence that large sediment volumes shed from the central EC ranges were trapped by intrabasin structures in the eastern EC (Lerma Valley). The characteristic lithologies exposed along the Puna margin are absent from La Troja Formation conglomerates in both eastern EC and SBS, which indicates efficient sediment trapping in the western EC (Calchaquí Valley).

5.4.3 Sediment dynamics

5.4.3.1 Guanaco Formation

The geometries of well-defined conglomeratic channels embedded in well-sorted sandstones within the EC and an alternating mudstone-sandstone-conglomerate sequence in the SBS attest to an east-west gradient in the depositional environment. The common provenance signature in Guanaco Formation conglomerates throughout the EC and the SBS (see section 5.4.2.1 for one exception) with an unambiguous source area near the eastern Puna border suggests a single contiguous depositional system. Strata farther north in the Subandean Belt, characterized by facies relationships similar to those that we document here for the SBS (see also Gonzalez Villa, 2002), have been related to a fluvial megafan depositional environment (e.g., Horton & DeCelles, 2001; Leier *et al.*, 2005; Uba *et al.*, 2005, 2007, 2009). The Guanaco Formation may thus also be interpreted as a fluvial megafan; originating along the Puna border and shedding sediment >100 km into the foreland.

5.4.3.2 Piquete Formation

The characteristic lateral continuity of well imbricated conglomerate horizons in the eastern EC indicates deposition from unconfined flow at relatively high flow velocities, conditions that may be related to an alluvial fan environment below the intersection point (e.g., Blair & McPherson, 1994). Facies associations in the SBS are in accord with distal fan/alluvial plain depositional systems. The central EC provenance signature (see section 5.4.2.2) is prevalent in both eastern EC and SBS. The Piquete Formation thus appears to be the stratigraphic remnant of a formerly contiguous alluvial fan system, proximal in the eastern EC and distal in the SBS (cf. Gonzalez Villa, 2002).

5.4.3.3 La Troja Formation

The Quaternary La Troja Formation has not been described in detail so far making it timely to document its facies before interpreting the depositional environment and sediment dynamics. In both eastern EC and SBS, the La Troja Formation comprises poorly stratified and poorly sorted sandy gravels alternating with gravelly sands and clayey sands (see also Fig. 5.8a). The gravels are frequently matrix supported, but clast-supported cobbles exist in channel-like lenses. At some stratigraphic levels occasional boulders are embedded in gravelly sandstones. Siltstones are absent, with the exception of the upper stratigraphic

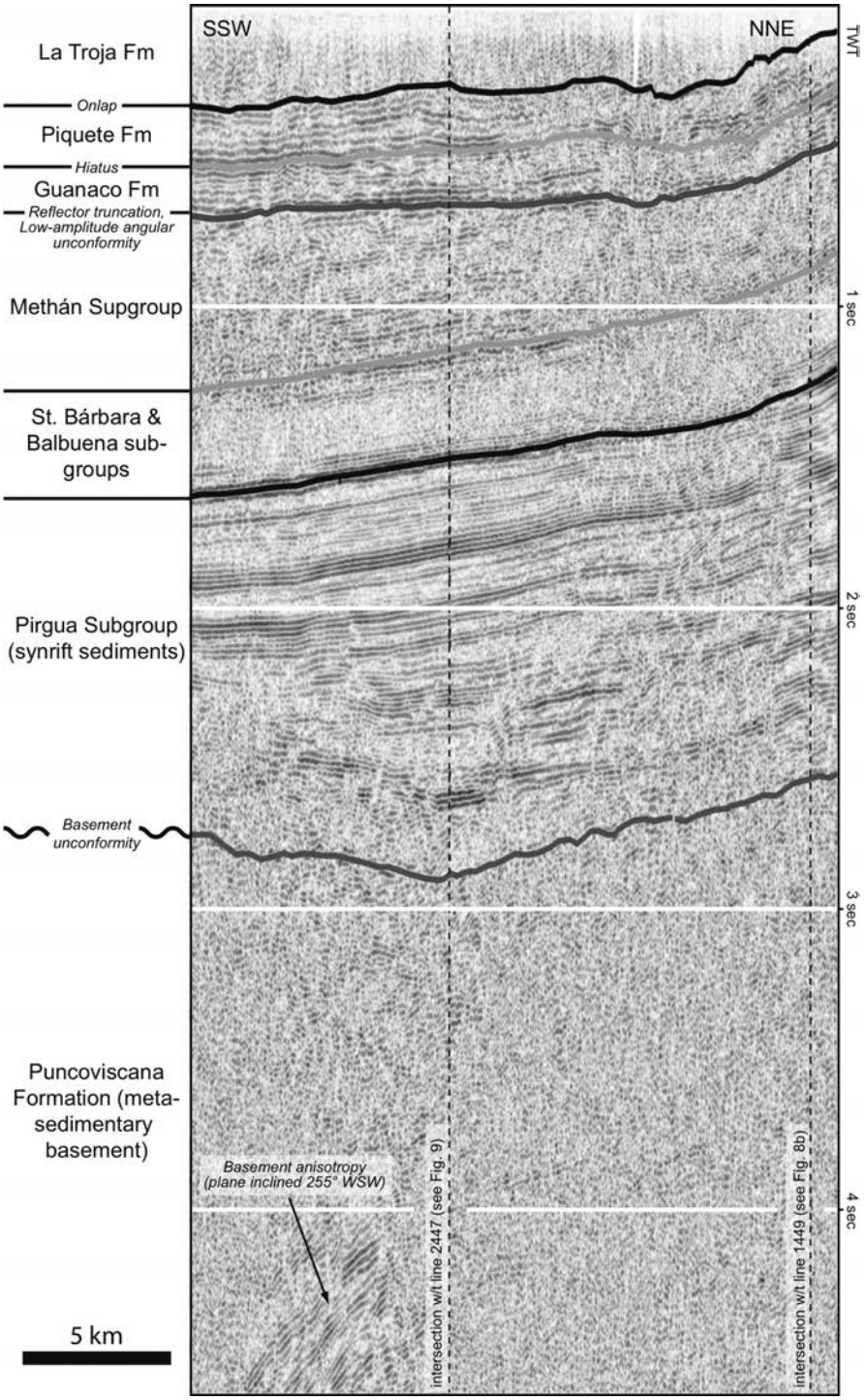

Figure 5.7 – Interpretation of seismic line 2504, situated in the syncline below the town Coronel Moldes, in the Lerma Valley (eastern EC; see Fig. 5.2b). Depth is shown in sec (TWT–two-way travel time). Correlation with the stratigraphic units is based on structural mapping, the nearby borehole CMo.X-1, and seismic facies interpretation. Note the low-amplitude angular unconformity separating the Metán Subgroup from the Guanaco Fm, imaged here as truncation of Metán Subgroup reflectors and the consequent thinning of the Metán Subgroup stratigraphic interval toward the right (NNE). See Fig. 5.8e for location.

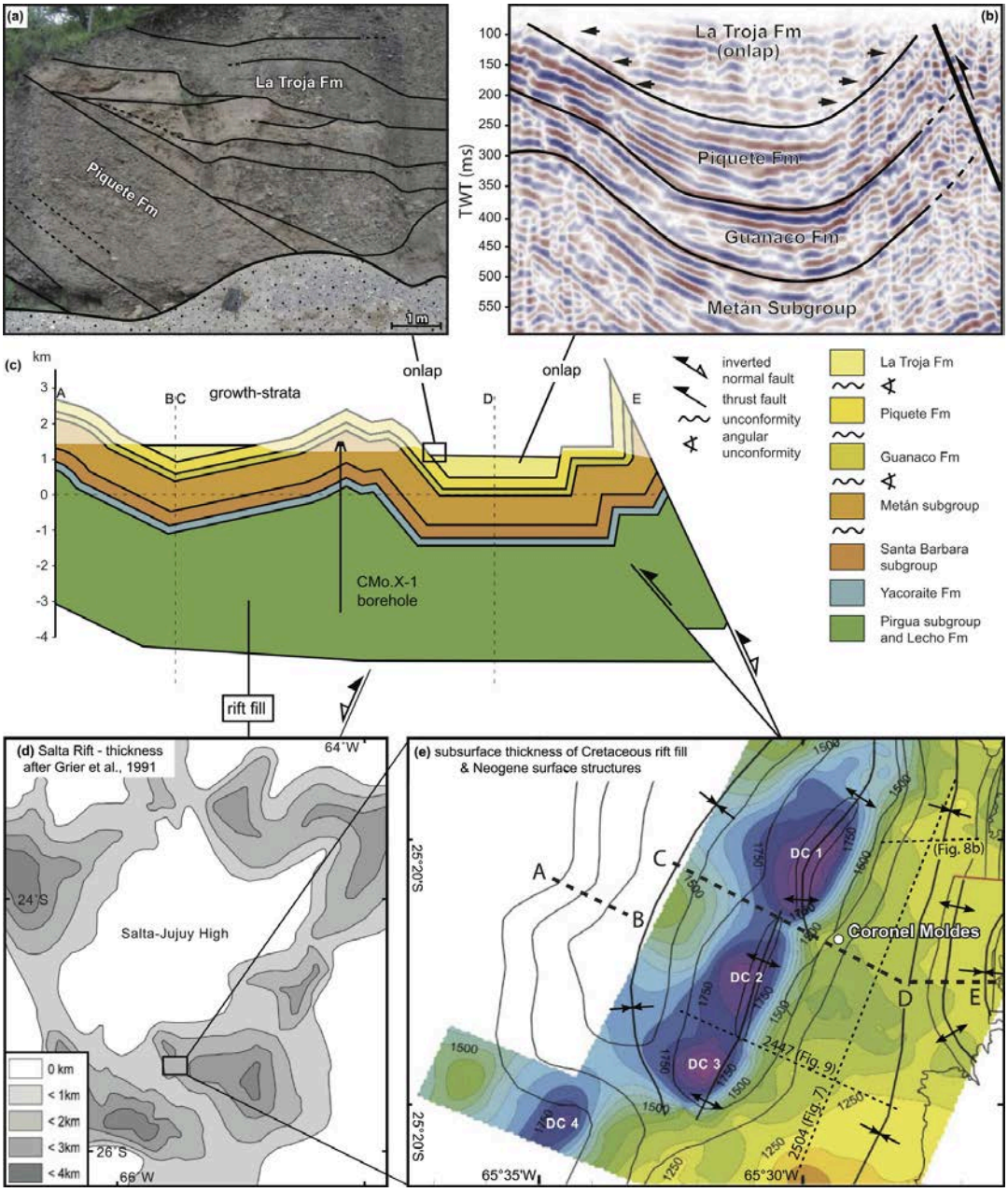

Figure 5.8 – Relationship between Cretaceous extensional structures and Quaternary compressional structures in the eastern EC (Lerma Valley); see Fig. 5.2a for location. (a, b) Onlap relationships of the La Troja Formation indicate that shortening occurred only after deposition of the Piquete Fm. (c) Geologic section across intrabasin structures near Coronel Moldes based on structural mapping, borehole data, and seismic interpretation. (d) The seismic grid is situated within the Cretaceous Salta Rift. (e) The thickness of the synrift stratigraphic interval is characterized by four distinct depocenters (DC 1 to 4). The close correlation between the compressive structures mapped in the field and the acoustic thickness (contoured here as milliseconds two-way traveltime (TWT)) of the rift fill requires inversion of the en echelon array of Cretaceous extensional structures during shortening. The exposed onlap (Fig. 5.8a) is visible along the Tajamar stream, near La Viña, about 20 km SSW of the geologic section (paleoflow station (h) in Fig. 5.2b).

levels of the Coronel Moldes syncline (i.e., west of the Coronel Moldes anticline), where massive banks of friable, chalky, muddy siltstones, containing only rare granules, are associated with infrequent, heavily cemented, longitudinal (i.e., N-S oriented) gravel-filled channels.

The facies associated with the remnant alluvial fan to the east of the Mojotoro Range (Fig. 5.11) are in stark contrast to those described above. Proximal to this range the La Troja Formation is exposed in vertical walls of fanglomerate with no discernible bedding, many tens of meters high (e.g., clast count station 19). The remnant fan surface slopes to the east and east sloping bedding, defined by alternating banks of gravelly sands and sandy gravels, becomes progressively better developed toward the toe of the fan. A massive fanglomerate outcrop, similar to the proximal Mojotoro fan, can be found in the eastern EC near Talapampa (clast count station 21). Here, gravel clasts are dominated by the peculiar hornblende-bearing volcanic lithology deriving from outcrops less than 10 km to the south.

Based on these observations, the depositional environment of the La Troja Formation is best described as proximal alluvial fan systems that developed where streams exit the different range fronts. The transition from proximal fanglomerates to more distal conglomerate/sandstone strata reflects fluvial processing on the fan surface. These fan systems are also affected by the deformation of the basin interior of both the eastern EC and the SBS; large volumes of the La Troja Formation sediments are accommodated by synclines that formed during deposition. The poor sorting and poorly developed bedding of the La Troja sediments filling these synclines may be attributed to the dominance of gravity flow, rather than fluvial, sediment transport mechanisms. It appears that La Troja sediments have not been transported far, but instead were stored adjacent to the various sediment source regions. The facies and provenance signatures of these deposits are thus characterized by pronounced spatial heterogeneity.

5.4.4 Moisture supply to the eastern flanks of the Andean orogen

Previous studies have highlighted the tectonic fragmentation and progressive aridification of the Andean hinterland in the immediate vicinity of the Puna as a driver of sedimentary processes and sustained severed drainage conditions in intermontane basins (e.g. Starck & Anzótegui, 2001; Kleinert & Strecker, 2001; Sobel & Strecker, 2003; Sobel *et al.*, 2003; Alonso *et al.*, 2006; Coutand *et al.*, 2006; Strecker *et al.*, 2007a,b). A detailed account of the present-day geomorphic conditions and related climate patterns for the broken Salta foreland are provided below, and two major controls on moisture supply to the hinterland are identified.

The first of these controls is related to the updraft of air caused by the atmospheric gravity wave that is generated when wind passes over a mountain range (e.g., Roe, 2005, and references therein). This density wave causes higher precipitation on the windward slope than on the leeward slope, where the density wave causes downdraft of the air and thus a rain shadow. Such asymmetric precipitation patterns, with higher precipitation on the eastern slopes, intercepting easterly and northeasterly moisture-bearing winds (e.g., Vera *et al.*, 2006a,b; Bookhagen & Strecker, 2008), occur along all ranges in the broken Salta foreland (Figs

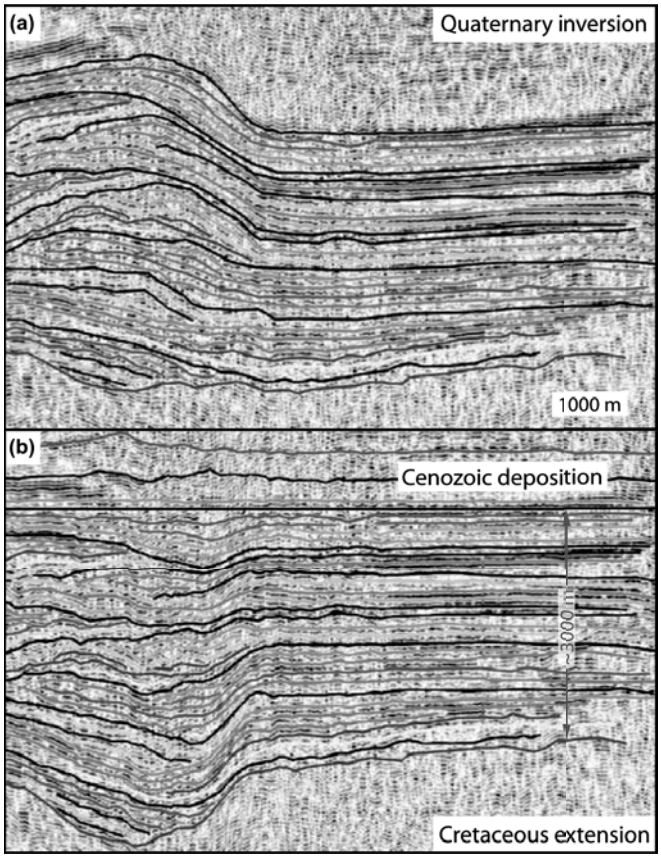

Figure 5.9 – Synrift depth interval of seismic line 2447 across the Coronel Moldes anticline (a) as imaged by the survey and (b) flattened along the oldest postrift reflector. The synrift depocenter in Fig. 5.9b occupies the core of the Coronel Moldes anticline (Fig. 5.9a). Neither the extensional fault nor the blind reverse fault that folds the synorogenic strata was imaged in the seismic data, suggesting drape folding during both extension and compression. See Fig. 5.8e for location.

5.13 and 5.14). However, our data suggests that ranges only reduce downwind rainfall significantly if they surpass a 3-km-radius relief of ~1 km (i.e., central EC, Aconquija, Quilmes ranges, and the eastern Puna border; Fig. 5.14). A relief threshold of this type is well founded in theoretical considerations and numerical simulations by Galewsky (2009). If the scale height (h) of a range increases relative to some measure of atmospheric conditions (i.e., U/N; U = horizontal wind speed; N = atmospheric buoyancy frequency) a regime change of the precipitation patterns causes hinterland aridification, rather than merely reduced precipitation on the lee slope of the range (Galewsky, 2009). Here it is shown that if ranges surpass this relief threshold, but do not completely shield the basins in their lee (i.e., Metán and Candelaria ranges partly shield the Lerma and Rosario valleys; Figs 5.13 and 5.14), moisture can pass into these basins where relief is low. Thus, although the Mojotoro range causes orographic precipitation, the low relief of this range allows moisture to penetrate into the Lerma Valley (swath 1 in Fig. 5.14) and consequently into the

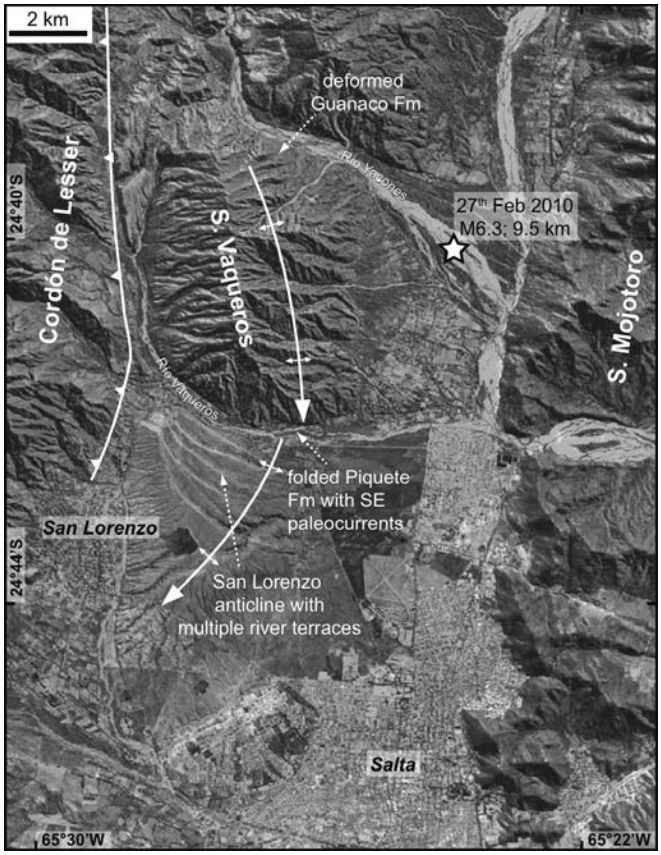

Figure 5.10 – Structural interpretation of the Sierra Vaqueros and San Lorenzo anticline. While the Guanaco and Piquete formations are folded in the Sierra de Vaqueros, the San Lorenzo anticline plunges SSW towards the Lerma Valley, also folding the conglomerates of the La Troja Fm. A series of incised river terraces record active southward growth of the structural array and the associated reorganization of the fluvial network. White star denotes the epicenter of a recent shallow earthquake (Mw = 6.3), further attesting to ongoing deformation. S.–Sierra

lee of the high-relief Sierra Metán (swath 2 in Fig. 5.14; see also Fig. 5.13). On longer time scales lateral and vertical fault growth along uplifting ranges will thus promote topographic growth and accrue relief, ultimately resulting in an efficient moisture barrier. In such a setting, moisture transport farther into the orogen interior is limited to thoroughfares formed by areas of reduced relief. Such thoroughfares may be associated with areas where mountain-bounding faults lose throw or where transfer structures have facilitated the exit of major drainages, fluvial downcutting, and valley formation (e.g., Strecker & Marrett, 1999; Strecker *et al.*, 2007a, Fig. 5.13b).

The second factor controlling moisture supply to the hinterland is related to thermodynamics rather than prevailing easterly wind directions. The Clausius-Clapeyron relation governs that the moisture content of the air column decreases with surface temperature/elevation (e.g., Holton, 1992; Roe *et al.*, 2002). The consequence of this relation is apparent in our data when considering the elevation of basins and

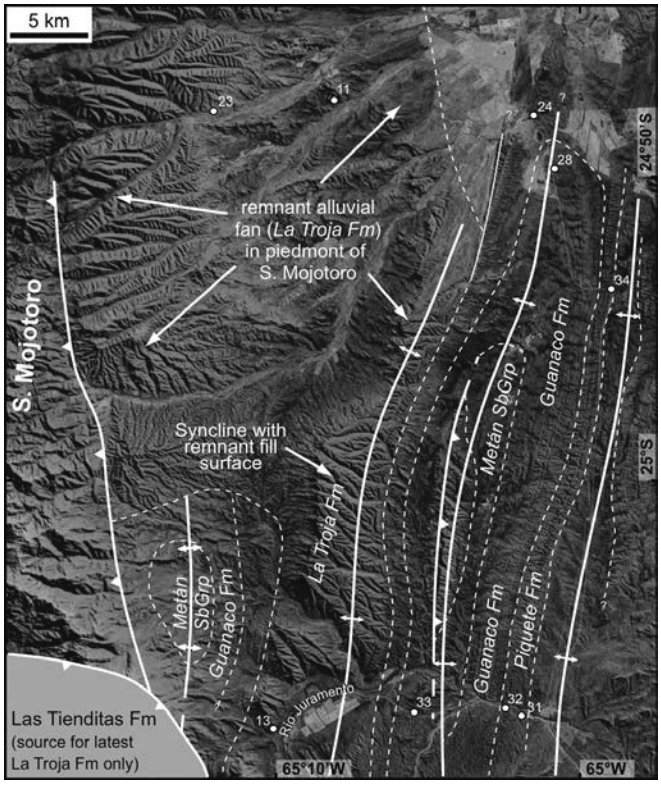

Figure 5.11 – Structural interpretation east of the Mojotoro Range. The La Troja Formation is preserved as remnant alluvial fan surfaces and constitutes the infill of the synclines. White points correspond to conglomerate clast count stations, labeled as in Table F.1.

throughfares, rather than range elevation. Once basin elevations have reached ~1500 to 2000 m (transition from green to yellow colors in Fig. 5.2b), the amount of rainfall decreases drastically (Figs 5.13 and 5.14) under present-day climatic conditions (i.e., at modern atmospheric lapse rates). For example, between the Santa María Valley (swath 3 in Fig. 5.14; basin elevation of ~1600 m) and the Calchaquí Valley (basin elevation at ~1900 m and higher; Fig. 5.2b) the amount of precipitation decreases from ~0.5 m/yr to <0.25 m/yr. This observation strikingly resembles the *Clausius-Clapeyron only* model scenario of Roe *et al.* (2002). Furthermore, these authors document a feedback between reduced uphill precipitation and steady state river profiles (in their case driven by tectonic uplift). In the Salta foreland, however, we documented above that the elevation difference between neighboring basins or even neighboring depocenters within one basin may also increase due to upstream sediment trapping. Thus, reduced precipitation at higher elevation reduces the efficiency of fluvial incision processes and thus promotes sediment trapping (Sobel *et al.*, 2003), which raises upstream basin elevation and thus further reduces precipitation. This constitutes a positive feedback.

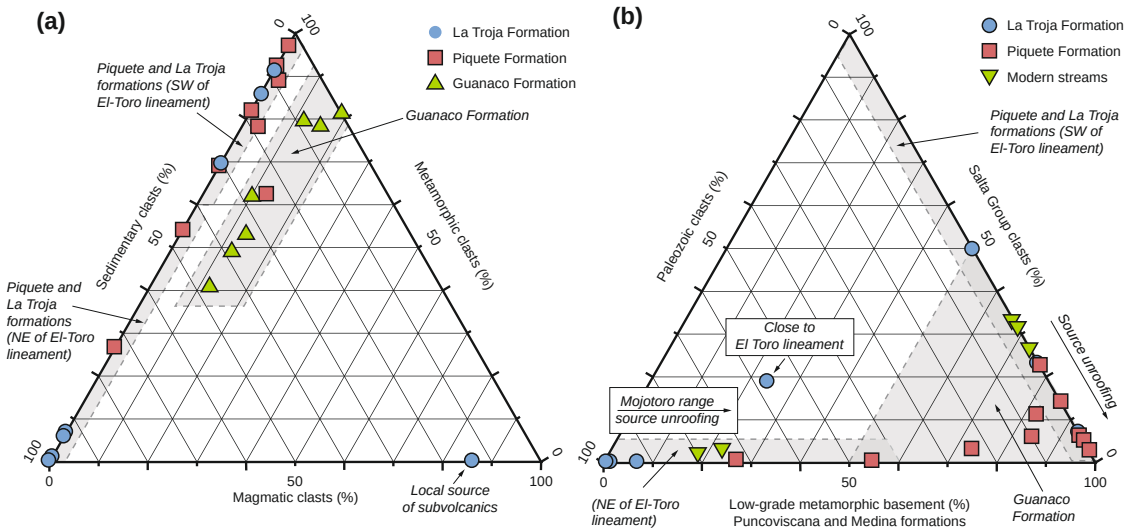

Figure 5.12 – Conglomerate composition and provenance signatures. (a) Guanaco Formation conglomerates are distinguishable from those of the Piquete and La Troja formations on the basis of the contribution of plutonic clasts with a Puna border provenance (the difference between Puna border derived high-grade metamorphic clasts and low-grade metamorphic Puncoviscana basement is not resolved here; this difference would make the Guanco conglomerates even more distinct). (b) Piquete and La Troja Formation conglomerates covary with the position of the El Toro lineament of the central EC ranges (see section 5.4.2). La Troja Formation conglomerates tend to contain proportionally more clasts from synrift (i.e., Cretaceous) or Paleozoic sedimentary cover than do Piquete Formation conglomerates or modern streambed loads, which we interpret as indicating range/source uplift followed by progressive unroofing. Clast count stations and details are listed in Table F.1. For details on the provenance of the La Troja Formation and specific marker lithologies see section 5.4.2.3.

One additional, potentially important interaction between intermontane sediment storage and precipitation may operate in the Puna plateau where long-term internal drainage conditions have resulted in essentially completely sediment-filled basins (e.g., Alonso *et al.*, 1991; Vandervoort *et al.*, 1995; Allmendinger *et al.*, 1997). The trapped sediment reduces the basin-to-range elevation difference and thus covers tectonically created relief (e.g., Sobel *et al.*, 2003; Strecker *et al.*, 2009, Fig. 5.13). One may speculate that the below-threshold internal relief of the plateau prevents orographic rainout related to the atmospheric gravity wave updraft at the 4-5 km high ranges shown in Fig. 5.14.

5.5 Discussion

Our records from the Salta foreland include all important elements and characteristics of the complex history of broken foreland systems. In addition, our analysis provides insight into the conspiring role of tectonics and climate in determining the temporally and spatially disparate evolution of sedimentary basins in this environment. Both aspects are discussed below in greater detail.

5.5.1 Tectonic fragmentation of the foreland basin

The restricted marine Anta Formation deposited during the Miocene Paranense transgression (Ramos & Alonso, 1995; Hernández *et al.*, 2005) provides an important time line during which the foreland system was still a contiguous entity with little relief (Fig. 5.15d). The eastern Puna margin was the sediment source for the strata constituting the Angastaco and Palo Pintado formations of the westernmost EC, which were deposited in an unrestricted foreland (Díaz & Malizzia, 1984; Starck & Anzótegui, 2001; Coutand *et al.*, 2006). However, during that time the establishment of internal drainage on the Puna Plateau was underway (e.g., Alonso *et al.*, 1991; Vandervoort *et al.*, 1995). Tectonism in the western EC (Coutand *et al.*, 2006; Deeken *et al.*, 2006) and a transition to more moist conditions (Starck and Anzótegui, 2001) led to facies-belt progradation toward the foreland, establishing the upward coarsening and thickening trend during the deposition of the Metán Subgroup and the Guanaco Formation (Fig. 5.3). The transition between the Metán and Jujuy subgroups in the eastern EC and SBS is marked by the uplift of the Durazno, Runno, and Negro ranges in the western EC (~13 Ma, Coutand *et al.*, 2006), and the Sierra Metán (and potentially the Ovejeria Range) at the EC/SBS transition (Cristallini *et al.*, 1997; Gonzalez Villa, 2002; Hain, 2008; Strecker *et al.*, 2009, Fig. 5.15c). These events may correlate with the establishment of the low-amplitude angular unconformity in the Lerma Valley (Fig. 5.7). The difference in preserved thickness of the coeval Guanaco Formation between the eastern EC (0-900 m) and the SBS (>2000 m, Gebhard *et al.*, 1974; Vergani & Starck, 1988, 1989a; Gonzalez Villa, 2002) potentially reflects this deformation episode, which may have been accompanied by the coalescence of localized depocenters adjacent to the uplifting basement ranges. The areally extensive Guanaco Formation megafan deposits derived from the Puna margin signify an essentially contiguous depositional system. The partitioning of deformation between the far western EC along the Puna margin (e.g., Coutand *et al.*, 2006) and the uplift of an isolated sediment source at the EC/SBS boundary (i.e., Sierra Metán, Hain, 2008; Strecker *et al.*, 2009, this study) constitutes a highly disparate pattern of deformation at ~10 Ma (Fig. 5.15c).

Significant compartmentalization of the foreland basin system occurred with the uplift of the central EC ranges at ~5 Ma, which altered three important aspects of the basin characteristics and surface process dynamics (Fig. 5.15b): (1) the EC was segmented into a western and an eastern depozone (the Calchaquí and Lerma valleys, respectively), (2) the conglomerate compositions of the coeval Piquete (eastern EC and SBS) and San Felipe formations (western EC) differ considerably, as sediment export from the western EC became restricted or eventually ceased entirely, and (3) the uplifted ranges of the central EC eventually acted as an efficient orographic barrier causing aridification and transient internal drainage, or at least reduced fluvial connectivity between the leeward intermontane basins in the western EC and the foreland (Coutand *et al.*, 2006). However, the Sierra de Mojotoro (Figs 5.2, 5.10, and 5.11) had apparently not yet been uplifted at that time and the fluvial systems that drained the eastern EC (i.e., Piquete fans; Fig. 5.15b) were unrestricted and remained connected with and exported sediment to the SBS.

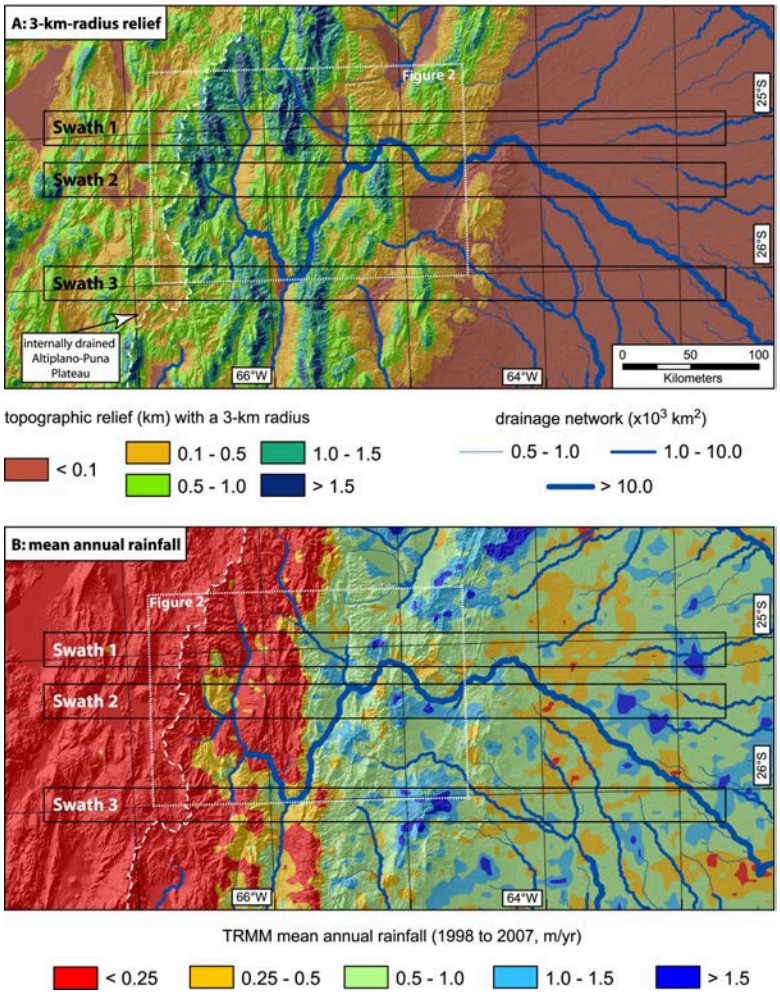

Figure 5.13 – (a) 3-km-radius relief and (b) mean annual rainfall (from TRMM – Tropical Rainfall Measurement Mission). TRMM data is averaged over 12 years (1998 to 2009) and processing methodology is described in Bookhagen & Strecker (2008) and Bookhagen & Burbank (2010). Black rectangles outline swath profile locations. White rectangle outlines the location of Fig. 5.2. The eastern border of the internally drained Altiplano-Puna Plateau is marked by the dashed white line; the width of rivers is scaled by drainage area.

Our new data helps identify the regional pattern of early Pliocene foreland fragmentation of the northern Sierras Pampeanas and the EC, but notably not the SBS. The contact between the Palo Pintado and the San Felipe formations, established as slightly younger than 5.27 ± 0.28 Ma (Coutand *et al.*, 2006) in the transition between the western EC and the Sierras Pampeanas, corresponds to magnetic reversal stratigraphic constraints on the transition between the Guanaco and Piquete formations in the eastern EC at <~6.9 Ma (Viramonte *et al.*, 1994; Reynolds *et al.*, 2000) and the SBS at ~5 Ma (Reynolds *et al.*, 1994, 2000). Moreover, in the northern Sierras Pampeanas uplift of the Aconquija and Calchaquíes ranges after 6 Ma (Sobel & Strecker, 2003), and of the Sierra de Quilmes after 5.4 Ma (Mortimer *et al.*, 2007),

are broadly coeval with fragmentation of the Salta foreland. Within the western EC, folding and subsequent erosion of the San Felipe Formation in the northern Calchaquí Valley took place before 2.4 Ma, as evidenced by a pyroclastic deposit that overlies paleotopography sculpted into the San Felipe Formation north of the town of Angastaco; these deposits are in turn overlain by Quaternary alluvial fan conglomerates (Strecker *et al.*, 2007a). Similarly, in the Santa María basin to the south the entire Mio-Pliocene Santa María Group was deformed between 3.4 and 2.5 Ma (Strecker *et al.*, 1989; Bossi *et al.*, 2001).

The latest stage of foreland fragmentation in the SBS and EC began during the Quaternary and is still locally ongoing (Fig. 5.15a). For example, the Vaqueros/San Lorenzo anticlines (Fig. 5.10) and the Lomas de Olmedo anticline in the far northeastern sector of the SBS (Ramos *et al.*, 2006) have experienced neotectonic deformation. Also pertaining to this episode, without evidence for Holocene deformation, are the uplift of the Sierra de Mojotoro and the accompanying intrabasin inversion of the Lerma Valley (eastern EC) and the SBS. For example, syndeformational to postdeformational deposits of the La Troja Formation have a strong compositional affinity to local sediment sources such as the central EC ranges or the ranges that separate the EC from the SBS (see section 5.4.2.3). Because uplift of the central SBS, including the Gonzalez, Lumbrera, San Antonio and Gallo ranges (Fig. 5.2b), was structurally related to the deformation within the adjacent basins, where the Piquete Formation was being folded (e.g., Kley & Monaldi, 2002), we suggest that these range-bounding faults also became active during the Quaternary (Fig. 5.15a). In addition, the unconformable alluvial fan deposits in the Mojotoro range piedmont (Fig. 5.11) record the unroofing of that range during the Quaternary. Angular unconformities and growth strata separating the Piquete and La Troja formations have also been noted by Salfity *et al.* (2004) and Carrera & Muñoz (2008), leading them to propose a Quaternary deformation phase. Deformed basin fills and strath terraces in the Quebrada del Toro of the central EC (Hilley & Strecker, 2005; Marrett & Strecker, 2000) , the Santa María Basin (Strecker *et al.*, 1989) and other adjacent areas (Ramos *et al.*, 2006; Carrera & Muñoz, 2008) further attest to Quaternary tectonic activity. Thus, Quaternary deformation is partitioned across the entire width of the Salta foreland.

Although the ranges of the central SBS reduce the fluvial connectivity between the SBS and the open, undeformed Chaco foreland, protracted internal drainage conditions related to tectonically controlled hydrologic isolation, such as in the western EC and the Sierras Pampeanas (e.g., Mortimer *et al.*, 2007; Strecker *et al.*, 2007a), were apparently not established. The Lerma Valley, however, experienced extensive transient deposition of lacustrine sediments, well above the current base level of the SBS and the Chaco foreland (Malamud *et al.*, 1996) at present-day elevations of 1100 m, 800 m and 300 m, respectively.

5.5.2 Tectonics, climate & sedimentation

Given the subtropical latitude (~25° S) of the Salta foreland a perennial dry climate associated with descending air of the Hadley cell may be expected. Today, however, seasonal winds (i.e., the South American Monsoon System) import tropical moisture to the region during the austral summer (e.g., Garreaud

et al., 2003; Vera *et al.*, 2006a; Seluchi *et al.*, 2003; Insel *et al.*, 2009). This highly seasonal climate pattern is thought to have persisted in the southern central Andes since 10-8 Ma (Strecker *et al.*, 2007a,b; Mulch *et al.*, 2010, Fig. 5.16), probably related to uplift of the Andes (Strecker *et al.*, 2007a; Ehlers & Poulsen, 2009; Insel *et al.*, 2009; Poulsen *et al.*, 2010). Below, we specifically consider the evolution of the local effects on climate patterns that caused the establishment of the present-day basin-to-basin gradients in moisture supply, rather than regional climate trends/shifts. Along these lines, we caution (1) that secular changes affecting subtropical (i.e., regional) climatic conditions since the establishment of the South American Monsoon are unresolved by our treatment and (2) that proxy-based paleoclimate reconstructions from distant locations (e.g., Mulch *et al.*, 2010) may not fully capture the history of external moisture supply to the Salta foreland.

The two mechanisms for hinterland aridification that we identified in the Salta foreland (section 5.4.4) have important implications for sediment dynamics: reduced moisture reaching the intermontane basins lowers the efficiency of fluvial erosion processes where rivers traverse the bedrock of the uplifting ranges (e.g., Roe *et al.*, 2002; Sobel *et al.*, 2003; Hilley & Strecker, 2005) such that sediment storage within the orogen is favored over fluvial connectivity. We find that this dynamic may also apply to basins that are not separated by ranges exposing bedrock (i.e., Calchaquí and Santa María valleys). Sediment trapping in the hinterland raises the mean basin elevations and leads to further hinterland aridification. This clearly creates a positive feedback between aridification, severed drainage, and sediment storage. In this interrelated tectonic and climatic context, the stratigraphic record of the broken foreland as a whole and the spatiotemporal distribution of provenance signals in particular, may be reconciled.

First, with the onset of the South American Low Level Jet as an integral part of the South American Monsoon (e.g., Garreaud, 1999; Vera *et al.*, 2006a,b) between 10 and 8 Ma citepStrecker:2007fy, Strecker:2007ws, Mulch:2010bz, seasonal moisture supply to the eastern flank of the Puna Plateau was largely unrestricted (e.g., Starck & Anzótegui, 2001; Kleinert & Strecker, 2001; Alonso *et al.*, 2006; Coutand *et al.*, 2006; Strecker *et al.*, 2007a; Vezzoli *et al.*, 2009, Fig. 5.16c). In southernmost Bolivia this coupling is expressed in increased sedimentation rates and the formation of fluvial megafans (Horton & DeCelles, 2001; Leier *et al.*, 2005; Uba *et al.*, 2005, 2007, 2009). We infer that these changing climatic conditions also produced the Guanaco Formation megafan in the Salta foreland, which preserves the Puna border provenance signature across a depozone covering distances in excess of 100 km (Fig. 5.16c). The isolated uplift of the Sierra Metán in the foreland provided an important local sediment source. However, (1) it did not constitute a laterally continuous orographic barrier, and thus could not prevent moisture from reaching the Puna border, and (2) it did not significantly restrict sediment export from the hinterland (Fig. 5.16c).

Second, at about 5 Ma, uplift of the central EC ranges intercepted sediment export from the western EC (Calchaquí Valley) promoting local sediment storage (e.g., Kleinert & Strecker, 2001; Strecker *et al.*,

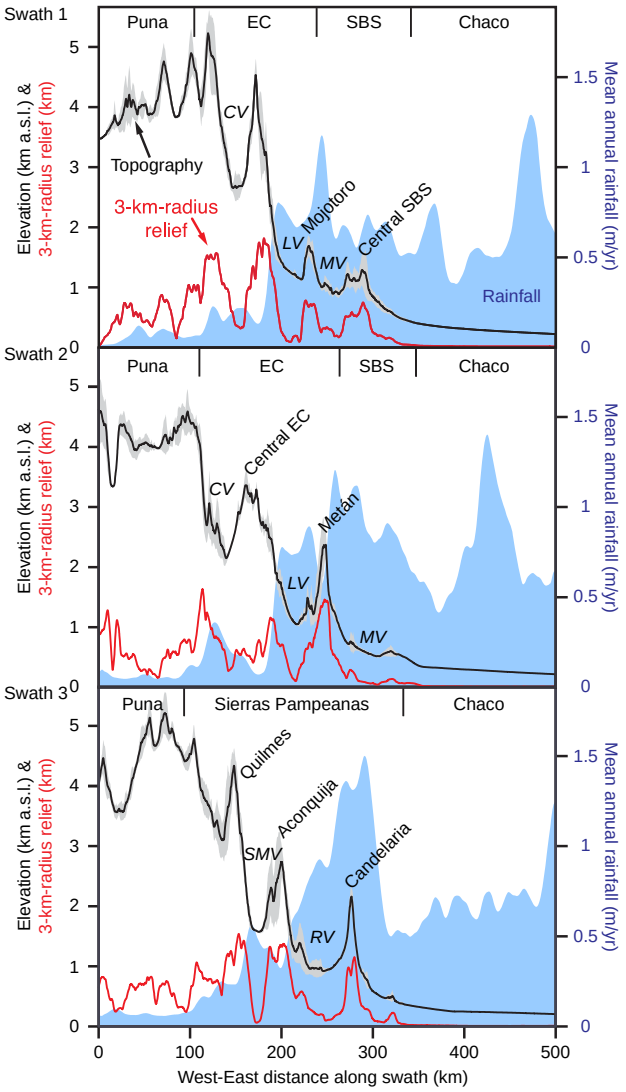

Figure 5.14 – Topography (black), 3-km-radius relief (red), and rainfall (blue) swath profiles; see Fig. 5.13 for swath locations. Swaths are 50 km (10 rainfall pixels) wide and 500 km long. Note the relationship between elevation, relief, and rainfall: in the northern swath (swath 1), the moderate elevation and low relief of Mojotoro Range does not result in an efficient moisture barrier. However, Aconquija Range in swath 3, with an elevation >2700 m and laterally continuous high relief, is an efficient orographic barrier. CV–Calchaquí Valley; LV–Lerma Valley; MV–Metán Valley; SMV–Santa María Valley; RV–Rosario Valley.

2007a). Consequently, throughout the eastern EC and the SBS the Puna border provenance signal was replaced with that of the central EC, suggesting that sediments derived from the Puna border were trapped in the hinterland rather than exported to the foreland (Fig. 5.16b). Orographic precipitation along the central EC ranges caused sediment transport and deposition of the Piquete Formation alluvial fans, which were smaller than the Guanaco megafan but still extended from the central EC ranges into the SBS (>60

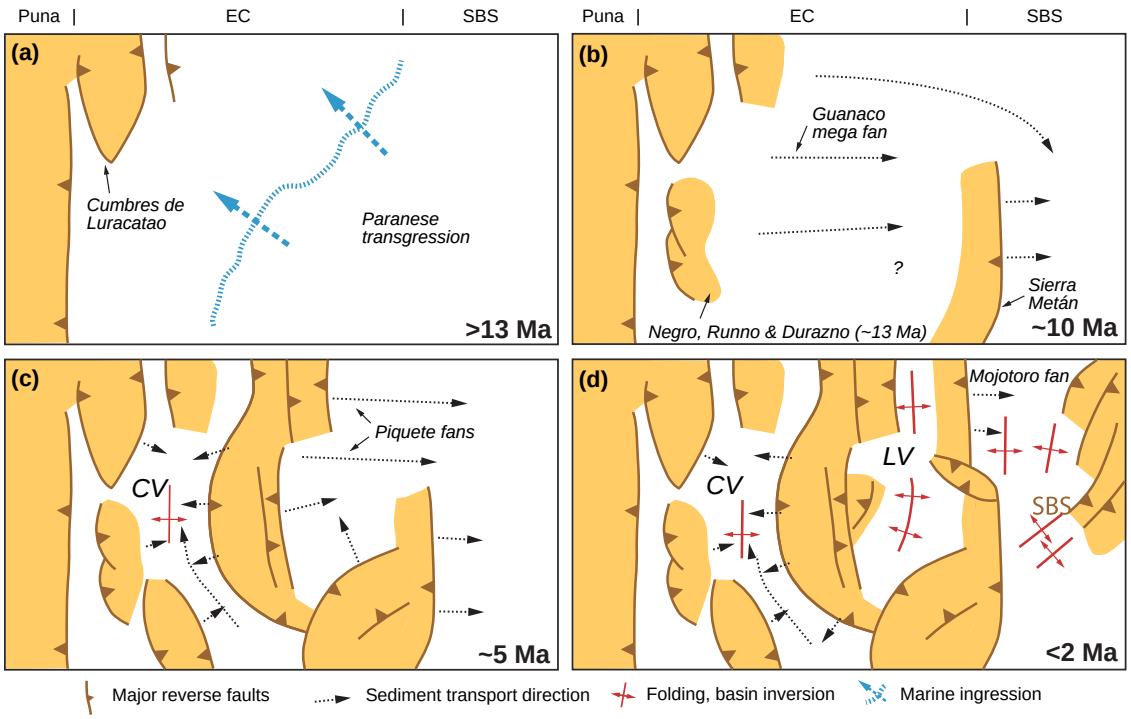

Figure 5.15 – (a-d) Schematic overview of the Neogene fragmentation history of the Salta foreland, corresponding to the geographic extent of Fig. 5.2. CV–Calchaquí valley; LV–Lerma valley

km; Fig. 5.16b). Between 3.4 and 2.4 Ma continued uplift of the central EC ranges caused an effective orographic barrier with abovethreshold relief, shielding the Calchaquí Valley from easterly moisture supply and thus giving rise to the modern arid conditions in the western EC ((e.g., Coutand *et al.*, 2006), which reduced fluvial transport capacity and thus further promoted sediment trapping and aridity in the Calchaquí Valley.

Third, Quaternary deformation has topographically isolated the Lerma Valley but has not yet resulted in an efficient orographic barrier capable of intercepting incoming easterly moisture-bearing winds (Fig. 5.16a). Nevertheless, sediments shed from the central EC into the Lerma Valley are stored in kilometer-scale alluvial fans and synclines related to basin inversion. This Quaternary sediment storage in the eastern EC contributes a significant fraction to the ~300 m elevation difference between the Lerma Valley and the SBS (Figs 5.2b and 5.14a). We suggest that the modern conditions of the Lerma Valley (eastern EC) are analogous to the Calchaquí Valley (western EC) after ~5 Ma and before 3.4 to 2.4 Ma; in both cases topographic isolation caused intermontane sediment trapping rather than export, and incomplete orographic shielding allowed for moisture to penetrate into the hinterland.

With respect to the dynamics of the adjacent Altiplano- Puna Plateau it is interesting to note that, with the late Miocene to Pliocene onset of the modern plateau precipitation regime (i.e., critical relief condi-

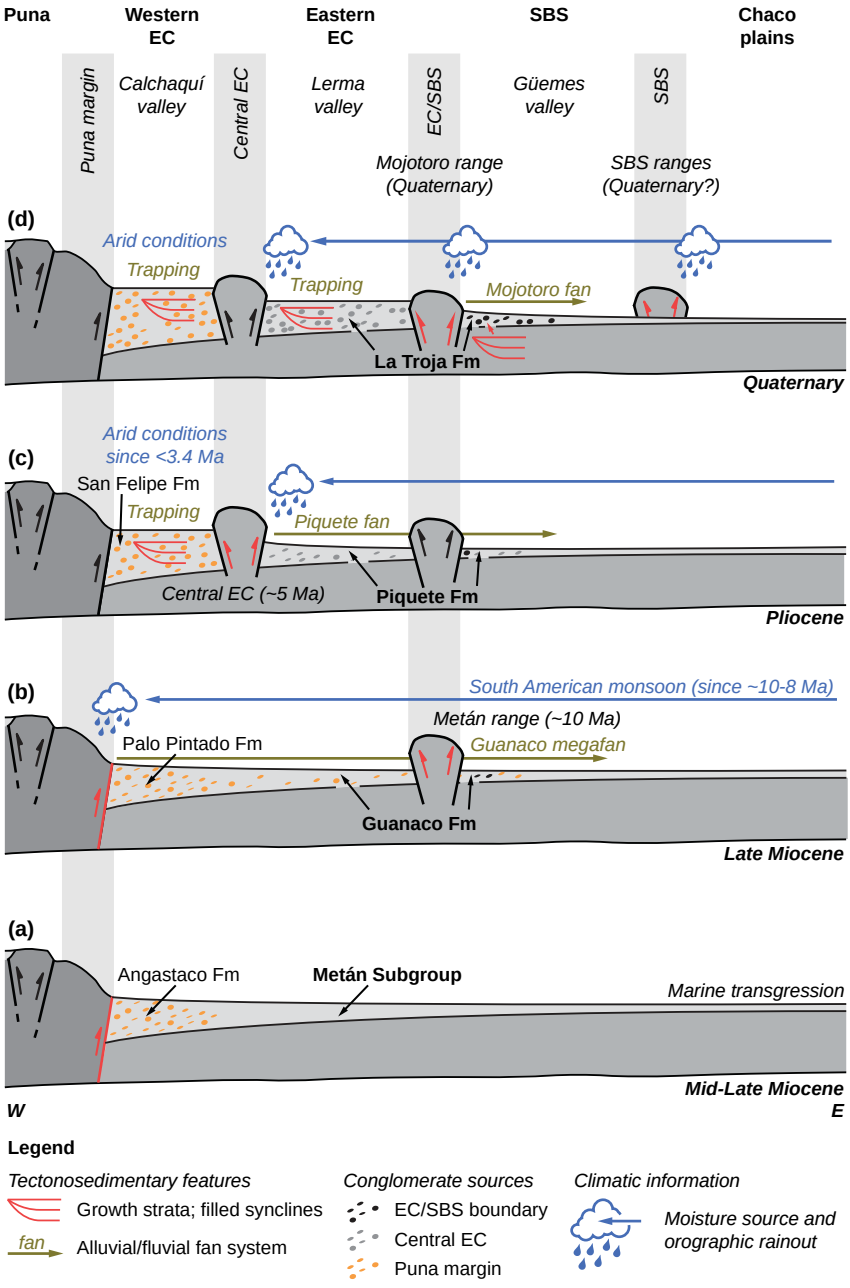

Figure 5.16 – (a-d) Schematic overview synthesizing the relationship between tectonic forcing, hinterland aridification, and sediment dynamics during the Miocene to Quaternary. This ~200 km wide section roughly corresponds with swath 1 from Figs 5.13 and 5.14. Note that the stratigraphic thickness is not to scale. A change from arid to more humid conditions at 10 to 8 Ma is related to the onset of the South American monsoon (Strecker *et al.*, 2007a,b; Mulch *et al.*, 2010). Semiarid conditions in the western EC after 3.4 Ma were described by Coutand *et al.* (2006). The mid-Miocene marine transgression is described by Ramos & Alonso (1995) and Hernández *et al.* (2005).

tions along the plateau margin), none of the basins created by foreland fragmentation have been permanently isolated from the drainage system, one proposed mode of lateral plateau growth (Sobel *et al.*, 2003; Barnes & Ehlers, 2009). In this regard one might speculate that, instead of facilitating the expansion of the plateau, the progressive hinterland aridification and associated sediment infilling achieved by foreland fragmentation preserves the present Puna border by guarding it from headwater erosion.

5.6 Summary & conclusion

In this study we have presented new stratigraphic, structural and climate observations that elucidate the relationships between tectonic forcing, precipitation patterns, and sediment dynamics of the broken Salta foreland in the southern central Andes. These observations argue for a three-phase history of progressive foreland compartmentalization: (1) at ~10 Ma uplift was partitioned between the western EC and the EC/SBS boundary, (2) at ~5 Ma uplift of the central EC ranges topographically isolated the western EC intermontane basin, and (3) since ~2 Ma diachronous deformation was partitioned across the entire foreland and has topographically isolated the eastern EC intermontane basin. The Quaternary deformation phase is ongoing. This first-order description of the timing and location of deformation provides hitherto unavailable constraints on the evolution of the Salta foreland domain.

We document evidence for progressive storage of sediment in the hinterland intermontane basins, which appears to be aggravated by both tectonic ponding of the drainage system and orographically induced hinterland aridity (see Fig. 5.16). Importantly, if sediments are trapped within rather than being exported from the orogen, they contribute to surface uplift in the basins and increase the topographic load. Herein, we identify basin elevation as one controlling factor of hinterland aridification, which suggests that intermontane sediment storage feeds back on basin-to-basin precipitation gradients. Furthermore, sediment trapping may also feed back on deformation because topographic loading raises lithostatic stress and causes deformation to propagate into the foreland. Overall, this study adds detail to the existing model of climate/tectonics interactions by providing specific examples of basin-scale and intrabasin sediment trapping even in the absence of internal drainage conditions.

Supporting information

Summary of U–Pb and U–Th zircon analytical data of volcanic ash samples in the Lerma Valley using CAMECA IMS 1270 ion microprobe at UCLA and conglomerate clast count data can be found in the appendix (see Appendix E and F).

Chapter 6

Surface uplift & convective rainfall along the southern Central Andes of NW Argentina (Angastaco Basin, ~25.5° S)*

Heiko Pingel[1], Ricardo N. Alonso[2], John Cottle[3], Scott Hynek[4], Andreas Mulch[5], Jacob Poletti[3], Alexander Rohrmann[1], Axel K. Schmitt[6], Daniel Stockli[7] and Manfred R. Strecker[1]

[1]Institut für Erd- & Umweltwissenschaften, Universität Potsdam, Germany; [2]Departamento de Geología, Universidad Nacional de Salta, Argentina; [3]Department of Earth Science and Earth Research Institute, University of California, Santa Barbara, USA; [4]Department of Geosciences & Earth, Environmental Systems Institute, Pennsylvania State University, University Park, USA; [5]Institut für Geowissenschaften, Goethe Universität Frankfurt, Senckenberg Biodiversity & Climate Research Centre (BiK-F), Frankfurt/Main, Germany; [6]Department of Earth & Space Sciences, University of California, Los Angeles, USA; [7]Department of Geological Sciences, University of Texas, Austin, USA

Abstract

In the south-central Andes of NW Argentina the orogenic Puna Plateau and the intermontane basins and ranges along its eastern flank constitute valuable archives that furnish spatiotemporal information on the uplift of the orogen and ensuing paleoenvironmental changes. Presently, rainfall in NW Argentina is focused along the windward flanks of the Eastern Cordillera and the Sierras Pampeanas and Santa Bárbara ranges of the broken foreland, while their intermontane basins and the Puna Plateau represent high-elevation regions with decreasing rainfall in westward direction. As in many other mountain belts this pronounced hydrologic and topographic gradient is reflected in the stable isotope composition of meteoric water. However, south of ca. 26° S the commonly observed relationship between stable isotope fractionation in modern stream water and elevation does not exist related to the presence of plateau-crossing westerly winds. Descending across the Puna margin this airflow causes an inversion with underlying humid air masses sourced to the east. In such a setting most of the annual rainfall is released during extreme hydrological events (i.e., deep-convective storms) governed by non-systematic fractionation processes. In light of the non-systematic present-day isotope characteristics, proxy

* *Manuscript in preparation*

materials retrieved from older basin strata may record environmental change forced by tectonic processes that are ultimately responsible for these conditions. Here, we present isotopic data of volcanic glass (δD_g), extracted from volcanic ash deposits interbedded with strata in different sedimentary basins along the eastern flank of the Puna Plateau. Combined with zircon U–Pb and (U–Th)/He geochronology, our data show clear variations in δD_g within the Angastaco Basin that track topographic growth, associated orographic effects and ensuing changes in atmospheric circulation patterns during the Mio-Pliocene.

6.1 Introduction

One of the most outstanding questions in the fields of tectonics and paleoenvironmental studies is how topography in mountain belts and rifts evolves over time (e.g., England & Molnar, 1990; Montgomery *et al.*, 2001; Reiners *et al.*, 2003; Sepulchre *et al.*, 2006; Petit *et al.*, 2007; Wichura *et al.*, 2010). This topic is of great interest to the geological, paleontological and geodynamic modeling communities, because answering this question may help deciphering potential feedback loops between surface uplift and climate change, associated erosion and sedimentation patterns (e.g., Sobel *et al.*, 2003; Alonso *et al.*, 2006; Strecker *et al.*, 2007a; Hilley & Coutand, 2009), but it is also relevant for the formation of supergene metallogenic deposits, and resource generation (e.g., Arancibia *et al.*, 2006; Bissig & Riquelme, 2010). In addition, as the process of surface uplift in mountain belts is often intimately coupled with changes in the amount and distribution of rainfall, spatiotemporal surface-uplift patterns are key to understanding paleoenvironmental conditions, and may consequently help to unravel speciation pathways or geogenomic characteristics in evolutionary biology (Baker *et al.*, 2014). The spatiotemporal evolution of the morphotectonic provinces comprising the southern central Andes illustrates these challenging issues very well. This region hosts the second largest Cenozoic orogenic plateau on Earth, high, plateau-flanking mountain ranges, and a foreland region characterized by broken sectors with individual basement-cored uplifts and adjacent fold-and-thrust belts. In addition, this part of the Andean orogen is impacted by easterly, moisture-bearing winds that impinge on the eastern flanks of the plateau resulting in pronounced climatic gradients across the mountain belt. The Altiplano-Puna Plateau has an average elevation of 3.7 km and constitutes one of the most important orographic barriers in the southern hemisphere (Isacks, 1988; Allmendinger *et al.*, 1997) and creates pronounced rainfall and surface-process gradients from east to west (e.g., Bookhagen & Strecker, 2008, 2012). While the eastern plateau flanks are humid with rainfall up to 3,000 mm/yr and relatively high denudation rates, the orogen interior is semi-arid to arid and transitions into one of the driest deserts known across the western flanks, where denudation rates are extremely low (Nishiizumi *et al.*, 2005; Bookhagen & Strecker, 2012). In the past, various plateau-evolution models have been proposed for the Andes (Isacks, 1988; Allmendinger *et al.*, 1997; Barnes & Ehlers, 2009), but timing and style of plateau uplift and the flanking ranges remain controversial (e.g., Garzione *et al.*, 2006; Schildgen *et al.*, 2007; Garzione *et al.*, 2008; Ehlers & Poulsen, 2009; Barnes & Ehlers, 2009; Mulch *et al.*, 2010; Quade *et al.*, 2015).

In addition to classical stratigraphic and paleontological approaches in deciphering plateau uplift (e.g., Wolfe *et al.*, 1997; Gregory-Wodzicki, 2000; Schildgen *et al.*, 2014), stable-isotope paleoaltimetry based on sedimentary strata recording changes in topography and hydrography has become an indispensable instrument for the reconstruction of surface uplift of orogenic plateaus and their flanks (e.g., Chamberlain *et al.*, 1999; Garzione *et al.*, 2000, 2004; Rowley *et al.*, 2001; Rowley & Garzione, 2007; Quade *et al.*, 2007; Mulch & Chamberlain, 2007; Mulch *et al.*, 2008; Hoke & Garzione, 2008; Garzione *et al.*, 2008; Mix *et al.*, 2011; Pingel *et al.*, 2014). Typically, stable isotope ratios based on paleorecords are compared with present-day isotopic compositions of surface waters or modeled δ-values in precipitation assuming Rayleigh condensation of an adiabatically ascending air mass (e.g., Rowley *et al.*, 2001), for which the elevation is known. However, among the many assumptions often required to interpret paleoaltimetry results, a major problem in correctly assessing environmental change due to uplift is the complex interplay between surface uplift, atmospheric circulation, and orographic rainfall (e.g., Mulch *et al.*, 2006; Gébelin *et al.*, 2013). This combination of processes affects the isotopic composition of rainfall, and hence, paleoelevation reconstructions (e.g., Garzione *et al.*, 2006, 2008; Quade *et al.*, 2007; Rohrmann *et al.*, 2014; Pingel *et al.*, 2014; Poulsen *et al.*, 2010; Ehlers & Poulsen, 2009; Blisniuk & Stern, 2005; Chamberlain *et al.*, 2012). Moreover, previous paleoaltimetry studies have often focused on orogen interiors, while comparable work in adjacent regions appears under-represented. This is, however, very important because moisture transport and the isotopic composition of rainfall in the orogen interior are directly influenced by upwind changes in topography and rainfall patterns along the tectonically active mountain fronts (e.g., Blisniuk *et al.*, 2005, 2006). As a consequence, isotopic changes induced along the margins (i.e., by atmospheric re-organization and changes in isotopic lapse rates) may remain undetected in plateau environments or they will not be interpreted as such, which could lead to considerable errors in determining paleoelevations (e.g., Mulch *et al.*, 2010; Insel *et al.*, 2012b). In light of the topographic and climatic gradients in most mountain belts, this problem is thus relevant for the plateau interiors and adjacent plateau flanks in the southern central Andes, and it is here, at the intersection of tectonic surface uplift, ensuing changes in rainfall and environmental conditions, where more detailed paleoaltimetry studies are needed.

Here, we present a hydrogen stable-isotope record from hydrated volcanic glass (δD_g) that has been extracted from abundant volcanic ash-fall deposits intercalated in Mio-Pliocene sedimentary rocks the intermontane Angastaco Basin and basins farther south between 25 and 28° S. A previous study in this area using this technique is based on limited data and argues for the existence of present-day elevations since at least late Miocene time (Carrapa *et al.*, 2014), a notion that is supported by geological observations across the southern flank of the Puna Plateau (Montero-López *et al.*, 2014). Our detailed δD_g record, however, suggests paleoenvironmental change along the eastern Andean flanks caused by interactions of topographic growth and moisture supply into the orogen, whereas a comparison of our glass record with

stable isotope data from the Puna Plateau to the west (Canavan *et al.*, 2014; Carrapa *et al.*, 2014; Quade *et al.*, 2015) additionally furnishes the possibility to view some of the δD_g variability observed in the Angastaco Basin in the context of changing atmospheric and rainfall patterns and closely related changes in stable isotope fractionation.

6.2 Geological setting

The southern Central Andes of northwestern Argentina record a complex geological history from the late Proterozoic to the Present. The geological evolution ranges from continental accretion and amalgamation of terranes with Proterozoic shields, to an extensional setting with rift-basin development at the end of the Mesozoic, and finally to compressional orogeny, induced by the subduction of the oceanic Nazca plate below the South American continent (e.g., Jordan *et al.*, 1983; Marquillas & Salfity, 1988; Ramos, 1988; Grier *et al.*, 1991; Ramos, 2008). During the Cretaceous and early Paleogene, extended areas in northwestern Argentina and southern Bolivia were affected by extensional processes and deposition of the Salta Group, comprising the Pirgua, Balbuena, and Santa Bárbara subgroups (e.g., Marquillas & Salfity, 1988; Marquillas *et al.*, 2005). First evidence for the onset of Cenozoic Andean shortening is constrained by late Eocene-Oligocene deformation in the area of the present-day Puna Plateau and regions farther east (Kraemer *et al.*, 1999; Deeken *et al.*, 2006; Coutand *et al.*, 2006; Hongn *et al.*, 2007). Late Eocene red beds of the Quebrada de los Colorados Formation and equivalent strata were deposited in a contiguous Andean foreland basin, extending across an area that presently constitutes the Puna Plateau and the Eastern Cordillera (e.g., Jordan & Alonso, 1987; Deeken *et al.*, 2006). Oligocene-Pliocene deformation and range uplift in those regions subsequently was characterized by diachronous compartmentalization of the Andean foreland, hydrologic isolation of the plateau region, and elevated intermontane basins aligned along its eastern margins (Kraemer *et al.*, 1999; Carrapa *et al.*, 2005; Deeken *et al.*, 2006; Strecker *et al.*, 2009).

The intermontane Angastaco Basin is an integral part of the N-S oriented Calchaquí valley at ~25.5° S, at an elevation ranging from approximately 1.7 to 2.2 km (Fig. 6.1). To the west, the Cumbres de Luracatao and a number of other reverse fault-bounded mountain ranges (Quílmes, Durazno, Runno, Cachi) separate the internally drained Puna Plateau in the western interior of the orogen from the externally drained intermontane basins of the Eastern Cordillera. To the east the basin is limited by the Sierra de los Colorados and Sierra León Muerto ranges. Presently, the basin is drained by the Río Calchaquí, which, after the confluence with the northward flowing Río Santa María, exits the region as the Río de las Conchas into the adjacent Lerma valley through a structurally controlled bedrock gorge.

As many other intermontane basins in NW Argentina, the Angastaco Basin contains a rich sedimentary record documenting a protracted paleoenvironmental and structural evolution of Cenozoic shortening. The onset of Cenozoic contraction at this latitude is constrained by Eo-Oligocene deformation along the present-day Puna margin (Kraemer *et al.*, 1999; Deeken *et al.*, 2006; Coutand *et al.*, 2006; Hongn *et al.*,

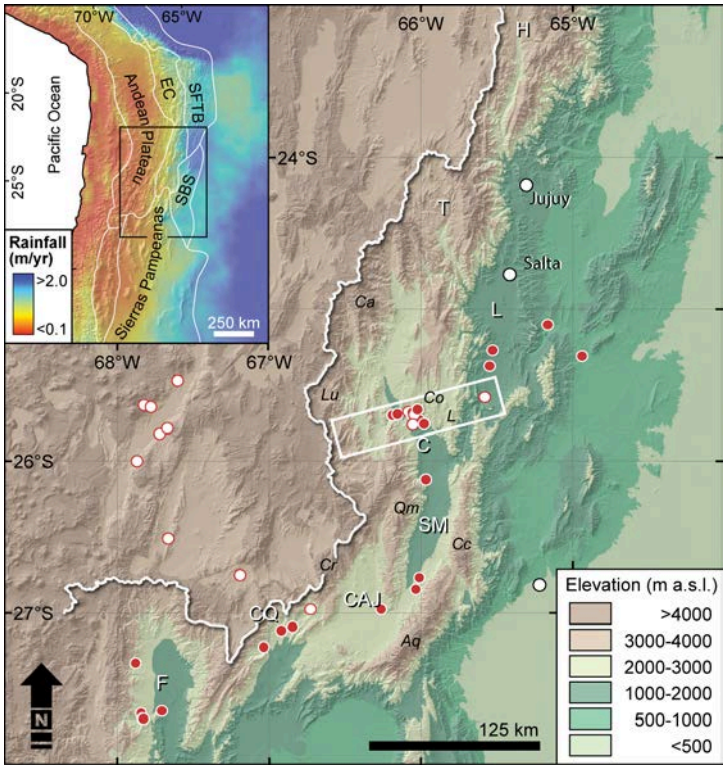

Figure 6.1 – (a) Morphotectonic map of southern Central Andes showing mean annual rainfall derived from National Aeronautics and Space Administration Tropical Rainfall Measurement Mission (after Strecker et al., 2007) and main moisture transport (white arrow) to the study area (black box). EC–Eastern Cordillera, SFTB–Subandean fold-thrust belt; SBS–Santa Bárbara system. (b) Digital elevation model with sample locations of our radiometrically dated Mio-Pleistocene volcanic ash samples (red, this study) and previously published ash samples (white, Canavan *et al.*, 2014; Carrapa *et al.*, 2014; Quade *et al.*, 2015) from across the southern Central Andes south of 25° S. White box indicates location and extend of Figure 6.2. White letters indicate basins: H–Humahuaca; T–Toro; L–Lerma; C–Calchquíes (including the Angastaco Basin); SM–Santa María; CAJ–El Cajón; CQ–Corral Quemado; F–Fiambala. Black letters indicate mountain ranges discussed in the text: Ca–Sierra Cachi; Lu–Cumbres de Luracatao; Co–Sierra de los Colorados; L–Sierra León Muerto; Qm–Sierra Quilmes; Cc–Cumbres Calchaqíes; Aq–Sierra Aconquija; Cr–Sierra Chango Real.

2007). Deposition in the Angastaco area commenced during the late Eocene with redbeds of the Quebrada de los Colorados Formation that were deposited into a contiguous foreland basin (Deeken *et al.*, 2006; Jordan & Alonso, 1987). By ~22.5-21 Ma, deformation along the present-day Puna margin resulted in structural separation of the Puna from the foreland after ~20 Ma (Deeken *et al.*, 2006; Coutand *et al.*, 2006; Galli *et al.*, 2014). The Nevado de Cachi range (Fig. 6.1) started exhuming around 15 Ma (Deeken *et al.*, 2006; Pearson *et al.*, 2012). By ~14 Ma fluvial sandstones and conglomerates of the Angastaco Formation, mainly sourced from the uplifting Cumbres de Luracatao, were unconformably deposited onto older sedimentary units (Coutand *et al.*, 2006; Deeken *et al.*, 2006; Galli *et al.*, 2014). This unconformity is not only found along the western basin margin, but also in the elevated Amblayo and Tonco areas to

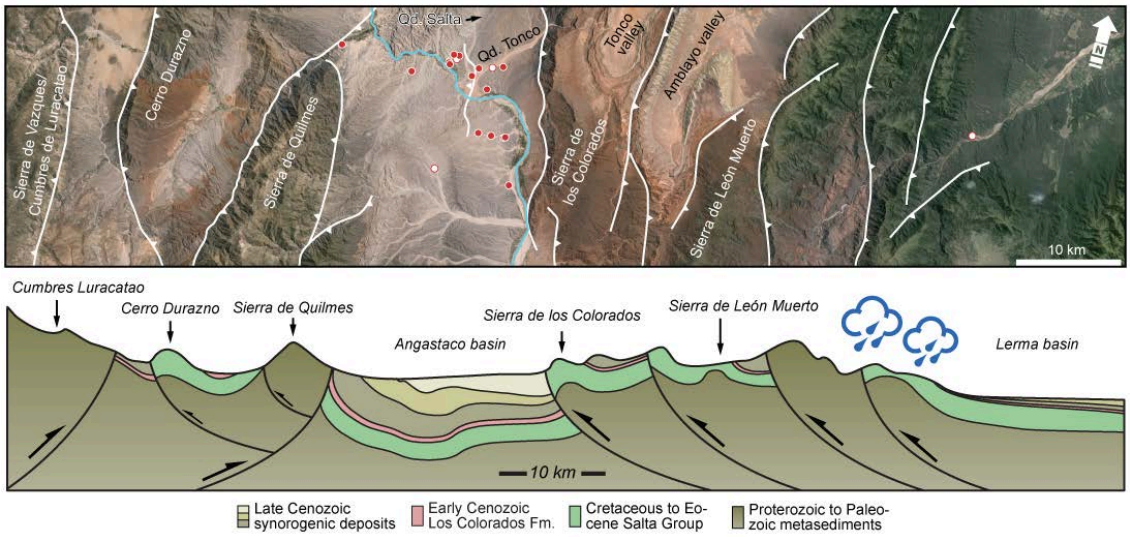

Figure 6.2 – (a) Satellite image of the studied Angastaco Basin and neighboring basins and ranges showing simplified range-bounding structures and locations of our volcanic glass hydrogen stable isotope samples (red, this study) and previously published samples from the Angastaco and Lerma basins (white, Carrapa *et al.*, 2014). (b) Schematic geological cross section after Coutand *et al.* (2006) and Deeken *et al.* (2006) showing major basins and ranges across Figure 6.2A. Clouds indicate regions of enhanced orographic precipitation.

the east of the present-day basin (Fig. 6.2), implying at least mid-Miocene deformation and erosion in the area of the Sierra de los Colorados and Sierra de León Muerto ranges (Galli *et al.*, 2014). Additionally, clast provenance in the Tonco area is associated with westward paleocurrent directions in the Angastaco Formation by ~10 Ma (Galli *et al.*, 2014). This supports the existence of local topography in the region at that time, which is confirmed by rapid exhumation of the Sierra de los Colorados since ca. 12-10 Ma and the Sierra León Muerto since ca. 8-6 Ma (Carrapa *et al.*, 2011). To the west, apatite fission-track data records exhumation of the Quílmes, Durazno, and Runno ranges between 12 and 7 Ma, which is corroborated by clast provenance and detrital apatites in the Angastaco Formation (Deeken *et al.*, 2006; Coutand *et al.*, 2006). The Angastaco Formation is overlain by fluvial mud- and sandstones of the Palo Pintado Formation (ca. 9-5.2 Ma, Marshall *et al.*, 1983; Coutand *et al.*, 2006; Bywater-Reyes *et al.*, 2010). Sedimentological evidence and fossil content suggest that parts of this unit were deposited during (sub-)tropical humid conditions, characterized by north to northeast draining, low-energy river systems, swamps, and small lakes (e.g., Starck & Anzótegui, 2001; Galli *et al.*, 2014). Clast provenance from the neighboring Lerma Basin to the east (Guanaco Formation) generally attests to fluvial connectivity between the two basins (Hain *et al.*, 2011), although active structures and probably related topography in the region presently separating the basins, may have severed fluvial connectivity. Deposition of the overlying Lower San Felipe Formation by 5.2 Ma (Bywater-Reyes *et al.*, 2010) followed an episode of basin-internal deformation, as documented by a major unconformity (Carrera & Muñoz, 2008). This was coeval with the disappear-

ance of Puna-derived metamorphic and volcanic clasts in the Lerma Basin (Hain *et al.*, 2011). These observations document the separation of the two regions by a continuous topographic barrier east of the Angastaco Basin. This interpretation is supported by the appearance of clasts from the Cretaceous Salta Group within sections of the San Felipe Formation in the Quebrada Salta, near the present-day eastern basin margin that are associated with west- to southwest-oriented sediment transport from source regions within the Sierra de los Colorados and Sierra de León Muerto ranges (Galli *et al.*, 2014). By ca. 4 Ma the conglomerates of the Upper San Felipe Formation record a more widespread appearance of easterly derived clasts (Bywater-Reyes *et al.*, 2010). Moreover, sedimentological evidence suggests the onset of arid conditions associated with orographic effects along the eastern basin-bounding ranges (Starck & Anzótegui, 2001; Coutand *et al.*, 2006). Subsequently, shortening in the Eastern Cordillera has led to basin-internal deformation and erosion marked by a regional unconformity with overlying Quaternary conglomerates (reviewed in Coutand *et al.*, 2006). Later, these gravels were partially eroded and removed from the basin, suggesting renewed fluvial connectivity with the foreland that characterizes the Angastaco Basin today.

6.3 Climatic conditions

The Andes constitute one of the most important orographic barriers in the southern hemisphere, impacting atmospheric circulation, rainfall, and surface processes (e.g., Bookhagen & Strecker, 2008, 2012). Regional easterly winds associated with the South American Monsoon transport large amounts of moisture from the southern tropical Atlantic Ocean across the Amazon Basin and towards the eastern flanks of the Andes, where orographic and atmospheric effects cause a southward deflection to form the South American low-level jet (Fig. 6.3A). During austral summer (December to February) this low-level jet follows a narrow pathway along the eastern margin of the orogen and transports significant amounts of moisture deep into the otherwise arid subtropical regions of the South American continent (e.g., Vera *et al.*, 2006a). This accounts for more than 80 percent of the annual rainfall along the Andean foothills and the orogen interior of southern Bolivia and northwestern Argentina (e.g., Prohaska, 1976). Westward transport of these air masses across the Andes results in enhanced orographic rainout along the eastern flanks and progressively reduced rainfall in the orogen interior (Bookhagen & Strecker, 2008). In northwestern Argentina this is expressed in annual rainfall of more than 1,000 mm/yr along the eastern flanks of the Eastern Cordillera and Sierras Pampeanas morphotectonic provinces, and less than 200 mm/yr in the orogen interior of the internally drained Puna Plateau (Fig. 6.1A). In addition, the subtropical regions east of the Andes are characterized by a seasonally N-S shifting, high-level westerly wind system that continuously transports dry and cold air across the orogen (Garreaud *et al.*, 2003). Downslope airflow along the eastern flanks causes a capping inversion that prevents humid air of the South American low-level jet from ascending, until the low-level jet is lifted to higher elevations due to its impingement with steep

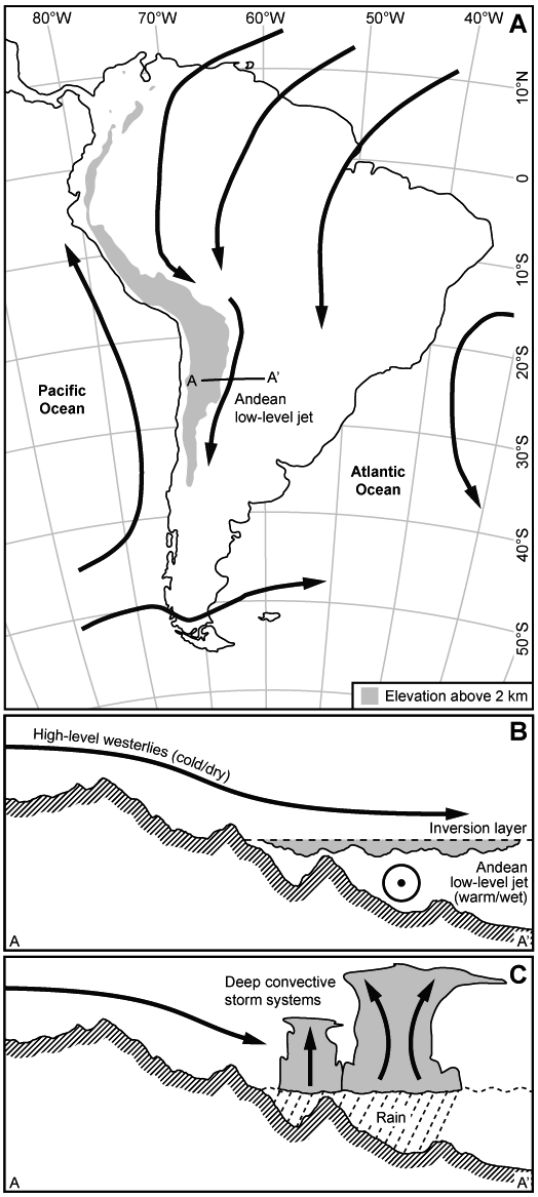

Figure 6.3 – (a) Generalized patterns of South American surface wind directions and moisture transport during austral summer (Dec-Feb). Moisture in the study area at ca. 25° S is sourced from air formed over the Atlantic Ocean and the Amazon Basin and transported across the continent. Upon arrival at the eastern flanks of the Andes Mountains winds are deflected to form the South American low-level jet that flows south along the Andean margin. (b) and (c) Conceptual model of interacting air flows south of 25° S (modified after Rohrmann *et al.*, 2014), where the descent of dry and cold westerlies prevents wet and warm air of the low-level jet to rise until sufficient solar energy is stored to break the capping inversion in-between. This causes strong vertical upward motion of moisture-laden air and the formation of convective rainfall, which presently is the main source of meteoric water at this latitude (Rohrmann *et al.*, 2014).

topography or when sufficient solar heating triggers rapid upwelling (Figs. 3B and 3C, Rasmussen & Houze, 2011). This energy release may result in extreme hydro-meteorological events with heavy rainout during deep convective storms, which presently seem to be the origin for most of the annual rainfall along the subtropical eastern Andes south of ca. 25° S latitude (Zipser *et al.*, 2006; Romatschke & Houze, 2010, 2013; Rohrmann *et al.*, 2014).

Geological evidence from the sedimentary record of marginal intermontane basins and in the foreland sectors of southern Bolivia and northwest Argentina suggest that the South American low-level jet was established between 10 and 8 Ma, implying that the Andes had gained sufficient elevations at that time (Starck & Anzótegui, 2001; Mulch *et al.*, 2010). If recent global circulation models are correct, at least 50 percent (ca. 2 km) of the modern Andean elevations must have been attained during the late Miocene (Insel *et al.*, 2009). At present, neither the onset of a convective setting is known, nor is there evidence for a former occurrence of this phenomenon.

6.4 Stable isotope & paleoaltimetry

Stable isotope compositions of oxygen and hydrogen of meteoric water often show a systematic relationship with elevation (e.g., Dansgaard, 1964). This is based on isotope fractionation during adiabatic expansion of water vapor when moisture-bearing air masses pass over mountainous terrain. To first order, this causes progressive cooling, condensation, and consequently, rainout, during which the heavy isotopes of oxygen and hydrogen are progressively removed from remaining water vapor (Rayleigh condensation). Several terrestrial materials incorporate meteoric water by specific isotope fractionation, preserving a systematically altered signal of the original isotopic composition of meteoric water (e.g., Friedman *et al.*, 1993b; Cerling *et al.*, 1997; Koch, 1998; Chamberlain *et al.*, 1999; Shane & Ingraham, 2002; Sachse *et al.*, 2012). In terrestrial settings, rhyolitic glass incorporates relatively large amounts of meteoric water and saturates ca. 5-10 k.y. after its deposition (Friedman *et al.*, 1993b; Mulch *et al.*, 2008; Cassel *et al.*, 2012; Dettinger & Quade, 2015). This hydration process occurs systematically, whereby the final δD_g represents an integrated signal of the meteoric water present during hydration that is preserved over geological time scales, allowing for reconstructions of paleoenvironmental conditions and for an examination of feedbacks between tectonic processes and climate (Friedman *et al.*, 1993b; Mulch *et al.*, 2008; Cassel *et al.*, 2012; Dettinger & Quade, 2015; Pingel *et al.*, 2014).

A recent study of stable isotope compositions in surface water from across the eastern Puna margin (between 22 and 28° S) has shown that specifics of hemisphere-scale atmospheric circulations, Andean topography, and thermal characteristics of areally extensive intermontane basins along the plateau margin may result in considerable complexities in isotopic fractionation with elevation (Rohrmann *et al.*, 2014). For example, these authors showed that the relationship between elevation and hydrogen and oxygen stable isotopes in modern water changes with increasing southern latitude. As a result, the modern hydrogen

isotopic lapse rate south of ~26° S is unusually low (-2.5‰/km) and not very robust, whereas the lapse rate north of 26° S is at about -16‰/km (Rohrmann *et al.*, 2014; Dettinger & Quade, 2015). This deviation from global average values south of 26° S has been related to non-systematic effects of atmospheric convection in subtropical regions that interfere with orographic rainout along the eastern Andean flanks (Rohrmann *et al.*, 2014). In an attempt to estimate past environmental conditions and paleoelevations it is therefore essential to determine whether or not the present-day characteristics existed previously and how trends in stable-isotope fraction may have changed over time due to tectonic forcing. Clearly, not taking these issues of non-systematic fractionation into account would lead to erroneous assessments of paleoelevation at these latitudes.

6.5 Methods

6.5.1 Geochronology

6.5.1.1 LA-MC-ICPMS U–Th–Pb zircon dating

Zircons were separated using standard crushing, heavy liquid, and magnetic separation techniques. When possible, 100 to 150 zircon grains per sample were handpicked, mounted in epoxy, and polished for U, Th, and Pb isotope analysis using a Laser Ablation Multi-Collector Inductively Coupled Plasma Mass Spectrometer (LA-MC-ICPMS), during two analytical sessions during September and December 2014, at the University of California, Santa Barbara. Zircons from the first session were mapped using a cathodoluminescence (CL) imaging system attached to a FEI Q400 FEG scanning electron microscope (SEM) at the University of California, Santa Barbara operated at 10 kV accelerating voltage and a beam current of 0.5 nA. CL images revealed simple concentric zonation in the majority of zircons (Fig. G.1 and G.2).

Instrumentation for radiometric analyses consists of a Nu Plasma MC-ICPMS and a 193 nm ArF laser ablation system. The analytical protocol is similar to that described by (Cottle *et al.*, 2013; Cottle, 2014). U–Th–Pb analyses were conducted for 15 sec using a spot diameter of 24 μm, a frequency of 4 Hz and 1.2 J/cm^2 fluence. The 91500-reference zircon (1065.4 ± 0.6 Ma ^{207}Pb/^{206}Pb ID-TIMS and 1062.4 ± 0.8 Ma ^{206}Pb/^{238}U ID-TIMS, Wiedenbeck *et al.*, 1995) was used to monitor and correct for mass bias as well as Pb/U and fractionation. To monitor data accuracy, a secondary reference zircon GJ-1 (601.7 ± 1.3 Ma ^{206}Pb/^{238}U ID-TIMS age, 608.5 ± 0.4 Ma ^{207}Pb/^{206}Pb ID-TIMS age, Jackson *et al.*, 2004) was analyzed once every ~7 unknowns and mass bias- and fractionation-corrected based on measured isotopic ratios of the primary reference zircon. Repeat analyses of GJ-1 yield a weighted mean ^{206}Pb/^{238}U age of 601.7 ± 1.0 Ma, MSWD = 0.7 (n = 27) for the first analytical session and 603.2 ± 1.2 Ma, MSWD = 1.2 (n = 67) for the second session. Data reduction, including corrections for baseline, instrumental drift, mass bias, down-hole fractionation and uncorrected age calculations was carried out using Iolite version 2.5 (Paton *et al.*, 2010). Data were corrected for common lead using the method of Andersen (2002). The uncertainty on the ^{207}Pb corrected age incorporates uncertainties on the measured ^{206}Pb/^{238}U and

$^{207}Pb/^{206}Pb$ ratios as well as a 2% uncertainty on the assumed common lead composition. Correction for excess ^{230}Th follows the method of Crowley *et al.* (2007) assuming Th/U[magma] = 4.0 ± 1.0. All uncertainties are quoted at the 95% confidence or 2σ level and include contributions from the external reproducibility of the primary reference material for the $^{207}Pb/^{206}Pb$ and $^{206}Pb/^{238}U$ ratios.

Due to significant pre-eruptive residence times and/or post-eruptive reworking most analyzed samples show a complex pattern of U–Pb zircon age distributions. Therefore, we systematically excluded older ages from our calculations of an average zircon crystallization age. It has been documented that the youngest population crystallization age precedes deposition by ~100 kyr (Schmitt *et al.*, 2001). Hence, we are confident to use the crystallization age of the samples as an approximation of the depositional age. Most samples yielded consistent $^{206}Pb/^{238}U$ ages, as indicated by near-unity values for the mean square of weighted deviates (MSWD), suggesting only minor reworking. In some cases, however, only a small percentage of crystals defined a coherent young population; in these cases we have interpreted the $^{206}Pb/^{238}U$ zircon age as the maximum depositional age. Results are summarized in Tables G.1 and G.2.

6.5.1.2 (U–Th)/He zircon dating

ZHe dating on primary volcanic zircons determines the age of cooling below the zircon-closure temperature of ~130-160°C (Reiners, 2005), and therefore, produces reliable eruptional/depositional ages. Zircon (U–Th)/He (ZHe) analysis was performed at the Isotope Geochemistry Laboratory of the University of Kansas following methods described in (Wolfe & Stockli, 2010). After standard heavy-liquid and magnetic separation procedures, eight euhedral and inclusion-free zircon crystals were hand picked and wrapped in Pt foil. Single-grain aliquots were heated with a 20 W Nd:YAG laser for 10 min at ~1,300°C and repeatedly reheated to ensure complete He-degassing (>99%). Extracted gas was spiked with a ^{3}He tracer, cryogenically purified, and measured by isotope dilution on a quadrupole noble gas mass spectrometer. After He extraction, zircon grains underwent pressure vessel digestion procedure, including spiking with an enriched ^{230}Th, ^{235}U, ^{149}Sm and REE tracer, subsequent two-stage dissolution using (1) a HF-HNO_3 mixture for 72h at 225°C, and (2) 6 N HCl for 12h at 200°C. All parent nuclide concentrations were measured by isotope dilution on a VG PQII quadrupole ICP-MS, comparing the spike against a gravimetric 1 ppb U–Th–Sm–REE normal solution. ZHe ages were calculated using standard alpha-ejection corrections (Farley *et al.*, 1996). Age uncertainties of ~8% (2σ) are estimated from the reproducibility of Fish Canyon Tuff zircon standard (28.4 ± 2.3 Ma, Wolfe & Stockli, 2010). Results are summarized in Table G.3.

6.5.1.3 SIMS U–Pb zircon dating

Volcanic ash samples were crushed, sieved, and treated with standard heavy-liquid and magnetic separation techniques to isolate zircon crystals. About 30 crystals per sample were handpicked, mounted in epoxy, polished and cleaned, and then gold-coated for microprobe analysis. Crystals free of inclusions, or

cracks were selected for U–Pb analysis using the CAMECA IMS 1270 ion microprobe at the University of California in Los Angeles, following instrument setup and relative sensitivity calibrations described in Grove *et al.* (2003) and Schmitt *et al.* (2003). The $^{206}Pb/^{238}U$ ages have been corrected for common Pb and initial disequilibrium. U–Pb age uncertainties estimated from the reproducibility of AS3 zircon (1099.1 Ma Paces & Miller, 1993) are 2.2%. Results are summarized in Table G.4.

6.5.2 Hydrogen stable isotopes

Volcanic ash samples were crushed, sieved, and treated with 10% hydrochloric acid for 15 min and 5% hydrofluoric acid for 30 sec in an ultrasonic bath to remove altered rims and adherent carbonate and clay minerals. Subsequently, samples were rinsed with water and dried at max. 70°C. For separates that needed further concentration, standard magnetic and density techniques were applied. Glass shards (125-250 μm) were handpicked using a cross-polarizing microscope. About 1.5 mg of each sample was packed in silver cups, loaded, and released to a helium-purged Thermo-Finnigan TC/EA (high-temperature conversion/elemental analyzer) equipped with a Costech zero-blank auto sampler. The extracted sample gas was admitted into a Thermo-Finnigan ConFlo III connected in continuous-flow mode to a Thermo-Finnigan MAT 253 stable-isotope mass spectrometer. Five internationally referenced standard materials and laboratory-working standards were run with our samples, random samples were duplicated and tested for consistency, and the raw isotope data were corrected for mass bias, daily drift of the thermal combustion reactor, and offset from the certified reference values. After correction, NBS30 (biotite), CH-7 (polyethylene), and NBS22 (oil) reference materials yielded δD = -64.3 ± 0.8‰, -104.5 ± 0.6‰, and -117.5 ± 1.1‰, respectively. Repeated measurements of various standards and unknowns yielded a precision of ± 3.0‰ for δD_g. All isotope measurements were performed at the Joint Goethe University-BiK-F Stable Isotope Facility, Frankfurt. All isotopic ratios are reported relative to V-SMOW (Vienna - standard mean ocean water).

To compare ancient volcanic glass stable-isotope compositions with modern conditions, present-day conditions were inferred from converting modern stream-water isotopic data from Rohrmann *et al.* (2014) into a corresponding glass composition (δD_{gc}) using the empirical glass-water fractionation equation of Friedman *et al.* (1993a). All δD results are summarized in Table H.1.

6.6 Results

6.6.1 U–Pb & ZHe geochronology

A single new U–Pb LA-ICPMS age estimate comes from a deformed section of the Guanaco Formation in the Metán subbasin of the Lerma Basin, ca. 20 km north of the town of Metán. The youngest zircons of this prominent volcanic ash (Ar-14-Ash-1) resulted in a mean U–Pb age of 7.39 ± 0.03 Ma. This new

age contrasts the formerly proposed 8.73 ± 0.25 Ma by Viramonte *et al.* (1994), who correlated garnet-bearing ash-fall deposits throughout NW Argentina with the Corte Blanco Tuff on the Puna Plateau.

We present 13 new U–Pb LA-ICPMS ages and one ZHe age from the Angastaco Basin. Sample Ang-080313-1 is a from a welded tuff exposed in the Angastaco Formation of the Corte El Cañón section east of the town of Angastaco. Previously dated to 13.4 ± 0.4 Ma (^{40}Ar/^{39}Ar, Grier & Dallmeyer, 1990), we obtain 12.17 ± 0.03 Ma (MSWD = 0.86; n = 21). Ang-Isa-7-R is from a stratigraphic position ca. 200 m upsection and yielded 11.98 ± 0.03 Ma (MSWD = 1.12; n = 29). About 500 m above the proposed transition between the Angastaco and Palo Pintado formations (maximum age 8.8 ± 0.5 Ma, Carrapa et al., 2012) the youngest age population of sample Ang-080313-3 indicates a deposition at 7.56 ± 0.02 Ma (MSWD = 1.09; n = 16). Farther upsection, Ang-080313-2 yielded an age of 6.61 ± 0.04 Ma (MSWD = 0.66; n = 5). Ang-070313-4 is from a reworked ash in the Palo Pintado Formation, ca. 150 m higher in the section and has a maximum age of 6.88 ± 0.10 Ma (n = 1). Given the age reversal with the previous sample and the reworked character of the ash deposit we will ignore this age in further discussions. Ang-070313-2 and Ang-070313-3 are both from a ca. 10-m-thick tuffaceous sandstone, ca. 25 to 50 m below a previously dated ash layer (5.98 ± 0.32 Ma, Bywater-Reyes *et al.*, 2010). Ang-070313-2 yielded a consistently young age population around 6.43 ± 0.04 Ma, while Ang-070313-3 shows no consistent age population. Based on the youngest crystal we are able to determine its maximum depositional age to 6.37 ± 0.08 Ma, which agrees with previously published age estimates (Bywater-Reyes *et al.*, 2010). At the southern tip of the Quebrada el Tonco, sample Ar-11-Ash-2/3 was collected from a faulted section in the San Felipe Formation (Carrapa *et al.*, 2011) and yielded 5.12 ± 0.04 Ma. A maximum age obtained from sample Ar-11-Ash-4 (4.60 ± 0.08 Ma) higher up in the same section is corroborated by sample Ar-11-Ash-5 from an along-strike position to the south with an age of 4.52 ± 0.02 Ma. Ang-070313-1 was collected close to the Río Calchaquí, ca. 6 km south of Payogastilla and suggests that the Upper San Felipe Formation continued to be deposited until at least 1.87 ± 0.03 Ma. Sample 005 is from a Quaternary fill unit west of Angastaco that unconformably overlies the San Felipe Formation and was dated to 1.05 ± 0.06 Ma using ZHe. Vc-050313-1 is from a white, unconsolidated ash layer interbedded in an alluvial-fan deposit, south of the town of Cafayate. Since the ages determined were below the limit of the LA-ICPMS method for this setup (<0.7 Ma), the age range defined for the sample is 0.35 ± 0.35 Ma.

Moreover, we present two previously unpublished U–Pb SIMS age estimates from the Corral Quemado area at 27° S latitude. CQ12 was sampled ca. 10 km west of the village of Puerta Corral Quemado in a deformed section of the sandstones of the late Miocene Chiquimil Formation. The two youngest zircon crystals suggest a maximum age of 8.74 ± 0.53 Ma. The second sample, CQ38, was collected about 12 km north of Puerta Corral Quemado in the coarse conglomeratic Corral Quemado Formation. A coherent population of zircon crystals yields an age of 3.65 ± 0.12 Ma.

6.6.2 Hydrogen stable isotopes

We analyzed 17 volcanic glass samples from ash beds in late Miocene to Pleistocene sediments from the intermontane Angastaco Basin, at elevations between 1.7 and 1.9 km, for their hydrogen isotope compositions. Together with recently published data (Carrapa *et al.*, 2014) this enables us to evaluate 24 well-dated hydrogen stable isotope results from the intermontane Angastaco Basin that approximately range between -95‰ and -65‰, spanning the last ~8.8 Myr (Fig. 6.4). The Angastaco dataset is characterized by nearly constant δD_g values around -75‰ until ~6.5 Ma. After this episode, the data shows a rapid decrease in δD_g between ~6.5 and 5.5 Ma of ca. -20‰, and is followed by a number of equally strong oscillations of decreasing and increasing δD_g values until ~4 Ma, where δD_g values become stable at about -70 to -75‰. Limited data from the interval between 4 Ma and 2 Ma suggest a renewed decrease in δD_g to ca. -85‰, while δD_g values of about -67 to -65‰ since ~1 Ma are similar to present-day conditions (δD_{gc} = -65‰).

Our data from the foreland regions east of the Angastaco Basin is very limited, however, four samples from elevations between 0.75 and 1.25 km show a limited range of δD_g values between -78 and -75‰ over the last 9.3 Myr. Data from Carrapa *et al.* (2014) suggests similar conditions at 14.4 ± 0.6 Ma (δD_g = -78‰).

In addition, we measured the hydrogen isotope ratios of 13 volcanic glass samples from radiometrically-dated ashes along the southern Puna Plateau margin. These sites include the Santa María Basin (n = 3), the El Cajón (n = 1) and Corral Quemado (n = 4), and the Fiambalá basins (n = 5; Fig. 6.1). Although, this dataset is insufficient to discuss the specifics of the evolution of the individual basins, it enables us to compare the results with some of the trends in the δD_g record of the Angastaco Basin. When including one additional sample from the Corral Quemado area (Carrapa *et al.*, 2014), we are able to present a dataset spanning the last ~8.5 Myr until ~3.5 Ma with a δD_g range of -95 to -70‰ (grey symbols in Fig. 6.4). Although the data density is much lower than for the Angastaco Basin, it is interesting to note that major trends in isotope values observed in the southern basins appear to be very similar. Between ~8.5 and 6.5 Ma δD_g values are consistently at -75‰ and subsequently decrease until ca. 5.5 to 5 Ma. Similar to the Angastaco Basin, this negative trend is followed by a positive excursion in δD_g. After a gap of more than 1 Myr, δD_g values are more dispersed.

6.6.3 Paleoaltimetry

To estimate paleoelevations for our δD_g record we use a Rayleigh distillation-related fractionation model (Rowley, 2007; Rowley *et al.*, 2001) with starting conditions (T_0 = 21.7°C; RH_0 = 67%) obtained from MOD11C2 night land surface temperatures and NCEP-NCAR 1000 mbar re-analysis published in Rohrmann *et al.* (2014). A comparison of these estimates with present-day elevations at the sampling sites reveals considerable deviations. The modern mean elevation of our samples in the broken foreland

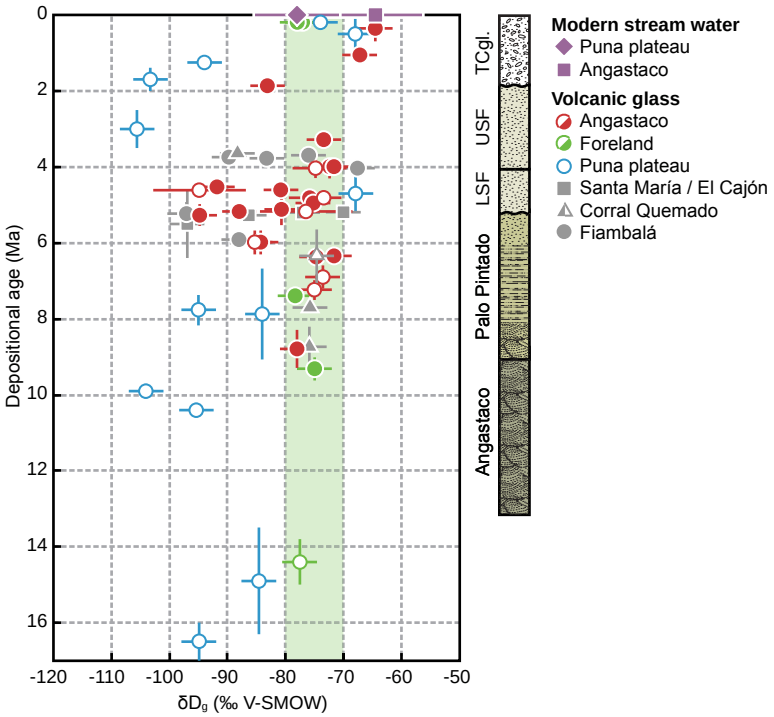

Figure 6.4 – Hydrogen stable isotope composition of volcanic glass samples from the Angastaco Basin (red), the foreland (green), and the Puna Plateau between of 25 and 28° S (blue) showing pronounced trends in δD_g against depositional age. Filled symbols indicate samples from this study and unfilled symbols were obtained from Canavan *et al.* (2014), (Carrapa *et al.*, 2014), and (Dettinger & Quade, 2015). Note the relatively high δD_g values on the Puna during the Quaternary and at ca. 5 Ma, which may document episodes with enhanced atmospheric convection as main mechanism for rainfall in the studied regions. Also shown are δD_g values from other intermontane basins to the south, which imply synchronous paleoenvironmental change between 25 and 28° S during the Neogene. Shaded area indicates the approximate δD_g range of foreland samples.

is about 1.1 km, while the modeled δD data grossly overestimate paleoelevations between 2.1 and 2.3 km (mean – mean elevation 2.2 km). Estimates for the Angastaco Basin, however, suggest overall similar elevations compared to the present day (mean 1.9 km), showing paleoelevations of 1.6-3.0 km (mean 2.3 km) over the past ~9 Myr. Finally, we applied the model to the Puna record. Here, paleoelevations between 1.8 and 3.3 km (mean 2.7 km) underestimate elevations at the sampling sites (mean 3.6 km). Notably, the model results calculated in Canavan *et al.* (2014) show elevations of ~4 km on the Puna for the past ~15 Myr.

We also estimate paleoelevations using the preferred lapse-rate model by Dettinger & Quade (2015) developed for regions to the north of Angastaco. Those results show generally higher elevations than our estimates from the Rayleigh model, which seems to fit better with sampling elevations in the Angastaco Basin and on the Puna.

Finally, we use a modern δD_g lapse rate determined between 22 and 26° S of ca. -16‰/km (Rohrmann *et al.*, 2014) to estimate the relative elevation change between the low-elevation broken foreland sector and the intermontane Angastaco Basin. Although this approach cannot be applied to the complete dataset, our results suggest surface uplift of the Angastaco Basin of about 1-1.3 km for the late Mio-Pliocene.

All paleoaltimetry estimates are listed in Table G.2.

6.7 Discussion

6.7.1 Hydrogen stable isotope record

Hydrogen stable isotope ratios of hydrated volcanic glass are closely linked to the isotopic composition of meteoric water at the time of deposition and during subsequent hydration (e.g., Friedman *et al.*, 1993b; Shane & Ingraham, 2002; Mulch *et al.*, 2008), which in turn is largely a function of temperature/elevation conditions at which rainfall occurs (e.g., Dansgaard, 1964). On this basis it has been shown that temporal changes in δD_g can be linked to tectonic and/or climatic processes and events in northwestern Argentina (Pingel *et al.*, 2014; Canavan *et al.*, 2014; Carrapa *et al.*, 2014; Dettinger & Quade, 2015) and North America (e.g., Mulch *et al.*, 2008; Cassel *et al.*, 2009, 2012). Nevertheless, a number of other factors are known to affect stable-isotope compositions of meteoric water. Possible influences along the eastern Andean margin are: (a) changes in global/regional air and sea-surface temperatures, which could alter the isotopic source signal and/or the atmospheric fractionation processes; and (b) changes in the location of the water-vapor source or changes in air-parcel trajectories across the Amazon Basin. To first order, these processes can be ruled out, because such source-related changes are likely to result in regionally significant shifts in stable isotopes in precipitation in the paleorecord and should be observable in stable isotope records throughout the eastern Andean flanks. This is not the case. As an example, the hydrogen stable isotope record from the Humahuaca Basin, ca. 250 km to the north, shows δD_g values that are characterized by a general trend of deuterium depletion between ca. 6 and 3 Ma without signs of significant variability as seen in the Angastaco Basin (Pingel *et al.*, 2014). Moreover, there is no evidence for shifts in the marine oxygen stable-isotope record at the considered time interval (e.g., Zachos *et al.*, 2008) that are either large enough or temporally comparable to our observed trends. The only other potential moisture source, the southeast Pacific Ocean, may have been blocked by the rising Andean orogen to the west prior to 10 Ma (Insel *et al.*, 2012b). Despite being located close to the northern transition zone of the westerlies it is unlikely that the moisture source for this sector of the Andes has changed since the late Miocene. On much shorter timescales involving the Quaternary, Haselton *et al.* (2002) concluded that there is no evidence for protracted northward shifts in moisture-bearing winds impacting the southern Puna Plateau.

For the above reasons, we prefer to interpret the results of our analysis in terms of local paleoenvironmental change, such as topographic growth and associated decrease in air temperatures; and enhanced rainout (amount effect, Dansgaard, 1964) in windward positions along the eastern Puna flanks. Both

processes are known to produce lower δ-values in meteoric water and, given the geodynamic setting of protracted crustal shortening and range uplift in this region, are the probable cause for negative trends in our stable isotope record. Positive shifts in hydrogen stable isotopes have been related to evaporation as a consequence of orographically forced aridity behind growing topography (Pingel *et al.*, 2014).

Another complication in interpreting stable-isotope records was recently described by Rohrmann *et al.* (2014), who relate an observed non-systematic isotope fractionation south of 26° S with an atmospheric setting that favors atmospheric convection over adiabatic lifting as the main cause for rainfall in the Andes at these latitudes. In this setting, meteoric water across the eastern Andean flanks shows very little to no relationship between the stable isotope composition and elevation, which causes similar δD_g values on the Puna Plateau, in the foreland, and in the intermontane basin regions in-between. Since our study area is located in a transitional zone at ~25.5° S, it is necessary to consider the possibility of this mechanism to have also affected the paleorecord of the Angastaco Basin and its neighboring regions. Indeed, when comparing hydrogen stable isotope data from hydrated volcanic glass in the Angastaco Basin, the southern basins, and the adjacent foreland with data from the Puna Plateau (Canavan *et al.*, 2014; Carrapa *et al.*, 2014; Quade *et al.*, 2015), we are able to identify two episodes that are indicative of non-systematic isotope fractionation. First, at about 5 Ma and secondly, during the Quaternary, which is consistent with the observed present-day conditions. These episodes are characterized by equally high δD_g values in the Angastaco Basin and on the Puna (-70 ± 5‰). In contrast, other episodes clearly show more negative δD_g values on the plateau compared to the intermontane basin record (Fig. 6.4), which reflects the topographic gradients that must have existed before 10 to 15 Ma. This suggests that, although today's isotope-elevation relationships as observed in present-day river and stream waters may be subject to processes different from simple orographic precipitation, air mass lifting and associated condensation, the resulting non-systematic isotope-elevation relationship may not have been a long-lived phenomenon throughout the Mio-Pliocene. The absence of a sufficient number of high-elevation isotopic data prevents a more in-depth investigation of this phenomenon.

6.7.2 Surface uplift & basin aridification vs. enhanced convection

Hydrogen stable isotope data of volcanic glass from the broken foreland east of the Angastaco Basin suggest stable climatic and topographic conditions since at least the late Miocene. This is based on five dated volcanic glass samples that show very little isotopic variation (mean δD_g = -77 ± 1‰, Fig. 6.4). Moreover, δD_g values of the two youngest samples (20 and 50 ka), are roughly comparable with modern δD_{gc} estimates of -67 ± 11‰ that have been converted from long-term GNIP measurements of rainfall in the nearby city of Salta (IAEA, 2015). This, and the fact that the foreland region of NW Argentina apparently has undergone only minor amounts of surface uplift compared to the orogen interior (average elevations of ca. 0.5-1.0 km), supports our assumption that the isotopic compositions, and therefore, their environmental forcing factors remained relatively stable over the course of the last 10 to 14 Myr.

Sedimentologic observations in the Angastaco Basin and the adjacent foreland indicate that both regions were part of a contiguous foreland basin until about 5 Ma (e.g., Hain *et al.*, 2011, (Fig. 6.5)). Hence, we are confident to combine these two datasets for this time period. Consequently, the basis for our interpretations is a dataset that spans the last ~14.4 Myr. During this time the Angastaco Basin experienced pronounced deformation and basin compartmentalization with the transition from a humid foreland basin into the presently elevated and hydrologically restricted intermontane basin setting (e.g., Starck & Anzótegui, 2001; Strecker *et al.*, 2007a). Consequently, changes in the stable isotope record should enable us to track paleoenvironmental changes and help to better constrain them in the regional context.

Previous work on hydrogen stable isotopes from volcanic glass in the Angastaco area suggested stable topographic conditions at its current elevation of ca. 2 km throughout the Mio-Pliocene (Carrapa *et al.*, 2014). The combination of data from Carrapa *et al.* (2014) and our new results provides a comprehensive data set that furnishes evidence for major paleoenvironmental change, which likely includes surface uplift, an increase in aridity with the onset of orographic effects along the basin-bounding ranges to the east, and ensuing impacts on atmospheric circulation. Again, these interpretations are based on significant δD_g variability observed through the investigated time period (Fig. 6.4: δD_g values decrease by 20‰ at 6.5-5 Ma, followed by a ca. 20‰ increase until ca. 5 Ma. Subsequently, δD_g values decrease again to values of -90 to -95‰ at about 4.5 Ma and increase by 20‰ at 4 Ma. Limited Plio-Pleistocene data inhibit the identification of specific trends in δD_g , but late Quaternary samples show that modern values were attained by at least 1 Ma.

The combined record shows no major trends in δD_g until ~6.5 Ma and remains stable at a mean δD_g of -76 ± 2‰. This supports the notion that surface elevations in the Angastaco Basin did not significantly depart from the rest of the foreland prior to 6.5 Ma.

Between ~6.5 and 5.5 Ma the data point to a rapid decrease in δD_g by 20‰, which we interpret as the result of surface uplift in the area of the former basin catchment. This interpretation is based on several observations. First, it has been shown that negative trends in δD_g are associated with surface uplift of intermontane basins along the Puna Plateau (Pingel *et al.*, 2014). Even though the overall signal we observe in the Angastaco Basin is more complicated compared to tectonically and topographically similar settings to the north (i.e., Humahuaca Basin at 23.5° S), it is reasonable to assume a comparable behavior with surface uplift through time. Furthermore, tectono-sedimentary and thermochronological data suggest that the Angastaco Basin and its bounding ranges experienced deformation and were exhumed during the late Miocene to Pliocene. For example, late Miocene (12-7 Ma) deformation and range uplift of the Cerro Durazno and Sierra Quílmes along the Puna Plateau margin(e.g., Deeken *et al.*, 2006; Coutand *et al.*, 2006) has been linked with the onset of enhanced orographic rainout in the Angastaco area since about 9 Ma and the establishment of humid conditions, as documented by the rich faunal and floral fossil record of the Palo Pintado Formation (e.g., Starck & Anzótegui, 2001; Deeken *et al.*, 2006; Coutand *et al.*, 2006;

Bona *et al.*, 2013). Deformation along the present-day eastern basin margin caused rapid exhumation of the Sierra de los Colorados since ca. 12-10 Ma and the Sierra León Muerto since ca. 8-6 Ma (Carrapa *et al.*, 2011). In this setting, ongoing deformation affected structures within the Angastaco Basin to cause basin-internal deformation (Carrera & Muñoz, 2008). This is also shown by the major unconformity at the bottom of the San Felipe Formation that documents intra-basin deformation prior to 5-6 Ma (e.g., Carrera & Muñoz, 2008).

On the other hand, a -20‰ shift in δD_g appears too large for tectonic surface uplift and enhanced rainout over a relatively short period of one million years. However, enhanced sedimentation of about 0.35 to 0.65 km/My between ca. 6.5 and 5.0 Ma (Bywater-Reyes *et al.*, 2010; Galli *et al.*, 2014) may have contributed to the amount of surface uplift in an extended and actively deforming broken foreland setting surrounded by uplifting topography of varying degree at that time (Galli *et al.*, 2014; Carrapa *et al.*, 2011). In such a setting, large amounts of sediment of the Palo Pintado Formation could have been trapped behind growing structures to the east and progressively filled the continuously growing accommodation space, while after 5 Ma, these structures finally disconnected the fluvial system from the foreland and prevented further eastward sediment transport (Hain *et al.*, 2011).

After ca. 5.5 Ma our record is characterized by one strong positive and negative δD_g excursions, which likely reflect atmospheric and/or orographic effects. In detail, our record shows a positive trend with maximum δD_g values of ca. -75‰ at ~5 Ma. Previous studies related such abrupt shifts to enhanced aridification due to the attainment of threshold elevations in a windward position and associated orographic shielding (Pingel *et al.*, 2014). Interestingly, in the Angastaco Basin this shift occurs coevally with the onset of coarse gravel and conglomerate deposition of the San Felipe Formation; a lithological unit that has been associated with generally semi-arid, seasonal conditions (Coutand *et al.*, 2006; Bywater-Reyes *et al.*, 2010). In this context it is noteworthy that we found a ca. 30-cm-thick evaporitic layer within the San Felipe Formation, dated to 4.8 ± 0.2 Ma (Bywater-Reyes *et al.*, 2010). Therefore, we suggest that aridity caused deuterium enrichment of our record through enhanced evaporation during sub-cloud evaporation or soil-water formation (e.g., Quade *et al.*, 2007).

One explanation for enhanced hinterland aridification is that the basin-bounding ranges to the east must have attained threshold elevations to efficiently interfere with westward moisture transport, which may be supported by an earlier onset of rapid exhumation, and thus inferred uplift, in the area (e.g., Carrapa *et al.*, 2011). On the other hand, this episode also coincides with unusually high δD_g values on the Puna Plateau of -68‰ (Canavan *et al.*, 2014), suggesting an additional or alternative mechanism, by which deuterium enrichment in the basin may have been caused by non-systematic fractionation in the wake of atmospheric conditions that favored convective storms (convection setting), similar to the present-day synoptic situation. Because this setting prevents or reduces moisture-laden air masses to penetrate far into the orogen, intermontane regions are likely to become more arid. Moreover, it is also conceivable that

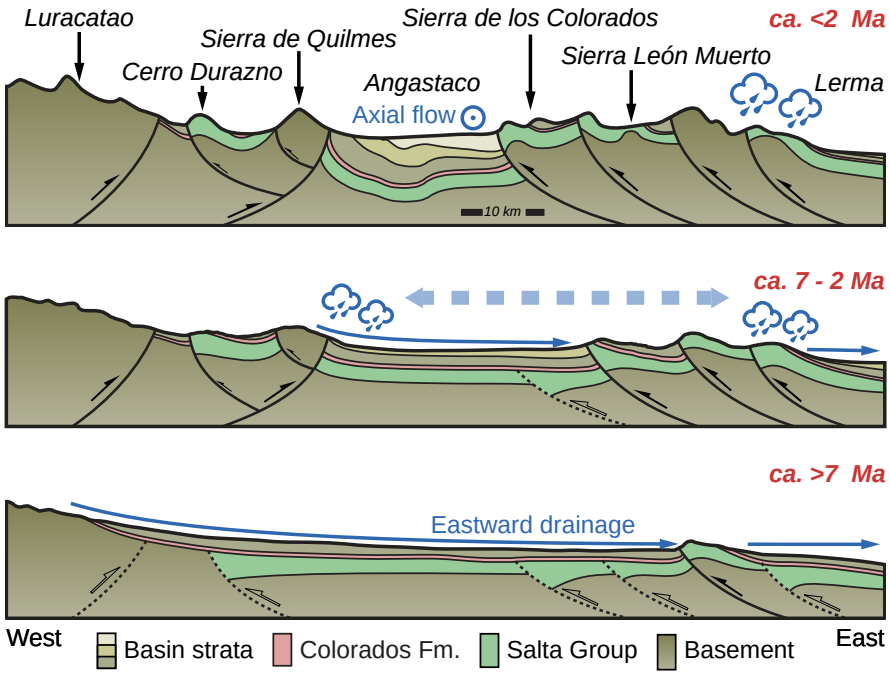

Figure 6.5 – Conceptual model showing the structural and orographic development of the Angastaco Basin and neighboring ranges with time. Prior to 7 Ma the Angastaco Formation was deposited in large foreland basin setting that may have been partly fragmented prior to 10 Ma by range uplifts in the area of the present-day Sierra León Muerto. After 7 Ma deformation and range uplifts along basin-bounding structures as well as intra-basin deformation led to enhanced sediment supply and storage behind evolving structures and associated surface uplift of the Angastaco Basin. This was accompanied by rapid shifts in the strength of the presently observed convective setting and may have also caused drastic changes in moisture availability in the Angastaco area, once topography to the east was large enough. At present, the combined effects of atmospheric convection and orographic precipitation along the eastern basin-bounding ranges act on the hydrology of the basin.

the capping inversion that forms the boundary between dry westerlies and the Andean low-level jet during such conditions causes the reduction of orographic threshold elevations. As a result lower-elevation mountain ranges become effective orographic barriers. In northwest Argentina, elevation thresholds of efficient orographic barriers seem to be attained, when a 3-km relief of 1-2 km is exceeded (Hain *et al.*, 2011). This potentially very dynamic mechanism may explain the observed rapid shifts in our data, because they are unlikely to have been caused by feedbacks of tectonics, climate, and erosion across eastern topography. In summary, we suggest that δD_g variability after 5 Ma is governed by the variable strength and or latitudinal location of high-level westerlies, likely in combination with near-threshold elevations to the east (Fig. 6.5).

For the last ~4 Ma the isotope record is limited; however, a ~2 Ma ash sample in the Upper San Felipe Formation shows a δD_g of -85‰, while younger δD_g values of ca. -65‰ may indicate increased aridity. Because δD_g values from the Puna Plateau are also very high at that time (-70 ± 5‰), we are confident that

today's convection setting must have been established by then. As a consequence of ongoing range uplift to the east (Sierras de los Colorados and León Muerto), Pleistocene basin aridification may additionally be related to efficient orographic shielding observed today (Fig. 6.5).

6.7.3 Paleoaltimetry

Complexities in the δD_g record, caused by atmospheric patterns and enhanced aridity in the lee of growing topography, prevent us from estimating paleoelevations at 25-28° S latitude in a conventional way, i.e., by assuming purely adiabatic processes for the total of our δD_g record. Another challenge is that foreland elevations cannot be sufficiently predicted by current models. Consequently, it is challenging to quantify elevation change between the low-elevation foreland and the elevated Angastaco Basin. However, one approach is to select a time interval, when non-systematic fractionation effects can be inferred to have been minimal. Changes in δD_g over such a time period can then be compared with modern lapse rates from nearby regions unaffected by unwanted interference, such as the Eastern Cordillera north of 25° S. In the case of the Angastaco Basin, between 6.5 and 5.5 Ma, we observe a ca. -20‰ shift in δD_g, where non-systematic influences may be excluded. The modern lapse rate of ca. -16‰/km between 22 to 25° S (Rohrmann *et al.*, 2014), enables us to estimate the relative change in elevation between the foreland and the Angastaco Basin of ca. 1.3 km. Given the large errors associated with this approach, our estimate is within the possible range of the expected surface uplift from a foreland position at ca. 0.5 to 1 km initial elevation and the current elevation of the Angastaco Basin at 1.8 to 2 km. As discussed earlier, this change in elevation apparently occurs very rapidly over the timespan of approximately one million years. Since this appears to be very unlikely, an alternative interpretation to gain such uplift rates is needed. Because we see evidence for atmospheric conditions similar to today also in the past, it may be possible that rather than increased uplift enhanced atmospheric convection processes prior to 6.5 Ma may have masked a potential elevation signal. Therefore, the onset of surface uplift in the Angastaco area may have started earlier, a scenario supported by the local deformation history. Nonetheless, the minimum signal observed at ca. 5.5 Ma appears to represent the surface uplift gained at that time.

6.7.4 Links between southern basins flanking the southern Puna

From north to south, the Santa María (26.5° S), El Cajón, and Corral Quemado basins (27° S), and the Bolsón de Fiambala (27.5° S), constitute a group of intermontane basins along the eastern and southern flanks of the southern Puna Plateau (Fig. 6.1). Although, the δD_g records from these basins are insufficient to discuss their individual basin and topographic development, one important observation can be made when comparing the data with the Angastaco record: Despite the low data density the records from these southern basins complement each other in a remarkable way (Fig. 6.4). For example, between ~8.5 and 6.5 Ma, δD_g values remain consistently at -75‰ and subsequently decrease until ca. 5.5 to 5 Ma, followed by a positive excursion in δD_g. This leads us to suggest that mechanisms causing δD_g trends

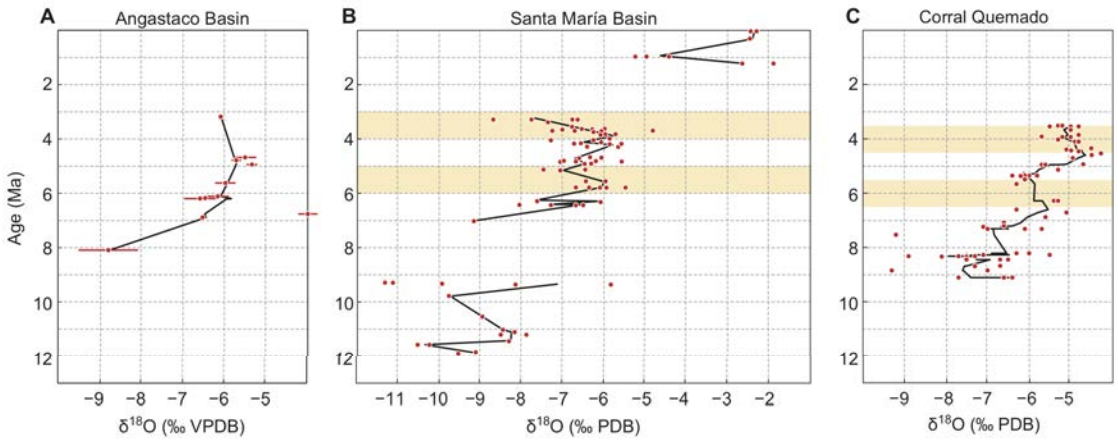

Figure 6.6 – Oxygen stable isotope composition of published soil carbonate records showing a general long-term trend towards more positive $\delta^{18}O$ values. A: Angastaco Basin (Bywater-Reyes *et al.*, 2010); B: Santa María Basin (Kleinert & Strecker, 2001); C: Corral Quemado (Latorre *et al.*, 1997). Yellow areas indicate episodes of negative short-term $\delta^{18}O$ trends. Note, similar trends in B and C between 7 and 3 Ma. Differences in C may relate to limited stratigraphic age constraints.

in the Angastaco Basin may also have influenced stable isotope signals farther south. In this context it is reasonable to assume a common mechanism to have been responsible for the stable isotope composition of meteoric waters south of 25° S. In light of the present-day patterns it appears that westerlies crossing the plateau in eastward direction and the associated concentrated occurrence of convective storms may represent a viable mechanism to explain some of the patterns.

Soil carbonates from the Angastaco, Santa María, and the Corral Quemado basins generally show a similar, positive long-term trend in both, $\delta^{13}C_{sc}$ and $\delta^{18}O_{sc}$ that indicate increasing regional aridity and/or wet-dry seasonality (Fig. 6.6, Latorre *et al.*, 1997; Kleinert & Strecker, 2001; Bywater-Reyes *et al.*, 2010). This is also shown by the $\delta^{13}C$ and $\delta^{18}O$ data in mammalian fossil tooth enamel from the Corral Quemado area (Hynek *et al.*, 2012). These authors argue that variable short-term trends in $\delta^{13}C$ and $\delta^{18}O$ on the scale of 1 to 2 Myr are likely caused by hydrological rather than climate change, either associated with regional variations in moisture sources or local changes in soil evaporation as a result of orographic barrier effects along the Sierra Aconquija and Cumbres Calchaquíes (Fig. 6.1) farther east. Similar short-term shifts can also be observed in the soil carbonate record from the Corral Quemado area and to some degree in the Santa María record (Fig. 6.6). For example, positive shifts between 7 and 3 Ma are offset by ~0.5 Myr relative to the Corral Quemado record. This could be related to the stratigraphic age control in the Santa María record that is tied to a limited number of radiometric ages, while the Corral Quemado record was additionally constrained by magnetostratigraphy (Butler *et al.*, 1984; Latorre *et al.*, 1997). The lack of sufficient data from the Angastaco Basin does not permit a more detailed interpretation of short-term

variations. These systematic shifts cannot be explained by regional climate change impacting the eastern flanks of the Central Andes, because stable isotope records obtained north of 25° S show significantly different trends (Mulch *et al.*, 2010).

Notably, soil carbonate $\delta^{18}O_{sc}$ from the southern basins contrast trends in our δD_g compilation (Fig. 6.6). This may be related to the seasonal nature of soil-carbonate formation. While soil carbonates are thought to form during the second half of the rainy warm season (e.g., Peters *et al.*, 2013), glass shards incorporate surface water over thousands of years until saturation (Friedman *et al.*, 1993b; Mulch *et al.*, 2008). This causes a bias of soil carbonate isotope records towards the dry season during which the atmospherically induced convection setting is affected by the lack of sufficient low-level moisture supply into this region. Nonetheless, slightly negative trends (1-1.5‰ PDB) in the $\delta^{18}O_{sc}$ record from the Corral Quemado area and the Santa María basin at 6.5-5.5 Ma and 4.5-3.5 Ma roughly coincide with inferred episodes of reduced convection as a mechanism for rainfall, which supports a regional atmospheric effect on stable isotopes south of 25° S.

However, in the past there may have been other processes of regional importance that potentially could have influenced stable isotope compositions in precipitation. For example, the southern regions underwent a similar tectono-sedimentary history: (a) In the Santa María basin (~1.2-2 km), late Cenozoic sedimentation initiated prior to 13-10 Ma and was followed by accumulation of more than 6 km of coarsening-upward sequences partly comprising sediment from eastern sources (Villanueva Garcia & Ovejero, 1998; Bossi *et al.*, 2001). This interpretation is supported by thermochronological results from the northern Calchaquíes and eastern Aconquija ranges to the east that suggest a complex structural history, including late Cenozoic exhumation, which likely resulted in early topographic highs in those regions (Sobel & Strecker, 2003; Löbens *et al.*, 2013). Significant exhumation and deformation of the Sierra Aconquija is documented since ca. 9 Ma and enhanced erosion along its eastern flanks by ~3 Ma supports the development of an orographic barrier with associated increased rainout (Löbens *et al.*, 2013). (b) Similarly, sedimentation in the El Cajón area (~2.5-3 km) started at 13.6 ± 0.5 Ma (Mortimer *et al.*, 2007; Pratt *et al.*, 2008). Late Cenozoic deformation and exhumation patterns of the Sierra Quilmes infer southward propagation of deformation. Thermochronologic evidence from the northern extend of the Quilmes range, close to the Angastaco Basin, suggest deformation since ~14 Ma (Carrapa *et al.*, 2011), while in the central parts, deformation occurred by ca. 10 Ma (Pratt *et al.*, 2008). Finally, the southern tip of the Sierra Quilmes started deforming after 6 Ma, which led to basin compartmentalization between the El Cajón and Santa María basins (Strecker *et al.*, 1989; Mortimer *et al.*, 2007). Other (c) The Corral Quemado area (1.7-2.5 km) is located east of the Sierra Chango Real at ~27° S. While this range was already affected by rapid exhumation between ca. 38 and 29 Ma (Coutand *et al.*, 2001), its late Cenozoic reactivation may have occurred since ca. 13.5 Ma (Pratt *et al.*, 2008). The oldest sediments documented in this region predate 7.14 Ma (Latorre *et al.*, 1997). Compartmentalization between Corral Quemado and El Cajón was

established well after 3.6 Ma by a growing anticline located between both areas (Hynek, 2011). (d) Finally, located at the transition between the southern margin of the Puna Plateau and the Sierras Pampeanas, the Fiambalá Basin (1.6-2.5 km) is confined by the Sierra de las Planchadas to the west, which shows evidence for late Eocene exhumation (Coughlin *et al.*, 1998; Carrapa *et al.*, 2006). The plateau margin to the north is thought to have been exhumed during the Early to Middle Miocene and may have established its current relief by 9 Ma (Carrapa *et al.*, 2006). The oldest Cenozoic sedimentary deposits in this region are sourced to the west and much older than 8 Ma (Carrapa *et al.*, 2008). Initial clast contributions from eastern sources are documented at ~6 Ma and postdate the onset of deformation along the eastern basin margin.

In summary, deposition in the southern basins, but also including the Angastaco Basin, largely commenced during mid- to late Miocene time and was accompanied by the deposition of thick coarsening-upward sequences (e.g., Strecker *et al.*, 1989; Bossi *et al.*, 2001; Strecker *et al.*, 2009; Mortimer *et al.*, 2007; Carrapa *et al.*, 2008). Most regions record initial basin compartmentalization prior to 6 Ma, while their separating ranges experienced an earlier onset of deformation (e.g., Sobel & Strecker, 2003; Carrapa *et al.*, 2008; Pratt *et al.*, 2008; Löbens *et al.*, 2013; Hain *et al.*, 2011). This must have been associated with intra-basin deformation and perhaps surface uplift, which would be a reasonable explanation for relatively low δD_g values (ca. -95‰) recorded in the Angastaco, Santa María/El Cajón, and Fiambalá basins after 6 Ma.

Convincing evidence for the onset of arid conditions related to orographic barrier effects in other basins than the Santa María and Angastaco Basins is limited. Still, similar trends in various stable isotope records suggest a common link in the climatic development of the southern basins. Paleoenvironmental inferences from paleosoil characteristics and oxygen and carbon stable isotopes from soil carbonates in the Santa María Basin suggest an onset of enhanced aridity in the late Pliocene between 3 and 2.5 Ma due to uplift of the Sierra Aconquija and Cumbres Calchaquíes to the east (Kleinert & Strecker, 2001; Löbens *et al.*, 2013). Tangible evidence for enhanced aridity in the El Cajón area is restricted to gypsiferous layers intercalated with a lacustrine unit aged >8 Ma (Mortimer *et al.*, 2007; Pratt *et al.*, 2008), but does not unambiguously imply sustained aridity. A sharp increase in soil carbonate $\delta^{13}C$ after 4 Ma relates to a C4-plant composition of ~70% in the Corral Quemado area (Latorre *et al.*, 1997) and led other researchers to favor increased aridity as the cause (e.g., Schoenbohm *et al.*, 2015). However, the fact that $\delta^{18}O$ values from the same record do not follow this shift, argues against a climatic trigger (Hynek, 2011). Occasional mud cracks in middle to late Miocene mudstones from the Fiambalá Basin represent an episodically dry environment (Carrapa *et al.*, 2008), but also do not imply sustained aridity in this region. Hence, it cannot be entirely ruled out that late Pliocene surface barrier uplift in the areas of the Sierra de León Muerto, Cumbres Calchaquíes, and Sierra Aconquija, caused the formation of a contiguous orographic barrier, which resulted in subsequent hinterland aridification that has characterized the southern basins until today.

6.8 Conclusions

The δD_g record from intermontane basins along the eastern and southern flanks of the Puna Plateau (south of 25° S) reveal a complex relationship between the hydrogen stable isotope composition of volcanic glass, tectonosedimentary events, orographically induced climate change, and the effects of an atmospherically-induced convection setting. This prohibits the interpretation of the δD_g record in terms of changing rainfall patterns (orographic barrier effects) and renders stable-isotope-based paleoaltimetry challenging. Using published δD_g results from the adjacent plateau region, we can identify at least two episodes with enhanced convection at about 5 Ma and, consistently with present-day conditions, during the Quaternary. Excluding these episodes from paleoaltimetric interpretations enables us to suggest similar initial elevations of the foreland and the intermontane Angastaco Basin until ca. 7 to 6.5 Ma, which was followed by surface uplift on the order of ca. 1.3 km due to ongoing tectonic and sedimentary processes within the basin and along the basin-bounding structures. δD_g data from neighboring intermontane basins to the south suggest similar tectonic events in this region and underline the regional influence of enhanced convection on the stable isotope composition of rainfall. Despite the obvious complexities involved when interpreting isotopes in precipitation records in regions, where fundamental changes in rainout regime have occurred over time, we are able to document parts of the uplift history of the intermontane Angastaco Basin and the influence of changing atmospheric flow conditions on stable isotope fractionation in rainfall along the eastern Andean margin.

Supporting information

Summary of U–Pb and U–Th/He zircon analytical data of volcanic ash samples and data tables of hydrogen stable isotope analyses of volcanic glass, modern stream water samples, and paleoaltimetry estimates can be found in the appendix (see Appendix G and H).

Chapter 7
Discussion & conclusions

The principal aim of this study was to establish a comprehensive chronology of tectonic events, changes in topographic and climatic conditions, and ensuing surface processes along the eastern margin of the southern Central Andes in NW Argentina. Two main regions were identified to carry out this investigation: the semi-arid intermontane Humahuaca Basin, in the transition between the Andean Puna Plateau and the humid broken foreland of the Santa Bárbara System between approximately 23 and 24° S and in the adjacent semi-arid intermontane Angastaco Basin at about 25° S to the southwest (Fig. 7.1). The rationale of this choice was to gain a better understanding of the spatiotemporal development of tectonic and climatic conditions in both regions and to reconstruct their transition from a formerly contiguous, humid foreland-basin setting to a semi-arid to arid intermontane environment as observed today, as the result of lateral orogenic growth. An unambiguous characterization of orogenic growth mechanisms, their impact on climatic conditions, and possible feedback loops between them, is essential to rigorously assess the geological and paleoenvironmental inventory of sedimentary basins and to disentangle interacting deep-seated and surficial processes involved in mountain building. Ultimately, such studies help identify different forcing mechanisms that drive landscape evolution in high-mountain environments and that provide the pathways for speciation (e.g., Hoorn *et al.*, 2010; Weir & Price, 2011) and the routing of sediment toward depositional centers in the foreland, where they may influence the generation of economically relevant resources (e.g., Beaumont, 1981; Dunn *et al.*, 1995; Echavarría *et al.*, 2003). The individual research chapters of this thesis attempted to address these issues to provide new insight into non-collisional mountain building and sedimentary basin evolution in areas characterized by the reactivation of inherited basement anisotropies and the resulting formation of broken forelands.

7.1 Tectonics, climate & surface processes

The results from the intermontane Humahuaca Basin, presented in Chapter 3, provide the first detailed estimates on the timing of foreland fragmentation and its subsequent tectono-sedimentary development in the transition between the Eastern Cordillera and the Santa Bárbara System. Previous studies in this region mainly focused on sedimentary facies interpretations and radiometric and paleomagnetic dating of the fossiliferous Pliocene Uquía Formation in the northern sector of the Humahuaca Basin (Marshall

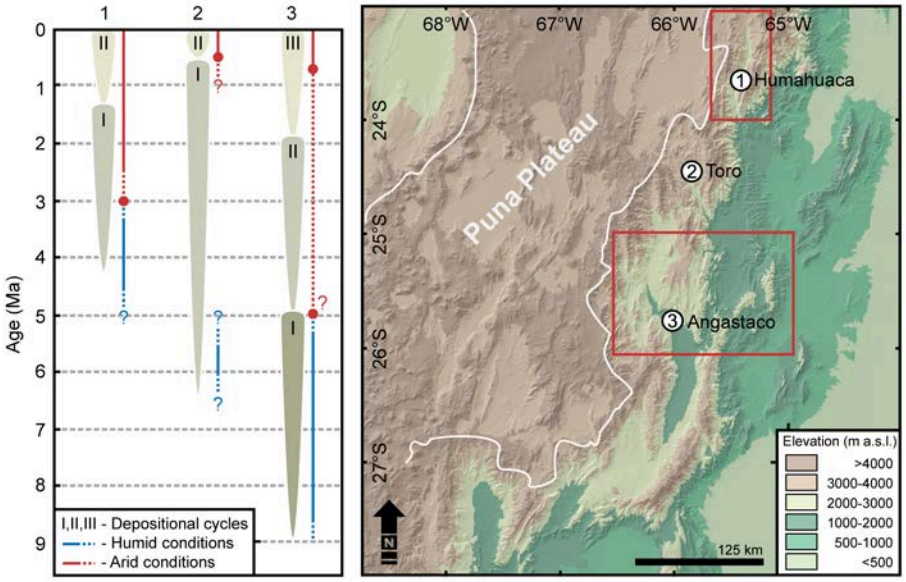

Figure 7.1 – Spatiotemporal evolution of basin filling and climatic conditions of intermontane basins along the eastern Puna-Plateau margin, showing the main cycles of intermontane basin filling. Note, the non-systematic processes among the basins with time.

et al., 1983; Walther *et al.*, 1998; Reguero *et al.*, 2007), while other lithological units were less studied, with the exception of the ubiquitous Pleistocene basin fills (Tchilinguirian & Pereyra, 2001; Robinson *et al.*, 2005; Sancho *et al.*, 2008). With the newly presented data, generated during this study, a chronology of the basin-internal deformation and sedimentation processes is now available, which was derived from the exposed rich late Miocene to Pleistocene sedimentary basin record.

In the Humahuaca Basin, initial intermontane basin sedimentation at ca. 4.2 Ma followed foreland fragmentation, severing of the fluvial system, and formation of accommodation space in the upstream reaches of growing topography. Later, during the Pleistocene, repeated basin filling and excavation were likely influenced by tectonism across the outlet region, ensuing aridification in the lee of rising topography, and concomitant fluctuations in the efficiency of river incision and sediment removal. Field observations of deformed erosion surfaces and an assessment of fault activity suggest an intriguingly systematic link between episodes of internal deformation following large-scale sediment removal from the intermontane basins of the Eastern Cordillera. In the Humahuaca Basin this process occurred during at least two periods. First, after a basin-wide removal of basin sediments <1.5 Ma, and second, when a younger phase of deformation affected the basin in the course of successive fluvial incision and terrace cutting into thick basin-fill conglomerates. The cause for these alternating episodes of filling, sediment evacuation, and renewed faulting in the interior of the orogen is being debated, but a possible mechanism may involve local changes in the shallow crustal stress field related to changing overburden. In such a scenario, faults

are inactive during periods of extensive and voluminous basin fills. Conversely, following the removal of sedimentary fills, the lithostatic pressure and thus the vertical stresses acting on reverse faults in the basins is reduced, leading to fault re-activation and potentially out-of-sequence faulting. Similar observations have been made in other intermontane basins of NW Argentina (Hilley & Strecker, 2005; Strecker *et al.*, 2007a). Likewise, Hetzel & Hampel (2005) investigated the potential for Pleistocene reactivation of normal faults in the western U.S. during the regression of pluvial Lake Bonneville and deglaciation in the Wasatch Range and the adjacent Basin and Range province. Another example involves a study from Taiwan, where Steer *et al.* (2014) showed that erosion influences the seismicity of active thrust faults.

In combination with previous studies on deformation and exhumation processes in the area of the present-day Puna Plateau at this latitude farther west (e.g., Deeken *et al.*, 2004, 2005; Letcher, 2007), it is possible to reconstruct the spatiotemporal history of orogenic growth in this sector of the southern central Andes. This history can be generally described by an eastward-migrating deformation pattern, although the finer details of this evolution point to a diachronous and spatially disparate behavior of the deforming foreland regions. Indeed, deformation started ca. 100 km km to the west with exhumation of the Sierra del Tanque and Sierra de Cobre in the late Oligocene (Deeken *et al.*, 2005; Letcher, 2007). Farther east, the Sierra Aguilar was exhuming since Eo-Oligocene time (Insel *et al.*, 2012a) and the western flank of the Humahuaca Basin, an integral part of the eastern margin of the Puna Plateau, experienced exhumation at ca. 15 Ma (Deeken *et al.*, 2004). In contrast, deformation along the eastern basin-bounding Tilcara Ranges started between approximately 10 and 6 Ma (Siks & Horton, 2011, this study); the area between the foothills of the Tilcara Ranges in the foreland and the Santa Bárbara System, about 50 km to the east, started deforming at about 5 Ma (Reynolds *et al.*, 1994, 2000). As discussed in Chapter 3 deformation in the Humahuaca Basin and its adjacent mountain ranges continued and, as recorded by deformed Quaternary fluvial terrace surfaces and alluvial fans, is still ongoing.

The hydrogen stable isotope study presented in Chapter 4, is one of the first applications of this proxy along the Puna margin to evaluate the topographic evolution of orogenic plateau flanks. Observed δD_g shifts are closely related to the tectonic and topographic history of the Humahuaca Basin and a subsequent regional climatic response and reveal Mio-Pliocene surface uplift. This was accompanied by a changeover from a humid climate, as in the present-day foreland, to the semi-arid conditions currently observed in this intermontane setting. Moreover, the stable isotope data reveals that leeward basin aridification started to be effective once windward range uplifts in the Tilcara Ranges to the east had attained a threshold elevation to efficiently block moisture-bearing winds. Consequently, this process of establishing orographic barriers by basement uplifts in eastward direction ultimately has helped maintain low amounts of precipitation and internal drainage conditions on the plateau, because moisture transport into the orogen interior has been successively reduced.

The analysis of present-day spatial rainfall patterns along the eastern Andean flank in Chapter 5 suggests that the threshold elevation for effective orographic rainout is coupled to a 3-km-radius of relief above ~1 km. The present-day relief of the Tilcara Ranges exceeds this threshold relief by ca. 1 km. Consequently, with the onset of enhanced aridity in the Humahuaca Basin between approximately 2.5 and 3.5 Ma, the Tilcara Ranges may have been at an elevation of ca. 3.0-3.5 km (presently at 4.0-4.5 km). Estimated rates for this regional surface uplift of ~0.3-0.4 km/Myr are similar to rates calculated from the isotopic data between 6.0 and 3.5 Ma, which show rates of ca. 0.5 km/Myr when applying the regional modern isotopic lapse rate presented in Chapter 4. However, because stable isotope paleoaltimetry is still associated with large uncertainties, absolute measurements of elevation change are difficult to interpret and can only provide crude estimates of surface-uplift rates.

Relationships between tectonic uplift and tectonic forcing of climatic conditions in the Eastern Cordillera support earlier models of lateral plateau growth following range uplift and hinterland aridification in concert with reduced/severed fluvial connectivity and ensuing filling of the plateau area (e.g., Sobel *et al.*, 2003). In such a setting the fluvial system becomes increasingly inefficient to transport and export large volumes of sediment away from the orogen interior toward the foreland. This, and the fact that the plateau-bounding regions are all still seismically active and record active deformation, raises the possibility that further range uplift along the plateau-margin basins will aid hinterland aridification, eventually leading to reduced fluvial connectivity of intermontane basins from the foreland, ensuing basin isolation, internal drainage, and basin filling, eventually followed by the incorporation of the basin into the drainage system of the adjacent plateau. As such, marginal mountain ranges like the Eastern Cordillera and their intermontane basins may act as a buffer to variable climatic conditions with an increased short-term availability of rainfall and runoff, which will not lead to headward incision into the plateau, thus storing and preserving thick sedimentary fills.

Although deformation patterns along the eastern Andean flank may appear to be synchronous at first sight, closer inspection of the development of deformation patterns and sedimentary fills of individual intermontane basins implies a non-systematic, diachronous, and spatially disparate behavior. For example, in the Angastaco Basin at ca. 26° S, deformation started already prior to 14 Ma (e.g., Hongn *et al.*, 2007; Del Papa *et al.*, 2013; Galli *et al.*, 2014). Uplifts east of the present-day basin may have caused restricted drainage and reduced sediment transport into the foreland since 9 Ma and resulted in severed fluvial conditions by 5 Ma (Chapter 5). However, clast compositions of the Guanaco Formation in the Santa Bárbara region to the east imply a sediment source in the present-day Metán Range farther east since ca. 10 Ma. This range is approximately 50 km east of the Eastern Cordillera and highlights the diachronous nature of uplift in this region. During the Quaternary, deformation has been accommodated across virtually the entire broken foreland. Similar to observations made in the Humahuaca Basin, Chapter 5, documents

evidence for progressive sediment storage within intermontane basins that appears to be associated with tectonic defeat of fluvial incision, followed by orographic hinterland aridification.

These observations are important, because very similar processes were described in the Toro basin at 24.5° S and other basins along the eastern flank of the Puna. In the Toro Basin deformation involving the underlying basement may have started during the late Miocene as documented by growth structures in the Agujas Formation (>10 to <8 Ma) (Mazzuoli *et al.*, 2008; DeCelles *et al.*, 2011; Vezzoli *et al.*, 2012). By 6.4 Ma range uplift to the east prevented further eastward transport of sediments across the Sierra Pasha Sur toward the foreland (Viramonte *et al.*, 1994; Reynolds *et al.*, 2000; Hilley & Strecker, 2005). This led to changes in erosion and sedimentation processes in the developing Toro basin and the deposition of the largely conglomeratic Alfarcito Formation of late Miocene to Pliocene age, which, at its base, contains plant-fossil evidence for more humid conditions in the past (Strecker *et al.*, 2007a). It is yet unclear though, for how long these wetter conditions persisted, but an increase in aridity may correspond to the deposition of basin-filling conglomerates after 0.98 Ma, which superseded a phase of deformation and basin excavation (Marrett & Strecker, 2000; Hilley & Strecker, 2005).

A comparison of the climatic and tectono-sedimentary patterns of the Humahuaca, Toro, and Angastaco Basins (Fig. 7.1) shows many similarities in the style of intermontane basin development in NW Argentina, such as repeated basin filling and excavation. However, there are apparently no clear correlative temporal relationships. This suggests that at million-year timescales intermontane basin processes in this region were primarily determined by tectonic deformation and its impact on the fluvial system in an increasingly arid climate, rather than climate change alone.

Hydrogen-stable isotope analyses from the Angastaco Basin and basins farther south (presented in Chapter 6) reveal intriguing trends in their δD_g records that might be related to variable atmospheric flow patterns, which have recently been observed to alter the present-day isotope composition of meteoric water (Rohrmann *et al.*, 2014). Present-day oxygen and hydrogen stable-isotope compositions of water from small streams and rivers across the eastern Andean flank showed that in the subtropical Andes south of ca. 25° S the commonly observed isotope-elevation relationship breaks down. This phenomenon was mainly explained with atmospheric processes favoring enhanced convective rainout, which causes non-systematic isotope fractionation with temperature and elevation across the eastern flank of the orogen. Although a systematic recurrent mechanism behind those variations cannot be explained for the study area at present, episodes representing times of reduced convective rainfall may afford the opportunity to gain more insight into the elevation history of the basins and their adjacent ranges. Importantly, the data presented suggests relatively low elevation, comparable to the foreland, until possibly 7 Ma, followed by surface uplift. Thereafter, results are inconclusive in terms of the character of paleoenvironmental change, but suggest enhanced aridity due to windward range uplift as early as 5 Ma (supported by evaporitic layers in the San Felipe Formation), but at least by 1 Ma. This time span is broadly consistent with previous

estimates of enhanced aridity in the Angastaco Basin, proposing maximum aridity in the basin by 5 Ma (Bywater-Reyes *et al.*, 2010) or the onset of tectonically induced aridity between 5.2 to 2.4 Ma (Coutand *et al.*, 2006; Strecker *et al.*, 2007a).

Although the timing and style of foreland fragmentation and intermontane basin formation in the Angastaco and Humahuaca areas are very similar, some fundamental differences exist in their δD_g records. The interpretation of the δD_g signal from the Humahuaca Basin - indicative for uplift and subsequent aridification - is relatively straightforward, which is owed to seemingly similar atmospheric circulation patterns, and therefore a well-pronounced isotope-elevation relationship in NW Argentina, since at least late Miocene time (this study). The late Miocene to Pleistocene δD_g signal from the Angastaco Basin, however, suggests a rather complex history of uplift and subsequent aridification, which is likely related to variable atmospheric conditions, such as the influence of convective rainfall, changing the commonly expected isotopic relationship with elevation. Even though it is possible to extract limited paleoaltimetric information from the Angastaco record, the results presented in Chapter 6 call for caution when attempting the interpretation of stable isotope records based on meteoric waters, if modern atmospheric conditions, due to a combination of tectonically and climatically controlled processes, are complex and still not fully understood.

7.2 Hydrogen stable isotopes from hydrated volcanic ashes

In addition to paleoenvironmental inferences based on surface uplift and associated climate change in intermontane basins along the eastern Puna-Plateau margin in NW Argentina, this thesis has provided new insights into Mio-Pleistocene paleo-atmospheric conditions using hydrogen stable isotope compositions of hydrated glass from volcanic ashes intercalated in clastic sedimentary basin sequences. In addition, this study highlights the need to compare high-elevation stable isotope data from the Puna Plateau with coeval datasets from sections obtained along the plateau margin to better understand paleoenvironmental change within the orogen interior.

Hydrogen stable isotope measurements on volcanic glass have been used for some time now to reconstruct paleoenvironmental conditions in a variety of settings (e.g., Friedman *et al.*, 1992, 1993a,b). More recent applications of this paleo-climate and paleo-elevation proxy have dealt with the topographic history of the Sierra Nevada in western North America (Mulch *et al.*, 2008; Cassel *et al.*, 2012, 2014). In South America δD_g values from the Altiplano Plateau in Peru suggest the attainment of modern elevations by about 16 Ma (Saylor & Horton, 2014), ca. 6 Myr earlier than proposed for regions farther east in the Bolivian Altiplano (Garzione *et al.*, 2006, 2008). In contrast, Insel *et al.* (2012b) have shown that simulated changes of $\delta^{18}O$ (or δD) values do not systematically follow surface elevations, but are rather a function of threshold elevations that cause abrupt climate change. Therefore, rapid and dramatic change

in stable isotope composition derived from orogenic plateau regions may also represent a response to gradual surface uplift.

Dettinger (2013) and Dettinger & Quade (2015) tested the validity of δD_g as a proxy for paleoelevations in NW Argentina between ca. 23 and 27° S and confirmed the empirical glass-water fractionation equation of (Friedman *et al.*, 1993a), which translates hydrogen-glass compositions into the equivalent of its parent meteoric water. Canavan *et al.* (2014) presented a δD_g record from late Eocene to Pleistocene volcanic ash deposits on the southern Puna Plateau and inferred the existence of high topography, similar to modern elevations, throughout this time interval. However, this is in contrast to previous findings that suggest that the onset of the South American low-level jet, as an integral part of the South American Monsoon system, is associated with the development of at least 50% of modern elevations (~2,000 m) along the present-day Puna-Plateau margin at about 8 to 10 Ma (Lenters & Cook, 1997; Ehlers & Poulsen, 2009; Poulsen *et al.*, 2010; Mulch *et al.*, 2010). Other problems in interpreting stable isotope records for paleoaltimetric purposes in the Andean plateau realm of that age is that the source water cannot be sufficiently identified at the moment, nor can burial heating be excluded. Carrapa *et al.* (2014) report δD_g data from the plateau-bounding, intermontane Angastaco Basin at about 25° S. Based on their limited data they infer that this basin attained its current elevation of ca. 2,000 m by at least 10 to 6 Ma. However, an alternative interpretation to this inference is suggested in Chapter 6, based on additional δD_g results from the same basin and adjacent foreland sectors. The new data suggest that until about 7 Ma the Angastaco basin and other basins to the south were at similar elevations compared to the foreland regions to the east. Moreover, this study of paleo-records suggests that changing atmospheric patterns and daily heat storage within large intermontane basins interfered with hydrogen stable-isotope compositions via modulating the general style of rainfall (convective vs. adiabatic) along the eastern Puna Plateau margin. This finding is supported by recently obtained data on the modern distribution of stable-isotope compositions across this region, which is fundamentally impacted by convective processes (Rohrmann *et al.*, 2014). Interestingly, north of 25° S, however, such problems currently do not seem to hamper the interpretation of hydrogen stable isotopes (Rohrmann *et al.*, 2014), which is why, negative changes in δD_g in the Humahuaca Basin may be interpreted as a gain in surface elevations.

The stable isotope-based findings presented in this study were mainly derived from intermontane basins within the Eastern Cordillera and the broken foreland provinces east of the Puna Plateau. To decipher aspects of landscape evolution in these areas this is an adequate approach, because isotopic signals of rainfall produced by the ascent of moisture-bearing winds along the foothills of the Andes, generally correlate well with elevations at which rainfall occurs (Rohrmann *et al.*, 2014; Dettinger & Quade, 2015, this study). Effects on the composition of meteoric waters from the adjacent hinterland can thus be well associated with surface uplift and orographic barrier formation. However, in light of spatial differences in isotope compositions shown in this study and current debates on the timing and style of uplift as well

as the mechanisms driving plateau uplift, it is problematic to simply extrapolate information on tectono-sedimentary and paleoenvironmental changes obtained from hydrogen stable isotopes in the investigated regions into the plateau interior. Likewise, it appears questionable, whether the interpretation of equivalent datasets from the plateaus alone can provide quantitatively useful information on paleoelevations and/or climate change, when windward processes along the margin impact the stable isotope composition of the remaining moisture on the plateau (e.g., Blisniuk & Stern, 2005). Hence, future studies should strive to compare stable-isotope ratios from the eastern plateau margin with those from the plateau interior. With this approach it may be eventually possible to better understand how strongly changes in moisture supply along the plateau margins affect isotope compositions in the orogen interior, and consequently, what the remaining variations in δD_g may tell us about paleoenvironmental change on the plateau.

References

Aceñolaza, F. G., 2003. The Cambrian system in northwestern Argentina: Stratigraphical and palaeontological framework. Geologica Acta 1 (1), 22–39.

Allmendinger, R. W., Gubbels, T., 1996. Pure and simple shear plateau uplift, Altiplano-Puna, Argentina and Bolivia. Tectonophysics 259 (1-3), 1–13.

Allmendinger, R. W., Jordan, T. E., Kay, S. M., Isacks, B. L., 1997. The evolution of the Altiplano-Puna plateau of the Central Andes. Annual Review of Earth and Planetary Sciences 25 (1), 139–174.

Allmendinger, R. W., Ramos, V. A., Jordan, T. E., Palma, M., Isacks, B. L., 1983. Paleogeography and Andean structural geometry, northwest Argentina. Tectonics 2 (1), 1–16.

Allmendinger, R. W., Zapata, T. R., 2000. The footwall ramp of the Subandean decollement, northernmost Argentina, from extended correlation of seismic reflection data. Tectonophysics 321 (1), 37–55.

Alonso, R. N., Bookhagen, B., Carrapa, B., Coutand, I., Haschke, M., Hilley, G. E., Schoenbohm, L., Sobel, E. R., Strecker, M. R., Trauth, M. H., Villanueva, A., 2006. Tectonics, climate, and landscape evolution of the southern Central Andes: The argentine Puna Plateau and adjacent regions between 22 and 30° S. In: Oncken, O., Chong, G., Franz, G., Giese, P., Götze, H.-J., Ramos, V. A., Strecker, M. R., Wigger, P. (Eds.), The Andes - Active Subduction Orogeny. Springer Berlin Heidelberg, pp. 265–283.

Alonso, R. N., Jordan, T. E., Tabbutt, K. T., Vandervoort, D. S., 1991. Giant evaporite belts of the Neogene central Andes. Geology 19 (4), 401–404.

Andersen, T., 2002. Correction of common lead in U–Pb analyses that do not report ^{204}Pb. Chemical Geology 192 (1-2), 59–79.

Arancibia, G., Matthews, S. J., de Arce, C. P., 2006. K–Ar and 40Ar/39Ar Geochronology of supergene processes in the Atacama Desert, northern Chile: Tectonic and climatic relations. Journal of the Geological Society 163 (1), 107–118.

Baker, P. A., Fritz, S. C., Dick, C. W., Eckert, A. J., Horton, B. K., Manzoni, S., Ribas, C. C., Garzione, C. N., Battisti, D. S., 2014. The emerging field of geogenomics: Constraining geological problems with genetic data. Earth Science Reviews 135, 38–47.

Baldis, B. A. J., Gorrono, A., Ploszkiewicz, J. V., Sarudiansky, R. M., 1976. Geotectónica de la Cordillera Oriental, Sierras Subandinas y comarcas adyacentes. In: VI Congreso Geológico Argentino. pp. 3–22.

Barnes, J. B., Ehlers, T. A., 2009. End member models for Andean Plateau uplift. Earth Science Reviews 97 (1-4), 105–132.

Beaumont, C., 1981. Foreland basins. Geophysical Journal of the Royal Astronomical Society 65 (2), 291–329.

Bevis, M., Isacks, B. L., 1984. Hypocentral trend surface analysis: Probing the geometry of Benioff Zones. Journal of Geophysical Research 89, 6153–6170.

Bianchi, A. R., Yañez, C. E., 1992. Las precipitaciones en el Noroeste Argentino. Tech. rep., Estacion Experimental Agropecuaria Salta, Argentina.

Bianucci, H., Homovc, J., 1982. Tectogénesis de un sector de la cuenca del Subgrupo Pirgua, Noroeste Argentina. In: V Congreso Latinoamericano Geológico. pp. 539–546.

Bissig, T., Riquelme, R., 2010. Earth and Planetary Science Letters. Earth and Planetary Science Letters 299 (3-4), 447–457.

Blair, T. C., McPherson, J. G., 1994. Alluvial fans and their natural distinction from rivers based on morphology, hydraulic processes, sedimentary processes, and facies assemblages. Journal of Sedimentary Research 64A (3), 450–489.

Blisniuk, P. M., Stern, L. A., 2005. Stable isotope paleoaltimetry: A critical review. American Journal of Science 305 (10), 1033–1074.

Blisniuk, P. M., Stern, L. A., Chamberlain, C. P., Idleman, B., Zeitler, P. K., 2005. Climatic and ecologic changes during Miocene surface uplift in the Southern Patagonian Andes. Earth and Planetary Science Letters 230 (1-2), 125–142.

Blisniuk, P. M., Stern, L. A., Chamberlain, C. P., Zeitler, P. K., Ramos, V. A., Sobel, E. R., Haschke, M., Strecker, M. R., Warkus, F., 2006. Links between Mountain Uplift, Climate, and Surface Processes in the Southern Patagonian Andes. In: Oncken, O., Chong, G., Franz, G., Giese, P., Götze, H.-J., Ramos, V. A., Strecker, M. R., Wigger, P. (Eds.), The Andes - Active Subduction Orogeny. Springer Berlin Heidelberg, pp. 429–440.

Bobst, A. L., Lowenstein, T. K., Jordan, T. E., Godfrey, L. V., Ku, T. L., Luo, S., 2001. A 106 ka paleoclimate record from drill core of the Salar de Atacama, northern Chile. Palaeogeography, Palaeoclimatology, Palaeoecology 173 (1), 21–42.

Boll, A., Hernández, R. M., 1986. Interpretación estructural del área Tres Cruces. Boletín de Informaciones Petroleras 7, 2–14.

Bona, P., Starck, D., Galli, C., Gasparini, Z., Reguero, M., 2013. Caiman cf. Latirostris (Alligatoridae, Caimaninae) in the late Miocene Palo Pintado Formation, Salta province, Argentina: paleogeographic and paleoenvironmental considerations. Ameghiniana 51 (1), 25–36.

Bookhagen, B., Burbank, D. W., 2006. Topography, relief, and TRMM-derived rainfall variations along the Himalaya. Geophysical Research Letters 33 (L08405).

Bookhagen, B., Burbank, D. W., 2010. Toward a complete Himalayan hydrological budget: Spatiotemporal distribution of snowmelt and rainfall and their impact on river discharge. Journal of Geophysical Research 115 (F03019).

Bookhagen, B., Haselton, K. R., Trauth, M. H., 2001. Hydrological modelling of a Pleistocene landslide-dammed lake in the Santa María Basin, NW Argentina. Palaeogeography, Palaeoclimatology, Palaeoecology 169 (1), 113–127.

Bookhagen, B., Strecker, M. R., 2008. Orographic barriers, high-resolution TRMM rainfall, and relief variations along the eastern Andes. Geophysical Research Letters 35 (L06403).

Bookhagen, B., Strecker, M. R., 2012. Spatiotemporal trends in erosion rates across a pronounced rainfall gradient: Examples from the southern Central Andes. Earth and Planetary Science Letters 327-328 (C), 97–110.

Bosio, P. P., Powell, J., Papa, C. d., Hongn, F., 2009. Middle Eocene deformation-sedimentation in the Luracatao Valley: Tracking the beginning of the foreland basin of northwestern Argentina. Journal of South American Earth Sciences 28 (2), 142–154.

Bossi, G. E., Georgieff, S. M., Gavriloff, I., Ibaņez, L. M., Muruaga, C. M., 2001. Cenozoic evolution of the intramontane Santa María basin, Pampean Ranges, northwestern Argentina. Journal of South American Earth Sciences 14 (7), 725–734.

Bourdon, B., Wörner, G., Zindler, A., 2000. U-series evidence for crustal involvement and magma residence times in the petrogenesis of Parinacota volcano, Chile. Contributions To Mineralogy And Petrology 139 (4), 458–469.

Burbank, D. W., Bookhagen, B., Gabet, E. J., Putkonen, J., 2012. Modern climate and erosion in the Himalaya. Comptes Rendus Geosciences 344 (11-12), 610–626.

Butler, R. F., Marshall, L. G., Drake, R. E., Curtis, G. H., 1984. Magnetic polarity stratigraphy and 40K/40Ar dating of Late Miocene and Early Pliocene continental deposits. Catamarca Province, NW Argentina. The Journal of Geology 92 (6), 623–636.

Bywater-Reyes, S., Carrapa, B., Clementz, M., Schoenbohm, L., 2010. Effect of late Cenozoic aridification on sedimentation in the Eastern Cordillera of northwest Argentina (Angastaco basin). Geology 38 (3), 235–238.

Cahill, T., Isacks, B. L., Whitman, D., Chatelain, J.-L., Perez, A., Chiu, J. M., 1992. Seismicity and tectonics in Jujuy Province, northwestern Argentina. Tectonics 11 (5), 944–959.

Canavan, R. R., Carrapa, B., Clementz, M. T., Quade, J., DeCelles, P. G., Schoenbohm, L. M., 2014. Early Cenozoic uplift of the Puna Plateau, Central Andes, based on stable isotope paleoaltimetry of hydrated volcanic glass. Geology 42 (5), 447–450.

Carrapa, B., Adelmann, D., Hilley, G. E., Mortimer, E., Sobel, E. R., Strecker, M. R., 2005. Oligocene range uplift and development of plateau morphology in the southern central Andes. Tectonics 24 (TC4011).

Carrapa, B., Hauer, J., Schoenbohm, L., Strecker, M. R., Schmitt, A. K., Villanueva, A., Sosa Gomez, J., 2008. Dynamics of deformation and sedimentation in the northern Sierras Pampeanas: An integrated study of the Neogene Fiambala basin, NW Argentina. Geological Society of America Bulletin 120 (11-12), 1518–1543.

Carrapa, B., Huntington, K. W., Clementz, M., Quade, J., Bywater-Reyes, S., Schoenbohm, L. M., Canavan, R. R., 2014. Uplift of the Central Andes of NW Argentina associated with upper crustal shortening, revealed by multi-proxy isotopic analyses. Tectonics 33, 1039–1054.

Carrapa, B., Strecker, M. R., Sobel, E. R., 2006. Cenozoic orogenic growth in the Central Andes: Evidence from sedimentary rock provenance and apatite fission track thermochronology in the Fiambala Basin, southernmost Puna Plateau margin (NW Argentina). Earth and Planetary Science Letters 247 (1-2), 82–100.

Carrapa, B., Trimble, J. D., Stockli, D. F., 2011. Patterns and timing of exhumation and deformation in the Eastern Cordillera of NW Argentina revealed by (U–Th)/He thermochronology. Tectonics 30 (TC3003).

Carrera, N., Muñoz, J., 2008. Thrusting evolution in the southern Cordillera Oriental (northern Argentine Andes): Constraints from growth strata. Tectonophysics 459 (1-4), 107–122.

Carrera, N., Muñoz, J. A., Sabat, F., Mon, R., Roca, E., 2006. The role of inversion tectonics in the structure of the Cordillera Oriental (NW Argentinean Andes). Journal of Structural Geology 28 (11), 1921–1932.

Cassel, E. J., Breecker, D. O., Henry, C. D., Larson, T. E., Stockli, D. F., 2014. Profile of a paleo-orogen: High topography across the present-day Basin and Range from 40 to 23 Ma. Geology 42 (11), 1007–1010.

Cassel, E. J., Graham, S. A., Chamberlain, C., 2009. Cenozoic tectonic and topographic evolution of the northern Sierra Nevada, California, through stable isotope paleoaltimetry in volcanic glass. Geology 37 (6), 547–550.

Cassel, E. J., Graham, S. A., Chamberlain, C., Henry, C. D., 2012. Early Cenozoic topography, morphology, and tectonics of the northern Sierra Nevada and western Basin and Range. Geosphere 8 (2), 229–249.

Castellanos, A., 1950. El Uquiense, sedimentos neógenos de Uquía (Senador Perez) en la Provincia de Jujuy (Argentina). Serie Técnico Científico. Facultad de Ciencias Matemáticas Físicas y Químicas y Naturales de la Universidad Nacional del Litoral, Rosario, Argentina.

Cerling, T. E., Harris, J. M., Macfadden, B. J., Leakey, M. G., Quade, J., Eisenmann, V., Ehleringer, J. R., 1997. Global vegetation change through the Miocene/Pliocene boundary : Article : Nature. Nature 389 (6647), 153–158.

Chamberlain, C., Mix, H. T., Mulch, A., Hren, M. T., Kent-Corson, M. L., Davis, S. J., Horton, T. W., Graham, S. A., 2012. The Cenozoic climatic and topographic evolution of the western North American Cordillera. American Journal of Science 312 (2), 213–262.

Chamberlain, C., Poage, M., 2000. Reconstructing the paleotopography of mountain belts from the isotopic composition of authigenic minerals. Geology 28 (2), 115–118.

Chamberlain, C. P., Poage, M., Craw, D., Reynolds, R., 1999. Topographic development of the Southern Alps recorded by the isotopic composition of authigenic clay minerals, South Island, New Zealand. Chemical Geology 155 (3-4), 279–294.

Clapperton, C. M., 2004. Glaciation in Bolivia before 3.27 Myr. Nature 277 (5695), 375–377.

Cottle, J. M., 2014. In-situ U–Th/Pb geochronology of (urano)thorite. American Mineralogist 99 (10), 1985–1995.

Cottle, J. M., Burrows, A. J., Kylander-Clark, A., Freedman, P. A., Cohen, R. S., 2013. Enhanced sensitivity in laser ablation multi-collector inductively coupled plasma mass spectrometry. Journal of Analytical Atomic Spectrometry 28 (11), 1700–1706.

Coughlin, T., O'Sullivan, P., Kohn, B. P., Holcombe, R., 1998. Apatite fission-track thermochronology of the Sierras Pampeanas, central western Argentina; implications for the mechanism of plateau uplift in the Andes. Geology 26 (11), 999–1002.

Coutand, I., Carrapa, B., Deeken, A., Schmitt, A. K., Sobel, E. R., Strecker, M. R., 2006. Propagation of orographic barriers along an active range front: Insights from sandstone petrography and detrital apatite fission-track thermochronology in the intramontane Angastaco basin, NW Argentina. Basin Research 18 (1), 1–26.

Coutand, I., Cobbold, P. R., de Urreiztieta, M., Gautier, P., Chauvin, A., Gapais, D., Rossello, E. A., López-Gamundí, O., 2001. Style and history of Andean deformation, Puna plateau, northwestern Argentina. Tectonics 20 (2), 210–234.

Craig, H., 1961. Isotopic Variations in Meteoric Waters. Science 133 (3465), 1702–1703.

Cristallini, E. O., Cominguez, A. H., Ramos, V., 1997. Deep structure of the Metan-Guachipas region: Tectonic inversion in northwestern Argentina. Journal of South American Earth Sciences 10 (5), 403–421.

Crowley, J. L., Schoene, B., Bowring, S. A., 2007. U–Pb dating of zircon in the Bishop Tuff at the millennial scale. Geology 35 (12), 1123–1126.

Dahlen, F. A., 1990. Critical taper model of fold-and-thrust belts and accretionary wedges. Annual Reviews in Earth and Planetary Sciences 18, 55–99.

Dansgaard, W., 1964. Stable isotopes in precipitation. Tellus 16 (4), 436–468.

Davis, S. J., Mulch, A., Carroll, A. R., Horton, T. W., Chamberlain, C. P., 2009. Paleogene landscape evolution of the central North American Cordillera: Developing topography and hydrology in the Laramide foreland. Geological Society of America Bulletin 121 (1/2), 100–116.

DeCelles, P. G., Carrapa, B., Horton, B. K., Gehrels, G. E., 2011. Cenozoic foreland basin system in the central Andes of northwestern Argentina: Implications for Andean geodynamics and modes of deformation. Tectonics 30 (TC6013).

DeCelles, P. G., Giles, K. A., 1996. Foreland basin systems. Basin Research 8 (2), 105–123.

Deeken, A., Sobel, E. R., Coutand, I., Haschke, M., Riller, U., Strecker, M. R., 2006. Development of the southern Eastern Cordillera, NW Argentina, constrained by apatite fission track thermochronology: From early Cretaceous extension to middle Miocene shortening. Tectonics 25 (TC6003).

Deeken, A., Sobel, E. R., Haschke, M., Riller, U., 2005. Age of initiation and growth pattern of the Puna plateau, NW-Argentina, constrained by AFT thermochronology. 19th Colloquium on Latin American Geosciences, Abstract Volume Terra Nostra 5 (1), 39.

Deeken, A., Sobel, E. R., Haschke, M., Strecker, M. R., Riller, U., 2004. Age of initiation and growth pattern of the Puna plateau, NW-Argentina, constrained by AFT thermochtonology. In: 10th International Conference on FT Dating and Thermochronology, 8-15 August. Amsterdam, Netherlands, Electronic abstract volume, TEC-17-P.

Del Papa, C., Hongn, F., Powell, J., Payrola, P., Do Campo, M., Strecker, M. R., Petrinovic, I. A., Schmitt, A. K., Pereyra, R., 2013. Middle Eocene-Oligocene broken-foreland evolution in the Andean Calchaqui Valley, NW Argentina: Insights from stratigraphic, structural and provenance studies. Basin Research, 1–20.

Dettinger, M. P., 2013. Calibrating and testing the volcanic glass paleoaltimeter in South America. MSc Thesis, University of Arizona, Arizona, U.S.A.

Dettinger, M. P., Quade, J., 2015. Testing the analytical protocols and calibration of volcanic glass for the reconstruction of hydrogen isotopes in paleoprecipitation. In: Decelles, P. G., Ducea, M. N., Carrapa, B., Kapp, P. A. (Eds.), Geodynamics of a Cordilleran Orogenic System: The Central Andes of Argentina and Northern Chile. Geological Society of America Memoirs, pp. 261–276.

Díaz, J. I., Malizzia, D. C., 1984. Estudio geolgico y sedimentolgico del Terciario superior del Valle Calchaquí (Dpto. San Carlos; Salta). Boletín Sedimentológico 2 (1), 8–28.

Dunn, J. F., Hartshorn, K. G., Hartshorn, P. W., 1995. Structural Styles and Hydrocarbon Potential of the Sub-Andean Thrust Belt of Southern Bolivia. In: Tankard, A. J., Suarez-Soruco, R., Welsink, H. J. (Eds.), Petroleum Basins of South America. AAPG Memoirs, pp. 523–543.

Durand, F. R., Rossi, J. N., 1999. Metamorfismo del sector noroeste de las Cumbres Calchaquíes, sierra de san javier y serranías del noroeste de Tucumán. In: Bonorino, G. G., Omarini, R., Viramonte, J. (Eds.), Geología del Noroeste Argentino. Relatorio del XIV Congreso Geológico Argentino. Salta, pp. 52–57.

Echavarría, L., Hernandez, R., Allmendinger, R. W., Reynolds, J., 2003. Subandean thrust and fold belt of northwestern Argentina: Geometry and timing of the Andean evolution. AAPG Bulletin 87 (6), 965–985.

Ehlers, T. A., Poulsen, C. J., 2009. Influence of Andean uplift on climate and paleoaltimetry estimates. Earth and Planetary Science Letters 281 (3-4), 238–248.

England, P., Molnar, P., 1990. Surface uplift, uplift of rocks, and exhumation of rocks. Geology 18 (12), 1173–1177.

Ernst, W. G., 2010. Young convergent-margin orogens, climate, and crustal thickness–A Late Cretaceous-Paleogene Nevadaplano in the American Southwest? Lithosphere 2 (2), 67–75.

Farley, K. A., Wolf, R. A., Silver, L. T., 1996. The effects of long alpha-stopping distances on (U-Th)/He ages. Geochimica et Cosmochimica Acta 60 (21), 4223–4229.

Fleck, R. J., Sutter, J. F., Elliot, D. H., 1977. Interpretation of discordant $^{40}Ar/^{39}Ar$ age-spectra of Mesozoic tholeiites from Antarctica. Geochimica et Cosmochimica Acta 41 (1), 15–32.

Francis, P., de Silva, S. L., 1989. Application of the Landsat Thematic Mapper to the identification of potentially active volcanoes in the Central Andes. Remote Sensing of Environment 28, 245–255.

Friedman, I., Gleason, J., Sheppard, R. A., Gude, A. J., 1993a. Deuterium fractionation as water diffuses into silicic volcanic ash. In: Swart, P. K., Lohmann, K. C., McKenzie, J., Savin, S. (Eds.), Climate Change in Continental Isotopic Records. American Geophysical Union, Washington D.C., U.S.A., pp. 321–323.

Friedman, I., Gleason, J., Warden, A., 1993b. Ancient climate from deuterium content of water in volcanic glass. In: Swart, P. K., Lohmann, K. C., McKenzie, J., Savin, S. (Eds.), Climate Change in Continental Isotopic Records. American Geophysical Union, Washington D.C., U.S.A., pp. 309–319.

Friedman, I., Gleason, J., Wilcox, R., 1992. Modeling of ancient climate from deuterium content of water in volcanic glass. Quaternary International 13/14, 201–203.

Gabet, E., Burbank, D. W., Pratt-Sitaula, B., Putkonen, J., Bookhagen, B., 2008. Modern erosion rates in the High Himalayas of Nepal. Earth and Planetary Science Letters 267 (3-4), 482–494.

Galewsky, J., 2009. Rain shadow development during the growth of mountain ranges: An atmospheric dynamics perspective. Journal of Geophysical Research 114 (F01018).

Galli, C. I., Coira, B., Alonso, R. N., Reynolds, J. H., Matteini, M., Hauser, N., 2014. Tectonic controls on the evolution of the Andean Cenozoic foreland basin: Evidence from fluvial system variations in the Payogastilla Group, in the Calchaquí, Tonco and Amblayo Valleys, NW Argentina. Journal of South American Earth Sciences 52 (C), 234–259.

Galli, I. C., Hernández, R. M., Reynolds, J. H., 1996. Análisis paleoambiental y ubicación geocronológica del Subgrupo Metán (Grupo Orán, Neógeno) en el río Piedras, Departamento Metán, Salta, Argentina. Boletín de Informaciones Petroleras, Tercera Serie 12 (46), 98–107.

Galliski, M. A., Viramonte, J. G., 1988. The Cretaceous paleorift in northwestern Argentina: a petrologic approach. Journal of South American Earth Sciences 1 (4), 329–342.

Garcia-Castellanos, D., 2007. The role of climate during high plateau formation. Insights from numerical experiments. Earth and Planetary Science Letters 257 (3-4), 372–390.

Garreaud, R., Vuille, M., Clement, A. C., 2003. The climate of the Altiplano: observed current conditions and mechanisms of past changes. Palaeogeography, Palaeoclimatology, Palaeoecology 194 (1-3), 5–22.

Garreaud, R. D., 1999. Multiscale analysis of the summertime precipitation over the Central Andes. Monthly Weather Review 127 (5), 901–921.

Garzione, C. N., Dettman, D., Horton, B. K., 2004. Carbonate oxygen isotope paleoaltimetry: evaluating the effect of diagenesis on paleoelevation estimates for the Tibetan plateau. Palaeogeography, Palaeoclimatology, Palaeoecology 212 (1-2), 119–140.

Garzione, C. N., Hoke, G. D., Libarkin, J. C., Withers, S., MacFadden, B., Eiler, J., Ghosh, P., Mulch, A., 2008. Rise of the Andes. Science 320 (5881), 1304–1307.

Garzione, C. N., Molnar, P., Libarkin, J. C., MacFadden, B. J., 2006. Rapid late Miocene rise of the Bolivian Altiplano: Evidence for removal of mantle lithosphere. Earth and Planetary Science Letters 241 (3-4), 543–556.

Garzione, C. N., Quade, J., Decelles, P. G., English, N. B., 2000. Predicting paleoelevation of Tibet and the Himalaya from δ^{18}O vs. altitude gradients in meteoric water across the Nepal Himalaya. Earth and Planetary Science Letters 183 (1-2), 215–229.

Gébelin, A., Mulch, A., Teyssier, C., Jessup, M. J., Law, R. D., Brunel, M., 2013. The Miocene elevation of Mount Everest. Geology 41 (7), 799–802.

Gebhard, J. A., Guidice, A. R., Gascon, J. O., 1974. Geología de la comarca entre el Río Juramento y Arroyo las Tortugas, provincias de Salta y Jujuy, República Argentina. Revista Asociación Geológica Argentina 29, 359–375.

Gile, L. H., Peterson, F. F., Grossman, R. B., 1965. The K horizon: A master soil horizon of carbonate accumulation. Soil Science 99, 74–82.

Gonfiantini, R., 1984. Internal report on an advisory group meeting on stable isotope reference samples for geochemical and hydrological investigations. International Atomic Energy Agency, 77p.

González Bonorino, G., del Valle Abascal, L., 2012. Drainage and base-level adjustments during evolution of a late Pleistocene piggyback basin, Eastern Cordillera, Central Andes of northwestern Argentina. Geological Society of America Bulletin 124 (11-12), 1858–1870.

Gonzalez Villa, R. E., 2002. El subgrupo Jujuy (Neogeno) entre los 24° - 26° LS y 64° - 66° LO, tramo cento austral de la cadena subandina Argentina, provincias de Salta y Jujuy. PhD Thesis, Universidad Nacional de Salta, Salta, Argentina.

Gregory-Wodzicki, K., 2000. Uplift history of the Central and Northern Andes: a review. Geological Society of America Bulletin 112 (7), 1091–1105.

Grier, M. E., 1990. The influence of the Cretaceous Salta rift basin on the development of Andean structural geometries, NW Argentine Andes. PhD Thesis, Cornell University, Ithaca, NY, U.S.A.

Grier, M. E., Dallmeyer, R. D., 1990. Age of the Payogastilla Group: Implications for foreland basin development, NW Argentina. Journal of South American Earth Sciences 3 (4), 269–278.

Grier, M. E., Salfity, J. A., Allmendinger, R. W., 1991. Andean reactivation of the Cretaceous Salta rift, northwestern Argentina. Journal of South American Earth Sciences 4 (4), 351–372.

Grove, M., Jacobson, C. E., Barth, A. P., Vucic, A., 2003. Temporal and spatial trends of Late Cretaceous-early Tertiary underplating of Pelona and related schist beneath southern California and southwestern Arizona. In: Johnson, S. E., Paterson, S. R., Fletcher, J. M., Girty, G. H., Kimbrough, D. L., Martin-Barajas, A. (Eds.), Tectonic evolution of northwestern México and the southwestern USA. Geological Society of America Special Papers 374, Boulder, Colorado, pp. 381–406.

Gubbels, T. L., Isacks, B. L., Farrar, E., 1993. High-level surfaces, plateau uplift, and foreland development, Bolivian central Andes. Geology 21, 695–698.

Hain, M. P., 2008. Neogene foreland evolution of the southern Central Andes and its relationship to ancient strain history and varying climates - an integrated approach. Diploma Thesis, Potsdam University, Potsdam, Germany.

Hain, M. P., Strecker, M. R., 2008. Control of Cretaceous extensional and inherited basement structures on position and style of Andean shortening - a case study from the valle de Lerma, Salta, NW Argentina. In: XVII Congreso Geológico Argentino. pp. 23–24.

Hain, M. P., Strecker, M. R., Bookhagen, B., Alonso, R. N., Pingel, H., Schmitt, A. K., 2011. Neogene to Quaternary broken foreland formation and sedimentation dynamics in the Andes of NW Argentina (25° S). Tectonics 30 (TC2006).

Haines, P. W., Hand, M., Sandiford, M., 2001. Palaeozoic synorogenic sedimentation in central and northern Australia: a review of distribution and timing with implications for the evolution of intracontinental orogens. Australian Journal of Earth Sciences 48 (6), 911–928.

Halama, R., Konrad-Schmolke, M., Sudo, M., Marschall, H. R., Wiedenbeck, M., 2014. Effects of fluid–rock interaction on $^{40}Ar/^{39}Ar$ geochronology in high-pressure rocks (Sesia-Lanzo Zone, Western Alps). Geochimica et Cosmochimica Acta 126, 475–494.

Haselton, K., Hilley, G., Strecker, M. R., 2002. Average Pleistocene climatic patterns in the southern Central Andes: Controls on mountain glaciation and paleoclimate implications. The Journal of Geology 110 (2), 211–226.

Hernández, R. M., Jordan, T. E., Farjat, A. D., Echavarría, L., Idleman, B. D., Reynolds, J. H., 2005. Age, distribution, tectonics, and eustatic controls of the Paranense and Caribbean marine transgressions in southern Bolivia and Argentina. Journal of South American Earth Sciences 19 (4), 495–512.

Hess, J. C., Lippolt, H. J., 1994. Compilation of K-Ar measurements on HD-B1 standard biotite 1994 status report. In: Odin, G. S. (Ed.), Phanerozoic time scale, Bulletin of Liaison and Informatics, IGCP project 196. Vol. 196. pp. 19–23.

Hetzel, R., Hampel, A., 2005. Slip rate variations on normal faults during glacial – interglacial changes in surface loads. Nature 435 (7038), 81–84.

Hilley, G., Coutand, I., 2009. Links between topography, erosion, rheological heterogeneity, and deformation in contractional settings: Insights from the central Andes. Tectonophysics 495 (2010), 78–92.

Hilley, G. E., Strecker, M. R., 2005. Processes of oscillatory basin filling and excavation in a tectonically active orogen: Quebrada del Toro Basin, NW Argentina. Geological Society of America Bulletin 117 (7-8), 887–901.

Hoke, G. D., Garzione, C. N., 2008. Paleosurfaces, paleoelevation, and the mechanisms for the late Miocene topographic development of the Altiplano plateau. Earth and Planetary Science Letters 271 (1-4), 192–201.

Hoke, G. D., Giambiagi, L. B., Garzione, C. N., Mahoney, J. B., Strecker, M. R., 2014a. Neogene paleoelevation of intermontane basins in a narrow, compressional mountain range, southern Central Andes of Argentina. Earth and Planetary Science Letters 406 (C), 153–164.

Hoke, G. D., Liu-Zeng, J., Hren, M. T., Wissink, G. K., Garzione, C. N., 2014b. Stable isotopes reveal high southeast Tibetan Plateau margin since the Paleogene. Earth and Planetary Science Letters 394 (C), 270–278.

Holton, J. R., 1992. An introduction to dynamic meteorology, 3rd Edition. International geophysics series. Academic Press, San Diego, New York.

Hongn, F. D., DelPapa, C., Powell, J., Petrinovic, I., Mon, R., Deraco, V., 2007. Middle Eocene deformation and sedimentation in the Puna-Eastern Cordillera transition (23°-26° S): Control by preexisting heterogeneities on the pattern of initial Andean shortening. Geology 35 (3), 271–274.

Hongn, F. D., Mon, R., Petrinovic, I. A., Del Papa, C. E., 2008. Inversión tectónica en el Noroeste Argentino: Influencia de las heterogeneidades del basamento. In: XVII Congreso Geológico Argentino. pp. 25–26.

Hongn, F. D., Mon, R., Petrinovic, I. A., Del Papa, C. E., Powell, J. E., 2010. Inversión y reactivación tectónicas cretácicocenozoicas en el Noroeste Argentino: influencia de las heterogeneidades del basamento neoproterozoico-paleozoico inferior. Revista Asociación Geológica Argentina 66 (1-2), 38–53.

Hongn, F. D., Riller, U., 2007. Tectonic evolution of the western margin of Gondwana inferred from syntectonic emplacement of paleozoic granitoid plutons in Northwest Argentina. The Journal of Geology 115 (2), 163–180.

Hoorn, C., Wesselingh, F. P., Ter Steege, H., Bermudez, M. A., Mora, A., Sevink, J., Sanmartin, I., Sanchez-Meseguer, A., Anderson, C. L., Figueiredo, J. P., Jaramillo, C., Riff, D., Negri, F. R., Hooghiemstra, H., Lundberg, J., Stadler, T., Sarkinen, T., Antonelli, A., 2010. Amazonia Through Time: Andean Uplift, Climate Change, Landscape Evolution, and Biodiversity. Science 330 (6006), 927–931.

Horton, B. K., DeCelles, P. G., 2001. Modern and ancient fluvial megafans in the foreland basin system of the central Andes, southern Bolivia: Implications for drainage network evolution in fold-thrust belts. Basin Research 13 (1), 43–63.

Howard, K. A., John, B. E., 1997. Fault-related folding during extension: Plunging basement-cored folds in the Basin and Range. Geology 25 (3), 223–226.

Hynek, S., 2011. Mio-Pliocene geology of the southern Puna plateau margin, Argentina. PhD Thesis, University of Utah, Salt Lake City, Utah, U.S.A.

Hynek, S. A., Passey, B. H., Prado, J. L., Brown, F. H., Cerling, T. E., Quade, J., 2012. Small mammal carbon isotope ecology across the Miocene–Pliocene boundary, northwestern Argentina. Earth and Planetary Science Letters 321-322, 177–188.

IAEA, W., 2013. Global Network of Isotopes in Precipitation. Tech. rep.
URL http://www.iaea.org/water

IAEA, W., 2015. Global Network of Isotopes in Precipitation. Tech. rep.
URL http://www.iaea.org/water

Insel, N., Grove, M., Haschke, M., Barnes, J. B., Schmitt, A. K., Strecker, M. R., 2012a. Paleozoic to early Cenozoic cooling and exhumation of the basement underlying the eastern Puna plateau margin prior to plateau growth. Tectonics 31 (TC6006).

Insel, N., Poulsen, C. J., Ehlers, T. A., 2009. Influence of the Andes mountains on South American moisture transport, convection, and precipitation. Climate Dynamics 35 (7-8), 1477–1492.

Insel, N., Poulsen, C. J., Ehlers, T. A., Sturm, C., 2012b. Response of meteoric δ^{18}O to surface uplift-Implications for Cenozoic Andean Plateau growth. Earth and Planetary Science Letters 317-318, 262–272.

Isacks, B. L., 1988. Uplift of the Central Andean plateau and bending of the Bolivian orocline. Journal of Geophysical Research 93 (B4), 3211–3231.

Ishizuka, O., 1998. Vertical and horizontal variations of the fast neutron flux in a single irradiation capsule and their significance in the laser-heating ^{40}Ar/^{39}Ar analysis: Case study for the hydraulic rabbit facility of the JMTR reactor, Japan. Geochemical Journal 32, 243–252.

Jackson, S. E., Pearson, N. J., Griffin, W. L., Belousova, E. A., 2004. The application of laser ablation-inductively coupled plasma-mass spectrometry to in situ U–Pb zircon geochronology. Chemical Geology 211 (1-2), 47–69.

James, D. E., 1971. Plate tectonic model for the evolution of the Central Andes. Geological Society of America Bulletin 82 (12), 3325–3346.

Janecke, S. U., Vandenburg, C. J., Blankenau, J. J., 1998. Geometry, mechanisms and significance of extensional folds from examples in the Rocky Mountain Basin and Range province, U.S.A. Journal of Structural Geology 20 (7), 841–856.

Ježek, P., Willner, A. P., Aceñolaza, F. G., Miller, H., 1985. The Puncoviscana trough — a large basin of Late Precambrian to Early Cambrian age on the pacific edge of the Brazilian shield. International Journal of Earth Sciences (Geol.Rundschau) 74 (3), 573–584.

Jordan, T. E., Allmendinger, R. W., 1986. The Sierras Pampeanas of Argentina: A modern analogue of Rocky Mountain foreland deformation. American Journal of Science 286 (10), 737–764.

Jordan, T. E., Alonso, R. N., 1987. Cenozoic stratigraphy and basin tectonics of the Andes mountains, 20°-28° S. AAPG Bulletin 71 (1), 49–64.

Jordan, T. E., Isacks, B. L., Allmendinger, R. W., Brewer, J. A., Ramos, V. A., Ando, C. J., 1983. Andean tectonics related to geometry of subducted Nazca plate. Geological Society of America Bulletin 94 (3), 341–361.

Kay, S. M., Coira, B., Viramonte, J., 1994. Young mafic back arc volcanic rocks as indicators of continental lithospheric delamination beneath the Argentine Puna Plateau, central Andes. Journal of Geophysical Research 99 (B12), 24323–24339.

Kent-Corson, M. L., Sherman, L., Mulch, A., Chamberlain, C. P., 2006. Cenozoic topographic and climatic response to changing tectonic boundary conditions in Western North America. Earth and Planetary Science Letters 252 (3-4), 453–466.

Kleinert, K., Strecker, M. R., 2001. Climate change in response to orographic barrier uplift: Paleosol and stable isotope evidence from the late Neogene Santa Maria basin, northwestern Argentina. Geological Society of America Bulletin 113 (6), 728–742.

Kley, J., 1996. Transition from basement-involved to thin-skinned thrusting in the Cordillera Oriental of southern Bolivia. Tectonics 15 (4), 763–775.

Kley, J., Gangui, A. H., Krüger, D., 1996. Basement-involved blind thrusting in the eastern Cordillera Oriental, southern Bolivia: evidence from cross-sectional balancing, gravimetric and magnetotelluric data. Tectonophysics 259 (1), 171–184.

Kley, J., Monaldi, C. R., 2002. Tectonic inversion in the Santa Barbara System of the central Andean foreland thrust belt, northwestern Argentina. Tectonics 21 (6), 1061.

Kley, J., Müller, J., Tawackoli, S., Jacobshagen, V., Manutsoglu, E., 1997. Pre-Andean and Andean-age deformation in the Eastern Cordillera of southern Bolivia. Journal of South American Earth Sciences 10 (1), 1–19.

Kley, J., Rossello, E. A., Monaldi, C. R., Habighorst, B., 2005. Seismic and field evidence for selective inversion of Cretaceous normal faults, Salta rift, northwest Argentina. Tectonophysics 399 (1-4), 155–172.

Koch, P. L., 1998. Isotopic reconstruction of past continental environments. Annual Reviews in Earth and Planetary Sciences 26 (1), 573–613.

Kraemer, B., Adelmann, D., Alten, M., Schnurr, W., 1999. Incorporation of the Paleogene foreland into the Neogene Puna plateau: The Salar de Antofalla area, NW Argentina. Journal of South American Earth Sciences 12 (2), 157–182.

Lal, D., Harris, N. B. W., Sharma, K. K., Gu, Z., Ding, L., Liu, T., Dong, W., Caffee, M. W., Jull, A. J. T., 2003. Erosion history of the Tibetan Plateau since the last interglacial: constraints from the first studies of cosmogenic 10Be from Tibetan bedrock. Earth and Planetary Science Letters 217 (1-2), 33–42.

Latorre, C., Quade, J., McIntosh, W. C., 1997. The expansion of C4 grasses and global change in the late Miocene: stable isotope evidence from the Americas. Earth and Planetary Science Letters 146, 83–96.

Leier, A. L., DeCelles, P. G., Pelletier, J. D., 2005. Mountains, monsoons, and megafans. Geology 33 (4), 289–292.

Lenters, J., Cook, K. L., 1997. On the origin of the Bolivian high and related circulation features of the South American climate. Journal of the Atmospheric Sciences 54 (5), 656–678.

Letcher, A. J., 2007. Deformation history of the Susques basin (~23° S, 66° W), Puna Plateau, NW Argentina: New constraints by apatite (U–Th)/He thermochronology and $^{40}Ar/^{39}Ar$ geochronology, and implications for plateau formation in the central Andes. MSc Thesis, Stanford University, CA, U.S.A.

Löbens, S., Sobel, E. R., Bense, F. A., Wemmer, K., Dunkl, I., Siegesmund, S., 2013. Refined exhumation history of the northern Sierras Pampeanas, Argentina. Tectonics 32 (3), 453–472.

Machette, M. N., 1985. Calcic soils of the southwestern United States. Geological Society of America Special Papers 203, 1–22.

Malamud, B. D., Jordan, T. E., Alonso, R. A., Gallardo, E. F., 1996. Pleistocene Lake Lerma, Salta Province, NW Argentina. In: XIII Congreso Geológico Argentino. pp. 103–116.

Marquillas, R. A., del Papa, C., Sabino, I. F., 2005. Sedimentary aspects and paleoenvironmental evolution of a rift basin: Salta Group (Cretaceous-Paleogene), northwestern Argentina. International Journal of Earth Sciences 94 (1), 94–113.

Marquillas, R. A., Salfity, J. A., 1988. Tectonic framework and correlations of the cretaceous-ecocene salta group; Argentina. In: Bahlburg, H., Breitkreuz, C., Giese, P. (Eds.), Lecture Notes in Earth Sciences. Springer Berlin Heidelberg, pp. 119–136.

Marrett, R. A., Allmendinger, R. W., Alonso, R. N., Drake, R. E., 1994. Late Cenozoic tectonic evolution of the Puna Plateau and adjacent foreland, northwestern Argentine Andes. Journal of South American Earth Sciences 7, 179–207.

Marrett, R. A., Strecker, M. R., 2000. Response of intracontinental deformation in the central Andes to late Cenozoic reorganization of South American Plate motions. Tectonics 19 (3), 452–467.

Marshak, S., Karlstrom, K., Timmons, J. M., 2000. Inversion of Proterozoic extensional faults: An explanation for the pattern of Laramide and Ancestral Rockies intracratonic deformation, United States. Geology 28 (8), 735–738.

Marshall, L. G., Butler, R. F., Drake, R. E., Curtis, G. H., 1982. Geochronology of type Uquian (late Cenozoic) land mammal age, Argentina. Science 216, 986–989.

Marshall, L. G., Hoffster, R., Pascual, R., 1983. Mammals and stratigraphy: geochronology of the continental mammal-bearing Tertiary of South America. Palaeovertebrata: Mémoire extraordinaire. Laboratoire de paléontologie des vertébrés de l'Ecole pratique des hautes études, Montpellier, France.

Masek, J., Isacks, B. L., Gubbels, T. L., Fielding, E., 1994. Erosion and tectonics at the margins of continental plateaus. Journal of Geophysical Research 99 (B7), 13941–13956.

Mazzuoli, R., Vezzoli, L., Omarini, R., Acocella, V., Gioncada, A., Matteini, M., Dini, A., Guillou, H., Hauser, N., Uttini, A., 2008. Miocene magmatism and tectonics of the easternmost sector of the Calama–Olacapato–El Toro fault system in Central Andes at ~24° S: Insights into the evolution of the Eastern Cordillera. Geological Society of America Bulletin 120 (11-12), 1493–1517.

McPherson, H. M., 2008. Climate and tectonic controls on sedimentation and deformation in the Fiambalá Basin of the southern Puna Plateau, northwest Argentina. MSc Thesis, Ohio State University, Columbus, OH, U.S.A.

McQuarrie, N., 2002. The kinematic history of the central Andean fold-thrust belt, Bolivia: Implications for building a high plateau. Geological Society of America Bulletin 114 (8), 950–963.

McQuarrie, N., Ehlers, T. A., Barnes, J. B., Meade, B., 2008. Temporal variation in climate and tectonic coupling in the central Andes. Geology 36 (12), 999–1002.

Meade, B., Conrad, C., 2008. Andean growth and the deceleration of South American subduction: Time evolution of a coupled orogen-subduction system. Earth and Planetary Science Letters 275 (1-2), 93–101.

Merrihue, C., Turner, G., 2012. Potassium-argon dating by activation with fast neutrons. Journal of Geophysical Research 71 (11), 2852–2857.

Meyer, B., Tapponnier, P., Bourjot, L., Metivier, F., Gaudemer, Y., Peltzer, G., Shunmin, G., Zhitai, C., 1998. Crustal thickening in Gansu-Qinghai, lithospheric mantle subduction, and oblique, strike-slip controlled growth of the Tibet plateau. Geophysical Journal International 135 (1), 1–47.

Mix, H. T., Mulch, A., Kent-Corson, M. L., Chamberlain, C. P., 2011. Cenozoic migration of topography in the North American Cordillera. Geology 39 (1), 87–90.

Molnar, P., England, P., 1990. Late Cenozoic uplift of mountain ranges and global climate change: chicken or egg? Nature 346 (6279), 29–34.

Mon, R., Hongn, F. D., 1991. The structure of the Precambrian and Lower Paleozoic Basement of the Central Andes between 22° and 32° S Lat. International Journal of Earth Sciences (Geol.Rundschau) 80 (3), 745–758.

Mon, R., Salfity, J. A., 1995. Tectonic evolution of the Andes of northern Argentina. In: Tankard, A. J., Suarez-Soruco, R., Welsink, H. J. (Eds.), Petroleum Basins of South America. AAPG Memoirs, pp. 269–283.

Monaldi, C. R., Gonzalez, R. E., Salfity, J. A., 1996. Thrust fronts in the Lerma valley (Salta, Argentina) during the Piquete Formation deposition (Pliocene-Pleistocene). 3rd International Symposium on Andean Geodynamics, St. Malo, France, 447–450.

Montero-López, C., Strecker, M. R., Schildgen, T. F., Hongn, F. D., Guzmán, S., Bookhagen, B., Sudo, M., 2014. Local high relief at the southern margin of the Andean plateau by 9 Ma: evidence from ignimbritic valley fills and river incision. Terra Nova 26 (6), 454–460.

Montgomery, D. R., Balco, G., Willett, S. D., 2001. Climate, tectonics, and the morphology of the Andes. Geology 29 (7), 579–582.

Mora, A., Gaona, T., Kley, J., Montoya, D., Parra, M., Quiroz, L. I., Reyes, G., Strecker, M. R., 2009. The role of inherited extensional fault segmentation and linkage in contractional orogenesis: a reconstruction of Lower Cretaceous inverted rift basins in the Eastern Cordillera of Colombia. Basin Research 21 (1), 111–137.

Mora, A., Parra, M., Strecker, M. R., Kammer, A., Dimaté, C., Rodríguez, F., 2006. Cenozoic contractional reactivation of Mesozoic extensional structures in the Eastern Cordillera of Colombia. Tectonics 25 (TC2010).

Mortimer, E., Carrapa, B., Coutand, I., Schoenbohm, L., Sobel, E. R., Gomez, J. S., Strecker, M. R., 2007. Fragmentation of a foreland basin in response to out-of-sequence basement uplifts and structural reactivation: El Cajón–Campo del Arenal basin, NW Argentina. Geological Society of America Bulletin 119 (5-6), 637–653.

Moya, M. C., 1988. Lower Ordovician in the southern part of the argentine Eastern Cordillera. In: Bahlburg, H., Breitkreuz, C., Giese, P. (Eds.), The Southern Central Andes. Springer, Berlin, Germany, pp. 55–69.

Mulch, A., Chamberlain, C., 2007. Stable Isotope Paleoaltimetry in Orogenic Belts The Silicate Record in Surface and Crustal Geological Archives. Reviews in Mineralogy and Geochemistry 66 (1), 89–118.

Mulch, A., Graham, S. A., Chamberlain, C. P., 2006. Hydrogen isotopes in Eocene river gravels and paleoelevation of the Sierra Nevada. Science 313 (5783), 87–89.

Mulch, A., Sarna-Wojcicki, A. M., Perkins, M. E., Chamberlain, C., 2008. A Miocene to Pleistocene climate and elevation record of the Sierra Nevada (California). Proceedings of the National Academy of Sciences 105 (19), 6819–6824.

Mulch, A., Teyssier, C., Cosca, M. A., Chamberlain, C. P., 2007. Stable isotope paleoaltimetry of Eocene core complexes in the North American Cordillera 26 (4).

Mulch, A., Teyssier, C., Cosca, M. A., Vanderhaeghe, O., Vennemann, T. W., 2004. Reconstructing paleoelevation in eroded orogens. Geology 32 (6), 525.

Mulch, A., Uba, C. E., Strecker, M. R., Schoenberg, R., Chamberlain, C. P., 2010. Late Miocene climate variability and surface elevation in the Central Andes. Earth and Planetary Science Letters 290 (1-2), 173–182.

Nishiizumi, K., Caffee, M. W., Finkel, R. C., Brimhall, G., Mote, T., 2005. Remnants of a fossil alluvial fan landscape of Miocene age in the Atacama Desert of northern Chile using cosmogenic nuclide exposure age dating. Earth and Planetary Science … 237, 499–507.

Omarini, R. H., 1983. Caracterización Litológica, Diferencíon y Génesis de la Formación Puncoviscana entre el Valle de Lerma y la Faja Eruptiva de la Puna. PhD Thesis, Universidad Nacional de Salta, Salta, Argentina.

Owen, J. J., Amundson, R., Dietrich, W. E., Nishiizumi, K., Sutter, B., Chong, G., 2010. The sensitivity of hillslope bedrock erosion to precipitation. Earth Surface Processes and Landforms 36 (1), 117–135.

Paces, J. B., Miller, J. D., 1993. Precise U–Pb ages of Duluth complex and related mafic intrusions, northeastern Minnesota - geochronological insights to physical, petrogenetic, paleomagnetic, and tectonomagmatic processes associated with the 1.1 Ga mid-continent rift system. Journal of Geophysical Research 98 (B8), 13,997–14,013.

Parra, M., Mora, A., Jaramillo, C., Strecker, M. R., Sobel, E. R., Quiroz, L., Rueda, M., Torres, V., 2009a. Orogenic wedge advance in the northern Andes: Evidence from the Oligocene-Miocene sedimentary record of the Medina Basin, Eastern Cordillera, Colombia. Geological Society of America Bulletin 121 (5-6), 780–800.

Parra, M., Mora, A., Sobel, E. R., Strecker, M. R., González, R., 2009b. Episodic orogenic front migration in the northern Andes: Constraints from low-temperature thermochronology in the Eastern Cordillera, Colombia. Tectonics 28 (TC4004).

Paton, C., Woodhead, J. D., Hellstrom, J. C., Hergt, J. M., Greig, A., Maas, R., 2010. Improved laser ablation U–Pb zircon geochronology through robust downhole fractionation correction. Geochemistry Geophysics Geosystems 11 (Q0AA06).

Pearson, D. M., Kapp, P. A., Reiners, P. W., Gehrels, G. E., Ducea, M. N., Pullen, A., Otamendi, J. E., Alonso, R. N., 2012. Major Miocene exhumation by fault-propagation folding within a metamorphosed, early Paleozoic thrust belt: Northwestern Argentina. Tectonics 31 (4), 1–24.

Penck, W., 1920. Der Südrand der Puna de Atacama (NW-Argentinien): Ein Beitrag zur Kenntnis des Andinen Gebirgstypus und zu der Frage der Gebirgsbildung. Vol. 37 of Abhandlungen der Sächsischen Akademie der Wissenschaften. B.G. Teubner, Leipzig.

Peters, N. A., Huntington, K. W., Hoke, G. D., 2013. Earth and Planetary Science Letters. Earth and Planetary Science Letters 361 (C), 208–218.

Petit, C., Fournier, M., Gunnell, Y., 2007. Tectonic and climatic controls on rift escarpments: Erosion and flexural rebound of the Dhofar passive margin (Gulf of Aden, Oman). Journal of Geophysical Research 112 (B03406).

Pingel, H., Alonso, R. N., Mulch, A., Rohrmann, A., Sudo, M., Strecker, M. R., 2014. Pliocene orographic barrier uplift in the southern Central Andes. Geology 42 (8), 691–694.

Pingel, H., Strecker, M. R., Alonso, R. N., Schmitt, A. K., 2013. Neotectonic basin and landscape evolution in the Eastern Cordillera of NW Argentina, Humahuaca Basin (~24° S). Basin Research 25, 554–573.

Placzek, C., Quade, J., Patchett, P. J., 2006. Geochronology and stratigraphy of late Pleistocene lake cycles on the southern Bolivian Altiplano: Implications for causes of tropical climate change. Geological Society of America Bulletin 118 (5-6), 515–532.

Placzek, C. J., Granger, D. E., Matmon, A., Quade, J., Ryb, U., 2015. Geomorphic process rates in the central Atacama Desert, Chile: Insights from cosmogenic nuclides and implications for the onset of hyperaridity. American Journal of Science 314 (10), 1462–1512.

Poulsen, C. J., Ehlers, T. A., Insel, N., 2010. Onset of convective rainfall during gradual late Miocene rise of the central Andes. Science 328 (5977), 490–493.

Pratt, J. R., Schoenbohm, L. M., Mortimer, E., Strecker, M. R., 2008. Basin Compartmentalization in the Foreland: El Cajon Basin, Southwestern Argentina. EOS, Transactions, American Geophysical Union 89 (53).

Prohaska, F., 1976. The climate of Argentina, Paraguay and Uruguay. In: Schwerdtfeger, W. (Ed.), Climates in Central and South America. Elsevier Amsterdam, pp. 13–112.

Quade, J., Dettinger, M. P., Carrapa, B., 2015. The growth of the central Andes, 22° S–26° S. In: DeCelles, P. G., Ducea, M. N., Carrapa, B., Kapp, P. A. (Eds.), Geodynamics of a Cordilleran Orogenic System: The Central Andes of Argentina and Northern Chile. Geological Society of America Memoirs, pp. 1–33.

Quade, J., Garzione, C. N., Eiler, J., 2007. Paleoelevation reconstruction using pedogenic carbonates. Reviews in Mineralogy and Geochemistry 66 (1), 53–87.

Ramos, V., Alonso, R. N., 1995. El Mar Paranense en la provincia de Jujuy. Revista del Instituto de Geología y Minería 10, 73–80.

Ramos, V., Alonso, R. N., Strecker, M. R., 2006. Estructura y neotectónica de Las Lomas de Olmedo, zona de transición entre los Sistemas Subandino y de Santa Bárbara, Provincia de Salta. Revista Asociación Geológica Argentina 61 (4), 579–588.

Ramos, V. A., 1988. Tectonics of the Late Proterozoic-Early Paleozoic: a collisional history of southern South America. Episodes 11 (3), 168–174.

Ramos, V. A., 2008. The Basement of the Central Andes: The Arequipa and Related Terranes. Annual Reviews in Earth and Planetary Sciences 36 (1), 289–324.

Ramos, V. A., Cristallini, E. O., Pérez, D., 2002. The Pampean flat-slab of the Central Andes. Journal of South American Earth Sciences 15 (1), 59–78.

Rasmussen, K. L., Houze, Jr., R. A., 2011. Orogenic convection in subtropical South America as seen by the TRMM satellite. Monthly Weather Review 139 (8), 2399–2420.

Rech, J. A., Currie, B. S., Michalski, G., Cowan, A. M., 2006. Neogene climate change and uplift in the Atacama Desert, Chile. Geology 34 (9), 761–764.

Reguero, M. A., Candela, A. M., 2008. Bioestratigrafía de las secuencias neógenas tardías de la Quebrada de Humahuaca, provincia de Jujuy. In: XVII Congreso Geológico Argentino. pp. 286–296.

Reguero, M. A., Candela, A. M., Alonso, R. N., 2007. Biochronology and biostratigraphy of the Uquía Formation (Pliocene–early Pleistocene, NW Argentina) and its significance in the Great American Biotic Interchange. Journal of South American Earth Sciences 23 (1), 1–16.

Reid, M. R., Coath, C. D., Mark Harrison, T., McKeegan, K. D., 1997. Prolonged residence times for the youngest rhyolites associated with Long Valley Caldera: ^{230}Th-^{238}U ion microprobe dating of young zircons. Earth and Planetary Science Letters 150 (1-2), 27–39.

Reiners, P. W., 2005. Zircon (U-Th)/He thermochronometry. Reviews in Mineralogy and Geochemistry 58 (1), 151–179.

Reiners, P. W., Brandon, M. T., 2006. Using thermochronology to understand orogenic erosion. Annual Reviews in Earth and Planetary Sciences 34 (1), 419–466.

Reiners, P. W., Ehlers, T. A., Mitchell, S. G., Montgomery, D. R., 2003. Coupled spatial variations in precipitation and long-term erosion rates across the Washington Cascades. Nature 426 (6967), 645–647.

Reynolds, J. H., Galli, C. I., Hernández, R. M., Idleman, B. D., Kotila, J. M., Hilliard, R. V., Naeser, C. W., 2000. Middle Miocene tectonic development of the transition zone, Salta Province, northwest Argentina: Magnetic stratigraphy from the Metán Subgroup, Sierra de González. Geological Society of America Bulletin 112 (11), 1736–1751.

Reynolds, J. H., Hernández, R. M., Galli, C. I., Idleman, B. D., 2001. Magnetostratigraphy of the Quebrada La Porcelana section, Sierra de Ramos, Salta Province, Argentina: age limits for the Neogene Oran Group and uplift of the southern Sierras Subandinas. Journal of South American Earth Sciences 14 (7), 681–692.

Reynolds, J. H., Idleman, B. D., Hernández, R. M., Naeser, C. W., 1994. Preliminary chronostratigraphic constraints on neogene tectonic activity in the eastern cordillera and santa bárbara system, salta province, nw argentina. In: Geological Society of America Abstracts with Programs. Vol. 26. p. 503.

Richter, A., 2002. Provenance analysis of the San Felipe Formation (Pliocene) and Quaternary terrace gravels, Angastaco Basin, Calchaquí Valley, NW Argentina. SFB 267 deformation processes in the Andes, DFG progress report, Potsdam University, Potsdam, Germany.

Riller, U., Oncken, O., 2003. Growth of the central Andean Plateau by tectonic segmentation is controlled by the gradient in crustal shortening. The Journal of Geology 111 (3), 367–384.

Rivelli, F. R., Flores, E. M., 2009. Protección de márgenes en el río grande, tramo las quebradas trancas - Tilcara. In: Cuarto Simposio Regional sobre Hidráulica de Ríos. Salta, Argentina, pp. 1–4.

Robinson, R. A. J., Spencer, J. Q. G., Strecker, M. R., Richter, A., Alonso, R. N., 2005. Luminescence dating of alluvial fans in intramontane basins of NW Argentina. In: Harvey, A. M., Mather, A. E., Stokes, M. (Eds.), Alluvial Fans: Geomorphology, Sedimentology, Dynamics. Geological Society of London, London, pp. 153–168.

Rodríguez Fernández, R., Heredia, N., Seggiaro, R. E., González, M. A., 1999. Estructura andina de la Cordillera Oriental en el área de la Quebrada de Humahuaca, Provincia de Jujuy, NO de Argentina. Trabajos de Geología 21, 321–332.

Roe, G. H., 2005. Orographic precipitation. Annual Reviews in Earth and Planetary Sciences 33 (1), 645–671.

Roe, G. H., Montgomery, D. R., Hallet, B., 2002. Effects of orographic precipitation variations on the concavity of steady-state river profiles. Geology 30 (2), 143–146.

Rohrmann, A., Strecker, M. R., Bookhagen, B., Mulch, A., Sachse, D., Pingel, H., Alonso, R. N., Schildgen, T. F., Montero-López, C., 2014. Can stable isotopes ride out the storms? The role of convection for water isotopes in models, records, and paleoaltimetry studies in the central Andes. Earth and Planetary Science Letters 407, 187–195.

Rolleri, O. E., 1976. Sistema de Santa Bárbara. Una nueva provincia geológica argentina. In: VI Congreso Geológico Argentino. pp. 239–256.

Romatschke, U., Houze, R. A., 2010. Extreme Summer Convection in South America. Journal of Climate 23 (14), 3761–3791.

Romatschke, U., Houze, Jr., R. A., 2013. Characteristics of Precipitating Convective Systems Accounting for the Summer Rainfall of Tropical and Subtropical South America. Journal of Hydrometeorology 14 (1), 25–46.

Rowley, D., Pierrehumbert, R., Currie, B. S., 2001. A new approach to stable isotope-based paleoaltimetry: implications for paleoaltimetry and paleohypsometry of the High Himalaya since the Late Miocene. Earth and Planetary Science Letters 188 (1-2), 253–268.

Rowley, D. B., 2007. Stable isotope-based paleoaltimetry: theory and validation. Reviews in Mineralogy and Geochemistry 66 (1), 23–52.

Rowley, D. B., Garzione, C. N., 2007. Stable isotope-based paleoaltimetry. Annual Reviews in Earth and Planetary Sciences 35 (1), 463–508.

Ruíz Huídobro, O. J., 1968. Descripción geológica de la Hoja 7e, Salta: Provincias de Salta y Jujuy, carta geológico-económica de la República Argentina, escala 1:200,000. Boletín del Instituto Nacional de Geología y Minería (Argentina) 109, 1–46.

Russo, A., Serraiotto, A., 1978. Contribución al conocimiento de la estratigrafía terciaria en el noroeste argentino. In: VII Congreso Geológico Argentino. pp. 715–730.

Sachse, D., Billault, I., Bowen, G. J., Chikaraishi, Y., Dawson, T. E., Feakins, S. J., Freeman, K. H., Magill, C. R., McInerney, F. A., van der Meer, M. T. J., Polissar, P., Robins, R. J., Sachs, J. P., Schmidt, H.-L., Sessions, A. L., White, J. W. C., West, J. B., Kahmen, A., 2012. Molecular Paleohydrology: Interpreting the Hydrogen-Isotopic Composition of Lipid Biomarkers from Photosynthesizing Organisms. Annual Reviews in Earth and Planetary Sciences 40, 1–29.

Salfity, J. A., 1982. Evolución paleogeografica del grupo Salta (Cretácieo-Eogénico), Argentina. In: V Congreso Latinoamerican Geología. pp. 11–26.

Salfity, J. A., Brandán, E. M., Monaldi, C. R., Gallardo, E. F., 1984. Tectónica compresiva Cuaternaria en la Cordillera Oriental Argentina latitud de Tilcara (Jujuy). In: IX Congreso Geológico Argentino. pp. 427–434.

Salfity, J. A., Gallardo, E. F., Sastre, J. E., Esteban, J., 2004. El lago cuaternario de Angastaco, Valle Calchaquí, Salta. Revista Asociación Geológica Argentina 59 (2), 313–316.

Salfity, J. A., Monaldi, C. R., Guidi, F., Salas, R. J., 1998. Mapa geológico de la provincia de Salta, República Argentina. Servicio Geológico Minero Argentino.

Salfity, J. A., Monaldi, C. R., Marquillas, R. A., Gonzales, R. E., 1993. La inversion tectonica del Umbral de los Gallos en la cuenca del Grupo Salta durante la fase incaica. In: XII Congreso Geológico Argentino y II Congreso de Exploración de Hidrocarburos. pp. 200–210.

Sánchez, M. C., Marquillas, R. A., 2010. Facies y ambientes del grupo Salta (cretácico-paleógeno) en Tumbaya, Quebrada de Humahuaca, provincia de Jujuy. Revista Asociación Geológica Argentina 67 (3), 383–391.

Sánchez, M. C., Salfity, J. A., 1999. La cuenca cámbrica del Grupo Mesón en el Noroeste Argentino: Desarrollo estratigráfico y paleogeográfico. Actas del Geologica Hispanica 34 (2–3), 123–139.

Sancho, C., Pena, J. L., Rivelli, F., Rhodes, E., Munoz, A., 2008. Geomorphological evolution of the Tilcara alluvial fan (Jujuy Province, NW Argentina): Tectonic implications and paleoenvironmental considerations. Journal of South American Earth Sciences 26 (1), 68–77.

Saylor, J. E., Horton, B. K., 2014. Nonuniform surface uplift of the Andean plateau revealed by deuterium isotopes in Miocene volcanic glass from southern Peru. Earth and Planetary Science Letters 387 (C), 120–131.

Schildgen, T. F., Hodges, K. V., Whipple, K. X., Reiners, P. W., Pringle, M. S., 2007. Uplift of the western margin of the Andean plateau revealed from canyon incision history, southern Peru. Geology 35 (6), 523.

Schildgen, T. F., Yıldırım, C., Cosentino, D., Strecker, M. R., 2014. Linking slab break-off, Hellenic trench retreat, and uplift of the Central and Eastern Anatolian plateaus. Earth Science Reviews 128, 147–168.

Schmitt, A. K., de Silva, S. L., Trumbull, R. B., Emmermann, R., 2001. Magma evolution in the Purico ignimbrite complex, northern Chile: Evidence for zoning of a dacitic magma by injection of rhyolitic melts following mafic recharge. Contributions to Mineralogy and Petrology 140 (6), 680–700.

Schmitt, A. K., Grove, M., Harrison, T. M., Lovera, O., Hulen, J., Walters, M., 2003. The Geysers - Cobb Mountain Magma System, California (Part 1): U–Pb zircon ages of volcanic rocks, conditions of zircon crystallization and magma residence times. Geochimica et Cosmochimica Acta 67 (18), 3423–3442.

Schmitt, A. K., Stockli, D. F., Hausback, B. P., 2006. Eruption and magma crystallization ages of Las Tres Vírgenes (Baja California) constrained by combined $^{230}Th/^{238}U$ and (U–Th)/He dating of zircon. Journal of Volcanology and Geothermal Research 158 (3-4), 281–295.

Schmitt, A. K., Stockli, D. F., Lindsay, J. M., Robertson, R., Lovera, O. M., Kislitsyn, R., 2010. Episodic growth and homogenization of plutonic roots in arc volcanoes from combined U–Th and (U–Th)/He zircon dating. Earth and Planetary Science Letters 295 (1-2), 91–103.

Schoenbohm, L., Carrapa, B., Bywater, S., 2008. Climatic and tectonic controls on deposition of the Punaschotter conglomerate in Neogene marginal basins of the Puna Plateau (NW Argentina): Evidence from zircon U–Pb geochronology. In: AGU Fall Meeting. San Francisco, USA.

Schoenbohm, L. M., Carrapa, B., 2009. Structural evidence for lithospheric foundering in the Puna Plateau, NW Argentina. In: AGU Joint Assembly. Toronto, Ontario, Canada.

Schoenbohm, L. M., Carrapa, B., McPherson, H. M., Pratt, J. R., Bywater-Reyes, S., Mortimer, E., 2015. Climate and tectonics along the southern margin of the Puna Plateau, NW Argentina: Origin of the late Cenozoic Punaschotter conglomerates. In: Decelles, P. G., Ducea, M. N., Carrapa, B., Kapp, P. A. (Eds.), Geodynamics of a Cordilleran Orogenic System: The Central Andes of Argentina and Northern Chile. Geological Society of America Memoirs, pp. 251–260.

Schwarz, W. H., Trieloff, M., 2007. Intercalibration of ^{40}Ar-^{39}Ar age standards NL-25, HB3gr hornblende, GA1550, SB-3, HD-B1 biotite and BMus/2 muscovite. Chemical Geology 242 (1-2), 218–231.

Seluchi, M. E., Saulo, A. C., Nicolini, M., Satyamurty, P., 2003. The northwestern Argentinean low: A study of two typical events. Monthly Weather Review 131 (10), 2361–2378.

Sepulchre, P., Ramstein, G., Fluteau, F., Tiercelin, J.-J., Brunet, M., 2006. Tectonic uplift and eastern Africa aridification. Science 313 (5792), 1419–1423.

Shane, P., Ingraham, N., 2002. δD values of hydrated volcanic glass: A potential record of ancient meteoric water and climate in New Zealand. New Zealand Journal of Geology and Geophysics 45 (4), 453–459.

Sial, A. N., Ferreira, V. P., Toselli, A. J., Aceñolaza, F. G., Pimentel, M. M., Parada, M. A., Alonso, R. N., 2001. C and Sr isotopic evolution of carbonate sequences in NW Argentina: Implications for a probable Precambrian-Cambrian transition. Carbonates and Evaporites 16 (2), 141–152.

Siks, B. C., Horton, B. K., 2011. Growth and fragmentation of the Andean foreland basin during eastward advance of fold-thrust deformation, Puna plateau and Eastern Cordillera, northern Argentina. Tectonics 30 (TC6017).

Sobel, E. R., Dumitru, T. A., 1997. Thrusting and exhumation around the margins of the western Tarim basin during the India-Asia collision. Journal of Geophysical Research 102 (B3), 5043–5063.

Sobel, E. R., Hilley, G. E., Strecker, M. R., 2003. Formation of internally drained contractional basins by aridity-limited bedrock incision. Journal of Geophysical Research 108 (B7), 2344.

Sobel, E. R., Strecker, M. R., 2003. Uplift, exhumation and precipitation: Tectonic and climatic control of Late Cenozoic landscape evolution in the northern Sierras Pampeanas, Argentina. Basin Research 15 (4), 431–451.

Starck, D., Anzótegui, L. M., 2001. The late Miocene climatic change - persistence of a climatic signal through the orogenic stratigraphic record in northwestern Argentina. Journal of South American Earth Sciences 14 (7), 763–774.

Starck, D., Vergani, G., 1996. Desarrollo tecto-sedimentario del Cenozoico en el sur de la Provincia de Salta-Argentina. In: XIII Congreso Geológico Argentino. pp. 433–452.

Steer, P., Simoes, M., Cattin, R., Shyu, J. B. H., 2014. Erosion influences the seismicity of active thrust faults. Nature Communications 5 (5564).

Steiger, R. H., Jäger, E., 1977. Subcommission on geochronology: convention on the use of decay constants in geo- and cosmochronology. Earth and Planetary Science Letters 36, 359–362.

Strecker, M. R., Alonso, R. N., Bookhagen, B., Carrapa, B., Coutand, I., Hain, M. P., Hilley, G. E., Mortimer, E., Schoenbohm, L., Sobel, E. R., 2009. Does the topographic distribution of the central Andean Puna Plateau result from climatic or geodynamic processes? Geology 37 (7), 643–646.

Strecker, M. R., Alonso, R. N., Bookhagen, B., Carrapa, B., Hilley, G. E., Sobel, E. R., Trauth, M. H., 2007a. Tectonics and climate of the southern central Andes. Annual Reviews in Earth and Planetary Sciences 35, 747–787.

Strecker, M. R., Cerveny, P., Bloom, A. L., Malizia, D., 1989. Late Cenozoic tectonism and landscape development in the foreland of the Andes: Northern Sierras Pampeanas (26°-28° S), Argentina. Tectonics 8 (3), 517–534.

Strecker, M. R., Hilley, G. E., Bookhagen, B., Sobel, E. R., 2011. Structural, geomorphic, and depositional characteristics of contiguous and broken foreland basins: Examples from the eastern flanks of the Central Andes in Bolivia and NW Argentina. In: Busby, C., Azor, A. (Eds.), Tectonics of Sedimentary Basins: Recent Advances. Wiley-Blackwell, pp. 508–521.

Strecker, M. R., Marrett, R. A., 1999. Kinematic evolution of fault ramps and its role in development of landslides and lakes in the northwestern Argentine Andes. Geology 27 (4), 307–310.

Strecker, M. R., Mulch, A., Uba, C. E., Schmitt, A. K., Chamberlain, C. P., 2007b. Climate change in the southern central Andes at 8 Ma. Geochimica et Cosmochimica Acta 71 (15), A980.

Streit, R. L., Burbank, D. W., Strecker, M. R., Alonso, R. N., 2012. Neogene-Quaternary tectonics, sedimentation, and erosion in the Quebrada de Humahuaca and Casa Grande basins, intermontane Basins on the margin of the Puna Plateau (23-24° S), NW Argentina. In: AGU Fall Meeting. San Francisco, USA.

Sudo, M., Uto, K., Anno, K., Ishizuka, O., Uchiumi, S., 1998. SORI93 biotite: A new mineral standard for K-Ar dating. Geochemical Journal 32.

Talling, P. J., Lawton, T. F., Burbank, D. W., Hobbs, R. S., 1995. Evolution of latest Cretaceous–Eocene nonmarine deposystems in the Axhandle piggyback basin of central Utah. Geological Society of America Bulletin 107 (3), 297–315.

Tapponnier, P., Meyer, B., Avouac, J.-P., Peltzer, G., Gaudemer, Y., Guo, S., Xiang, H., Yin, K., Chen, Z., Cai, S., 1990. Active thrusting and folding in the Qilian Shan, and decoupling between upper crust and mantle in northeastern Tibet. Earth and Planetary Science Letters 97, 382–403.

Tchilinguirian, P., Pereyra, F. X., 2001. Geomorfología del sector Salinas Grandes-Quebrada de Humahuaca, provincia de Jujuy. Revista Asociación Geológica Argentina 56, 3–15.

Turner, J. C. M., 1960. Estratigrafía de la Sierra de Santa Victoria y adyacencias. Boletín Academia Nacional de Ciencias Córdoba 41 (2), 163–196.

Turner, J. C. M., 1970. The andes of northwestern Argentina. Geologische Rundschau 59 (3), 1028–1063.

Uba, C. E., Heubeck, C., Hulka, C., 2005. Facies analysis and basin architecture of the Neogene Subandean synorogenic wedge, southern Bolivia. Sedimentary Geology 180 (3-4), 91–123.

Uba, C. E., Kley, J., Strecker, M. R., Schmitt, A. K., 2009. Unsteady evolution of the bolivian Subandean thrust belt: The role of enhanced erosion and clastic wedge progradation. Earth and Planetary Science Letters 281 (3-4), 134–146.

Uba, C. E., Strecker, M. R., Schmitt, A. K., 2007. Increased sediment accumulation rates and climatic forcing in the central Andes during the late Miocene. Geology 35 (11), 979–982.

Uto, K., Ishizuka, O., Matsumoto, A., Kamioka, H., Togashi, S., 1997. Laser-heating $^{40}Ar/^{39}Ar$ dating system of the Geological Survey of Japan: System outline and preliminary results. Bulletin of the Geological Survey of Japan 48, 23–46.

Vandervoort, D. S., Jordan, T. E., Zeitler, P., Alonso, R. N., 1995. Chronology of internal drainage development and uplift, southern Puna plateau, argentine central Andes. Geology 23 (2), 145–148.

Vásquez, M., Altenberger, U., Romer, R. L., Sudo, M., Moreno-Murillo, J. M., 2010. Magmatic evolution of the Andean Eastern Cordillera of Colombia during the Cretaceous: Influence of previous tectonic processes. Journal of South American Earth Sciences 29 (2), 171–186.

Vera, C., Baez, J., Douglas, M., Emmanuel, C. B., Marengo, J., Meitin, J., Nicolini, M., Nogues-Paegle, J., Paegle, J., Penalba, O., 2006a. The South American low-level jet experiment. American Meteorological Society Bulletin 87 (1), 63–77.

Vera, C., Higgins, W., Amador, J., Ambrizzi, T., Garreaud, R., Gochis, D., Gutzler, D., Lettenmaier, D., Marengo, J., Mechoso, C. R., Nogues-Paegle, J., Dias, P. L. S., Zhang, C., 2006b. Toward a unified view of the American monsoon systems. Journal of Climate 19 (20), 4977–5000.

Vergani, G., Starck, D., 1988. Geología del Sur de la Provincia de Salta - Parte I: Estratigrafía y evolución tectosedimentaria del Cenozoico entre el Valle de Lerma. Report, Yacimientos Petrol Fiscales, Buenos Aires.

Vergani, G., Starck, D., 1989a. Aspectos estructurales del Valle de Lerma al sur de la ciudad de Salta. Boletín Informatica Petrologia, 2–9.

Vergani, G., Starck, D., 1989b. Geología del Sur de la Provincia de Salta - Parte II: Estratigrafía y evolución tectosedimentaria del Cenozoico entre el Valle Calchaquí y Metán, report, Yacimientos Petrol. Report, Yacimientos Petrol Fiscales, Buenos Aires.

Vezzoli, L., Acocella, V., Omarini, R., Mazzuoli, R., 2012. Miocene sedimentation, volcanism and deformation in the Eastern Cordillera (24.5° S, NW Argentina): tracking the evolution of the foreland basin of the Central Andes. Basin Research 24 (6), 637–663.

Vezzoli, L., Matteini, M., Hauser, N., Omarini, R., Mazzuoli, R., Acocella, V., 2009. Non-explosive magma–water interaction in a continental setting: Miocene examples from the Eastern Cordillera (central Andes; NW Argentina). Bulletin of Volcanology 71 (5), 509–532.

Villanueva Garcia, A., Ovejero, R., 1998. Procedencia de las arenitas de las formaciones San José y Las Arcas (Neógeno) en la localidad de Entre Ríos. Revista Asociación Geológica Argentina 53, 158–166.

Viramonte, J. G., Kay, S. M., Becchio, R., Escayola, M., Novitski, I., 1999. Cretaceous rift related magmatism in central-western South America. Journal of South American Earth Sciences 12 (2), 109–121.

Viramonte, J. G., Omarini, R. H., Araña Saavedra, V., Aparicio, A., García Cacho, A., Parica, C., 1984. Edad, genesis y mecanismos de erupción de las riolitas granatiferas de San Antionio de los Cobres, Privincia de Salta (Argentina). In: IX Congreso Geológico Argentino. pp. 216–233.

Viramonte, J. G., Reynolds, J. H., Del Papa, C. E., 1994. The Corte Blanco garnetiferous tuff: a distinctive late Miocene marker bed in northwestern Argentina applied to magnetic polarity stratigraphy in the Río Yacones, Salta .... Earth and Planetary Science Letters 121, 519–531.

Walther, A. M., Orgeira, M. J., Reguero, M. A., Verzi, D. H., Vilas, J., Alonso, R. N., Gallado, E., Kelly, S., Jordan, T. E., 1998. Estudio Paleomagnético, Paleontológico y Radimétrico de la Formación Uquía (Plio-Pleistoceno) en Esquina Blanca (Jujuy). In: X Congreso Latinoamericano de Geología y VI Congreso Nacional de Geología Económica. p. 77.

Wegmann, M. I., Riller, U., Hongn, F. D., Glodny, J., Oncken, O., 2008. Age and kinematics of ductile deformation in the Cerro Durazno area, NW Argentina: Significance for orogenic processes operating at the western margin of Gondwana during Ordovician – Silurian times. Journal of South American Earth Sciences 26 (1), 78–90.

Weir, J. T., Price, M., 2011. Andean uplift promotes lowland speciation through vicariance and dispersal in Dendrocincla woodcreepers. Molecular Ecology 20 (21), 4550–4563.

Whipple, K. X., Meade, B., 2006. Orogen response to changes in climatic and tectonic forcing. Earth and Planetary Science Letters 243 (1-2), 218–228.

Whitman, D., Isacks, B. L., Kay, S. M., 1996. Lithospheric structure and along-strike segmentation of the Central Andean Plateau: seismic Q, magmatism, flexure, topography and tectonics. Tectonophysics 259 (1-3), 29–40.

Wichura, H., Bousquet, R., Oberhänsli, R., Strecker, M. R., Trauth, M. H., 2010. Evidence for middle Miocene uplift of the East African Plateau. Geology 38 (6), 543–546.

Wiedenbeck, M., Alle, P., Corfu, F., Griffin, W. L., Meier, M., Oberli, F., Quadt, A. v., Roddick, J. C., Spiegel, W., 1995. Three natural zircon standards for U–Th–Pb, Lu–Hf, trace element and REE analyses. Geostandards newsletter 19 (1), 1–23.

Wilke, F. D. H., O'Brien, P. J., Gerdes, A., Timmerman, M. J., Sudo, M., Khan, M. A., 2010. The multistage exhumation history of the Kaghan Valley UHP series, NW Himalaya, Pakistan from U–Pb and $^{40}Ar/^{39}Ar$ ages. European Journal of Mineralogy 22 (5), 703–719.

Willett, S. D., 1999. Orogeny and orography: The effects of erosion on the structure of mountain belts. Journal of Geophysical Research 104 (B12), 28957–28981.

Wolfe, J. A., Schorn, H. E., Forest, C. E., Molnar, P., 1997. Paleobotanical Evidence for High Altitudes in Nevada During the Miocene. Science 276 (5319), 1672–1675.

Wolfe, M. R., Stockli, D. F., 2010. Zircon (U–Th)/He thermochronometry in the KTB drill hole, Germany, and its implications for bulk He diffusion kinetics in zircon. Earth and Planetary Science Letters 295 (1-2), 69–82.

Zachos, J., Pagani, M., Sloan, L., Thomas, E., Billups, K., 2001. Trends, rhythms, and aberrations in global climate 65 Ma to present. Science 292 (5517), 686–693.

Zachos, J. C., Dickens, G. R., Zeebe, R. E., 2008. An early Cenozoic perspective on greenhouse warming and carbon-cycle dynamics. Nature 451 (7176), 279–283.

Zeitler, P. K., Meltzer, A. S., Koons, P. O., Craw, D., Hallet, B., 2001. Erosion, Himalayan geodynamics, and the geomorphology of metamorphism. GSA Today 11, 4–9.

Zipser, E. J., Liu, C., Cecil, D. J., Nesbitt, S. W., Yorty, D. P., 2006. Where are the most intense thunderstorms on earth? Bull. Amer. Meteor. Soc. 87 (8), 1057–1071.

Appendix A

U–Pb zircon geochronology

Table A.1 – Summary of U–Pb zircon analytical data of volcanic ash samples in the Humahuaca Basin using CAMECA IMS 1270 ion microprobe at UCLA.

Sample/ grain	Analysis date	$^{238}U/^{206}Pb$	$^{238}U/^{206}Pb$ $\pm1\sigma$	$^{207}Pb/^{206}Pb$	$^{207}Pb/^{206}Pb$ $\pm1\sigma$	Level of Concordia	$^{204}Pb/^{206}Pb$ x 10^{-3}	$^{204}Pb/^{206}Pb$ $\pm1\sigma$ x 10^{-3}	$^{206}Pb/^{238}U$ age (Ma)	$^{206}Pb/^{238}U$ age $\pm1\sigma$ (Ma)	U (ppm)	U/ Th	UO^+/U^+	$^{206}Pb^*$ (%)		Weighted average $^{206}Pb/^{238}U$ age $\pm2\sigma$ (Ma)
Maimará Formation																
08HUM03 - S 23.7104° W 65.4741°																
1	Jul-09	1504.9	54.1	0.0611	0.0054	0.16	2.926	1.690	4.28	0.16	803	1.45	8.5	98.1	4.18	0.11
2	Jul-09	1464.1	68.6	0.0909	0.0107	0.12	11.170	6.339	4.24	0.21	289	2.70	8.5	94.3		MSWD = 0.68
3	Jul-09	1485.0	64.8	0.0589	0.0053	-0.04	n.d.	n.d.	4.34	0.19	873	1.25	8.3	98.4		
4	Jul-09	1426.3	69.8	0.0604	0.0066	0.50	2.670	1.569	4.52	0.22	921	2.04	8.3	98.2		
5	Jul-09	1594.9	59.5	0.0637	0.0049	0.33	1.690	1.122	4.03	0.15	1150	1.71	8.5	97.8		
6	Jul-09	1575.5	58.1	0.0583	0.0047	0.02	0.839	0.593	4.11	0.15	2036	2.00	8.5	98.4		
7	Jul-09	1619.7	86.6	0.0618	0.0084	0.32	5.106	2.556	3.97	0.22	772	1.27	8.3	98.0		
8	Jul-09	1526.3	78.0	0.0887	0.0092	0.33	8.550	4.284	4.08	0.22	436	2.65	8.3	94.6		
9	Jul-09	1581.3	61.0	0.0642	0.0064	-0.02	2.718	1.409	4.06	0.16	1298	1.49	8.3	97.7		
10	Jul-09	1486.3	63.6	0.0712	0.0056	-0.20	1.160	1.161	4.27	0.19	845	1.43	8.1	96.8		
08HUM05 - S 23.7000° W 65.4609°																
1	Jul-09	1099.9	29.3	0.0813	0.0017	-0.01	3.059	0.434	5.70	0.16	9506	7.55	8.8	95.5	† 4.21	0.14
2	Jul-09	650.6	41.4	0.0665	0.0088	0.42	5.370	3.104	9.73	0.64	206	1.66	8.4	97.4	†	MSWD = 1.1
3	Jul-09	1472.1	65.7	0.0643	0.0103	0.36	2.873	2.187	4.35	0.20	491	1.30	8.5	97.7		
4	Jul-09	1408.1	84.5	0.0630	0.0049	-0.08	1.904	1.100	4.57	0.28	1347	2.90	8.4	97.8		
5	Jul-09	1475.4	76.0	0.1143	0.0140	0.02	12.870	7.446	4.08	0.24	278	3.84	8.4	91.3		
6	Jul-09	178.2	12.2	0.7379	0.0060	-0.04	45.550	2.997	4.27	3.40	982	2.25	7.9	11.6		
7	Jul-09	1543.7	64.3	0.0630	0.0048	-0.34	4.079	1.878	4.18	0.18	922	2.46	8.6	97.8		
8	Jul-09	1455.4	63.3	0.0692	0.0059	-0.07	n.d.	n.d.	4.38	0.20	589	2.06	8.8	97.0		
9	Jul-09	1689.8	80.2	0.0727	0.0082	-0.17	7.527	3.469	3.77	0.19	564	1.60	8.9	96.6		
10	Jul-09	1528.1	55.8	0.0664	0.0070	-0.24	n.d.	n.d.	4.20	0.16	1039	2.36	8.5	97.4		
11	Jul-09	1107.3	49.9	0.0549	0.0042	0.07	5.476	2.072	5.84	0.26	888	1.77	8.2	98.9	†	
12	Jul-09	1144.2	74.8	0.0909	0.0119	0.05	5.891	4.172	5.40	0.38	321	2.58	7.7	94.3	†	
13	Jul-09	1442.6	63.5	0.0902	0.0111	-0.03	11.170	5.011	4.28	0.21	328	1.12	8.7	94.4		
14	Jul-09	1450.5	70.7	0.0780	0.0090	0.05	0.630	1.206	4.36	0.22	317	4.25	8.5	95.9		
08HUM06 - S 23.7001° W 65.4613°																
1	Jul-09	1265.8	65.4	0.0582	0.0079	0.29	6.528	3.958	5.09	0.27	361	1.23	8.1	98.5	4.82	0.15
2	Jul-09	219.3	8.6	0.6651	0.0166	-0.02	39.550	3.268	6.23	1.60	967	2.35	7.8	20.9		MSWD = 0.87
3	Jul-09	1271.3	49.5	0.0785	0.0053	0.05	2.305	1.116	4.85	0.20	1564	0.37	8.1	95.9		
4	Jul-09	1360.4	55.7	0.0567	0.0060	-0.15	2.685	2.045	4.76	0.20	476	2.56	8.5	98.6		
5	Jul-09	1398.4	58.7	0.0736	0.0081	0.15	5.689	2.756	4.50	0.20	674	0.82	8.1	96.5		
6	Jul-09	647.2	31.8	0.0598	0.0057	0.25	8.873	3.199	9.86	0.49	352	1.48	8.1	98.3	†	
7	Jul-09	1271.8	50.9	0.0511	0.0074	-0.15	1.712	1.713	5.12	0.21	407	1.83	9.0	99.4		
8	Jul-09	462.3	15.7	0.5512	0.0168	0.13	38.600	4.409	5.02	0.60	671	1.63	8.3	35.4		
9	Jul-09	1348.1	85.4	0.1090	0.0146	0.26	16.060	7.799	4.48	0.31	196	2.01	8.5	92.0		
10	Jul-09	1342.6	50.8	0.0687	0.0059	0.24	10.520	2.958	4.73	0.18	967	1.02	8.3	97.1		
11	Jul-09	268.6	16.7	0.6961	0.0152	-0.07	41.160	3.638	4.14	2.07	755	1.85	8.7	16.9		
12	Jul-09	767.5	42.0	0.0926	0.0153	0.32	7.683	5.443	7.97	0.48	108	1.36	9.0	94.1	†	
13	Jul-09	1287.8	55.1	0.0634	0.0047	-0.04	3.800	1.519	4.98	0.22	1362	2.23	8.3	97.8		
08HUM07 - S 23.7007° W 65.4625°																
1	Jul-09	1373.6	52.1	0.0805	0.0045	-0.13	4.404	1.700	4.58	0.18	1404	3.27	8.2	95.6	4.3	0.14
2	Jul-09	1509.2	46.9	0.0540	0.0038	0.09	n.d.	n.d.	4.33	0.13	1065	4.19	8.8	99.0		MSWD = 1.8
3	Jul-09	1415.2	59.5	0.0845	0.0098	0.09	n.d.	n.d.	4.41	0.20	604	1.35	8.3	95.1		
4	Jul-09	1405.5	54.9	0.1381	0.0066	0.06	12.640	2.823	4.14	0.18	1251	2.36	8.6	88.2		
5	Jul-09	1561.0	61.7	0.0567	0.0043	-0.12	2.053	1.244	4.16	0.16	1381	2.41	8.4	98.7		
6	Jul-09	1346.3	53.8	0.0677	0.0098	-0.29	n.d.	n.d.	4.75	0.20	496	3.55	8.4	97.2		
7	Jul-09	1401.1	51.0	0.0538	0.0051	0.08	2.332	1.547	4.64	0.17	849	1.82	8.4	99.0		
8	Jul-09	1564.5	79.8	0.0761	0.0115	0.34	12.520	6.506	4.06	0.22	275	4.19	8.5	96.2		
9	Jul-09	1460.7	69.6	0.0705	0.0074	0.00	5.094	3.078	4.37	0.21	541	2.90	8.2	96.9		
10	Jul-09	1627.6	77.9	0.0555	0.0050	-0.27	2.024	1.432	4.00	0.19	871	1.97	8.6	98.8		
11	Jul-09	1596.9	89.3	0.0927	0.0114	0.61	5.449	3.619	3.88	0.23	348	1.61	8.7	94.1		
12	Jul-09	1459.6	66.3	0.0686	0.0050	-0.21	3.733	1.868	4.39	0.20	1061	4.46	8.3	97.1		
13	Jul-09	1570.1	57.2	0.0551	0.0045	0.26	1.242	0.946	4.15	0.15	911	2.27	9.6	98.9		

(continued)

Sample/ grain	Analysis date	$^{238}U/^{206}Pb$	$^{238}U/^{206}Pb$ $\pm1\sigma$	$^{207}Pb/^{206}Pb$	$^{207}Pb/^{206}Pb$ $\pm1\sigma$	Level of Concordia	$^{204}Pb/^{206}Pb$ x 10^{-3}	$^{204}Pb/^{206}Pb$ $\pm1\sigma$ x 10^{-3}	$^{206}Pb/^{238}U$ age (Ma)	$^{206}Pb/^{238}U$ age (Ma) $\pm1\sigma$	U (ppm)	U/ Th	UO^+/U^+	$^{206}Pb^*$ (%)		Weighted average $^{206}Pb/^{238}U$ age $\pm2\sigma$ (Ma)	
09HUM12 - S 23.5913° W 65.4229°																	
1	Jul-09	759.9	27.6	0.0462	0.0031	-0.21	n.d.	n.d.	8.56	0.31	866	1.84	8.2	100.0	†	5.79	0.19
2	Jul-09	47.6	2.0	0.7922	0.0029	0.00	56.280	1.885	6.33	7.77	1029	1.83	7.9	4.6	†		MSWD = 1.9
3	Jul-09	1098.5	42.1	0.0565	0.0081	0.15	0.772	0.772	5.88	0.23	862	2.97	8.3	98.7			
4	Jul-09	1056.9	37.6	0.0547	0.0043	-0.01	1.018	0.775	6.11	0.22	1129	1.69	8.4	98.9			
5	Jul-09	508.6	20.9	0.4903	0.0151	0.25	34.530	3.814	5.57	0.59	764	2.41	8.2	43.2			
6	Jul-09	1042.5	41.0	0.0516	0.0041	0.08	1.416	0.818	6.23	0.24	1377	3.87	8.2	99.3			
7	Jul-09	1025.5	61.1	0.0893	0.0067	0.01	3.822	1.445	6.03	0.38	1173	3.05	9.4	94.5			
8	Jul-09	1020.7	38.0	0.0622	0.0027	-0.08	12.380	1.987	6.26	0.24	1985	1.47	8.4	97.9	†		
9	Jul-09	1148.6	39.1	0.0509	0.0030	-0.04	0.391	0.391	5.67	0.19	1928	2.29	8.5	99.4			
10	Jul-09	1076.8	32.0	0.0494	0.0017	-0.04	0.654	0.273	6.05	0.18	5970	2.88	8.4	99.6		5.79	0.19
11	Jul-09	197.3	8.2	0.6458	0.0147	-0.03	41.340	2.479	7.67	1.83	1251	0.87	8.0	23.3	†		MSWD = 1.9
12	Jul-09	1036.7	41.2	0.0549	0.0048	0.13	0.685	0.685	6.24	0.25	878	3.77	8.3	98.9	†		
13	Jul-09	844.6	36.3	0.2680	0.0123	-0.28	14.990	2.123	5.56	0.38	1820	3.89	8.3	71.6			
14	Jul-09	972.8	36.9	0.0835	0.0034	-0.07	2.707	1.207	6.41	0.25	1871	4.37	8.2	95.2	†		
15	Jul-09	1166.5	41.2	0.0535	0.0029	-0.06	0.350	0.351	5.57	0.20	1685	3.99	8.5	99.1			
16	Jul-09	1244.4	46.9	0.0535	0.0050	0.08	1.490	1.054	5.23	0.20	725	3.47	8.9	99.1			
17	Jul-09	729.4	24.0	0.0506	0.0021	-0.04	0.810	0.420	8.88	0.29	2129	5.96	8.4	99.4	†		
18	Jul-09	1122.8	35.9	0.0539	0.0031	-0.18	0.309	0.309	5.77	0.19	2027	2.46	8.5	99.0			
19	Jul-09	977.5	41.8	0.0583	0.0039	0.06	0.773	0.685	6.58	0.28	1113	3.20	8.2	98.4	†		
20	Jul-09	936.3	44.3	0.0832	0.0078	-0.42	8.228	2.097	6.64	0.34	1009	2.06	8.5	95.3	†		
10HUM02 - S 23.6160° W 65.4204°																	
1	Jun-10	1097.5	39.3	0.0827	0.0073	-0.03	8.407	3.763	5.69	0.22	438	1.91	8.7	95.3		5.06	0.12
2	Jun-10	703.2	17.0	0.0629	0.0047	-0.10	4.616	1.783	9.06	0.23	667	1.48	9.1	97.9	†		MSWD = 1.4
3	Jun-10	1220.6	67.6	0.1197	0.0168	-0.02	16.180	9.848	4.87	0.31	91	1.27	8.7	90.6			
4	Jun-10	1251.6	32.9	0.0623	0.0039	-0.10	1.008	0.713	5.12	0.14	1218	0.87	8.7	97.9			
5	Jun-10	1276.0	40.4	0.0685	0.0074	-0.13	3.061	2.165	4.99	0.17	377	1.03	8.8	97.1			
6	Jun-10	1092.4	28.6	0.1580	0.0082	0.08	7.438	1.904	5.12	0.17	1172	0.59	8.5	85.7			
7	Jun-10	1311.3	37.0	0.0646	0.0062	0.23	12.190	3.780	4.88	0.14	547	1.16	8.8	97.6			
8	Jun-10	1242.5	38.1	0.0685	0.0099	0.18	1.171	1.391	5.12	0.17	348	1.25	8.8	97.1			
9	Jun-10	975.6	23.3	0.2421	0.0087	-0.02	16.690	3.986	5.04	0.18	469	1.21	8.9	74.9			
10	Jun-10	1207.0	40.6	0.0839	0.0101	-0.03	6.722	3.883	5.18	0.19	240	2.80	8.8	95.2			
11	Jun-10	1219.8	44.9	0.1558	0.0116	-0.41	9.736	4.358	4.64	0.22	290	1.94	8.8	86.0			
12	Jun-10	1239.2	38.4	0.0798	0.0069	-0.24	7.214	3.609	5.06	0.17	317	1.40	8.8	95.7			
13	Jun-10	182.3	4.6	0.6883	0.0139	0.05	56.390	5.308	6.41	1.27	321	1.14	8.8	17.9			
14	Jun-10	650.2	38.7	0.4503	0.0187	-0.30	33.100	5.558	4.87	0.79	577	0.98	9.1	48.3			
10HUM21 - S 23.7060° W 65.4760°																	
1	Jun-10	1064.3	48.3	0.0880	0.0104	-0.05	8.437	3.447	5.83	0.29	405	2.84	8.6	94.7		5.92	0.12
2	Jun-10	999.0	50.6	0.1526	0.0174	-0.23	12.220	7.062	5.67	0.36	123	2.20	8.7	86.4			MSWD = 1.4
3	Jun-10	1122.6	33.9	0.0725	0.0049	0.26	10.750	2.894	5.64	0.18	758	1.61	8.9	96.6			
4	Jun-10	1049.4	31.8	0.0584	0.0040	0.01	3.403	1.581	6.14	0.19	673	1.66	8.8	98.4			
5	Jun-10	1118.9	31.9	0.0595	0.0055	-0.07	4.410	2.067	5.76	0.17	548	2.70	8.9	98.3			
6	Jun-10	1044.2	32.2	0.0678	0.0091	0.15	4.054	2.341	6.09	0.20	362	1.84	8.9	97.2			
7	Jun-10	1052.4	27.9	0.0636	0.0059	-0.09	2.512	1.385	6.08	0.17	627	1.70	8.8	97.8			
8	Jun-10	1050.1	28.3	0.0568	0.0086	-0.07	5.677	2.265	6.15	0.18	536	2.11	8.8	98.6			
9	Jun-10	1047.3	33.6	0.0693	0.0050	0.02	6.508	2.462	6.07	0.20	649	2.09	8.4	97.0			
10	Jun-10	1062.9	31.0	0.0782	0.0086	0.21	11.770	3.345	5.91	0.19	594	1.83	8.6	95.9			
11	Jun-10	1081.8	39.1	0.1442	0.0196	0.33	19.970	9.222	5.31	0.25	133	2.23	8.7	87.5			
12	Jun-10	1042.3	32.5	0.0817	0.0066	-0.14	9.856	3.809	6.00	0.20	370	2.18	8.6	95.5			
13	Jun-10	978.5	27.5	0.0699	0.0046	-0.11	2.663	1.469	6.48	0.19	614	2.93	8.7	97.0	†		
14	Jun-10	1082.6	31.1	0.0929	0.0097	0.26	8.890	4.620	5.69	0.18	222	1.86	8.8	94.0			
15	Jun-10	1039.9	30.3	0.0651	0.0040	-0.04	4.257	1.623	6.14	0.18	867	2.19	8.7	97.6			
10HUM23 - S 23.6991° W 65.4595°																	
1	Jun-10	1364.8	37.4	0.0975	0.0095	0.24	18.960	6.097	4.51	0.14	351	2.02	8.9	93.4		4.8	0.1
2	Jun-10	1355.9	37.7	0.0972	0.0098	0.31	10.180	4.162	4.53	0.14	458	1.31	9.0	93.5			MSWD = 1.5
3	Jun-10	1301.6	39.3	0.1189	0.0170	-0.08	57.630	9.699	4.55	0.18	493	0.64	8.8	90.7			
4	Jun-10	887.3	36.6	0.2550	0.0204	-0.13	81.820	13.420	5.41	0.37	585	1.42	9.0	73.3			

(continued)

Sample/ grain	Analysis date	$^{238}U/^{206}Pb$	$^{238}U/^{206}Pb$ ±1σ	$^{207}Pb/^{206}Pb$	$^{207}Pb/^{206}Pb$ ±1σ	Level of Concordia	$^{204}Pb/^{206}Pb$ x 10^{-3}	$^{204}Pb/^{206}Pb$ ±1σ x 10^{-3}	$^{206}Pb/^{238}U$ age (Ma)	$^{206}Pb/^{238}U$ age (Ma) ±1σ	U (ppm)	U/ Th	UO^+/U^+	$^{206}Pb^*$ (%)		Weighted average $^{206}Pb/^{238}U$ age ±2σ (Ma)
5	Jun-10	794.9	27.6	0.3768	0.0140	-0.14	42.820	5.768	4.77	0.35	548	1.56	8.9	57.7		
6	Jun-10	482.6	14.8	0.5888	0.0197	0.18	28.760	5.939	4.19	0.55	196	2.44	8.8	30.6		
7	Jun-10	1153.3	38.4	0.1529	0.0155	0.11	32.940	9.781	4.92	0.21	184	1.53	8.8	86.4		
8	Jun-10	935.5	23.8	0.0561	0.0042	0.19	1.632	0.816	6.90	0.18	1055	2.74	8.8	98.7	†	
9	Jun-10	1338.2	39.9	0.0730	0.0087	0.05	2.453	1.735	4.73	0.15	503	1.05	8.7	96.6		
10	Jun-10	1333.7	40.2	0.0818	0.0079	-0.10	6.021	3.478	4.70	0.15	310	1.27	8.9	95.4		
11	Jun-10	1334.6	39.2	0.0864	0.0105	-0.07	8.187	4.515	4.67	0.16	247	1.40	8.9	94.9		
12	Jun-10	1298.9	44.9	0.0780	0.0078	-0.10	0.590	1.094	4.85	0.18	309	1.26	8.8	95.9		
13	Jun-10	240.8	9.5	0.6702	0.0226	-0.02	41.220	5.388	5.50	1.56	174	1.65	8.8	20.2		
14	Jun-10	817.0	30.6	0.2316	0.0153	-0.25	70.220	8.318	6.11	0.35	419	1.82	8.9	76.3	†	
15	Jun-10	1145.9	58.6	0.1364	0.0130	-0.07	32.630	10.000	5.05	0.31	215	0.81	8.4	88.5		
16	Jun-10	1162.3	33.5	0.1256	0.0122	0.11	8.410	4.640	5.06	0.18	256	0.89	8.5	89.8		
17	Jun-10	1255.0	35.0	0.0734	0.0080	-0.16	14.380	3.464	5.05	0.15	818	2.03	8.6	96.5		
18	Jun-10	1315.3	46.4	0.1112	0.0126	0.19	25.170	7.374	4.58	0.19	330	1.24	8.6	91.7		
19	Jun-10	1300.4	31.3	0.0674	0.0040	0.03	8.909	2.155	4.92	0.12	1326	3.28	8.9	97.3		
20	Jun-10	1279.1	31.6	0.0613	0.0034	0.06	5.160	1.194	4.99	0.13	2639	0.44	8.6	98.1		
21	Jun-10	1288.8	34.6	0.0711	0.0045	0.03	5.583	1.893	4.94	0.14	1107	2.65	8.6	96.8		
Tilcara Formation																
08HUM01 - S 23.6896° W 65.4557°																
1	Jul-09	1368.9	85.3	0.0839	0.0131	-0.07	20.390	9.168	4.57	0.30	229	2.03	8.0	95.2	†	3.66 0.2
2	Jul-09	1786.4	109.1	0.0677	0.0066	-0.21	1.791	1.792	3.57	0.22	513	0.90	8.6	97.2		MSWD = 1.6
3	Jul-09	1076.3	46.2	0.2774	0.0162	-0.08	40.380	10.280	4.28	0.30	252	0.99	8.6	70.4		
4	Jul-09	1581.5	96.8	0.1465	0.0148	-0.12	30.270	12.740	3.59	0.27	163	0.59	8.8	87.2		
5	Jul-09	1133.4	55.8	0.0595	0.0050	0.29	2.432	1.405	5.68	0.28	767	2.65	8.6	98.3	†	
6	Jul-09	1865.0	83.8	0.0722	0.0116	-0.12	10.960	4.706	3.39	0.16	457	0.70	8.8	96.7		
7	Jul-09	1399.8	59.0	0.0643	0.0045	0.00	7.843	2.655	4.57	0.20	1026	1.23	8.3	97.7	†	
8	Jul-09	1698.9	69.9	0.0671	0.0053	0.07	2.232	1.482	3.71	0.16	998	0.49	8.4	97.3		
9	Jul-09	1275.7	62.0	0.0736	0.0085	0.06	1.220	1.221	4.95	0.25	663	1.56	8.1	96.5	†	
10	Jul-09	1646.1	72.1	0.0880	0.0095	0.19	4.052	3.086	3.79	0.18	397	1.92	8.6	94.6		
11	Jul-09	1304.1	60.7	0.1578	0.0088	-0.25	8.667	2.747	4.32	0.24	915	1.90	8.4	85.7	†	
08HUM08 - S 23.6991° W 65.4699°																
1	Jul-09	1802.8	109.2	0.0766	0.0104	0.17	6.823	3.677	3.52	0.22	597	1.64	8.3	96.1		3.52 0.08
2	Jul-09	1781.9	53.3	0.0697	0.0078	0.10	1.160	1.160	3.58	0.11	818	1.37	8.8	97.0		MSWD = 0.44
3	Jul-09	1876.2	108.4	0.0892	0.0114	0.24	2.636	2.637	3.32	0.20	352	1.27	8.4	94.5		
4	Jul-09	1807.3	99.3	0.0762	0.0099	0.17	5.866	3.897	3.52	0.20	400	2.61	8.4	96.2		
5	Jul-09	1837.2	115.8	0.0978	0.0136	-0.09	12.450	6.902	3.37	0.23	295	3.24	8.3	93.4		
6	Jul-09	1798.9	101.6	0.0733	0.0086	-0.01	2.227	2.229	3.55	0.21	509	2.25	8.3	96.5		
7	Jul-09	995.0	30.4	0.0530	0.0023	-0.18	1.244	0.557	6.52	0.20	2262	5.14	8.8	99.1	†	
8	Jul-09	1809.3	76.3	0.0870	0.0088	0.15	n.d.	n.d.	3.44	0.15	580	0.93	8.5	94.8		
9	Jul-09	1637.5	93.3	0.0977	0.0178	-0.14	n.d.	n.d.	3.77	0.24	260	4.09	8.4	93.4		
10	Jul-09	9.5	0.7	0.8145	0.0079	-0.02	59.210	2.784	11.9	68.42	199	0.61	8.0	1.8	†	
09HUM05 - S 23.5734° W 65.4080°																
1	Jul-09	758.7	27.9	0.0616	0.0042	-0.02	0.153	0.293	8.43	0.32	746	5.30	8.4	98.0	†	2.5 0.1
2	Jul-09	565.0	30.2	0.0614	0.0051	-0.29	3.295	1.708	11.26	0.62	394	1.72	8.3	98.1	†	MSWD = 1.4
3	Jul-09	561.2	21.4	0.0519	0.0030	0.06	1.026	0.681	11.49	0.44	761	5.16	8.4	99.3	†	
4	Jul-09	2351.3	172.5	0.1484	0.0217	-0.12	n.d.	n.d.	2.43	0.22	185	0.75	8.6	86.9		
5	Jul-09	1907.3	107.7	0.0802	0.0097	0.01	7.616	4.406	3.30	0.20	367	1.11	8.6	95.6	†	
6	Jul-09	1035.1	52.1	0.0740	0.0091	0.18	1.151	1.350	6.09	0.32	361	2.28	8.2	96.4	†	
7	Jul-09	2495.6	116.5	0.0751	0.0085	-0.03	2.047	2.048	2.56	0.12	629	1.14	8.5	96.3		
8	Jul-09	1830.8	150.8	0.1355	0.0175	-0.08	15.220	10.140	3.18	0.30	181	1.01	8.1	88.6		
9	Jul-09	2663.8	116.4	0.1022	0.0132	0.54	9.656	6.439	2.32	0.11	557	1.30	8.5	92.8		
10	Jul-09	919.1	26.5	0.0533	0.0025	0.14	0.423	0.256	7.05	0.20	3536	29.65	8.6	99.1	†	
11	Jul-09	2469.1	150.0	0.1414	0.0176	0.52	3.570	3.573	2.38	0.17	359	1.78	8.5	87.8		
12	Jul-09	1171.0	71.3	0.0843	0.0151	0.54	5.822	4.123	5.32	0.35	192	2.14	8.7	95.1	†	
13	Jul-09	1363.1	79.9	0.0858	0.0098	0.44	10.210	4.579	4.57	0.28	400	1.88	8.3	94.9	†	
14	Jul-09	1760.3	113.1	0.1021	0.0159	-0.14	2.368	2.779	3.48	0.25	285	1.44	8.3	92.8	†	
15	Jul-09	1850.5	107.9	0.0809	0.0112	0.31	9.940	5.509	3.40	0.21	323	1.27	8.5	95.6	†	

(continued)

Sample/ grain	Analysis date	$^{238}U/^{206}Pb$	$^{238}U/^{206}Pb$ $\pm1\sigma$	$^{207}Pb/^{206}Pb$	$^{207}Pb/^{206}Pb$ $\pm1\sigma$	Level of Concordia	$^{204}Pb/^{206}Pb$ x 10^{-3}	$^{204}Pb/^{206}Pb$ $\pm1\sigma$ x 10^{-3}	$^{206}Pb/^{238}U$ age (Ma)	$^{206}Pb/^{238}U$ age (Ma) $\pm1\sigma$	U (ppm)	U/ Th	UO^+/U^+	$^{206}Pb^*$ (%)		Weighted average $^{206}Pb/^{238}U$ age $\pm2\sigma$ (Ma)	
16	Jul-09	2600.1	112.2	0.0695	0.0099	-0.04	1.574	1.575	2.46	0.11	972	0.80	8.4	97.0			
17	Jul-09	2513.8	127.7	0.0617	0.0080	0.09	3.391	2.399	2.57	0.13	861	0.94	8.4	98.0			
18	Jul-09	2322.3	118.1	0.0798	0.0097	-0.06	9.156	5.298	2.71	0.15	541	0.79	8.2	95.7			
19	Jul-09	2566.1	79.7	0.0645	0.0059	-0.02	0.987	0.988	2.50	0.08	1386	0.76	8.5	97.6			
20	Jul-09	701.8	34.7	0.0622	0.0064	-0.29	0.965	0.965	9.09	0.46	418	3.14	8.2	98.0	†		
Quaternary gravels																	
08HUM11 - S 23.6896° W 65.4628°																	
1	Jul-09	1073.3	50.7	0.0649	0.0060	0.07	3.855	2.336	5.96	0.29	464	5.56	8.3	97.6	†	1.06	0.1
2	Jul-09	523.6	25.6	0.0603	0.0049	0.27	7.189	2.671	12.2	0.61	346	2.02	8.2	98.2	†		
3	Jul-09	1506.7	56.3	0.0688	0.0058	0.12	10.680	2.818	4.22	0.16	1394	1.03	8.1	97.1	†		
4	Jul-09	1512.9	74.2	0.0580	0.0057	0.09	0.950	0.951	4.27	0.21	824	1.32	8.3	98.5	†		
5	Jul-09	1142.9	49.2	0.0658	0.0059	0.31	2.206	1.560	5.59	0.25	584	2.19	8.7	97.5	†		
6	Jul-09	1626.5	62.4	0.0852	0.0105	0.03	4.618	3.270	3.85	0.16	370	2.01	8.7	95.0	†		
7	Jul-09	1483.9	79.3	0.1138	0.0102	-0.18	24.890	7.918	4.05	0.24	353	1.63	8.3	91.4	†		
8	Jul-09	829.9	29.8	0.0585	0.0023	0.00	5.342	1.019	7.74	0.28	3502	3.51	8.3	98.4	†		
9	Jul-09	1264.2	65.4	0.2488	0.0202	0.24	23.660	7.935	3.82	0.29	281	0.73	8.5	74.1	†		
10	Jul-09	676.6	21.5	0.0515	0.0037	0.00	0.307	0.307	9.55	0.31	1335	3.78	8.5	99.3	†		
11	Jul-09	1557.6	65.8	0.0661	0.0057	-0.05	1.276	1.276	4.11	0.18	802	1.69	8.4	97.4	†		
12	Jul-09	1183.9	45.0	0.0762	0.0088	0.11	12.100	4.954	5.32	0.21	315	1.97	8.5	96.2	†		
13	Jul-09	614.3	29.1	0.0652	0.0074	-0.41	4.868	2.693	10.3	0.51	267	1.27	8.1	97.6	†		
14	Jul-09	11.4	0.5	0.0571	0.0007	0.06	0.115	0.060	541	21	235	2.00	8.2	100.2	†		
15	Jul-09	6161.4	336.7	0.0988	0.0113	-0.01	7.949	4.768	1.06	0.06	1573	1.81	8.3	93.3			
16	Jul-09	5694.8	402.1	0.1598	0.0214	0.22	27.580	12.420	1.06	0.09	637	2.46	8.2	85.5			
17	Jul-09	909.9	31.3	0.0600	0.0022	-0.02	2.282	0.595	7.06	0.24	4156	9.25	8.2	98.2	†		
18	Jul-09	1551.8	61.9	0.0538	0.0054	0.27	6.449	2.699	4.19	0.17	874	1.50	8.4	99.0	†		

$1\sigma = 1\sigma$ standard error
n.d. = not detected
† excluded from age calculations
all ages relative to standard zircon AS3 (1099.1 Ma) and corrected for ^{230}Th disequilibrium using $D_{230} = 0.2$
UO^+/U^+ calibration: range = 8.0-8.6 (July 2009) and 8.2-8.8 (June 2010)
AS3 age reproducibility = 2.7% (1 standard deviation; n = 36; July 2009) and 2.2% (n = 17; July 2009)
* common Pb correction using Southern California anthropogenic $^{208}Pb/^{206}Pb = 0.8283$
U concentrations estimated from standard zircon 91500 (U = 81 ppm); uncertainty approx. 13% (rel.)
U/Th mass ratio from $^{208}Pb/^{206}Pb$ vs. Th/U for AS3 standard zircon

Appendix B

Stratigraphic correlation of volcanic ashes

B.1 Stratigraphic correlations

Four out of 17 volcanic ash samples presented in this study have been stratigraphically correlated with previously dated horizons (Fig. B.1): (a) Sample 10HUM22 is located in the Incahuasi section and interbedded between two radiometrically dated samples (08HUM05 and 08HUM06; Fig. B.1). Therefore, the age of 10HUM22 must be within the range of 4.8 ± 0.2 Ma and 4.2 ± 0.1 Ma. As a result, 10HUM22 is assigned an age of 4.6 ± 0.5 Ma, with the error covering the range of possible ages. (b) Samples 10HUM26 and MAI240307-01 both come from the basal part of the Maimará section (Fig. B.1). This section is the northern continuation of the Incahuasi section (ca. 4.8 to 3.5 Ma), which can be deduced from major lithologies exposed at both outcrops - thick consolidated mud- and sandstones of the Maimará Formation, interbedded with conglomerates and alluvial fan deposits. Moreover, the lowermost ash in a nearby section in the Quebrada de Maimará (with identical characteristics) shows a U-Pb zircon age of 5.7 ± 0.1 Ma (10HUM02). Since both sampled ashes in the Maimará Formation neither belong to the lowermost, nor to the uppermost section of the Maimará Formation, the age for both samples has to be roughly between 4.5 and 5.5 Ma, which results in an age estimate of 5.0 ± 0.5 Ma. (c) Sample 10HUM20 was collected from an ash lens in the Quaternary conglomeratic gravels. Stratigraphically about 200 m below our sample, another volcanic ash shows a radiometric age of 0.8 Ma (Strecker *et al.*, 2007a). Hence, 10HUM20 must have been deposited between 0.8 Ma and present, which lead to the crude age estimate of 0.5 ± 0.5 Ma.

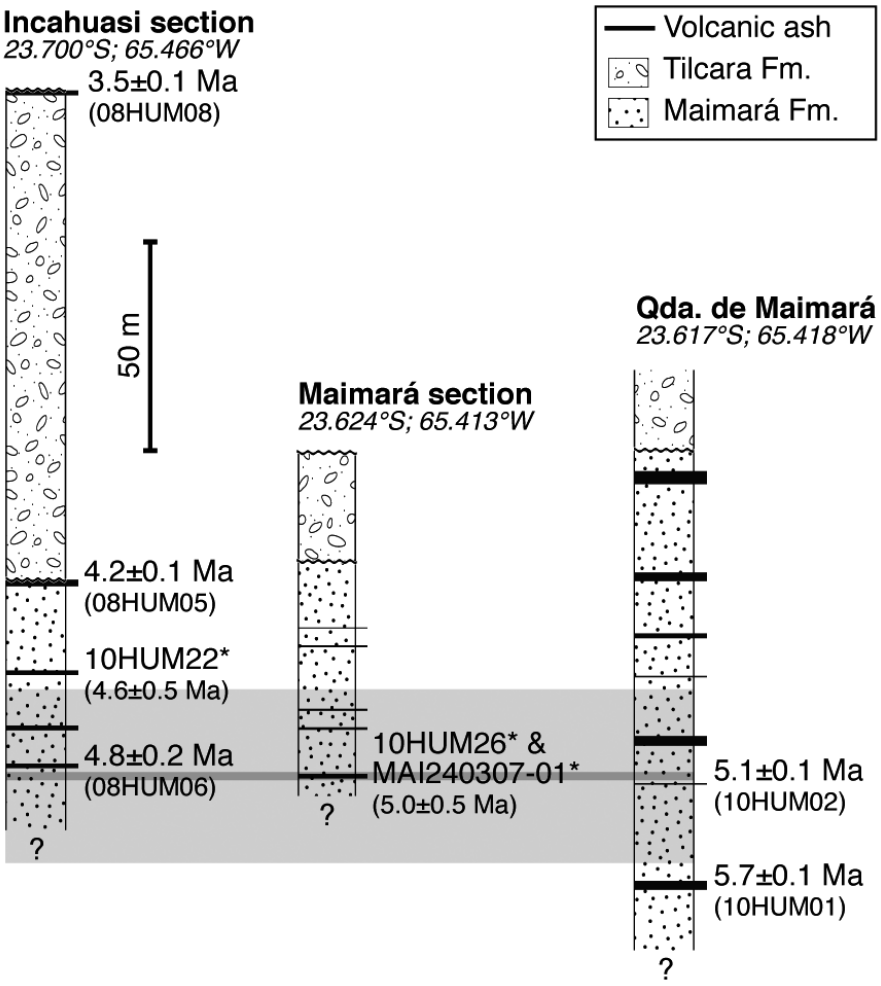

Figure B.1 – Stratigraphic sections from Incahuasi and Maimará showing radiometrically dated ash layers (Pingel *et al.*, 2013) in the Maimará Formation. Stars indicate correlated samples. Gray area shows estimated age range of 10HUM26 and MAI240307-01.

Appendix C

Hydrogen-isotope analysis

The analysis of stable hydrogen isotopes in volcanic glass from ash-fall layers is based on the observation that rhyolitic glass incorporates large amounts of water (~3-8 wt%) during the post-eruptive hydration process and becomes saturated after only 1-10 k.y. (Friedman *et al.*, 1992, 1993a,b; Shane & Ingraham, 2002; Mulch *et al.*, 2008; Dettinger, 2013). Friedman et al. (1993a; 1993b) empirically determined the isotopic fractionation between the environmental water present during hydration and the water that subsequently diffuses into the glass structure. To a certain degree this permits estimating the isotopic composition of environmental water (δD_w) at the time of the ash emplacement by converting isotope ratios of volcanic glass (δD_g) using the following equation:

$$\delta D_w = 1.0343 \cdot (1000 + \delta D_g) - 1000 \tag{C.1}$$

The most common source of this environmental water can be assumed to derive from meteoric sources, because (a) volcanic ashes are deposited instantaneously onto the Earth's surface and (b) the time needed for full hydration is relatively short (1-10 ky). Importantly, it has been shown that the stable hydrogen isotope signal of volcanic glass remains stable over geological time (Friedman *et al.*, 1992, 1993a,b; Mulch *et al.*, 2008; Cassel *et al.*, 2012; Dettinger, 2013). Moreover, the isotope signatures in volcanic glass represent mixed compositions averaged over thousands of years, and thus, independent of small-scale variations (i.e., daily to centennial) in the isotopic composition of meteoric water. This renders the stable hydrogen isotope composition of hydrated volcanic glass an important proxy for the isotopic composition of ancient meteoric water and therefore, ideal to decipher environmental changes that are related to changes in the isotopic composition of precipitation on the timescales of mountain building.

C.1 Volcanic glass samples

Volcanic ash samples were crushed and sieved and then treated with 10% hydrochloric acid for 15 min and 5% hydrofluoric acid for 30 sec in an ultrasonic bath to remove altered and birefringent rims and adherent carbonate and clay minerals. Subsequently, samples were rinsed with water and dried at max. 70°C. Where separates needed further concentration standard magnetic and density techniques were applied. Glass shards (125-250 μm) were handpicked using a cross-polarizing microscope. About 1.5 mg of each sample was packed in silver foil, loaded, and released to a helium-purged Thermo-Finnigan TC/EA (high temperature conversion/elemental analyzer) equipped with a Costech zero-blank auto sampler. The extracted sample gas was admitted into a Thermo-Finnigan ConFlo III connected in continuous-flow mode to a Thermo-Finnigan MAT 253 stable-isotope mass spectrometer. Five internationally referenced standard materials and laboratory-working standards were run with our samples, random samples were duplicated and tested for consistency, and the raw isotope data were corrected for mass bias, daily drift of

the thermal combustion reactor, and offset from the certified reference values. After correction, NBS30 (biotite), CH-7 (polyethylene), and NBS22 (oil) reference materials yielded δD = -64.3 ± 0.8‰ -104.5 ± 0.6‰ -117.5 ± 1.1‰ respectively. Repeated measurements of various standards and unknowns yielded a precision of ±3.0‰ for δD_g . Duplicates of three samples (08HUM05, 08HUM07, and 10HUM22) yielded a standard deviation of less than 3.0‰. This is also the precision presented for all δD_g data. One triplet of sample 08HUM03 yielded an average δD_g value of -83.2 ± 2.8‰. All isotope measurements were performed at the Joint Goethe University-BiK-F Stable Isotope Facility, Frankfurt. All isotopic ratios are reported relative to V-SMOW.

C.2 Modern stream water samples

Measurements were performed on 1-ml aliquots using an LGR 24d liquid isotope water analyzer. δD_w values were corrected based on internal laboratory standards yielding precisions typically <0.6‰ (2σ). All isotope measurements were performed at the Joint Goethe University-BiK-F Stable Isotope Facility, Frankfurt. All isotopic ratios are reported relative to V-SMOW.

C.3 Stable isotope compositions of hydrated volcanic glass

We obtained hydrogen isotope ratios from 17 ash samples collected between the years 2007 and 2010 in the sedimentary strata of the intermontane Humahuaca Basin (~23-24°S lat) in NW Argentina (Table C.1). Moreover, the glass isotope data shows no significant trend with latitude (Fig. C.1).

C.4 Water content of volcanic glass

The NBS-30 biotite is an IAEA standard with a well know composition, e.g., water content (3.68 wt%) (Gonfiantini, 1984). Per measuring cycle of ca. 35 standards and unknowns, three NBS-30 standards were run to calibrate unknowns. Because its water content is known, NBS-30 also helps to estimate the water content of hydrated volcanic glass samples from the same measuring cycle (Table C.2). The water content of volcanic glass was calculated by comparing the averaged ratio between volt-second peak area (determined by mass spectrometry) and NBS-30 mass to that of unknowns:

$$\frac{\text{Area all}_{\text{Smp}} \cdot \frac{M_{\text{Std}} \cdot 3.68\ \text{wt\%}}{100 \cdot \text{Area all}_{\text{Std}}}}{M_{\text{Smp}}} \cdot 100, \tag{C.2}$$

where M is mass and Area all is the volt-second peak area.

C.5 Stable isotope compositions of modern stream-water and rainfall

We collected six modern stream-water samples in the Humahuaca Basin (in March 2010, 2011, and 2012) from elevations similar to the sampled ashes and measured their stable oxygen and hydrogen isotopic composition (Table C.3).

Using Eq. C.1 we can convert these compositions into a modern hydrogen-glass composition and compare results from late Mio-Pliocene samples with present-day conditions (Table C.3). Table C.3 also shows the average annual isotope composition of rainfall from 3 long-term stations (IAEA, 2013) near Purmamarca, Molinos, and Salta in NW Argentina. All $\delta^{18}O$ and δD values fall closely along the global mean

water line (GMWL; Craig, 1961):

$$\delta D = 8 \cdot (\delta^{18}O) + 10‰, \tag{C.3}$$

which indicates minor evaporation of stream waters and rainfall in this region (Figs C.2). This data also shows a systematic relationship between δD_w and elevation (lapse rate) of -24.2‰/km (Fig. C.3). However, our lapse rate is only based on a limited number of samples. Recently, Dettinger (2013) presented an isotopic lapse rate for the Eastern Cordillera (-13.7‰/km). Most of their samples were collected along transects across the eastern Andean margin, through the Quebrada del Toro and Quebrada de Escoipe, at roughly 24.5°S latitude. This is approximately only 100 to 150 km south of our study area and represents the best available published isotopic lapse rate, for our study area, at this time. Other modern water samples used in their compilation and lapse rate calculations are from four nearby low to mid-elevation GNIP stations from elevations between 187 and 1,300 m (IAEA, 2013). Our modern isotopic water data shows some deviation from this dataset. Because of that, when relating our observed trends in the hydrogen isotopic composition of volcanic glass data to changes in elevation, we use a combined dataset (Fig. C.4). This new dataset produces a lapse rate of -14.5‰/km with a precision of ±1.1 km (2σ).

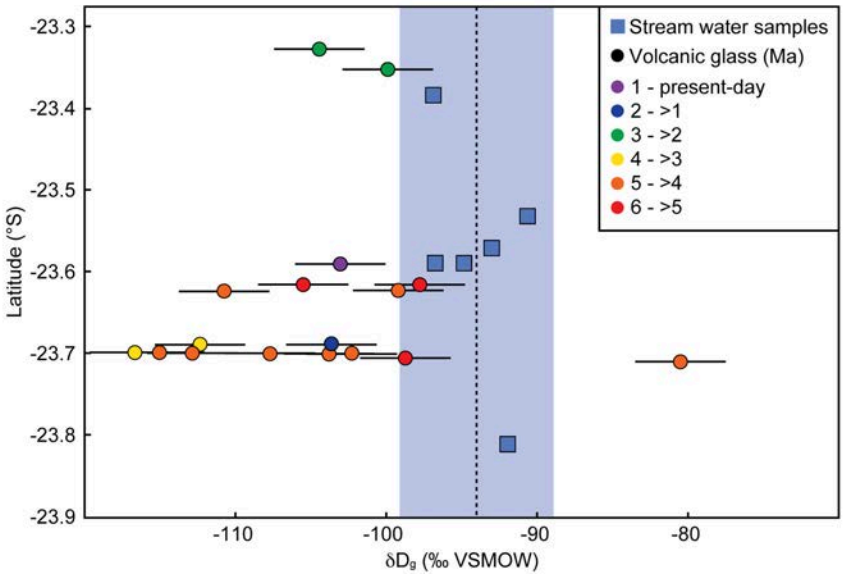

Figure C.1 – δD_g of glass (color-coded circles) and δD_{gc} from stream water samples (blue squares) vs. latitude showing no significant trends in the stable isotope data with latitude.

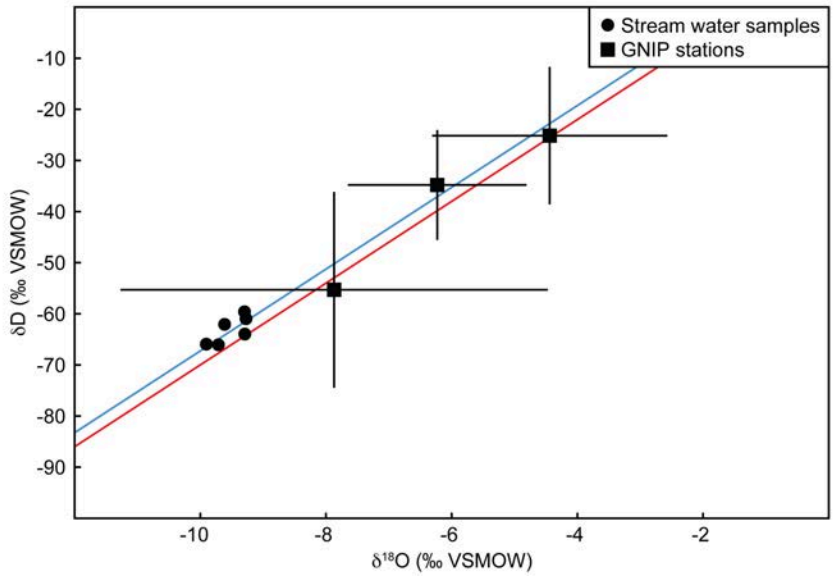

Figure C.2 – $\delta^{18}O$ vs. δD from stream-water samples collected in March 2010, 2011, and 2012 in the Humahuaca Basin and 3 GNIP stations (IAEA, 2013) showing a good correlation with the global mean water line (red line, GMWL; Craig, 1961) and the local mean water line from the Eastern Cordillera at 24.5°S lat (blue line; Dettinger, 2013).

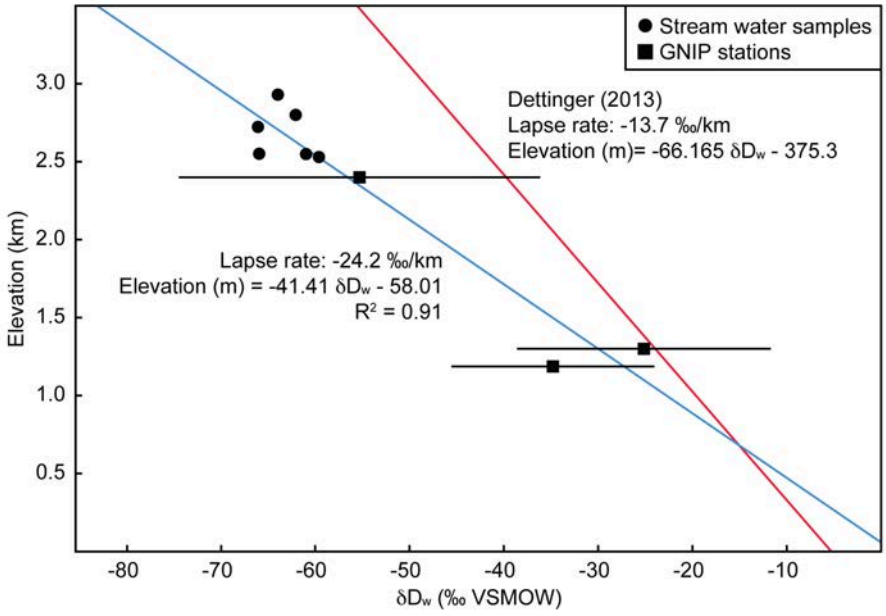

Figure C.3 – Systematic relationship of δD from stream-water samples and GNIP stations (IAEA, 2013) with elevation (-24.2 ‰/km, blue line). Red line shows the isotopic lapse rate of Dettinger (2013) determined for NW Argentina (-13.7 ‰/km).

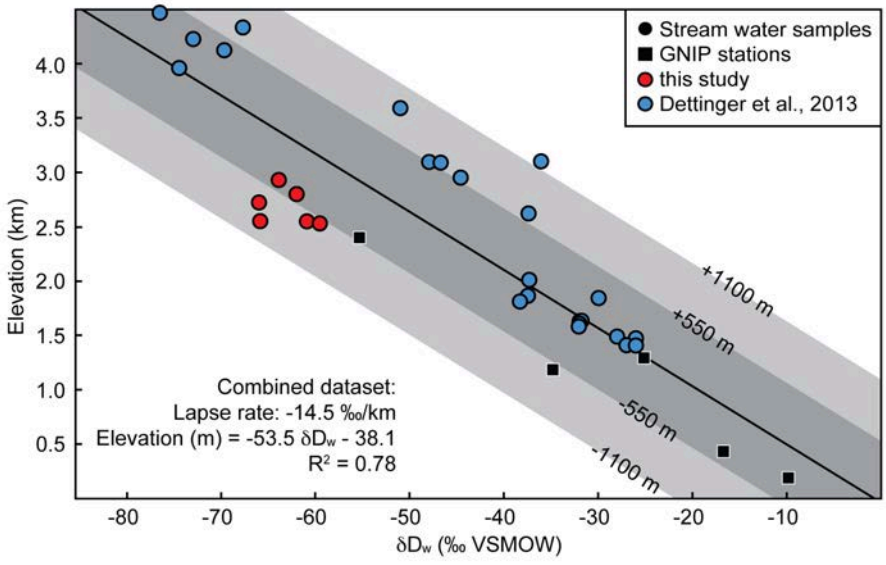

Figure C.4 – Combined dataset of modern water samples from this study and Dettinger (2013) showing a δD vs. elevation relationship of -14.5 ‰/km. Black line is the regression line (black) with 1σ and 2σ envelopes.

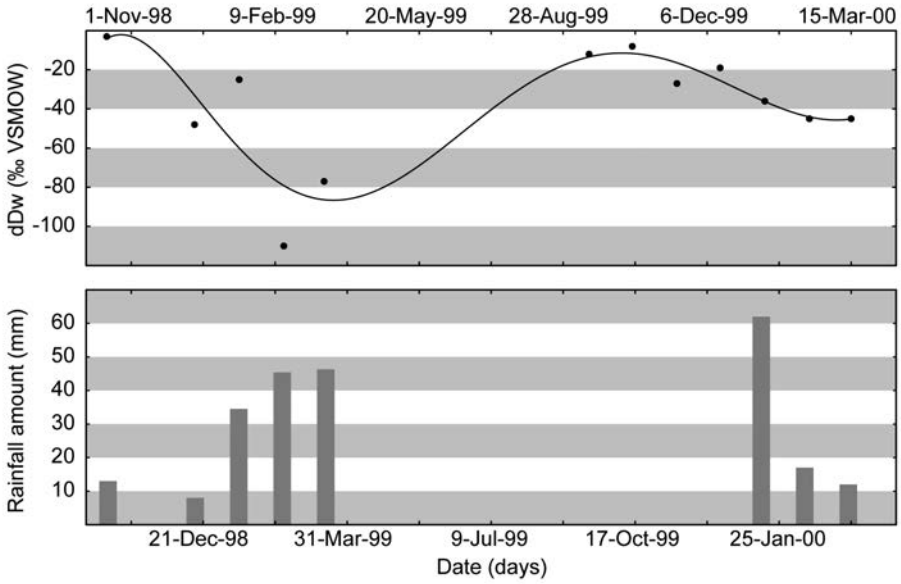

Figure C.5 – δD in precipitation and rainfall amount at Purmamarca GNIP station in the Humahuaca Basin at ~2,400 m a.s.l. (IAEA, 2013) showing (a) the lack of continuous measurements and (b) high annual variability in stable isotopes and rainfall amounts.

Table C.1 – Hydrogen stable isotope analysis of volcanic glass

Sample	Lat. (°)	Lon. (°)	Elev. (m)	Age (Ma)	Dating method	Individual analyses		δD_g (‰)	Av. δD_g (‰)	StDv
10HUM20	-23.591	-65.382	2770	0.5±0.5	stratigraphic	-103.0	-	-	-	-
08HUM11	-23.690	-65.463	2480	1.1±0.1	U-Pb Zircon*	-103.6	-	-	-	-
10HUM08	-23.328	-65.356	2900	2.5±0.1	Zircon FT†	-104.4	-	-	-	-
UQ270307-02	-23.353	-65.369	2860	2.63±0.02	Ar/Ar biotite	-99.9	-	-	-	-
08HUM08	-23.699	-65.470	2500	3.5±0.1	U-Pb Zircon*	-116.7	-	-	-	-
08HUM01	-23.690	-65.456	2400	3.7±0.2	U-Pb Zircon*	-112.3	-	-	-	-
08HUM03	-23.710	-65.474	2500	4.2±0.1	U-Pb Zircon*,§	-80.5	-83.0	-86.0	-83.2	2.8
08HUM05	-23.700	-65.461	2360	4.2±0.1	U-Pb Zircon*	-112.5	-113.2	-	-112.9	0.5
08HUM07	-23.701	-65.462	2380	4.3±0.1	U-Pb Zircon*	-105.7	-101.9	-	-103.8	2.7
10HUM22	-23.701	-65.462	2370	4.6±0.5	stratigraphic	-103.9	-100.6	-	-102.3	2.3
10HUM23	-23.699	-65.460	2350	4.8±0.1	U-Pb Zircon*	-115.0	-	-	-	-
08HUM06	-23.700	-65.461	2370	4.8±0.2	U-Pb Zircon*	-107.7	-	-	-	-
10HUM26	-23.624	-65.412	2430	5.0±0.5	stratigraphic	-110.7	-	-	-	-
MAI240307-01	-23.623	-65.411	2440	5.0±0.5	stratigraphic	-99.2	-	-	-	-
10HUM02	-23.616	-65.420	2570	5.1±0.1	U-Pb Zircon*	-105.5	-	-	-	-
10HUM01	-23.616	-65.420	2550	5.7±0.1	U-Pb Zircon*	-97.8	-	-	-	-
10HUM21	-23.706	-65.476	2600	5.9±0.1	U-Pb Zircon*	-98.7	-	-	-	-

Note: All samples were measured using TC/EA and Thermo-Finnigan MAT 253 stable-isotope mass spectrometer at Goethe University, Germany
If not otherwise indicated ages are from this study.
*Pingel *et al.* (2013)
†Walther *et al.* (1998)
§Excluded from further analyses

Table C.2 – Raw data for NBS30 biotite standard & water content calculation

Cycle	No	Weight (mg)	Area all (Vs)	*Water conc. (mg)	§MP	Mean MP	No	Sample Code	Weight (mg)	Area all (Vs)	†Water conc. (mg)	Water (wt%)
07022012-1	4	1.503	35.987	0.0553	0.0015	0.0015	9	MAI240307-01	1.552	61.616	0.095	6.1
	24	1.618	38.624	0.0595	0.0015		11	08HUM03	1.545	58.589	0.090	5.8
	45	1.595	37.898	0.0587	0.0015		12	10HUM08	1.534	59.857	0.092	6.0
							13	08HUM06	1.537	59.097	0.091	5.9
							14	10HUM01	1.522	59.712	0.092	6.1
							16	08HUM05 I	1.525	55.539	0.086	5.6
08022012-1	3	1.495	40.137	0.0550	0.0014	0.0014	8	10HUM05 II	1.517	55.179	0.078	5.2
	24	1.525	37.943	0.0561	0.0015		10	08HUM01	1.564	62.643	0.089	5.7
	45	1.558	40.475	0.0573	0.0014		11	10HUM21	1.510	57.656	0.082	5.4
							12	08HUM08	1.536	63.443	0.090	5.9
							13	08HUM11	1.564	41.062	0.058	3.7
							17	10HUM23	1.543	41.236	0.059	3.8
08022012-2	3	1.563	38.176	0.0575	0.0015	0.0015	38	10HUM02	1.484	49.265	0.074	5.0
	24	1.581	38.504	0.0582	0.0015							
	46	1.628	39.657	0.0599	0.0015							
09022012-2	3	1.540	37.824	0.0567	0.0015	0.0015	9	UQ270307-02	1.515	53.224	0.079	5.2
	20	1.640	41.184	0.0604	0.0015							
	40	1.608	39.502	0.0592	0.0015							
25042013-1	8	1.550	34.633	0.0570	0.0016	0.0016	11	10HUM22 I	1.598	55.118	0.091	5.7
	25	1.583	35.306	0.0583	0.0016		12	10HUM26	1.490	48.349	0.079	5.3
	47	1.606	36.223	0.0591	0.0016		13	10HUM20	1.460	32.425	0.053	3.6
							41	08HUM07 I	1.555	56.299	0.092	5.9
26042013-1	5	1.568	34.167	0.0577	0.0017	0.0017	9	10HUM22 II	1.572	54.716	0.092	5.8
	26	1.578	34.575	0.0581	0.0017		14	08HUM07 II	1.065	32.558	0.055	5.1
	43	1.590	35.002	0.0585	0.0017							
27032014-1	4	1.699	36.121	0.0625	0.0017	0.0017	10	08HUM03 I	1.652	50.891	0.087	5.3
	25	1.676	36.114	0.0617	0.0017		11	08HUM03 II	1.408	47.951	0.082	5.8
	47	1.523	33.273	0.0560	0.0017							

Water content of NBS30: 3.68 wt% (Gonfiantini, 1984)

*Water concentration is calculated using weight and known wt% of NBS30

§MP-Multiplier

†Water concentration is calculated by multiplying "Area all" with the "Mean multiplier" of the corresponding measuring cycle.

Table C.3 – Results of modern water stable isotopes

Sample	$\delta^{18}O$ (‰)	δD_w (‰)	δD_{gc} (‰)*	Lat. (°)	Lon. (°)	Elev. (km)
Río Huasamayo	-9.3±n.a.	-64.0±n.a.	-94.8	-23.590	-65.367	2930
Río Huichaira I	-9.6±n.a.	-62.1±n.a.	-93.0	-23.571	-65.451	2800
Río Huichara II	-9.9±.04	-65.9±.4	-96.8	-23.590	-65.410	2551
Río Yacoraite	-9.7±.05	-66.1±.1	-96.9	-23.384	-65.341	2723
Río Juella	-9.3±.03	-59.6±.1	-90.6	-23.532	-65.378	2530
Río Tumbaya	-9.3±.02	-61.0±.1	-92.0	-23.812	-65.533	2549
GNIP Purmamarca	-7.9±3.4	-55.3±19.2	-	-23.750	-65.500	2400
GNIP Molinos	-4.4±1.9	-25.2±13.5	-	-24.110	-65.190	1300
GNIP Salta	-6.2±1.4	-34.8±10.8	-	-24.780	-65.400	1187

Note: All samples were measured using LGR 24d liquid isotope water analyzer at Goethe University, Frankfurt (Germany). Where available, errors for average $\delta^{18}O$ and δD_w values are given in 1σ. Average δD_{gc} in the Humahuaca Basin is -94.0 ± 5.1‰ (error indicates 2 standard deviation).

GNIP: Global Network of Isotopes in Precipitation

*Reconstructed isotopic glass composition using fractionation equation (Eq. C.1) described in Friedman *et al.* (1993a)

Appendix D

$^{40}Ar/^{39}Ar$ biotite dating of sample UQ270307-2

Here we describe the treatments and methodologies to estimate the depositional age ($^{40}Ar/^{39}Ar$ age) of the UQ270307-02 volcanic ash sample that was collected in March 2007 from the sedimentary strata of the intermontane Humahuaca Basin in the Eastern Cordillera of NW Argentina. The crystal-rich ash is interbedded in the middle to upper section of the fossil-bearing Uquía Formation (Castellanos, 1950; Marshall *et al.*, 1982; Walther *et al.*, 1998; Reguero *et al.*, 2007) and was collected 2860 m a.s.l. at 23.353° S lat and 65.369° W lon. $^{40}Ar/^{39}Ar$ dating of potassium-bearing minerals is based on the measurement of the ratio of ^{40}Ar (a naturally occurring radioactive decay product of ^{40}K), accumulating in the mineral structure below a certain closure temperature, over ^{39}Ar (a product of irradiating ^{39}K with fast neutrons in a nuclear reactor; Merrihue & Turner, 2012). For a volcanic rock this means that the $^{40}Ar/^{39}Ar$ age may represent the timing of eruption and deposition, if the sample has not been reheated due to secondary processes (e.g., exposure to intrusive magmatic rocks).

D.1 Sample preparation

Biotite (Bt) mineral separation was performed at the Department for Earth and Environmental Sciences at Potsdam University (Germany) following standard separation techniques. The sample UQ270307-02 was crushed and wet-sieved to extract desired grain sizes (400-500 μm). After chemical treatment in both acetic acid (10% conc.) and hydrogen peroxide (3% conc.), the sample was thoroughly rinsed with deionized water to remove adhered secondary carbonates and organic matter. Inclusion-free Bt was then handpicked under a binocular microscope.

D.2 $^{40}Ar/^{39}Ar$ dating

The inclusion-free, euhedral Bt crystals were packed in commercial-grade Al foil and placed in a 99.999% pure Al-sample holder (35 mm diameter and 43 mm height) in which several holes were drilled for loading samples. Finally, the sample holder was wrapped in 0.5-mm thick Cd foil to cut off unnecessary thermal neutron flux. Neutron activation of the samples was performed at the Geesthacht Neutron Facility (GeNF) of the GKSS research centre of Geesthacht (Germany) for 4 days, where the fast neutron flux is about $1{\cdot}10^{12}$ n cm^{-2} s^{-1}. The samples were irradiated together with the Fish Canyon Tuff sanidine age standard in order to obtain the J value parameters for monitoring neutron flux. This standard was prepared and dated as 27.5 Ma at the Geological Survey of Japan (Uto *et al.*, 1997; Ishizuka, 1998). Moreover, two K-Ar age standard biotites, SORI93 biotite (92.6 ± 0.6 Ma; Sudo *et al.*, 1998) and HD-B1 biotite (24.21 ± 0.32 Ma, 24.18 ± 0.09 Ma; Hess & Lippolt, 1994; Schwarz & Trieloff, 2007) were irradiated and analyzed in order to confirm the accuracy of the system. K_2SO_4 and CaF_2 crystals were also irradiated together

to correct the interference of Ar isotopes produced by the interaction of neutrons with K and Ca in the sample.

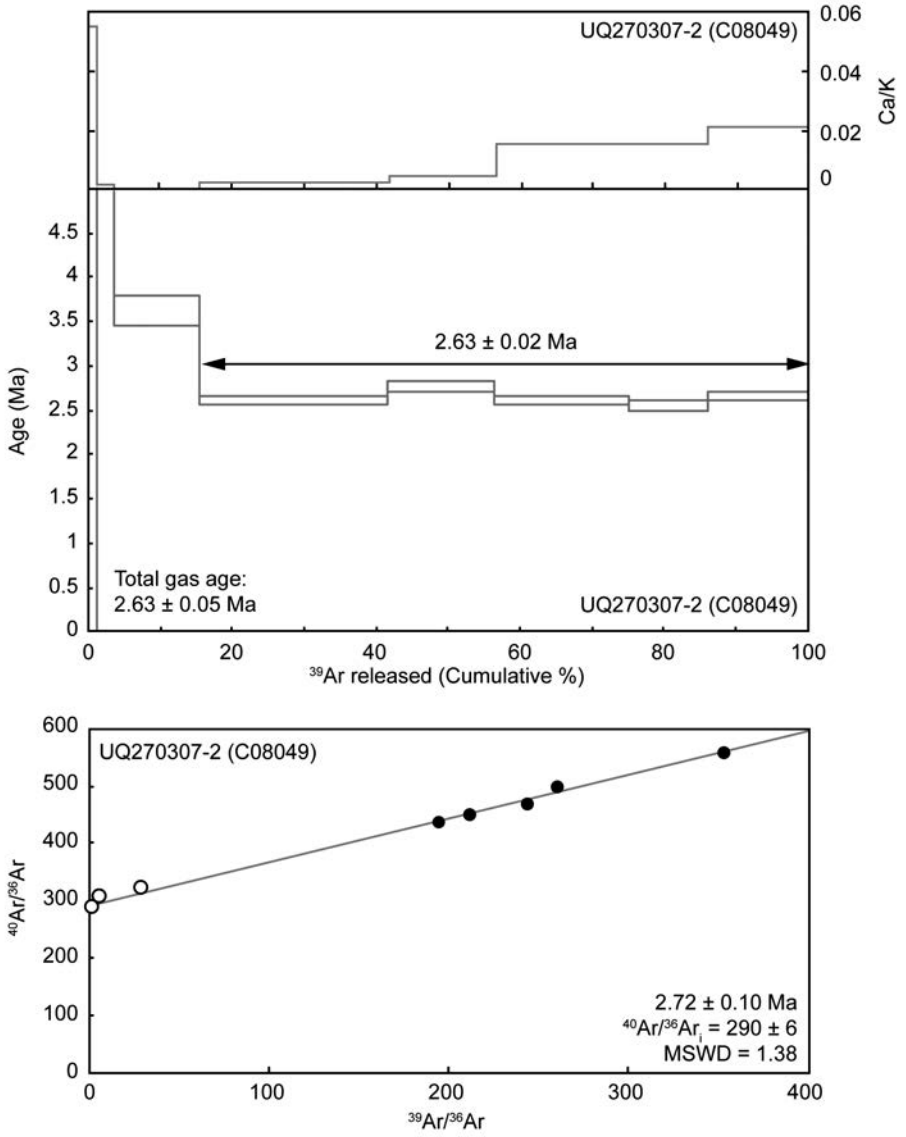

Figure D.1 – Age spectrum, $^{37}Ar_{Ca}/^{39}Ar_K$ ratios, and normal isochron by $^{40}Ar/^{39}Ar$ analysis, C08049, of UQ270307-2 biotite. All errors indicate 1 sigma error.

After one month's cooling at GeNF, samples were brought to Potsdam then Ar-isotope analysis was performed at the $^{40}Ar/^{39}Ar$ geochronology laboratory, Institute of Earth and Environmental Sciences, University of Potsdam (Germany). The analytical system at Potsdam University has been described in the recent literature (Vásquez *et al.*, 2010; Wilke *et al.*, 2010; Halama *et al.*, 2014) and consists of: (a) a New Wave Gantry Dual Wave laser ablation system with a 50 W CO_2 laser (wavelength 10.6 μm) for heating and extracting sample gas, (b) an ultra-high vacuum purification line with SAES getters and a cold trap used at the frozen temperature of ethanol, and (c) a high-sensitivity Micromass 5400 noble gas

mass spectrometer equipped with an electron multiplier for pulse counting, which effectively works for very small amounts of gas.

Single stepwise heating of the sample has been conducted with a defocused continuous CO_2 laser beam for 1 minute. Then, the extracted gas has been exposed to the SAES getters and a cold trap for 10 minutes to gain a pure Ar-sample gas. Finally, the Ar gas was admitted to the mass spectrometer to determine the Ar-isotope ratios. The isotopic ratios of each analysis have finally been obtained after corrections of blank, mass discrimination by the analysis of atmospheric argon, interference of Ar isotopes derived from Ca and K, and the decay of the Ar isotopes (^{37}Ar and ^{39}Ar) produced by the irradiation. Age and error calculation followed descriptions in Uto *et al.* (1997).

Fifteen biotite grains were used for single stepwise heating analysis (Laboratory ID: C08049). Table D.1 and Figure D.1 show the results of that analysis. The obtained plateau (total ^{39}Ar fraction is 84.5%) satisfies the criterion by Fleck *et al.* (1977) and the plateau age is 2.63 ± 0.02 Ma (Fig. D.1). All errors presented here are 1 sigma error. The normal isochron age calculated with the plateau steps following York (1968) is 2.72 ± 0.10 Ma (Fig. D.1). The y-intercept of the normal isochron (290 ± 6) implies that the initial $^{40}Ar/^{36}Ar$ ratio of the biotite does not differ from the atmospheric $^{40}Ar/^{36}Ar$ ratio (295.5; Steiger & Jäger, 1977). As both ages agree within error, we prefer the more precise plateau age (2.63 ± 0.02 Ma) for the UQ270307-2 biotite.

Table D.1 – $^{40}Ar/^{39}Ar$ analytical results of UQ270307-2 biotite, C08049

Laser Output†	$^{40}Ar/^{39}Ar$	$^{37}Ar/^{39}Ar$	$^{36}Ar/^{39}Ar$ ($x10^{-3}$)	$^{37}Ar_{Ca}/^{39}Ar_K$	$^{40}Ar^*$ (%)	$^{39}Ar_K$ (%)	$^{40}Ar^*/^{39}Ar_K$	Age(±1s) (Ma)
Sample ID: UQ270307-2 (biotite) Laboratory ID: C08049								
J = 0.00198								
1.60%	224.17 ± 0.7	0.032 ± 0.005	774.27 ± 3.67	0.03	-2.06	1.26	-4.62 ± -0.91	-16.58 ± -3.27
2.00%	50.49 ± 0.12	0.001 ± 0.003	163.58 ± 0.51	0	4.27	2.41	2.16 ± 0.1	7.69 ± 0.37
2.60%	11.06 ± 0.02	0 ± 0.004	33.98 ± 0.16	0	9.18	11.81	1.02 ± 0.05	3.62 ± 0.16
3.20%	2.25 ± 0	0.002 ± 0.001	5.14 ± 0.05	0	32.49	26.22	0.73 ± 0.01	2.61 ± 0.05
3.60%	1.91 ± 0.01	0.003 ± 0.002	3.84 ± 0.06	0	40.59	14.78	0.77 ± 0.02	2.76 ± 0.07
4.20%	2.12 ± 0	0.009 ± 0.004	4.72 ± 0.04	0.01	34.43	18.54	0.73 ± 0.01	2.61 ± 0.04
4.60%	1.93 ± 0.01	0.009 ± 0.004	4.11 ± 0.06	0.01	37	10.96	0.71 ± 0.02	2.54 ± 0.07
5.20%	1.58 ± 0.01	0.012 ± 0.003	2.84 ± 0.03	0.01	47.04	14.01	0.74 ± 0.01	2.65 ± 0.04
					Plateau age (4 steps from 3.2% to 5.2%):			*2.63 ± 0.02*
					Total gas age:			*2.63 ± 0.05*
					Normal isochron age (of plateau steps):			*2.72 ± 0.1*
					Inverse isochron age (of plateau steps):			*2.72 ± 0.1*

†100% corresponds to 50W output of CO_2 laser. All the errors indicate 1 sigma error. *radiogenic ^{40}Ar

Appendix E

U–Pb & U–Th zircon geochronology

Table E.1 – Summary of U–Pb zircon analytical data[a]

sample/ grain	$^{238}U/^{206}Pb$	$^{238}U/^{206}Pb$ $\pm1\sigma$	$^{207}Pb/^{206}Pb$	$^{207}Pb/^{206}Pb$ $\pm1\sigma$	Corr. of Concordia Ellipses	$^{206}Pb/^{238}U$ Age (Ma)	$\pm1\sigma$ (Ma)	U (ppm)	Th (ppm)	UO^+/U^+[b]	^{206}Pb[c] (%)
Ash2											
1	744	66	0.0627	0.0145	-0.16	8.56	0.79	270	120	8.5	98
10	660	47	0.0548	0.0082	0.1	9.74	0.71	750	450	8.3	99
2	650	47	0.0487	0.0037	-0.09	9.99	0.71	2,600	360	8.4	100
3	725	62	0.062	0.0188	0.09	8.77	0.79	380	460	8.5	98
4[d]	577	56	0.045	0.005	-0.14	11.3	1.1	940	190	8	100
5[d]	593	48	0.0492	0.0044	-0.06	10.9	0.9	1,800	260	8	100
6	654	60	0.0666	0.0066	-0.14	9.69	0.92	1,500	320	8.3	97
7[d]	538	40	0.118	0.004	-0.05	10.9	0.9	3,600	4,700	8.1	91
8	517	57	0.278	0.082	-0.53	8.85	2.1	500	290	9	70
9	708	55	0.0548	0.0049	0.31	9.1	0.71	1,400	270	8.7	99
AshQ											
1[e]	163,000	28,000	0.318	0.085	0.3	0.1	0.05	8,500	2,200	8.4	65
2[e]	78,900	14,300	0.409	0.107	0.05	0.1	0.05	3,100	1,200	8.6	54
3[e]	55,600	16,000	0.505	0.224	0.41	0.1	0.05	860	360	8.2	41
4[e]	194,000	38,000	0.448	0.168	0.41	0.1	0.05	6,400	1,400	8.4	49
5[e]	41,100	16,600	1.16	0.85	0.64	0.1	0.05	260	180	8.6	-
AshU											
1	11.6	0.8	0.0575	0.0008	0.06	534	38	790	70	8.2	100
2[e]	51,500	20,400	0.745	0.314	0.56	0.1	0.05	760	220	8.3	11
3[e]	93,800	18,700	0.51	0.176	0.59	0.1	0.05	3,100	810	8.4	41
4[e]	125,000	26,000	0.328	0.118	0.81	0.1	0.05	6,200	1,800	8.4	64
5[e]	86,100	20,500	0.58	0.202	0.33	0.1	0.05	2,200	490	8.3	32
SA150406-01											
1[e]	70,800	22,800	0.724	0.266	0.34	0.1	0.05	790	580	8.7	13
2[e]	1,080	130	0.828	0.061	0.09	0.1	0.05	490	400	8.4	-
3[e]	126,000	22,000	0.315	0.106	0.31	0.1	0.05	6,400	2,000	8.4	66
4[e]	53,400	15,900	0.482	0.189	0.45	0.1	0.05	820	210	9.5	44
5[e]	9,010	1,900	0.617	0.206	0.34	0.1	0.05	350	260	8.4	27
SA150406-03											
2[e]	60,200	8,400	0.533	0.144	0.65	0.1	0.05	4,000	1,400	8.2	38
3[e]	1,590	240	0.829	0.053	0.02	0.1	0.05	490	410	8.2	-
4[e]	46,100	19,400	0.888	0.358	0.48	0.1	0.05	530	270	8.4	-
5[e]	39,600	9,600	0.484	0.276	0.47	0.1	0.05	800	210	8.3	44

[a] The reproducibility of the AS3 standard (Paces & Miller, 1993) is one relative standard deviation 2.7% (n = 36)
[b] UO^+/U^+ calibration range for AS3 is between 8.0 and 8.6
[c] Radiogenic after ^{207}Pb-based common Pb correction; $^{207}Pb/^{206}Pb$ common = 0.823
[d] Excluded from mean
[e] Approximate age after disequilibrium correction

Table E.2 – Summary of U–Th zircon analytical data[a]

Sample/Grain	(^{238}U/^{232}Th)	(^{230}Th/^{232}Th)	Age (ka)	+2σ	-2σ	U (ppm)
SA150406-01						
1	4.65 ± 0.19	2.95 ± 0.19	91	14	-14	650
2	3.85 ± 0.16	1.63 ± 0.25	37	12	-12	230
3	11.7 ± 0.44	6.3 ± 0.25	78	6	-6	5000
4	9.47 ± 0.4	5.8 ± 0.2	95	10	-8	3300
5	3.81 ± 0.23	1.79 ± 0.33	47	20	-18	260
6	1.58 ± 0.1	0.91 ± 0.11	27	20	-18	360
7	6.05 ± 0.77	5.72 ± 0.7	304	∞	-204	630
8	8.37 ± 0.31	6.13 ± 0.46	134	26	-24	630
9	2.94 ± 0.13	1.3 ± 0.22	33	16	-14	290
10	4.54 ± 0.16	1.85 ± 0.3	38	12	-12	270
11	3.83 ± 0.2	1.85 ± 0.37	49	22	-20	200
12	6.4 ± 0.27	4.74 ± 0.17	134	18	-16	2800
13	5.88 ± 0.37	4.79 ± 0.42	170	58	-46	430
14	3.74 ± 0.15	1.48 ± 0.31	31	16	-14	310
15	2.58 ± 0.18	2.36 ± 0.18	232	172	-94	1000
SA150406-03						
3	3.5 ± 0.14	1.31 ± 0.21	26	10	-10	360
2	8.31 ± 0.29	4.91 ± 0.22	88	8	-8	2600
4	6.13 ± 0.22	5.31 ± 0.26	206	48	-40	1200
5	8.85 ± 0.61	6.71 ± 0.45	146	36	-30	800
6	6 ± 0.29	3.49 ± 0.35	81	18	-16	460
7	10.5 ± 0.51	5.89 ± 0.26	82	10	-8	2700
8	8.4 ± 0.32	3.26 ± 0.77	44	18	-16	200
9	7.15 ± 0.39	6.94 ± 0.48	377	∞	-200	540
10	51.2 ± 2.44	47.95 ± 3.17	299	200	-102	750
11	3.23 ± 0.14	1.52 ± 0.21	42	14	-14	360
12	5.4 ± 0.21	2.76 ± 0.34	63	16	-14	310
13	4.04 ± 0.18	3.7 ± 1.06	248	∞	-206	90
16	6.66 ± 0.3	4.75 ± 0.21	124	18	-16	1900
AshQ						
1	6.84 ± 0.27	4.79 ± 0.2	119	14	-14	7900
2	7.88 ± 0.5	5.97 ± 0.34	144	30	-28	990
3	5.23 ± 0.19	3.05 ± 0.24	80	14	-12	700
4	12.6 ± 0.45	7.13 ± 0.22	85	6	-6	4400
5	4.17 ± 0.18	2.08 ± 0.41	55	24	-20	220
6	1.65 ± 0.06	1 ± 0.06	38	12	-10	1200
7	3.62 ± 0.13	1.62 ± 0.24	40	14	-14	320
8	2.88 ± 0.11	1.56 ± 0.21	53	18	-16	280
9	3.25 ± 0.15	1.55 ± 0.19	43	12	-12	390
10	12.6 ± 0.44	7.31 ± 0.4	89	10	-10	1400
11	3.82 ± 0.17	2.59 ± 0.32	101	32	-28	330
12	7.84 ± 0.31	4.04 ± 0.5	69	16	-14	620
13	2.93 ± 0.14	1.68 ± 0.22	62	22	-20	320
14	2.85 ± 0.24	2.71 ± 0.18	297	∞	-154	2200
15	7.25 ± 0.28	3.14 ± 0.49	51	14	-12	250
AshU						
2	10.1 ± 0.36	6 ± 0.54	91	16	-16	560
3	12.5 ± 0.51	7.26 ± 0.3	89	8	-8	2500
4	10.5 ± 0.37	5.73 ± 0.18	78	6	-6	5000
5	11.6 ± 0.58	8.04 ± 0.4	121	18	-16	1700
6	7.8 ± 0.47	4.82 ± 0.5	95	22	-20	560
7	7.97 ± 0.35	5 ± 0.19	97	10	-10	3200
8	4.83 ± 0.33	5.12 ± 0.39	∞	∞	∞	560
9	4.79 ± 0.22	1.94 ± 0.28	39	12	-10	370
10	9.33 ± 0.32	5.89 ± 0.32	100	12	-12	1900
11	4.81 ± 0.19	2.46 ± 0.35	60	18	-16	250
12	3.78 ± 0.14	2.04 ± 0.2	61	14	-12	560
13	12.4 ± 0.47	6.67 ± 0.33	78	8	-8	3100
14	2.83 ± 0.1	1.49 ± 0.28	50	24	-22	200
15	9.02 ± 0.63	4.73 ± 0.59	72	18	-16	410
16	5.96 ± 0.29	1.69 ± 0.38	22	10	-10	320

[a] Decay constants: $\lambda_{230} = 9.1577 \cdot 10^{-6}\ a^{-1}$; $\lambda_{232} = 4.9475 \cdot 10^{-11}\ a^{-1}$; $\lambda_{238} = 1.55125 \cdot 10^{-10}\ a^{-1}$; Ages are calculated from two point isochrons between zircon and melt using rhyolitic whole-rock compositions (^{230}Th)/(^{232}Th) = 0.724 and (^{238}U)/(^{232}Th) = 0.726 (Bourdon *et al.*, 2000). All errors are reported in 2σ.
∞–secular equilibrium.

Appendix F

Provenance analysis

Table F.1 – Conglomerate compositional data

Loc.	Fm.	Lat. (° S)	Lon. (° W)	No.	GSh	Puna border					Paleozoic		Rift fill			EC/SBS border		
						Plt	Mtm[a]	Mgm	Tgt	Qtz	Sst (qtz arenite)	Sst (misc. lithic)	red Sst lithic	Bas.	White carb.	Black carb.	Volc.	Misc.
3	stream	25.311	65.493	110	93	-	-	-	-	-	-	7	-	-	9	-	-	1
5	stream	25.349	65.527	100	90	-	-	-	-	-	-	2	-	-	8	-	-	-
7	stream	25.284	65.481	104	80	-	1	-	-	-	-	8	2	-	13	-	-	-
15	stream	25.335	64.936	100	85[b]	-	-	-	-	-	3	8	-	-	-	4	-	-
18	stream	25.051	65.197	113	21	-	-	-	-	1	74	5	2	-	1	9	-	-
20	stream	24.686	65.290	110	18	-	-	-	-	2	63	25	2	-	-	-	-	-
22	stream	25.577	65.570	100	51	5	6	-	-	1	-	8	17	7	1	-	4	-
27	stream	25.637	65.486	134	77[b]	-	-	-	-	-	-	54	2	1	-	-	-	-
35	stream	25.450	65.563	112	100	-	-	-	-	-	1	3	3	-	5	-	-	-
42	stream	25.623	65.611	109	59	-	-	-	-	-	-	-	27	6	14	-	3	-
43	stream	25.631	65.630	117	48	20	-	-	-	-	-	-	49	-	-	-	-	-
1	La Troja	25.271	65.542	72	48	-	-	-	-	-	-	-	9	-	12	-	-	3
4	La Troja	25.265	65.545	109	73	-	-	-	-	-	-	1	4	1	28	-	-	2
11	La Troja	24.790	65.123	108	7	-	-	-	-	1	80	17	-	-	-	-	-	3
13	La Troja	25.098	65.170	100	6	-	-	-	-	-	70	1	7	-	16	-	-	-
19	La Troja	24.705	65.245	103	1	-	-	-	-	-	35	67	-	-	-	-	-	-
21	La Troja	25.578	65.570	140	-	-	-	-	-	-	-	11	2	1	7	-	119	-
23	La Troja	24.802	65.223	76	-	-	-	-	-	-	53	23	-	-	-	-	-	-
30	La Troja	24.789	65.357	100	-	-	-	-	-	-	-	100	-	-	-	-	-	-
38	La Troja	25.444	65.591	93	85	-	-	-	-	-	-	1	1	-	6	-	-	-
40	La Troja	25.521	65.504	107	87	2	1	2	-	-	2	9	1	-	2	-	1	-
2	Piquete	25.347	65.544	100	89	1	-	-	-	-	-	5	-	1	4	-	-	-
9	Piquete	25.237	65.463	100	69	-	-	-	-	-	-	2	5	-	24	-	-	-
10	Piquete	25.269	65.533	100	82	-	-	-	-	-	-	2	1	-	15	-	-	-
24	Piquete	24.800	65.025	85	46	-	-	-	-	-	33	6	-	-	-	-	-	-
29	Piquete	24.711	65.449	135	36	-	-	-	-	-	98	1	-	-	-	-	-	-
31	Piquete	25.131	65.020	119	92	3	-	1	-	-	12	4	-	-	6	-	1	-
32	Piquete	25.129	65.028	112	87	1	1	-	-	-	8	1	-	-	5	-	9	-
34	Piquete	24.896	64.982	110	65	13	2	2	1	-	22	2	-	-	3	-	-	-
37	Piquete	25.444	65.591	108	105	-	-	-	-	-	-	-	-	-	3	-	-	-
39	Piquete	25.527	65.511	100	86	-	-	-	-	-	1	13	-	-	-	-	-	-
41	Piquete	25.310	65.498	119	110	-	-	-	-	-	-	1	-	-	8	-	-	-
6	Guanaco	25.289	65.440	50	20	1	-	-	-	-	1	1	-	2	21	-	3	1
8	Guanaco	25.232	65.437	75	41	7	14	-	-	3	-	3	-	-	1	-	4	2
12	Guanaco	25.289	64.928	60	44[b]	7	-	-	-	4	-	-	-	-	-	-	3	2
26	Guanaco	25.199	64.956	108	55[b]	2	5	7	-	-	20	10	-	-	-	-	9	-
28	Guanaco	24.827	65.014	109	38	8	1	12	-	13	11	21	-	-	-	-	5	-
33	Guanaco	25.129	65.091	110	53[b]	7	1	-	4	-	33	9	-	-	-	-	3	-
36	Guanaco	25.437	65.604	118	80	14	4	10	-	-	9	1	-	-	-	-	-	-

[a]greater than greenschist metamorphic grade; [b]recrystalized (i.e., Medina Fm); Loc–clast count station; Fm–sampled formation; Lat–Latitude; Lon–Longitude; No–Number of clasts counted; GSh–Greenshist (Puncoviscana Fm); Plt–plutonic; Mtm–metamorphic; Mgm–migmatitic/pegmatitic; Tgt–Tastil granite; Qtz–quartzitic; Sst–standstone; Bas–basaltic; Carb–carbonatic

Appendix G

U–Pb & (U–Th)/He zircon geochronology

Table G.1 – Summary of U–Th–Pb zircon analytical data of volcanic ash samples using LA-ICPMS at UCSB, first analytical session.

	Concentrations (ppm)				Isotope ratios								Isotopic age (Ma)				
Sample / grain	Pb	U	Th	Th/U	$^{207}Pb/^{206}Pb$	2σ (%)	$^{238}U/^{206}Pb$	2σ (%)	$^{207}Pb/^{235}U$	2σ (%)	$^{206}Pb/^{238}U$	2σ (%)	Rho	^{207}Pb and ^{230}Th-corrected $^{206}Pb/^{238}U$ age	2σ abs.			
ANG-080313-1																		
M2Q1A-1	1.0	490	172	0.349	0.05	3.29	532.48	1.37	0.0123	3.5603	0.0019	1.3723	0.39	12.169	0.167		w.m.	12.166
M2Q1A-2	2.1	595	377	0.633	0.05	2.87	526.04	1.46	0.0139	3.2159	0.0019	1.4562	0.45	12.226	0.178		±1s	0.016
M2Q1A-3	4.4	1916	798	0.414	0.05	2.64	527.98	1.41	0.0133	2.9916	0.0019	1.4115	0.47	12.226	0.172		±2s	0.032
M2Q1A-4	1.7	599	300	0.498	0.05	2.58	533.33	1.52	0.0124	2.9948	0.0019	1.5243	0.51	12.149	0.185		MSWD	0.857
M2Q1A-5	1.4	310	264	0.846	0.05	3.80	524.11	1.85	0.0137	4.2242	0.0019	1.8508	0.44	12.290	0.228		n	21
M2Q1A-6	1.5	587	277	0.469	0.05	3.29	531.35	1.62	0.0123	3.6678	0.0019	1.6200	0.44	12.193	0.197			
M2Q1A-7	1.7	348	292	0.833	0.05	3.27	506.07	1.27	0.0133	3.5059	0.0020	1.2668	0.36	12.780	0.163	†		
M2Q1A-8	1.8	602	297	0.486	0.05	2.73	500.75	1.49	0.0133	3.1103	0.0020	1.4886	0.48	12.925	0.192	†		
M2Q1A-9	2.1	673	367	0.543	0.05	2.56	516.53	1.24	0.0128	2.8453	0.0019	1.2415	0.44	12.531	0.156	†		
M2Q1A-10	3.7	1222	520	0.421	0.06	3.19	517.60	1.10	0.0170	3.3767	0.0019	1.1032	0.33	12.260	0.138	†		
M2Q1A-11	1.8	586	250	0.423	0.06	5.05	523.29	1.55	0.0164	5.2830	0.0019	1.5482	0.29	12.155	0.193	†		
M2Q1A-12	3.9	1373	663	0.481	0.05	1.99	514.40	1.28	0.0128	2.3678	0.0019	1.2844	0.54	12.596	0.161	†		
M2Q1A-13	2.5	825	453	0.547	0.05	2.26	527.70	0.98	0.0124	2.4669	0.0019	0.9813	0.40	12.284	0.121	†		
M2Q1A-14	4.2	2170	759	0.349	0.05	2.02	530.79	1.27	0.0122	2.3900	0.0019	1.2703	0.53	12.220	0.155			
M2Q1A-15	1.0	358	178	0.495	0.05	3.30	522.47	1.11	0.0125	3.4837	0.0019	1.1115	0.32	12.401	0.139	†		
M2Q1A-16	1.4	555	262	0.468	0.05	2.98	527.70	1.03	0.0121	3.1521	0.0019	1.0270	0.33	12.295	0.127	†		
M2Q1A-17	2.5	875	478	0.548	0.05	2.38	259.74	5.48	0.0271	5.9711	0.0039	5.4774	0.92	24.708	1.347	†		
M2Q1A-18	2.5	461	469	1.016	0.05	3.71	524.11	1.60	0.0123	4.0435	0.0019	1.6000	0.40	12.356	0.198	†		
M2Q1A-19	0.9	282	170	0.606	0.05	3.51	531.07	1.62	0.0123	3.8638	0.0019	1.6192	0.42	12.203	0.198			
M2Q1A-20	1.6	493	307	0.622	0.05	2.89	533.05	1.18	0.0127	3.1198	0.0019	1.1775	0.38	12.138	0.143			
M2Q1A-21	0.8	231	183	0.789	0.05	4.39	521.10	1.54	0.0121	4.6572	0.0019	1.5424	0.33	12.450	0.193	†		
M2Q1A-22	2.5	664	493	0.747	0.06	2.58	527.43	0.89	0.0149	2.7345	0.0019	0.8918	0.33	12.132	0.110			
M2Q1A-23	1.2	487	257	0.531	0.05	3.43	532.20	1.22	0.0126	3.6435	0.0019	1.2244	0.34	12.160	0.150			
M2Q1A-24	2.6	919	548	0.597	0.05	2.66	530.79	0.99	0.0131	2.8324	0.0019	0.9855	0.35	12.165	0.121			
M2Q1A-25	0.9	296	195	0.662	0.05	3.61	539.67	1.09	0.0125	3.7674	0.0019	1.0925	0.29	11.986	0.133			
M2Q1A-26	2.0	482	408	0.853	0.05	3.43	525.76	1.46	0.0126	3.7275	0.0019	1.4556	0.39	12.299	0.180	†		
M2Q1A-27	1.4	747	257	0.347	0.05	2.27	501.50	1.35	0.0134	2.6443	0.0020	1.3498	0.51	12.903	0.174	†		
M2Q1A-28	2.0	1109	351	0.318	0.05	2.19	521.10	1.35	0.0128	2.5695	0.0019	1.3469	0.52	12.426	0.167	†		
M2Q1A-29	1.3	411	222	0.545	0.05	3.17	524.93	1.36	0.0122	3.4452	0.0019	1.3554	0.39	12.357	0.168	†		
M2Q1A-30	3.0	778	517	0.662	0.05	2.06	526.04	1.36	0.0127	2.4685	0.0019	1.3579	0.55	12.305	0.166	†		
M2Q1A-31	3.8	3249	627	0.194	0.05	1.87	532.48	1.57	0.0125	2.4425	0.0019	1.5726	0.64	12.165	0.190			
M2Q1A-32	4.0	2775	704	0.254	0.05	1.76	527.98	1.41	0.0124	2.2574	0.0019	1.4115	0.63	12.278	0.172			
M2Q1A-33	1.8	659	315	0.481	0.05	2.47	528.82	1.46	0.0123	2.8669	0.0019	1.4630	0.51	12.255	0.179			
M2Q1A-34	2.1	819	353	0.434	0.05	2.54	526.32	1.51	0.0126	2.9545	0.0019	1.5064	0.51	12.302	0.185	†		
M2Q1A-35	0.9	398	159	0.401	0.05	3.22	533.90	1.53	0.0119	3.5645	0.0019	1.5258	0.43	12.171	0.185			
M2Q1A-36	1.1	538	194	0.366	0.05	2.32	536.48	0.99	0.0123	2.5229	0.0019	0.9934	0.39	12.076	0.120			
M2Q1A-37	1.5	521	245	0.473	0.05	3.24	531.35	1.72	0.0124	3.6712	0.0019	1.7214	0.47	12.179	0.209			
M2Q1A-38	2.4	1012	400	0.396	0.05	2.29	531.91	1.03	0.0122	2.5123	0.0019	1.0333	0.41	12.188	0.126			
M2Q1A-39	1.4	478	234	0.489	0.05	5.32	523.56	1.80	0.0141	5.6157	0.0019	1.7986	0.32	12.292	0.224			
M2Q1A-40	2.0	607	319	0.526	0.05	2.97	518.40	1.10	0.0144	3.1694	0.0019	1.1046	0.35	12.386	0.138	†		
ANG-ISA-7-R																		
M1Q3-1	2.1	423	351	0.829	0.05	3.45	531.07	1.13	0.0125	3.6281	0.0019	1.1261	0.31	12.182	0.139	†	w.m.	11.984
M1Q3-2	1.6	423	271	0.640	0.05	2.94	544.37	1.20	0.0121	3.1772	0.0018	1.1981	0.38	11.905	0.143		±1s	0.017
M1Q3-3	1.1	332	169	0.507	0.05	4.48	485.67	1.14	0.0129	4.6225	0.0021	1.1359	0.25	13.376	0.154	†	±2s	0.034
M1Q3-4	1.3	317	222	0.701	0.05	4.26	536.19	1.28	0.0129	4.4528	0.0019	1.2812	0.29	12.042	0.156		MSWD	1.116
M1Q3-5	1.2	238	174	0.726	0.05	3.92	463.61	1.48	0.0148	4.1894	0.0022	1.4780	0.35	13.919	0.207	†	n	29
M1Q3-6	2.8	555	489	0.880	0.05	2.89	539.96	1.39	0.0125	3.2095	0.0019	1.3890	0.43	11.978	0.166			
M1Q3-7	1.6	433	275	0.634	0.05	4.28	541.13	1.49	0.0122	4.5329	0.0018	1.4931	0.33	11.976	0.180			
M1Q3-8	5.5	485	457	0.942	0.16	3.68	456.41	1.54	0.0487	3.9871	0.0022	1.5437	0.39	12.135	0.214	†		
M1Q3-9	3.0	441	360	0.808	0.09	8.26	515.46	1.48	0.0243	8.3889	0.0019	1.4788	0.18	11.886	0.210	†		
M1Q3-10	1.1	261	191	0.727	0.05	5.16	527.98	1.36	0.0128	5.3378	0.0019	1.3622	0.26	12.251	0.170	†		
M1Q3-11	1.9	410	350	0.845	0.05	2.60	538.50	1.24	0.0121	2.8820	0.0019	1.2365	0.43	12.034	0.149			
M1Q3-12	2.6	455	447	0.976	0.06	3.74	530.50	1.22	0.0144	3.9374	0.0019	1.2211	0.31	12.081	0.150			
M1Q3-13	1.1	266	207	0.775	0.05	3.36	539.37	1.39	0.0126	3.6348	0.0019	1.3877	0.38	11.973	0.167			

(continued)

Sample / grain	Concentrations (ppm) Pb	U	Th	Th/U	Isotope ratios $^{207}Pb/^{206}Pb$	2σ (%)	$^{238}U/^{206}Pb$	2σ (%)	$^{207}Pb/^{235}U$	2σ (%)	$^{206}Pb/^{238}U$	2σ (%)	Rho	Isotopic age (Ma) ^{207}Pb and ^{230}Th-corrected $^{206}Pb/^{238}U$ age	2σ abs.			
M1Q3-14	2.0	415	371	0.891	0.05	3.12	544.37	1.15	0.0120	3.3257	0.0018	1.1488	0.35	11.897	0.137			
M1Q3-15	1.5	332	266	0.791	0.05	3.24	541.71	1.60	0.0123	3.6145	0.0018	1.5971	0.44	11.939	0.191			
M1Q3-16	0.9	225	142	0.633	0.06	4.20	530.79	1.72	0.0157	4.5427	0.0019	1.7197	0.38	11.996	0.208			
M1Q3-17	1.4	335	235	0.699	0.05	3.19	542.89	1.65	0.0117	3.5912	0.0018	1.6519	0.46	11.954	0.197			
M1Q3-18	2.1	432	350	0.803	0.05	2.98	542.59	1.29	0.0128	3.2524	0.0018	1.2942	0.40	11.894	0.154			
M1Q3-19	1.8	380	303	0.787	0.05	3.94	536.19	1.38	0.0121	4.1722	0.0019	1.3806	0.33	12.092	0.168			
M1Q3-20	1.4	300	215	0.707	0.05	3.41	528.26	1.56	0.0126	3.7546	0.0019	1.5614	0.42	12.240	0.191	†		
M1Q3-21	1.0	255	173	0.673	0.05	4.82	545.85	1.66	0.0121	5.1003	0.0018	1.6601	0.33	11.863	0.198			
M1Q3-22	0.9	246	141	0.573	0.05	4.04	527.15	1.17	0.0126	4.2041	0.0019	1.1669	0.28	12.283	0.145	†		
M1Q3-23	2.1	473	363	0.759	0.05	3.31	537.35	1.38	0.0122	3.5847	0.0019	1.3832	0.39	12.055	0.167			
M1Q3-24	1.7	386	283	0.729	0.05	3.70	545.85	1.76	0.0119	4.0995	0.0018	1.7645	0.43	11.872	0.209			
M1Q3-25	1.0	250	160	0.635	0.05	4.95	538.79	1.59	0.0120	5.2023	0.0019	1.5893	0.31	12.040	0.193			
M1Q3-26	1.9	394	280	0.702	0.06	4.06	528.54	1.66	0.0146	4.3909	0.0019	1.6626	0.38	12.130	0.203			
M1Q3-27	1.3	272	194	0.712	0.06	5.58	533.05	1.37	0.0145	5.7482	0.0019	1.3736	0.24	12.025	0.171			
M1Q3-28	1.9	393	274	0.687	0.07	3.00	517.60	1.34	0.0173	3.2895	0.0019	1.3391	0.41	12.231	0.165	†		
M1Q3-29	2.7	418	435	1.032	0.06	3.36	528.82	1.76	0.0167	3.7912	0.0019	1.7645	0.47	11.995	0.213			
M1Q3-30	1.4	347	246	0.700	0.05	4.42	544.07	1.40	0.0122	4.6362	0.0018	1.3982	0.30	11.899	0.168			
M1Q3-31	2.3	470	407	0.858	0.05	3.29	549.15	1.72	0.0121	3.7090	0.0018	1.7217	0.46	11.789	0.203			
M1Q3-32	1.3	336	217	0.637	0.05	3.36	535.05	1.53	0.0120	3.6895	0.0019	1.5287	0.41	12.123	0.185			
M1Q3-33	1.4	341	236	0.680	0.05	4.06	535.91	1.48	0.0129	4.3189	0.0019	1.4804	0.34	12.045	0.180			
M1Q3-34	2.6	268	188	0.693	0.14	7.35	455.37	2.11	0.0420	7.6457	0.0022	2.1093	0.28	12.562	0.320	†		
M1Q3-35	1.9	400	332	0.817	0.05	3.32	536.48	1.33	0.0121	3.5805	0.0019	1.3314	0.37	12.077	0.161			
M1Q3-36	0.7	166	118	0.700	0.05	5.91	523.29	1.40	0.0134	6.0769	0.0019	1.4005	0.23	12.327	0.178	†		
M1Q3-37	1.4	342	248	0.716	0.05	3.48	539.08	2.00	0.0122	4.0142	0.0019	2.0041	0.50	12.013	0.240			
M1Q3-38	1.4	369	238	0.637	0.05	3.70	533.90	1.53	0.0122	4.0026	0.0019	1.5258	0.38	12.138	0.186			
M1Q3-39	2.4	436	388	0.877	0.06	3.07	542.59	1.39	0.0143	3.3758	0.0018	1.3949	0.41	11.809	0.165			
M1Q3-40	1.1	298	175	0.579	0.05	4.69	542.01	1.65	0.0124	4.9723	0.0018	1.6494	0.33	11.926	0.198			
ANG-070313-3																		
M2Q1B-1	4.5	720	811	1.119	0.05	2.49	530.22	0.73	0.0125	2.5970	0.0019	0.7288	0.28	12.202	0.090	†	max. age	6.368
M2Q1B-2	1.7	361	287	0.793	0.05	3.44	487.33	1.01	0.0137	3.5881	0.0021	1.0097	0.28	13.266	0.136	†	±1s	-
M2Q1B-3	0.6	224	158	0.699	0.05	7.24	909.09	1.28	0.0078	7.3564	0.0011	1.2832	0.17	7.135	0.096	†	±2s	0.084
M2Q1B-4	1.6	181	279	1.522	0.05	5.58	520.02	1.54	0.0129	5.7860	0.0019	1.5395	0.27	12.418	0.195	†	MSWD	-
M2Q1B-5	4.1	1483	614	0.412	0.05	1.90	458.72	1.09	0.0144	2.1841	0.0022	1.0853	0.50	14.114	0.153	†	n	1
M2Q1B-6	3.0	553	549	0.983	0.05	4.23	526.04	1.56	0.0126	4.5025	0.0019	1.5555	0.35	12.296	0.192	†		
M2Q1B-7	2.0	497	358	0.711	0.05	3.30	530.22	1.37	0.0126	3.5684	0.0019	1.3672	0.38	12.214	0.167	†		
M2Q1B-8	1.5	242	224	0.915	0.05	5.28	410.17	1.29	0.0167	5.4338	0.0024	1.2903	0.24	15.720	0.208	†		
M2Q1B-9	4.1	678	837	1.216	0.05	2.30	527.43	1.36	0.0125	2.6748	0.0019	1.3610	0.51	12.267	0.167	†		
M2Q1B-10	2.3	462	478	1.023	0.05	3.69	536.48	0.99	0.0123	3.8250	0.0019	0.9934	0.26	12.068	0.122	†		
M2Q1B-11	1.1	1000	431	0.426	0.05	2.85	1005.03	1.12	0.0067	3.0638	0.0010	1.1225	0.37	6.480	0.073	†		
M2Q1B-12	1.0	301	268	0.878	0.05	3.99	584.11	1.16	0.0114	4.1553	0.0017	1.1642	0.28	11.077	0.131	†		
M2Q1B-13	1.8	794	428	0.531	0.05	2.19	528.82	0.89	0.0125	2.3687	0.0019	0.8934	0.38	12.244	0.110	†		
M2Q1B-14	34.2	310	169	0.543	0.06	1.55	13.11	1.40	0.5945	2.0871	0.0763	1.4028	0.67	474.132	6.524	†		
M2Q1B-15	2.7	458	482	1.039	0.05	2.89	531.91	1.08	0.0127	3.0884	0.0019	1.0801	0.35	12.154	0.132	†		
M2Q1B-16	0.8	456	247	0.535	0.05	5.14	956.94	1.25	0.0073	5.2950	0.0010	1.2525	0.24	6.787	0.087	†		
M2Q1B-17	0.9	266	144	0.534	0.09	4.70	764.53	1.46	0.0172	4.9225	0.0013	1.4642	0.30	8.002	0.125	†		
M2Q1B-18	5.0	1610	552	0.339	0.12	10.37	891.27	2.37	0.0180	10.6331	0.0011	2.3706	0.22	6.671	0.191	†		
M2Q1B-19	1.9	413	328	0.787	0.05	2.89	520.29	1.30	0.0128	3.1708	0.0019	1.2969	0.41	12.430	0.161	†		
M2Q1B-20	1.4	1156	502	0.430	0.05	3.51	986.19	1.56	0.0070	3.8375	0.0010	1.5615	0.41	6.594	0.102	†		
M2Q1B-21	2.3	458	396	0.860	0.05	3.07	535.62	1.63	0.0132	3.4793	0.0019	1.6318	0.47	12.019	0.196	†		
M2Q1B-22	1.5	327	255	0.775	0.05	4.26	524.11	1.45	0.0138	4.4984	0.0019	1.4515	0.32	12.275	0.180	†		
M2Q1B-23	3.4	499	486	0.972	0.07	3.06	516.00	1.73	0.0184	3.5095	0.0019	1.7252	0.49	12.224	0.212	†		
M2Q1B-24	2.5	656	835	1.280	0.06	6.15	956.94	1.17	0.0082	6.2600	0.0010	1.1653	0.19	6.714	0.083	†		
M2Q1B-25	4.9	1914	1586	0.827	0.05	2.12	1022.50	1.32	0.0066	2.5016	0.0010	1.3250	0.53	6.368	0.084			
M2Q1B-26	4.4	896	673	0.757	0.05	2.73	478.24	1.61	0.0138	3.1736	0.0021	1.6100	0.51	13.522	0.217	†		
M2Q1B-27	2.8	512	486	0.952	0.05	3.90	521.65	1.54	0.0139	4.1931	0.0019	1.5438	0.37	12.326	0.192	†		
M2Q1B-28	3.1	549	570	1.051	0.05	3.18	532.20	1.32	0.0120	3.4470	0.0019	1.3222	0.38	12.181	0.161	†		
M2Q1B-29	3.0	546	557	1.027	0.05	3.22	537.06	1.58	0.0125	3.5859	0.0019	1.5847	0.44	12.028	0.191	†		

(continued)

Sample / grain	Concentrations (ppm) Pb	U	Th	Th/U	Isotope ratios $^{207}Pb/^{206}Pb$	2σ (%)	$^{238}U/^{206}Pb$	2σ (%)	$^{207}Pb/^{235}U$	2σ (%)	$^{206}Pb/^{238}U$	2σ (%)	Rho	Isotopic age (Ma) ^{207}Pb and ^{230}Th-corrected $^{206}Pb/^{238}U$ age	2σ abs.			
M2Q1B-30	5.2	799	1025	1.303	0.06	3.40	537.06	1.18	0.0151	3.6046	0.0019	1.1848	0.33	11.872	0.143	†		
M2Q1B-31	4.4	791	737	0.941	0.05	2.50	476.42	1.16	0.0137	2.7608	0.0021	1.1613	0.42	13.582	0.158	†		
M2Q1B-32	4.0	667	709	1.080	0.05	2.57	521.92	1.59	0.0127	3.0248	0.0019	1.5940	0.53	12.393	0.197	†		
M2Q1B-33	5.3	818	946	1.175	0.05	2.72	534.19	1.23	0.0124	2.9837	0.0019	1.2282	0.41	12.099	0.149	†		
M2Q1B-34	2.9	752	532	0.718	0.05	2.14	513.61	1.24	0.0132	2.4738	0.0019	1.2356	0.50	12.585	0.155	†		
M2Q1B-35	1.2	1055	421	0.406	0.05	2.71	946.07	1.59	0.0072	3.1420	0.0011	1.5942	0.51	6.885	0.109	†		
M2Q1B-36	1.5	293	265	0.923	0.05	3.87	514.40	1.43	0.0143	4.1226	0.0019	1.4279	0.35	12.491	0.180	†		
M2Q1B-37	3.4	580	680	1.193	0.06	4.08	535.33	1.13	0.0143	4.2312	0.0019	1.1334	0.27	11.967	0.139	†		
M2Q1B-38	3.3	567	704	1.266	0.05	4.62	535.33	1.18	0.0130	4.7645	0.0019	1.1817	0.25	12.042	0.146	†		
M2Q1B-39	2.8	545	574	1.070	0.05	2.93	536.77	1.18	0.0132	3.1622	0.0019	1.1843	0.37	11.997	0.143	†		
M2Q1B-40	2.0	410	446	1.106	0.05	3.58	541.71	1.05	0.0126	3.7257	0.0018	1.0479	0.28	11.922	0.127	†		
M2Q1B-41	1.8	353	430	1.237	0.05	3.52	533.33	1.32	0.0130	3.7634	0.0019	1.3247	0.35	12.090	0.161	†		
ANG-080313-2																		
M2Q2A-1	24.4	379	128	0.345	0.06	1.56	13.06	1.18	0.5997	1.9559	0.0766	1.1820	0.60	475.528	5.520	†	w.m.	6.607
M2Q2A-2	2.3	499	382	0.776	0.05	3.59	518.13	1.53	0.0138	3.9001	0.0019	1.5345	0.39	12.423	0.191	†	±1s	0.018
M2Q2A-3	6.1	443	954	2.165	0.06	3.42	503.78	1.12	0.0172	3.5968	0.0020	1.1248	0.31	12.580	0.145	†	±2s	0.036
M2Q2A-4	2.4	220	432	1.993	0.05	5.21	532.77	1.67	0.0140	5.4738	0.0019	1.6747	0.31	12.023	0.205	†	MSWD	0.661
M2Q2A-5	0.6	258	200	0.786	0.05	6.32	986.19	1.75	0.0073	6.5601	0.0010	1.7495	0.27	6.571	0.117		n	5
M2Q2A-6	3.1	2375	1036	0.438	0.05	2.26	961.54	1.26	0.0068	2.5883	0.0010	1.2575	0.49	6.783	0.085	†		
M2Q2A-7	10.2	124	94	0.760	0.05	1.67	28.47	1.59	0.2483	2.3078	0.0351	1.5894	0.69	222.481	3.503	†		
M2Q2A-8	5.1	461	23	0.050	0.06	1.57	12.93	1.31	0.6053	2.0460	0.0773	1.3144	0.64	480.142	6.192	†		
M2Q2A-9	2.5	1655	771	0.469	0.05	2.58	926.78	1.39	0.0071	2.9352	0.0011	1.3905	0.47	7.036	0.097	†		
M2Q2A-10	10.0	219	48	0.219	0.06	1.64	13.12	1.38	0.5956	2.1448	0.0762	1.3792	0.64	473.593	6.410	†		
M2Q2A-11	1.9	300	351	1.176	0.06	3.39	535.05	1.28	0.0143	3.6241	0.0019	1.2789	0.35	11.966	0.155	†		
M2Q2A-12	9.5	219	25	0.114	0.06	1.56	10.48	1.12	0.8133	1.9241	0.0954	1.1235	0.58	585.917	6.447	†		
M2Q2A-13	42.3	251	198	0.790	0.06	1.59	13.04	1.12	0.5922	1.9473	0.0767	1.1214	0.58	476.738	5.253	†		
M2Q2A-14	5.6	283	26	0.093	0.06	1.55	13.21	1.03	0.5880	1.8563	0.0757	1.0282	0.55	470.487	4.757	†		
M2Q2A-15	2.1	432	357	0.830	0.05	3.88	533.05	1.23	0.0129	4.0693	0.0019	1.2260	0.30	12.106	0.150	†		
M2Q2A-16	32.4	743	139	0.188	0.06	1.54	12.67	1.72	0.6180	2.3131	0.0789	1.7219	0.74	489.619	8.256	†		
M2Q2A-17	3.0	509	526	1.034	0.05	3.47	536.77	1.33	0.0130	3.7186	0.0019	1.3320	0.36	12.005	0.161	†		
M2Q2A-18	1.2	285	210	0.739	0.05	4.54	563.06	1.49	0.0118	4.7773	0.0018	1.4938	0.31	11.521	0.173	†		
M2Q2A-19	1.7	421	299	0.707	0.05	4.08	531.91	1.57	0.0122	4.3748	0.0019	1.5711	0.36	12.180	0.192	†		
M2Q2A-20	0.7	898	104	0.116	0.05	2.37	455.17	1.63	0.0147	2.8757	0.0022	1.6263	0.57	14.204	0.230	†		
M2Q2A-21	8.0	317	36	0.111	0.06	1.59	12.99	1.36	0.6039	2.0888	0.0770	1.3552	0.65	478.129	6.357	†		
M2Q2A-22	2.3	834	311	0.372	0.05	2.54	377.64	1.41	0.0171	2.9067	0.0026	1.4132	0.49	17.125	0.242	†		
M2Q2A-23	1.2	213	147	0.689	0.05	4.87	409.33	1.63	0.0180	5.1335	0.0024	1.6339	0.32	15.666	0.260	†		
M2Q2A-24	0.4	226	121	0.533	0.05	5.67	986.19	1.75	0.0068	5.9316	0.0010	1.7495	0.29	6.600	0.116			
M2Q2A-25	10.2	233	44	0.187	0.06	1.64	12.92	1.04	0.6018	1.9409	0.0774	1.0447	0.54	480.685	4.939	†		
M2Q2A-26	0.6	273	190	0.690	0.05	6.36	985.22	1.19	0.0075	6.4702	0.0010	1.1935	0.18	6.569	0.082			
M2Q2A-27	10.9	217	50	0.227	0.06	1.63	12.73	1.31	0.6082	2.0898	0.0786	1.3083	0.63	487.965	6.264	†		
M2Q2A-28	29.0	263	90	0.338	0.06	1.58	9.94	1.09	0.8390	1.9206	0.1007	1.0857	0.57	618.004	6.567	†		
M2Q2A-29	3.1	490	550	1.114	0.05	2.95	528.54	1.61	0.0124	3.3594	0.0019	1.6123	0.48	12.247	0.197	†		
M2Q2A-30	0.7	300	225	0.746	0.05	7.41	978.47	1.83	0.0068	7.6342	0.0010	1.8308	0.24	6.644	0.124			
M2Q2A-31	18.2	302	77	0.253	0.06	1.58	11.46	1.00	0.6886	1.8738	0.0873	1.0042	0.54	539.830	5.322	†		
M2Q2A-32	3.6	1826	1169	0.634	0.05	2.27	979.43	1.19	0.0068	2.5579	0.0010	1.1877	0.46	6.647	0.078			
M2Q2A-33	8.6	437	43	0.095	0.06	1.53	12.98	1.19	0.5983	1.9396	0.0770	1.1877	0.61	478.605	5.581	†		
M2Q2A-34	2.0	430	398	0.915	0.05	3.78	515.20	1.24	0.0136	3.9766	0.0019	1.2388	0.31	12.495	0.157	†		
M2Q2A-35	39.8	407	188	0.458	0.06	1.54	11.75	0.99	0.6718	1.8356	0.0851	0.9931	0.54	526.677	5.136	†		
M2Q2A-36	0.8	423	255	0.596	0.05	4.73	929.37	1.66	0.0072	5.0072	0.0011	1.6572	0.33	6.999	0.116	†		
M2Q2A-37	1.2	223	179	0.796	0.05	5.19	413.22	1.65	0.0163	5.4469	0.0024	1.6479	0.30	15.590	0.260	†		
M2Q2A-38	21.5	341	100	0.291	0.06	1.58	12.73	1.15	0.6119	1.9502	0.0786	1.1457	0.59	487.646	5.486	†		
M2Q2A-39	21.9	463	103	0.220	0.06	1.54	12.92	1.51	0.6015	2.1579	0.0774	1.5066	0.70	480.638	7.098	†		
M2Q2A-40	4.1	1039	680	0.655	0.05	3.32	496.52	1.86	0.0150	3.8045	0.0020	1.8561	0.49	12.933	0.240	†		
AR-11-ASH-4																		
M2Q2B-1	1.1	3099	466	0.150	0.05	1.91	1318.22	1.25	0.0051	2.2820	0.0008	1.2511	0.55	4.979	0.061	†	max. age	4.602
M2Q2B-2	1.8	2691	730	0.270	0.05	2.15	1289.16	1.23	0.0052	2.4725	0.0008	1.2280	0.50	5.086	0.062	†	±1s	-

(continued)

Sample / grain	Concentrations (ppm) Pb	U	Th	Th/U	Isotope ratios $^{207}Pb/^{206}Pb$	2σ (%)	$^{238}U/^{206}Pb$	2σ (%)	$^{207}Pb/^{235}U$	2σ (%)	$^{206}Pb/^{238}U$	2σ (%)	Rho	Isotopic age (Ma) ^{207}Pb and ^{230}Th-corrected $^{206}Pb/^{238}U$ age	2σ abs.			
M2Q2B-3	1.1	2333	404	0.173	0.05	2.44	1327.14	1.38	0.0053	2.8053	0.0008	1.3810	0.49	4.923	0.067	†	±2s	0.081
M2Q2B-4	1.2	2170	478	0.220	0.05	2.33	1322.75	2.17	0.0050	3.1843	0.0008	2.1747	0.68	4.964	0.106	†	MSWD	-
M2Q2B-5	1.6	3081	697	0.225	0.05	2.23	1320.66	1.28	0.0050	2.5676	0.0008	1.2773	0.50	4.970	0.063	†	n	1
M2Q2B-6	0.7	1399	268	0.191	0.05	3.22	1356.85	1.37	0.0053	3.5013	0.0007	1.3699	0.39	4.813	0.065	†		
M2Q2B-7	2.2	2574	713	0.277	0.06	3.15	1300.39	1.39	0.0065	3.4470	0.0008	1.3932	0.40	4.959	0.069	†		
M2Q2B-8	0.5	677	163	0.239	0.05	4.68	1231.53	1.56	0.0053	4.9307	0.0008	1.5601	0.32	5.326	0.083	†		
M2Q2B-9	1.8	2626	678	0.259	0.05	2.54	1219.51	1.66	0.0053	3.0360	0.0008	1.6623	0.55	5.377	0.088	†		
M2Q2B-10	1.8	3747	657	0.176	0.05	1.91	1236.09	1.45	0.0054	2.3963	0.0008	1.4487	0.60	5.297	0.075	†		
M2Q2B-11	2.0	406	319	0.787	0.06	6.23	529.94	1.72	0.0146	6.4652	0.0019	1.7172	0.27	12.086	0.213	†		
M2Q2B-12	1.3	2318	497	0.214	0.05	2.12	1289.99	1.21	0.0051	2.4429	0.0008	1.2051	0.49	5.083	0.060	†		
M2Q2B-13	1.6	2719	695	0.255	0.05	2.49	1344.09	1.56	0.0051	2.9361	0.0007	1.5608	0.53	4.873	0.075	†		
M2Q2B-14	0.6	1022	221	0.210	0.05	3.59	1355.01	1.70	0.0050	3.9702	0.0007	1.7012	0.43	4.840	0.081	†		
M2Q2B-15	1.8	1734	739	0.426	0.05	2.68	1283.20	0.97	0.0053	2.8485	0.0008	0.9725	0.34	5.096	0.049	†		
M2Q2B-16	35.1	2157	596	0.277	0.06	1.54	63.65	1.67	0.1251	2.2671	0.0157	1.6680	0.74	99.335	1.650	†		
M2Q2B-17	3.5	1943	542	0.280	0.10	4.06	1193.32	1.29	0.0116	4.2619	0.0008	1.2938	0.30	5.121	0.071	†		
M2Q2B-18	4.9	9930	1005	0.101	0.05	1.75	842.46	2.08	0.0085	2.7207	0.0012	2.0828	0.77	7.695	0.158	†		
M2Q2B-19	1.2	2039	479	0.236	0.05	2.50	1276.65	1.35	0.0053	2.8405	0.0008	1.3473	0.47	5.131	0.068	†		
M2Q2B-20	104.4	739	348	0.474	0.06	1.53	10.65	1.57	0.7800	2.1934	0.0939	1.5726	0.72	577.745	8.874	†		
M2Q2B-21	1.8	2354	715	0.306	0.05	2.04	1247.66	1.29	0.0053	2.4147	0.0008	1.2864	0.53	5.251	0.067	†		
M2Q2B-22	3.3	2220	859	0.389	0.05	2.02	893.66	1.51	0.0074	2.5269	0.0011	1.5147	0.60	7.291	0.109	†		
M2Q2B-23	9.2	2503	3250	1.163	0.05	2.19	1256.28	1.47	0.0056	2.6380	0.0008	1.4696	0.56	5.176	0.075	†		
M2Q2B-24	1.1	2064	433	0.208	0.05	2.55	1305.48	1.77	0.0051	3.1006	0.0008	1.7692	0.57	5.023	0.087	†		
M2Q2B-25	1.3	3054	553	0.183	0.05	2.07	1336.72	1.24	0.0050	2.4149	0.0007	1.2414	0.51	4.911	0.060	†		
M2Q2B-26	2.0	870	590	0.684	0.05	3.21	935.45	1.94	0.0077	3.7471	0.0011	1.9366	0.52	6.918	0.133	†		
M2Q2B-27	1.2	1506	465	0.310	0.05	2.72	1298.70	1.64	0.0052	3.1771	0.0008	1.6367	0.52	5.047	0.081	†		
M2Q2B-28	6.9	1429	2956	2.089	0.06	3.01	1342.28	1.56	0.0059	3.3855	0.0007	1.5589	0.46	4.782	0.074	†		
M2Q2B-29	3.3	5380	1284	0.241	0.05	1.83	1221	1.43	0.0054	2.3242	0.0008	1.4332	0.62	5.369	0.076	†		
M2Q2B-30	1.5	1177	242	0.208	0.09	2.16	1281.56	1.35	0.0097	2.55	0.0008	1.3518	0.53	4.847	0.065	†		
M2Q2B-31	1.2	1875	461	0.248	0.05	2.5	1287	1.21	0.0053	2.775	0.0008	1.2145	0.44	5.089	0.061	†		
M2Q2B-32	1	2990	411	0.138	0.05	1.97	1317	1.38	0.0051	2.4108	0.0008	1.3841	0.57	4.979	0.068	†		
M2Q2B-33	1.3	1089	457	0.424	0.05	3.12	1145.48	1.57	0.0057	3.4895	0.0009	1.5708	0.45	5.712	0.089	†		
M2Q2B-34	0	434	10	0.022	0.05	3.62	967.12	1.53	0.0069	3.9354	0.001	1.5344	0.39	6.75	0.103	†		
M2Q2B-35	2.5	4254	982	0.234	0.05	2.12	1265.82	1.48	0.0053	2.5854	0.0008	1.4795	0.57	5.18	0.075	†		
M2Q2B-36	1	1781	382	0.217	0.05	2.72	1257.86	1.47	0.0054	3.0883	0.0008	1.4712	0.48	5.209	0.076	†		
M2Q2B-37	0.5	453	205	0.459	0.06	5.14	1406.47	1.76	0.0058	5.4322	0.0007	1.7603	0.32	4.602	0.081			
M2Q2B-38	2.1	2166	861	0.402	0.05	2.38	1261.99	1.31	0.0054	2.7136	0.0008	1.3106	0.48	5.182	0.067	†		
M2Q2B-39	1.8	1998	788	0.399	0.05	2.19	1371.18	1.37	0.0051	2.5825	0.0007	1.3697	0.53	4.769	0.064	†		
M2Q2B-40	0.4	197	95	0.49	0.05	5.31	716.85	2.28	0.0098	5.7817	0.0014	2.2778	0.39	9.027	0.206	†		
AR-II-ASH-5																		
M2Q3A-1	1.7	1393	692	0.503	0.05	2.43	1379.31	1.47	0.005	2.8417	0.0007	1.4671	0.52	4.749	0.069	†	w.m.	4.523
M2Q3A-2	26.3	419	90	0.217	0.06	1.52	11.1	1.05	0.7406	1.8496	0.0901	1.0483	0.57	555.473	5.71	†	±1s	0.011
M2Q3A-3	0.8	1766	344	0.197	0.05	2.71	1345.9	1.44	0.0051	3.0647	0.0007	1.4358	0.47	4.875	0.069	†	±2s	0.021
M2Q3A-4	9.4	1539	440	0.289	0.07	1.74	221.24	3.57	0.046	3.9768	0.0045	3.575	0.9	28.145	1.002	†	MSWD	1.345
M2Q3A-5	3.9	1125	86	0.076	0.06	1.54	22.5	1.91	0.3525	2.4542	0.0445	1.9113	0.78	278.43	5.255	†	n	11
M2Q3A-6	1.3	1848	547	0.301	0.05	3.05	1409.05	1.17	0.0052	3.263	0.0007	1.1691	0.36	4.634	0.054	†		
M2Q3A-7	2.3	1583	977	0.623	0.05	2.33	1228.5	1.79	0.0055	2.9412	0.0008	1.7911	0.61	5.316	0.094	†		
M2Q3A-8	1.6	2469	763	0.31	0.05	2.2	1426.53	1.32	0.0047	2.5689	0.0007	1.3248	0.52	4.604	0.06	†		
M2Q3A-9	1.2	2109	560	0.267	0.05	2.88	1426.53	1.92	0.0048	3.4621	0.0007	1.9207	0.55	4.603	0.087	†		
M2Q3A-10	1.4	1948	691	0.36	0.05	2.52	1445.09	1.35	0.0046	2.8636	0.0007	1.353	0.47	4.549	0.061			
M2Q3A-11	1.2	2199	682	0.313	0.05	2.68	1463.49	1.23	0.0047	2.951	0.0007	1.2328	0.42	4.484	0.055			
M2Q3A-12	1.5	1657	601	0.367	0.06	6.13	1450.75	1.28	0.0059	6.2663	0.0007	1.2771	0.2	4.448	0.06	†		
M2Q3A-13	0.8	186	138	0.746	0.05	5.62	464.9	1.48	0.0159	5.8162	0.0022	1.4816	0.25	13.813	0.21	†		
M2Q3A-14	16.6	2108	749	0.357	0.06	1.68	248.08	1.41	0.0312	2.1876	0.004	1.4067	0.64	25.711	0.361	†		
M2Q3A-15	1.6	2011	734	0.366	0.05	2.26	1426.53	1.78	0.0047	2.8823	0.0007	1.7834	0.62	4.6	0.081			
M2Q3A-16	1.5	2031	694	0.344	0.05	2.52	1416.43	1.91	0.0048	3.1578	0.0007	1.908	0.6	4.629	0.087	†		
M2Q3A-17	1.9	509	300	0.596	0.05	3.25	487.57	1.32	0.0137	3.5048	0.0021	1.3175	0.38	13.262	0.175	†		
M2Q3A-18	0.4	949	134	0.141	0.05	2.48	1104.97	1.42	0.0061	2.8586	0.0009	1.4171	0.5	5.911	0.083	†		

(continued)

Sample / grain	Concentrations (ppm) Pb	U	Th	Th/U	Isotope ratios $^{207}Pb/^{206}Pb$	2σ (%)	$^{238}U/^{206}Pb$	2σ (%)	$^{207}Pb/^{235}U$	2σ (%)	$^{206}Pb/^{238}U$	2σ (%)	Rho	Isotopic age (Ma) ^{207}Pb and ^{230}Th-corrected $^{206}Pb/^{238}U$ age	2σ abs.			
M2Q3A-19	1	1687	437	0.259	0.05	3.27	1252.19	1.16	0.0053	3.4753	0.0008	1.1646	0.34	5.235	0.061	†		
M2Q3A-20	1.1	1900	492	0.258	0.05	2.52	1407.86	1.36	0.0047	2.8617	0.0007	1.3622	0.48	4.668	0.063	†		
M2Q3A-21	2.8	2209	921	0.418	0.05	2.66	1016.26	1.41	0.0068	3.0142	0.001	1.4126	0.47	6.406	0.09	†		
M2Q3A-22	1.4	2109	689	0.328	0.05	3.3	1445.09	1.8	0.0045	3.7627	0.0007	1.8047	0.48	4.551	0.081			
M2Q3A-23	1.2	2250	549	0.244	0.05	2.33	1393.34	1.43	0.005	2.7367	0.0007	1.428	0.52	4.705	0.066	†		
M2Q3A-24	1.2	1155	373	0.323	0.05	2.66	1079.91	1.59	0.0064	3.0963	0.0009	1.5924	0.51	6.035	0.095	†		
M2Q3A-25	1.7	1526	780	0.51	0.05	3.63	1449.28	1.53	0.0051	3.9381	0.0007	1.5331	0.39	4.493	0.068			
M2Q3A-26	1.1	1606	477	0.296	0.06	2.49	1439.47	1.35	0.0053	2.8278	0.0007	1.3485	0.48	4.523	0.06			
M2Q3A-27	1.6	2087	746	0.355	0.05	2.53	1418.44	1.91	0.0048	3.1672	0.0007	1.9106	0.6	4.624	0.087	†		
M2Q3A-28	1.2	2571	522	0.203	0.05	2.53	1342.28	1.69	0.005	3.0429	0.0007	1.6866	0.55	4.886	0.081	†		
M2Q3A-29	1.3	2869	564	0.196	0.05	2.45	1445.09	1.09	0.005	2.682	0.0007	1.0897	0.41	4.531	0.049			
M2Q3A-30	2.3	495	387	0.778	0.05	2.71	529.1	1.32	0.0127	3.0138	0.0019	1.3156	0.44	12.222	0.161	†		
M2Q3A-31	1.5	2042	650	0.316	0.05	2.42	1416.43	1.64	0.0052	2.9227	0.0007	1.6363	0.56	4.611	0.074	†		
M2Q3A-32	1	2223	430	0.193	0.05	2.25	1329.26	1.26	0.005	2.5828	0.0008	1.2599	0.49	4.939	0.061	†		
M2Q3A-33	1.8	2222	815	0.366	0.05	2.46	1467.57	1.33	0.0048	2.7987	0.0007	1.3303	0.48	4.464	0.058			
M2Q3A-34	1.7	1612	812	0.504	0.05	3.08	1415.03	1.33	0.0051	3.3521	0.0007	1.3287	0.4	4.614	0.061	†		
M2Q3A-35	3.2	3487	1557	0.442	0.05	1.93	1440.51	1.44	0.0046	2.4081	0.0007	1.4434	0.6	4.56	0.065			
M2Q3A-36	2	4476	951	0.212	0.05	1.97	1456.66	1.39	0.0046	2.4096	0.0007	1.3895	0.58	4.512	0.061			
M2Q3A-37	2.2	744	314	0.42	0.06	1.58	48.5	1.82	0.1625	2.4056	0.0206	1.8161	0.75	130.25	2.352	†		
M2Q3A-38	16.8	382	61	0.158	0.06	1.55	11.57	1.26	0.7059	1.9945	0.0864	1.2608	0.63	533.665	6.591	†		
M2Q3A-39	1.4	2487	704	0.281	0.05	2.53	1447.18	1.31	0.0047	2.8506	0.0007	1.3144	0.46	4.537	0.059			
M2Q3A-40	2.2	426	396	0.926	0.05	3.09	536.77	1.38	0.0127	3.3814	0.0019	1.3819	0.41	12.052	0.167	†		
ANG-070313-4																		
M2Q3B-1	0.7	306	199	0.651	0.06	5.08	910.75	1.45	0.0094	5.285	0.0011	1.4547	0.28	7.023	0.105	†	max. age	6.88
M2Q3B-2	7.1	476	32	0.066	0.06	1.57	13.26	1.22	0.5892	1.9878	0.0754	1.2211	0.61	468.538	5.619	†	±1s	-
M2Q3B-3	20	118	100	0.847	0.06	1.6	12.79	1.61	0.611	2.2707	0.0782	1.6139	0.71	485.654	7.681	†	±2s	0.103
M2Q3B-4	6.9	319	36	0.112	0.06	1.55	13.07	1.11	0.5946	1.9041	0.0765	1.1122	0.58	475.387	5.195	†	MSWD	-
M2Q3B-5	1.9	307	298	0.975	0.05	3.96	416.84	1.19	0.0162	4.1369	0.0024	1.1936	0.29	15.474	0.187	†	n	1
M2Q3B-6	8.2	419	40	0.095	0.06	1.57	13.24	1.01	0.5879	1.8643	0.0755	1.007	0.54	469.313	4.65	†		
M2Q3B-7	2.8	1998	732	0.367	0.05	2.04	636.13	0.97	0.0103	2.2557	0.0016	0.9664	0.43	10.213	0.098	†		
M2Q3B-8	2.4	644	404	0.63	0.05	3.08	477.1	1.74	0.0152	3.5408	0.0021	1.7431	0.49	13.491	0.235	†		
M2Q3B-9	1.1	265	202	0.765	0.05	4.47	488.52	2.4	0.0146	5.0688	0.002	2.3976	0.47	13.169	0.316	†		
M2Q3B-10	9.2	393	56	0.143	0.06	1.56	13.4	1.68	0.584	2.2953	0.0746	1.6845	0.73	463.823	7.66	†		
M2Q3B-11	8.4	359	44	0.122	0.06	1.54	13.19	1.53	0.594	2.175	0.0758	1.5349	0.71	471.013	7.088	†		
M2Q3B-12	4.9	717	709	0.996	0.05	2.29	376.51	1.77	0.0175	2.8902	0.0027	1.7665	0.61	17.156	0.302	†		
M2Q3B-13	26.1	186	109	0.591	0.06	1.58	11.47	1.36	0.699	2.0835	0.0872	1.3569	0.65	539.186	7.163	†		
M2Q3B-14	0.8	194	118	0.618	0.06	3.92	273.22	8.21	0.0294	9.0992	0.0037	8.212	0.9	23.299	1.905	†		
M2Q3B-15	4.1	942	667	0.72	0.05	2.39	447.23	1.56	0.0145	2.8569	0.0022	1.5582	0.55	14.482	0.225	†		
M2Q3B-16	5.2	887	639	0.729	0.05	2.32	360.62	1.19	0.0179	2.6086	0.0028	1.1918	0.46	17.929	0.214	†		
M2Q3B-17	30.6	210	78	0.373	0.07	1.55	7.38	1.49	1.324	2.1503	0.1355	1.4887	0.69	815.272	11.787	†		
M2Q3B-18	5	357	23	0.066	0.06	1.6	13.11	1.9	0.601	2.4827	0.0763	1.9018	0.77	473.921	8.829	†		
M2Q3B-19	12.8	140	57	0.412	0.06	1.65	12.7	1.19	0.6176	2.0353	0.0788	1.1895	0.58	489.033	5.713	†		
M2Q3B-20	2.4	1047	284	0.274	0.05	1.96	357.27	1.31	0.0181	2.3554	0.0028	1.3136	0.56	18.104	0.237	†		
M2Q3B-21	2	464	306	0.667	0.05	3.12	467.07	1.44	0.0142	3.4342	0.0021	1.4438	0.42	13.855	0.2	†		
M2Q3B-22	3.4	794	516	0.658	0.05	2.2	482.63	1.81	0.014	2.8472	0.0021	1.808	0.64	13.397	0.241	†		
M2Q3B-23	2.4	792	312	0.397	0.05	2.36	392.77	1.35	0.0167	2.7174	0.0025	1.3527	0.5	16.469	0.222	†		
M2Q3B-24	1.5	395	259	0.662	0.05	3.46	481.23	1.48	0.0137	3.7647	0.0021	1.4824	0.39	13.442	0.2	†		
M2Q3B-25	7	257	33	0.13	0.06	1.56	12.96	1.2	0.607	1.9657	0.0772	1.198	0.61	479.206	5.636	†		
M2Q3B-26	12.3	238	57	0.241	0.06	1.58	12.94	1.39	0.6059	2.1058	0.0773	1.3869	0.66	480.036	6.53	†		
M2Q3B-27	5	1562	875	0.571	0.05	1.96	476.42	1.51	0.014	2.4801	0.0021	1.5142	0.61	13.579	0.205	†		
M2Q3B-28	2.5	613	299	0.49	0.05	2.42	375.94	1.8	0.0184	3.0189	0.0027	1.8002	0.6	17.143	0.308	†		
M2Q3B-29	17.9	384	83	0.218	0.06	1.56	12.45	1.58	0.6337	2.219	0.0803	1.5758	0.71	497.969	7.686	†		
M2Q3B-30	22.2	223	99	0.444	0.06	1.6	12.05	1.53	0.664	2.213	0.083	1.5298	0.69	513.985	7.699	†		
M2Q3B-31	4.1	952	665	0.698	0.05	3.06	478.01	1.34	0.0153	3.336	0.0021	1.3396	0.4	13.453	0.181	†		
M2Q3B-32	1.6	649	288	0.444	0.05	3.09	485.91	1.59	0.0139	3.4703	0.0021	1.5871	0.46	13.317	0.211	†		
M2Q3B-33	6.2	2757	1296	0.469	0.05	1.75	533.05	1.42	0.0129	2.2579	0.0019	1.4233	0.63	12.126	0.172	†		
M2Q3B-34	4.9	1643	829	0.502	0.05	1.99	471.92	1.55	0.0138	2.5239	0.0021	1.546	0.61	13.726	0.211	†		

(continued)

Sample / grain	Concentrations (ppm) Pb	U	Th	Th/U	Isotope ratios $^{207}Pb/^{206}Pb$	2σ (%)	$^{238}U/^{206}Pb$	2σ (%)	$^{207}Pb/^{235}U$	2σ (%)	$^{206}Pb/^{238}U$	2σ (%)	Rho	Isotopic age (Ma) ^{207}Pb and ^{230}Th-corrected $^{206}Pb/^{238}U$ age	2σ abs.			
M2Q3B-35	50.8	488	257	0.527	0.06	1.54	13.07	1.22	0.5991	1.9614	0.0765	1.2184	0.62	475.222	5.684	†		
M2Q3B-36	0.8	222	97	0.433	0.05	4.81	362.98	1.88	0.0182	5.1685	0.0028	1.8825	0.36	17.793	0.337	†		
M2Q3B-37	1.7	450	318	0.702	0.05	3.13	496.77	1.39	0.0133	3.4191	0.002	1.385	0.41	13.035	0.181	†		
M2Q3B-38	0.9	1050	274	0.261	0.05	3.01	946.07	1.5	0.0073	3.3658	0.0011	1.5046	0.45	6.88	0.103			
M2Q3B-39	2.1	806	432	0.534	0.05	2.28	620.35	1.45	0.0103	2.7048	0.0016	1.4535	0.54	10.481	0.152	†		
M2Q3B-40	9.3	389	44	0.112	0.06	1.56	13.09	1.65	0.5953	2.2685	0.0764	1.6483	0.73	474.619	7.667	†		
ANG-080313-3																		
M2Q4B-1	1	540	309	0.572	0.05	4.66	838.93	1.35	0.0077	4.8525	0.0012	1.3541	0.28	7.759	0.106	†	w.m.	7.557
M2Q4B-2	2.5	847	710	0.833	0.05	4.18	827.81	1.19	0.0089	4.3467	0.0012	1.1866	0.27	7.793	0.094	†	±1s	0.01
M2Q4B-3	2.1	849	582	0.684	0.05	2.45	836.12	1.12	0.0076	2.6987	0.0012	1.121	0.42	7.799	0.087	†	±2s	0.021
M2Q4B-4	1.4	865	403	0.464	0.05	2.94	836.12	0.97	0.0077	3.0997	0.0012	0.9742	0.31	7.789	0.076	†	MSWD	1.087
M2Q4B-5	2.8	1169	984	0.833	0.05	2.74	871.08	1.08	0.0076	2.9482	0.0011	1.0808	0.37	7.466	0.081		n	16
M2Q4B-6	0.9	419	120	0.286	0.08	3.64	820.34	1.33	0.0142	3.8722	0.0012	1.3282	0.34	7.569	0.104			
M2Q4B-7	31.7	281	122	0.43	0.06	1.61	12.96	0.87	0.6007	1.8306	0.0772	0.8706	0.48	479.496	4.115	†		
M2Q4B-8	0.9	605	265	0.438	0.05	3.63	849.62	0.99	0.0078	3.7617	0.0012	0.9858	0.26	7.658	0.076	†		
M2Q4B-9	2.2	905	683	0.75	0.05	3.31	834.03	1.04	0.0079	3.4682	0.0012	1.0448	0.3	7.8	0.082	†		
M2Q4B-10	2.5	968	811	0.841	0.05	3.37	825.08	1.11	0.0082	3.5481	0.0012	1.1092	0.31	7.859	0.088	†		
M2Q4B-11	1.3	757	416	0.549	0.05	3.2	867.23	0.91	0.0079	3.3241	0.0012	0.9124	0.27	7.49	0.069			
M2Q4B-12	1.4	844	430	0.511	0.06	2.77	841.11	0.95	0.0092	2.9324	0.0012	0.9497	0.32	7.661	0.073	†		
M2Q4B-13	0.6	350	183	0.526	0.05	3.81	827.13	1.26	0.0083	4.0096	0.0012	1.2613	0.31	7.859	0.1	†		
M2Q4B-14	2.2	422	419	0.998	0.05	3.39	516.26	1.15	0.0123	3.5817	0.0019	1.1472	0.32	12.56	0.145	†		
M2Q4B-15	4.9	716	773	1.085	0.16	2.75	725.16	1.2	0.0305	2.9952	0.0014	1.1972	0.4	7.662	0.104	†		
M2Q4B-16	3.1	864	864	1.009	0.07	2.85	813.47	0.91	0.0119	2.9943	0.0012	0.9136	0.31	7.759	0.073	†		
M2Q4B-17	2.7	963	941	0.989	0.06	2.58	840.27	0.96	0.0093	2.7534	0.0012	0.9562	0.35	7.642	0.074	†		
M2Q4B-18	1.3	742	423	0.576	0.05	2.95	838.29	0.76	0.0077	3.0432	0.0012	0.7583	0.25	7.767	0.06	†		
M2Q4B-19	1	529	288	0.552	0.06	2.87	841.04	1.05	0.0101	3.0535	0.0012	1.0516	0.34	7.605	0.081			
M2Q4B-20	2.8	984	1164	1.203	0.05	2.46	856.46	0.95	0.0075	2.632	0.0012	0.9477	0.36	7.592	0.072			
M2Q4B-21	1.2	666	372	0.57	0.05	2.65	852.37	0.85	0.0089	2.7826	0.0012	0.8456	0.3	7.567	0.065			
M2Q4B-22	2.9	888	608	0.694	0.09	2.98	791.77	1.14	0.0149	3.1907	0.0013	1.1443	0.36	7.817	0.092	†		
M2Q4B-23	1.1	679	378	0.565	0.05	2.92	864.3	1.23	0.0076	3.1642	0.0012	1.2298	0.39	7.53	0.092			
M2Q4B-24	2.1	991	711	0.732	0.05	2.94	862.81	0.87	0.0076	3.0695	0.0012	0.8734	0.28	7.544	0.066			
M2Q4B-25	1.2	523	394	0.767	0.05	3.26	835.28	0.83	0.008	3.3687	0.0012	0.8346	0.25	7.78	0.066	†		
M2Q4B-26	1.2	774	385	0.505	0.05	3.31	865.05	1.07	0.0076	3.4774	0.0012	1.0749	0.31	7.53	0.081			
M2Q4B-27	1.6	765	478	0.631	0.05	4.02	826.45	0.97	0.0081	4.1387	0.0012	0.9659	0.23	7.867	0.077	†		
M2Q4B-28	1.2	495	391	0.807	0.05	4.31	863.56	1.23	0.0075	4.4836	0.0012	1.2289	0.27	7.539	0.094			
M2Q4B-29	1.7	872	514	0.598	0.05	3.15	862.07	1.39	0.0076	3.4432	0.0012	1.3864	0.4	7.559	0.104			
M2Q4B-30	1.8	814	592	0.739	0.05	2.92	835.35	0.85	0.0079	3.0449	0.0012	0.8481	0.28	7.785	0.067	†		
M2Q4B-31	5.1	1437	1552	1.102	0.05	2.5	846.74	1.06	0.0076	2.7175	0.0012	1.0571	0.39	7.68	0.081	†		
M2Q4B-32	1.1	427	233	0.554	0.07	4.86	806.45	1.02	0.0118	4.9608	0.0012	1.0183	0.21	7.846	0.086	†		
M2Q4B-33	3	1102	925	0.845	0.06	6.13	845.02	0.92	0.0098	6.198	0.0012	0.9243	0.15	7.586	0.078			
M2Q4B-34	1.8	801	557	0.706	0.05	2.56	832.64	1.19	0.008	2.8283	0.0012	1.1923	0.42	7.813	0.093	†		
M2Q4B-35	1.5	831	406	0.499	0.05	4.15	853.97	1.06	0.0084	4.2834	0.0012	1.0641	0.25	7.586	0.082			
M2Q4B-36	1.1	736	366	0.504	0.05	3.83	861.33	1.07	0.0077	3.9796	0.0012	1.0713	0.27	7.555	0.082			
M2Q4B-37	1.1	606	368	0.618	0.05	3.94	846.74	1.13	0.0076	4.1038	0.0012	1.1324	0.28	7.696	0.088	†		
M2Q4B-38	1.2	631	390	0.622	0.05	2.42	838.93	1.35	0.0079	2.7736	0.0012	1.3541	0.49	7.754	0.104	†		
M2Q4B-39	3.8	1201	1153	0.963	0.05	2.85	848.1	0.93	0.0088	2.9971	0.0012	0.9339	0.31	7.606	0.072			
M2Q4B-40	1.4	882	461	0.531	0.05	2.45	855.43	1.38	0.0077	2.813	0.0012	1.3771	0.49	7.609	0.104			
ANG-070313-1																		
M3Q1B-1	0.9	857	957	1.115	0.05	4.86	3306.88	1.73	0.0022	5.1592	0.0003	1.7274	0.33	2.012	0.034	†	w.m.	1.867
M3Q1B-2	0.6	1470	593	0.402	0.05	4.95	3144.65	1.59	0.0023	5.1972	0.0003	1.5901	0.31	2.134	0.033	†	±1s	0.005
M3Q1B-3	0.7	1787	635	0.356	0.05	3.2	3049.71	1.46	0.0024	3.5161	0.0003	1.4606	0.42	2.193	0.031	†	±2s	0.009
M3Q1B-4	0.6	1211	599	0.493	0.05	5.53	3263.71	1.74	0.0021	5.7992	0.0003	1.738	0.3	2.058	0.035	†	MSWD	0.246
M3Q1B-5	1.1	1228	1074	0.874	0.06	6.2	3389.83	2.86	0.0022	6.8285	0.0003	2.8576	0.42	1.96	0.054	†	n	2
M3Q1B-6	1	1190	1109	0.933	0.05	7.73	3418.8	2.21	0.0019	8.0361	0.0003	2.2111	0.28	1.965	0.043	†		
M3Q1B-7	12.2	274	52	0.188	0.06	1.64	15.73	1.47	0.5079	2.2071	0.0636	1.472	0.67	395.784	5.733	†		
M3Q1B-8	0.4	547	432	0.792	0.06	7.22	3243.59	1.45	0.0023	7.3689	0.0003	1.4512	0.2	2.047	0.03	†		

(continued)

Sample / grain	Concentrations (ppm)				Isotope ratios							Isotopic age (Ma)		
	Pb	U	Th	Th/U	$^{207}Pb/^{206}Pb$	2σ (%)	$^{238}U/^{206}Pb$	2σ (%)	$^{207}Pb/^{235}U$	2σ (%)	$^{206}Pb/^{238}U$	2σ (%)	Rho	^{207}Pb and ^{230}Th-corrected $^{206}Pb/^{238}U$ age	2σ abs.	
M3QLB-9	3.3	1477	3137	2.123	0.11	8.58	3211.3	2.24	0.0048	8.8655	0.0003	2.2402	0.25	1.888	0.048	†
M3QLB-10	3.5	1504	3481	2.306	0.12	6.84	3193.87	1.73	0.0054	7.0602	0.0003	1.7344	0.25	1.86	0.038	†
M3QLB-11	0.7	893	678	0.763	0.05	5.99	3386.39	1.83	0.0022	6.2591	0.0003	1.8305	0.29	1.972	0.035	†
M3QLB-12	0.7	1046	742	0.714	0.05	5.31	3394.43	1.83	0.0021	5.6185	0.0003	1.8346	0.33	1.971	0.035	†
M3QLB-13	0.3	952	240	0.252	0.06	5.64	2955.08	2.68	0.0026	6.2413	0.0003	2.6771	0.43	2.256	0.058	†
M3QLB-14	0.5	613	569	0.934	0.05	8.67	3285.15	1.72	0.0023	8.838	0.0003	1.717	0.19	2.028	0.035	†
M3QLB-15	8.6	498	309	0.625	0.07	1.59	37.17	1.06	0.2512	1.9097	0.0269	1.0553	0.55	167.344	1.764	†
M3QLB-16	0.5	562	532	0.951	0.07	7.17	3168.57	1.54	0.003	7.3298	0.0003	1.5409	0.21	2.057	0.033	†
M3QLB-17	44.7	595	209	0.353	0.07	1.53	13.15	1.02	0.7742	1.8431	0.076	1.0246	0.56	462.729	4.679	†
M3QLB-18	0.6	1052	688	0.658	0.07	4.52	3432.89	1.21	0.0026	4.6765	0.0003	1.207	0.26	1.919	0.023	†
M3QLB-19	0.4	650	511	0.789	0.05	9.32	3387.53	1.29	0.0021	9.4054	0.0003	1.2868	0.14	1.974	0.027	†
M3QLB-20	0.4	627	517	0.83	0.05	9.45	3365.87	1.4	0.0022	9.5569	0.0003	1.4047	0.15	1.985	0.029	†
M3QLB-21	1.6	593	550	0.934	0.25	2.7	2552.32	1.37	0.0137	3.0316	0.0004	1.3706	0.45	1.939	0.034	†
M3QLB-22	1.4	131	179	1.376	0.56	3.85	1257.86	2.69	0.062	4.696	0.0008	2.6884	0.57	1.789	0.149	†
M3QLB-23	0.5	769	528	0.693	0.06	6.46	3360.22	1.56	0.0024	6.6443	0.0003	1.5608	0.23	1.975	0.031	†
M3QLB-24	6.5	854	362	0.426	0.06	1.64	45.35	1.66	0.1759	2.3346	0.0221	1.6642	0.71	139.105	2.303	†
M3QLB-25	0.3	595	315	0.532	0.05	6.03	3354.58	1.62	0.0022	6.2421	0.0003	1.6221	0.26	1.998	0.032	†
M3QLB-26	0.4	607	456	0.757	0.06	9.13	3432.89	1.99	0.0022	9.3465	0.0003	1.9864	0.21	1.942	0.039	†
M3QLB-27	2.1	1046	1439	1.385	0.05	5	2073.4	1.34	0.0033	5.1782	0.0005	1.3408	0.26	3.162	0.043	†
M3QLB-28	0.3	275	224	0.824	0.05	15.98	2744.24	2.09	0.0026	16.1159	0.0004	2.0914	0.13	2.414	0.055	†
M3QLB-29	0.9	1967	528	0.268	0.05	1.75	302.11	10.89	0.0238	11.0278	0.0033	10.8876	0.99	21.227	2.298	†
M3QLB-30	6.3	407	311	0.768	0.07	2.5	132.98	6.67	0.0775	7.1225	0.0075	6.6677	0.94	46.687	3.101	†
M3QLB-31	0.3	604	315	0.522	0.05	6.42	3416.47	1.71	0.0022	6.6414	0.0003	1.7144	0.26	1.96	0.033	†
M3QLB-32	0.7	971	632	0.655	0.07	5.15	3483.11	1.95	0.0029	5.5037	0.0003	1.9462	0.35	1.875	0.036	
M3QLB-33	0.5	1035	541	0.525	0.06	4.45	3490.4	1.35	0.0022	4.65	0.0003	1.3524	0.29	1.913	0.025	†
M3QLB-34	0.4	759	414	0.547	0.05	6.32	3098.85	1.48	0.0023	6.4905	0.0003	1.4814	0.23	2.162	0.032	†
M3QLB-35	0.8	523	318	0.61	0.16	5.84	2881.01	2.05	0.0076	6.1921	0.0003	2.0498	0.33	2	0.047	†
M3QLB-36	0.7	1876	575	0.307	0.05	3.52	2999.4	1.22	0.0025	3.7238	0.0003	1.2172	0.33	2.228	0.026	†
M3QLB-37	0.8	706	348	0.494	0.13	6.65	3037.67	2.01	0.0057	6.9497	0.0003	2.0074	0.29	1.991	0.044	†
M3QLB-38	3	761	331	0.438	0.06	2.14	264.55	2.95	0.0308	3.6463	0.0038	2.9527	0.81	24.053	0.708	†
M3QLB-39	1	711	361	0.509	0.13	4.84	2530.36	2.04	0.0071	5.2535	0.0004	2.036	0.39	2.36	0.051	†
M3QLB-40	0.5	774	474	0.612	0.05	11.08	2798.77	2.1	0.0025	11.2802	0.0004	2.1034	0.19	2.38	0.051	†
M3QLB-41	0.8	961	779	0.812	0.08	4.62	3167.56	1.22	0.0035	4.7772	0.0003	1.2162	0.25	2.03	0.026	†
M3QLB-42	0.6	757	782	1.033	0.05	5.86	3321.16	1.39	0.0023	6.0246	0.0003	1.3884	0.23	1.999	0.028	†
M3QLB-43	1.3	1859	1943	1.045	0.05	4.16	3573.98	1.15	0.0021	4.3176	0.0003	1.1508	0.27	1.865	0.021	

2σ – 2σ standard error; w.m. = weighted mean age
† – excluded from age calculations

Table G.2 – Summary of U–Th–Pb zircon analytical data of volcanic ash samples using LA-ICPMS at UCSB, second analytical session.

	Concentrations (ppm)				Isotope ratios									Isotopic age (Ma)				
Sample / grain	Pb	U	Th	Th/U	$^{207}Pb/^{206}Pb$	2σ (%)	$^{238}U/^{206}Pb$	2σ (%)	$^{207}Pb/^{235}U$	2σ (%)	$^{206}Pb/^{238}U$	2σ (%)	Rho	^{207}Pb and ^{230}Th-corrected $^{206}Pb/^{238}U$ age	2σ abs.			
AR14-1																		
M1Q1C-1	2.2	1557	384	0.247	0.06	2.03	763.18	1.09	0.011	2.3084	0.0013	1.0936	0.47	8.381	0.259	†	w.m.	7.394
M1Q1C-2	0.9	270	102	0.378	0.09	3.11	734.81	1.22	0.0175	3.3383	0.0014	1.2154	0.36	8.319	0.268	†	±1s	0.013
M1Q1C-3	2.6	1741	109	0.062	0.08	6.49	704.72	1.36	0.0158	6.6351	0.0014	1.3562	0.2	8.845	0.297	†	±2s	0.027
M1Q1C-4	2.2	765	210	0.275	0.1	3.76	743.49	1.15	0.0184	3.931	0.0013	1.1486	0.29	8.173	0.257	†	MSWD	0.035
M1Q1C-5	0.9	968	222	0.23	0.05	1.54	783.7	1.06	0.0085	1.8675	0.0013	1.0553	0.57	8.3	0.254	†	n	3
M1Q1C-6	0.4	2402	91	0.038	0.05	0.94	670.15	1.05	0.0098	1.4089	0.0015	1.0505	0.75	9.696	0.296	†		
M1Q1C-7	2.8	1630	631	0.386	0.05	1.81	778.09	1.02	0.0092	2.0812	0.0013	1.0235	0.49	8.316	0.252	†		
M1Q1C-8	1.1	302	167	0.554	0.05	2.13	484.47	1.11	0.0137	2.4004	0.0021	1.107	0.46	13.346	0.415	†		
M1Q1C-9	1.5	1261	307	0.243	0.05	2.31	783.88	1.12	0.0094	2.5633	0.0013	1.1188	0.44	8.242	0.257	†		
M1Q1C-10	12.1	82	55	0.66	0.06	0.86	13.23	1.05	0.5923	1.3572	0.0756	1.0492	0.77	469.123	14.308	†		
M1Q1C-11	0.6	679	160	0.235	0.05	1.95	792.14	1.07	0.0083	2.2229	0.0013	1.0671	0.48	8.221	0.252	†		
M1Q1C-12	1.3	623	203	0.322	0.07	1.54	743.66	1.12	0.0127	1.9002	0.0013	1.1173	0.59	8.508	0.265	†		
M1Q1C-13	1.1	1263	252	0.198	0.05	1.36	738.01	1.11	0.0091	1.7601	0.0014	1.1123	0.63	8.799	0.274	†		
M1Q1C-14	1.2	538	274	0.504	0.05	3.15	727.33	1.09	0.0092	3.3276	0.0014	1.0853	0.33	8.925	0.275	†		
M1Q1C-15	1.4	883	209	0.234	0.06	1.61	764.58	1.05	0.0117	1.9206	0.0013	1.0527	0.55	8.323	0.254	†		
M1Q1C-16	1.3	937	227	0.239	0.06	4.44	772.14	1.1	0.0105	4.5699	0.0013	1.1021	0.24	8.305	0.258	†		
M1Q1C-17	1.1	711	288	0.397	0.05	1.7	785.98	1.16	0.0083	2.0593	0.0013	1.1568	0.56	8.28	0.261	†		
M1Q1C-18	0.9	336	167	0.489	0.06	2.61	712.25	1.52	0.0113	3.0168	0.0014	1.5161	0.5	8.993	0.316	†		
M1Q1C-19	1.3	737	367	0.488	0.05	3.34	881.06	1.52	0.0076	3.6729	0.0011	1.5205	0.41	7.384	0.26			
M1Q1C-20	0.8	406	206	0.501	0.05	4.12	773.99	1.47	0.0091	4.3797	0.0013	1.4745	0.34	8.361	0.291	†		
M1Q1C-21	0.6	499	187	0.368	0.05	2.84	879.35	1.28	0.0073	3.1132	0.0011	1.2753	0.41	7.419	0.243			
M1Q1C-22	16.6	135	61	0.443	0.06	0.81	13.07	1.36	0.6416	1.587	0.0765	1.3643	0.86	472.457	15.898	†		
M1Q1C-23	0.9	540	151	0.273	0.06	1.97	761.04	1.3	0.0115	2.3595	0.0013	1.3041	0.55	8.379	0.277	†		
M1Q1C-24	1.3	267	106	0.389	0.06	2.22	265.04	1.38	0.0289	2.6144	0.0038	1.3822	0.53	24.087	0.815	†		
M1Q1C-25	2.9	1445	642	0.436	0.06	4.19	788.64	1.38	0.0105	4.4101	0.0013	1.3768	0.31	8.117	0.274	†		
M1Q1C-26	0.6	304	158	0.512	0.06	6.62	868.06	1.32	0.0096	6.7507	0.0012	1.3242	0.2	7.376	0.245			
M1Q1C-27	0.5	435	116	0.261	0.05	4.64	759.88	1.57	0.0095	4.902	0.0013	1.5742	0.32	8.513	0.304	†		
M1Q1C-28	1.3	1535	360	0.232	0.05	1.32	793.65	1.33	0.0083	1.8708	0.0013	1.3275	0.71	8.202	0.273	†		
M1Q1C-29	1.1	800	309	0.381	0.05	1.83	786.16	1.49	0.0082	2.3581	0.0013	1.4871	0.63	8.285	0.289	†		
M1Q1C-30	0.6	268	128	0.47	0.07	3.23	766.28	1.47	0.0124	3.5491	0.0013	1.4666	0.41	8.255	0.286	†		
M1Q1C-31	2.4	376	129	0.34	0.16	1.51	573.39	1.8	0.0385	2.347	0.0017	1.7951	0.76	9.678	0.367	†		
M1Q1C-32	0.8	643	248	0.381	0.05	1.77	791.64	1.25	0.0083	2.1666	0.0013	1.2512	0.58	8.217	0.267	†		
M1Q1C-33	2.2	1659	472	0.281	0.05	3.35	789.27	1.67	0.0095	3.7469	0.0013	1.6734	0.45	8.175	0.3	†		
M1Q1C-34	1	865	261	0.298	0.05	1.8	784.93	1.37	0.0083	2.2605	0.0013	1.3738	0.61	8.29	0.28	†		
M1Q1C-35	1.1	1159	280	0.239	0.05	1.17	778.21	1.42	0.0085	1.8391	0.0013	1.4225	0.77	8.353	0.286	†		
M1Q1C-36	1	759	214	0.282	0.05	2.1	787.4	1.27	0.0094	2.4598	0.0013	1.2728	0.52	8.2	0.268	†		
M1Q1C-37	1.1	1180	276	0.233	0.05	1.41	791.14	1.33	0.0082	1.9383	0.0013	1.3256	0.68	8.235	0.274	†		
M1Q1C-38	0.4	1811	73	0.04	0.05	1.34	662.69	1.56	0.01	2.051	0.0015	1.5566	0.76	9.796	0.348	†		
M1Q1C-39	3.8	1356	741	0.541	0.06	2.82	765.11	1.89	0.011	3.3945	0.0013	1.8925	0.56	8.348	0.325	†		
M1Q1C-40	0.8	262	125	0.479	0.05	1.87	485.44	1.77	0.0134	2.5712	0.0021	1.7666	0.69	13.34	0.503	†		
M1Q1C-41	1.8	881	192	0.218	0.08	2.73	733.68	1.49	0.0154	3.1051	0.0014	1.487	0.48	8.476	0.296	†		
M1Q1C-42	1.3	1166	332	0.289	0.05	1.31	784.44	1.16	0.0084	1.7517	0.0013	1.1642	0.66	8.292	0.262	†		
M1Q1C-43	1	1717	246	0.147	0.05	1.16	766.87	1.83	0.0087	2.1649	0.0013	1.8309	0.85	8.482	0.325	†		
M1Q1C-44	0.7	700	181	0.264	0.05	2.14	778.82	1.72	0.0085	2.7487	0.0013	1.722	0.63	8.351	0.311	†		
M1Q1C-45	0.9	675	199	0.303	0.05	1.51	752.45	1.74	0.0095	2.3075	0.0013	1.7447	0.76	8.596	0.322	†		
M1Q1C-46	0.9	984	194	0.205	0.05	1.26	734.21	1.66	0.0089	2.0828	0.0014	1.6573	0.8	8.859	0.324	†		
M1Q1C-47	0.7	866	157	0.188	0.05	1.86	747.94	1.29	0.0094	2.2634	0.0013	1.295	0.57	8.655	0.285	†		
M1Q1C-48	1	1033	264	0.265	0.05	1.75	792.39	1.33	0.0084	2.197	0.0013	1.3266	0.6	8.207	0.273	†		
M1Q1C-49	1.6	740	170	0.239	0.08	1.96	738.23	1.23	0.0158	2.314	0.0014	1.2257	0.53	8.399	0.271	†		
AR11-3																		
M2Q2B-1	2.5	4391	1031	0.236	0.05	1.67	1291.66	1.18	0.0051	2.0469	0.0008	1.1835	0.58	5.075	0.162		w.m.	5.124
M2Q2B-2	3.2	3789	1330	0.35	0.05	1.16	1268.71	1.18	0.0052	1.6523	0.0008	1.1775	0.71	5.165	0.164		±1s	0.022
M2Q2B-3	5.7	5211	2491	0.478	0.05	1.11	1280.57	1.33	0.0051	1.7329	0.0008	1.3344	0.77	5.116	0.171		±2s	0.043
M2Q2B-4	3.2	3376	1330	0.393	0.05	1.57	1252.51	1.15	0.0053	1.9486	0.0008	1.1479	0.59	5.227	0.165		MSWD	1.91

(continued)

Sample / grain	Concentrations (ppm)				Isotope ratios								Isotopic age (Ma)						
	Pb	U	Th	Th/U	$^{207}Pb/^{206}Pb$	2σ (%)	$^{238}U/^{206}Pb$	2σ (%)	$^{207}Pb/^{235}U$	2σ (%)	$^{206}Pb/^{238}U$	2σ (%)	Rho	^{207}Pb and ^{230}Th-corrected $^{206}Pb/^{238}U$ age	2σ abs.				
M2Q2B-5	2.5	1626	558	0.341	0.05	1.57	698.81	1.31	0.0093	2.0415	0.0014	1.3051	0.64	9.296	0.307	†	n	28	
M2Q2B-6	3.4	4116	1426	0.344	0.05	1.43	1278.45	1.17	0.0052	1.8471	0.0008	1.1666	0.63	5.123	0.162				
M2Q2B-7	2.9	3707	1202	0.321	0.05	1.81	1275.02	1.19	0.0052	2.1715	0.0008	1.1928	0.55	5.135	0.164				
M2Q2B-8	4.3	4082	1789	0.433	0.05	1.65	1241.47	1.09	0.0054	1.9778	0.0008	1.0903	0.55	5.271	0.163				
M2Q2B-9	4.7	1213	1860	1.484	0.05	3	1148.11	1.26	0.0057	3.2504	0.0009	1.2616	0.39	5.669	0.185	†			
M2Q2B-10	2.8	5034	1160	0.227	0.05	1.33	1297.19	1.34	0.0052	1.8908	0.0008	1.3421	0.71	5.052	0.169				
M2Q2B-11	4.6	3877	1959	0.498	0.05	1.29	1274.7	1.24	0.0052	1.7898	0.0008	1.2361	0.69	5.138	0.166				
M2Q2B-12	2.3	2045	1024	0.494	0.05	2.37	1331.03	1.37	0.0049	2.7393	0.0008	1.3668	0.5	4.927	0.166				
M2Q2B-13	0.8	717	286	0.391	0.05	4.25	1187.65	1.41	0.0058	4.4832	0.0008	1.4125	0.32	5.496	0.188	†			
M2Q2B-14	3.3	11920	1128	0.094	0.05	0.96	990.2	1.19	0.007	1.5261	0.001	1.1892	0.78	6.576	0.21	†			
M2Q2B-15	3	3726	1271	0.339	0.05	1.34	1247.66	1.29	0.0053	1.8599	0.0008	1.2875	0.69	5.248	0.173				
M2Q2B-16	7.2	10780	2905	0.267	0.05	1.31	1233.65	1.33	0.0054	1.867	0.0008	1.3294	0.71	5.305	0.177				
M2Q2B-17	4.2	924	1605	1.704	0.05	3.11	1191.47	1.35	0.0057	3.3881	0.0008	1.3491	0.4	5.449	0.183	†			
M2Q2B-18	3.1	1602	1325	0.827	0.05	2.13	1303.1	1.36	0.0051	2.5283	0.0008	1.3624	0.54	5.015	0.169				
M2Q2B-19	5.4	5008	2109	0.42	0.05	2.23	1294.16	1.27	0.0054	2.5613	0.0008	1.2661	0.49	5.045	0.165				
M2Q2B-20	13.7	2158	2210	0.997	0.17	2.49	1072.96	1.55	0.0216	2.9336	0.0009	1.5469	0.53	5.146	0.183	†			
M2Q2B-21	4.8	4570	1954	0.426	0.05	1.35	1246.88	1.19	0.0054	1.7975	0.0008	1.1851	0.66	5.247	0.167				
M2Q2B-22	3.3	5046	1320	0.263	0.05	1.44	1297.52	1.28	0.0052	1.9292	0.0008	1.2834	0.67	5.048	0.166				
M2Q2B-23	2.8	2340	1090	0.467	0.05	2.01	1200.48	1.38	0.0056	2.4345	0.0008	1.3782	0.57	5.45	0.184	†			
M2Q2B-24	4.9	5753	1991	0.345	0.05	1.31	1277.79	1.12	0.0053	1.722	0.0008	1.123	0.65	5.117	0.16				
M2Q2B-25	6.1	4662	2371	0.509	0.05	1.21	1198.9	1.34	0.0054	1.8017	0.0008	1.3368	0.74	5.459	0.182	†			
M2Q2B-26	3.9	4121	1577	0.381	0.05	1.29	1267.75	1.37	0.0052	1.8847	0.0008	1.3712	0.73	5.168	0.174				
M2Q2B-27	5	3597	2003	0.555	0.05	1.27	1219.66	1.16	0.0053	1.7234	0.0008	1.165	0.68	5.368	0.17				
M2Q2B-28	4.2	345	1032	2.988	0.21	9.19	1066.1	3.05	0.0272	9.6843	0.0009	3.0472	0.31	4.832	0.244	†			
M2Q2B-29	9.6	6186	3933	0.632	0.05	1.13	1286.34	1.3	0.0052	1.7239	0.0008	1.3035	0.76	5.084	0.168				
M2Q2B-30	26.8	5722	10135	1.764	0.06	1.2	1287.5	1.24	0.0065	1.7238	0.0008	1.2404	0.72	4.97	0.161				
M2Q2B-31	4.4	3648	1598	0.433	0.05	1.93	1256.12	1.24	0.0056	2.2954	0.0008	1.2447	0.54	5.193	0.169				
M2Q2B-32	5.2	8233	2090	0.254	0.05	1.15	1259.92	1.18	0.0053	1.6505	0.0008	1.1819	0.72	5.201	0.166				
M2Q2B-33	10.4	3538	3897	1.11	0.05	1.66	1124.35	1.1	0.0059	1.9861	0.0009	1.0965	0.55	5.792	0.179	†			
M2Q2B-34	27.8	4520	627	0.14	0.06	1.03	325.73	4.99	0.0243	5.0927	0.0031	4.9873	0.98	19.573	1.368	†			
M2Q2B-35	3.1	1756	1177	0.672	0.05	2.55	1169.18	1.19	0.0057	2.8177	0.0009	1.1889	0.42	5.587	0.178	†			
M2Q2B-36	36.4	484	154	0.316	0.06	0.62	12.82	1.15	0.6113	1.311	0.078	1.1545	0.88	483.87	15.268	†			
M2Q2B-37	67.4	379	260	0.693	0.06	0.7	11.71	1.11	0.6815	1.3138	0.0854	1.1143	0.85	528.279	16.457	†			
M2Q2B-38	4	3568	1602	0.453	0.05	1.6	1253.6	1.24	0.0053	2.0251	0.0008	1.2364	0.61	5.218	0.169				
M2Q2B-39	12.1	508	65	0.129	0.06	0.66	14.59	1.33	0.5319	1.4823	0.0685	1.329	0.9	426.705	14.208	†			
M2Q2B-40	4	1789	1418	0.812	0.05	2.34	1171.78	1.39	0.0062	2.7204	0.0009	1.395	0.51	5.538	0.188	†			
M2Q2B-41	2.3	2279	886	0.399	0.05	2.13	1283.2	1.22	0.0052	2.4565	0.0008	1.2166	0.5	5.104	0.164				
M2Q2B-42	13.5	574	58	0.103	0.06	0.59	13.07	1.22	0.5977	1.3596	0.0765	1.2238	0.9	475.215	15.323	†			
M2Q2B-43	4	2767	1442	0.531	0.05	1.9	1213.89	1.25	0.0054	2.2763	0.0008	1.2516	0.55	5.388	0.175	†			
M2Q2B-44	2.7	2102	318	0.154	0.08	1.76	1251.56	1.43	0.0092	2.2705	0.0008	1.4329	0.63	5.006	0.172	†			
M2Q2B-45	4.7	5447	1915	0.355	0.05	1.1	1264.38	1.33	0.0054	1.7267	0.0008	1.3271	0.77	5.17	0.172				
M2Q2B-46	63.2	239	295	1.225	0.06	0.94	15.58	1.85	0.5268	2.0755	0.0642	1.851	0.89	398.846	15.361	†			
M2Q2B-47	116.3	16680	53050	3.132	0.05	1.26	1304.63	1.14	0.0053	1.6973	0.0008	1.1403	0.67	4.935	0.155				
M2Q2B-48	41.9	2503	1443	0.56	0.06	0.79	120.34	2.17	0.0657	2.3086	0.0083	2.1696	0.94	52.727	2.199	†			
M2Q2B-49	10.7	3513	1187	0.327	0.12	9.03	1175.09	1.83	0.0146	9.213	0.0009	1.8258	0.2	5.045	0.193	†			
M2Q2B-50	26.1	4628	11390	2.352	0.06	1.52	1300.22	1.15	0.0061	1.8996	0.0008	1.1457	0.6	4.928	0.155				
ANG220314-1																			
M2Q3A-1	3.9	392	14	0.035	0.06	0.56	11.51	1.42	0.6945	1.5306	0.0869	1.4234	0.93	536.877	18.383	†	w.m.	2.252	
M2Q3A-2	30.2	281	139	0.494	0.06	0.59	13.15	1.42	0.5938	1.5412	0.0761	1.423	0.92	472.262	16.168	†	±1s	0.026	
M2Q3A-3	0.4	1377	347	0.252	0.05	2.85	2700.51	1.49	0.0027	3.2197	0.0004	1.492	0.46	2.464	0.086	†	±2s	0.052	
M2Q3A-4	1.3	1153	890	0.699	0.1	2.88	2825.66	1.21	0.0049	3.1264	0.0004	1.2083	0.39	2.212	0.071	†	MSWD	1.417	
M2Q3A-5	3.9	546	18	0.033	0.06	0.58	13.1	1.27	0.5933	1.3995	0.0764	1.2718	0.91	474.298	15.521	†	n	3	
M2Q3A-6	12	221	118	0.528	0.06	0.59	12.83	1.29	0.6219	1.4141	0.078	1.2856	0.91	483.259	15.881	†			
M2Q3A-7	0.8	547	365	0.66	0.05	3.11	1468.43	1.37	0.0046	3.4031	0.0007	1.3723	0.4	4.462	0.151	†			
M2Q3A-8	7.2	239	32	0.134	0.06	0.7	12.86	1.37	0.6052	1.5414	0.0778	1.3714	0.89	482.912	16.284	†			
M2Q3A-9	0.8	338	274	0.799	0.05	4.72	1050.42	1.45	0.0064	4.9382	0.001	1.4503	0.29	6.196	0.214	†			
M2Q3A-10	21	481	44	0.091	0.07	0.54	5.75	1.25	1.742	1.3586	0.1739	1.2485	0.92	1033.967	33.596	†			

(continued)

Sample / grain	Concentrations (ppm) Pb	U	Th	Th/U	Isotope ratios $^{207}Pb/^{206}Pb$	2σ (%)	$^{238}U/^{206}Pb$	2σ (%)	$^{207}Pb/^{235}U$	2σ (%)	$^{206}Pb/^{238}U$	2σ (%)	Rho	Isotopic age (Ma) ^{207}Pb and ^{230}Th-corrected $^{206}Pb/^{238}U$ age	2σ abs.		
M2Q3A-11	15.3	147	33	0.221	0.07	0.64	7.29	1.24	1.2993	1.3917	0.1372	1.2374	0.89	826.725	26.77	†	
M2Q3A-12	5.2	1470	567	0.38	0.05	1.14	314.76	1.12	0.0205	1.5993	0.0032	1.1197	0.7	20.529	0.641	†	
M2Q3A-13	7.2	339	33	0.096	0.06	0.61	13.29	1.13	0.5886	1.282	0.0753	1.1263	0.88	467.604	14.622	†	
M2Q3A-14	7.2	437	33	0.075	0.06	0.57	13.2	1.14	0.5878	1.2703	0.0758	1.137	0.9	470.712	14.77	†	
M2Q3A-15	34.5	350	131	0.371	0.06	0.57	10.89	1.28	0.7452	1.4048	0.0918	1.2845	0.91	565.928	18.592	†	
M2Q3A-16	4.9	295	22	0.075	0.06	0.59	13.16	1.2	0.5912	1.3424	0.076	1.2043	0.9	472.13	15.132	†	
M2Q3A-17	9.7	416	41	0.097	0.06	0.6	12.88	1.14	0.6038	1.2867	0.0776	1.137	0.88	481.858	15.119	†	
M2Q3A-18	1	266	244	0.915	0.1	3.73	1014.2	1.58	0.0132	4.0487	0.001	1.5752	0.39	6.016	0.215	†	
M2Q3A-19	1.3	301	303	1.006	0.05	2.69	730.46	1.38	0.0094	3.0269	0.0014	1.379	0.46	8.864	0.3	†	
M2Q3A-20	16	92	28	0.308	0.08	0.58	5	1.19	2.191	1.3276	0.2002	1.1923	0.9	1175.128	37.522	†	
M2Q3A-21	34.2	319	144	0.45	0.06	0.58	12.14	1.18	0.6575	1.3171	0.0824	1.1826	0.9	509.934	16.233	†	
M2Q3A-22	6.3	184	19	0.102	0.06	0.65	10.94	1.4	0.775	1.5416	0.0914	1.396	0.91	561.57	19.074	†	
M2Q3A-23	12.5	159	46	0.289	0.06	0.77	11.88	1.26	0.6764	1.4732	0.0842	1.2561	0.85	520.712	16.959	†	
M2Q3A-24	5.5	218	22	0.102	0.06	0.7	13.15	1.39	0.592	1.5544	0.0761	1.3861	0.89	472.319	15.996	†	
M2Q3A-25	10.2	191	42	0.218	0.06	0.74	13.09	1.58	0.5972	1.7403	0.0764	1.5752	0.91	474.36	16.962	†	
M2Q3A-26	0.9	156	98	0.625	0.05	3.62	372.16	1.5	0.0176	3.9191	0.0027	1.4988	0.38	17.36	0.607	†	
M2Q3A-27	0.3	222	86	0.388	0.06	7.97	1078.75	1.55	0.0074	8.1238	0.0009	1.5518	0.19	5.979	0.212	†	
M2Q3A-28	3.8	189	16	0.086	0.06	0.62	13.24	1.21	0.5899	1.3643	0.0755	1.214	0.89	469.199	15.083	†	
M2Q3A-29	0.8	707	551	0.776	0.06	4.58	2925.69	1.43	0.0027	4.7992	0.0003	1.4313	0.3	2.258	0.077		
M2Q3A-30	6.7	192	31	0.159	0.06	0.71	13.78	1.42	0.5657	1.5882	0.0726	1.4182	0.89	451.19	15.425	†	
M2Q3A-31	25.4	337	107	0.317	0.06	0.67	12.84	1.2	0.6087	1.3685	0.0779	1.1952	0.87	483.536	15.454	†	
M2Q3A-32	1.9	292	232	0.792	0.05	1.66	382.56	1.38	0.0172	2.1624	0.0026	1.3837	0.64	16.875	0.571	†	
M2Q3A-33	0.8	480	370	0.77	0.05	2.82	1390.05	1.34	0.005	3.1237	0.0007	1.3384	0.43	4.696	0.157	†	
M2Q3A-34	6.5	299	29	0.099	0.06	0.61	13.33	1.21	0.5844	1.3556	0.075	1.2093	0.89	465.985	14.958	†	
M2Q3A-35	3.9	190	14	0.076	0.06	0.79	12.72	1.25	0.6226	1.4775	0.0786	1.2503	0.85	487.295	15.842	†	
M2Q3A-36	7.8	115	35	0.303	0.06	0.82	13.33	1.26	0.5872	1.5015	0.075	1.2559	0.84	466.056	15.177	†	
M2Q3A-37	6.7	214	30	0.139	0.06	0.63	13.23	1.19	0.5889	1.3498	0.0756	1.1918	0.88	469.509	14.989	†	
M2Q3A-38	2.4	2055	795	0.384	0.06	1.58	1018.33	3.9	0.0075	4.2053	0.001	3.8983	0.93	6.347	0.374	†	
M2Q3A-39	9.9	187	44	0.236	0.06	0.81	13.09	1.27	0.5962	1.5069	0.0764	1.2716	0.84	474.28	15.52	†	
M2Q3A-40	0.8	1598	773	0.478	0.05	2.49	3021.15	1.33	0.0024	2.8185	0.0003	1.3295	0.47	2.208	0.074		
M2Q3A-41	6.8	371	234	0.621	0.06	0.82	43.84	1.83	0.1795	2.0066	0.0228	1.8315	0.91	143.964	5.517	†	
M2Q3A-42	28.2	353	115	0.321	0.06	0.64	11.86	1.1	0.6693	1.2739	0.0843	1.1018	0.86	521.753	16.188	†	
M2Q3A-43	0.5	1318	497	0.371	0.05	3.36	2911.21	1.37	0.0024	3.6312	0.0003	1.3667	0.38	2.297	0.077		
M2Q3A-44	8.5	425	39	0.09	0.06	0.58	12.98	1.28	0.5979	1.4101	0.0771	1.2834	0.91	478.687	15.72	†	
M2Q3A-45	6.4	435	29	0.067	0.06	0.58	13.07	1.3	0.5956	1.4209	0.0765	1.2952	0.91	475.514	15.672	†	
M2Q3A-46	4.4	472	20	0.042	0.06	0.6	13.15	1.2	0.5924	1.3399	0.0761	1.1967	0.89	472.445	15.106	†	
M2Q3A-47	1.2	393	144	0.37	0.05	2.07	355.75	1.41	0.0183	2.5084	0.0028	1.4114	0.56	18.179	0.62	†	
M2Q3A-48	25.6	351	118	0.338	0.06	0.61	13.16	1.52	0.592	1.6385	0.076	1.5199	0.93	472.025	16.617	†	
M2Q3A-49	11.7	310	55	0.179	0.06	0.63	13.21	1.34	0.5909	1.4782	0.0757	1.3353	0.9	470.415	15.693	†	
M2Q3A-50	7.4	304	34	0.114	0.06	0.61	13.16	1.29	0.5926	1.4286	0.076	1.2907	0.9	471.928	15.533	†	
ANG070313-2																	
M3Q1D-1	0.7	499	208	0.415	0.05	3.73	1003.01	0.15	0.0067	5.5997	0.001	4.1771	0.75	6.486	0.401	w.m.	6.434
M3Q1D-2	0.3	157	91	0.579	0.06	8.88	1009.08	0.11	0.0084	9.5782	0.001	3.6019	0.38	6.361	0.356	±1s	0.019
M3Q1D-3	2.4	1660	824	0.495	0.05	1.87	984.25	0.07	0.0068	3.674	0.001	3.1607	0.86	6.623	0.342	±2s	0.039
M3Q1D-4	1	3024	312	0.103	0.05	2.05	1011.12	0.07	0.0065	3.7446	0.001	3.1334	0.84	6.46	0.332	MSWD	0.598
M3Q1D-5	2.1	2412	690	0.287	0.05	2.14	1023.54	0.1	0.0066	4.0754	0.001	3.4709	0.85	6.372	0.349	n	41
M3Q1D-6	1.7	1749	578	0.331	0.05	1.95	1027.75	0.12	0.0065	4.2096	0.001	3.7305	0.89	6.349	0.364		
M3Q1D-7	2.5	494	421	0.845	0.05	2.28	541.13	0.1	0.0124	4.1524	0.0018	3.4679	0.84	11.946	0.653	†	
M3Q1D-8	2.7	3356	886	0.262	0.05	1.89	1019.37	0.08	0.0064	3.7376	0.001	3.2242	0.86	6.41	0.335		
M3Q1D-9	2.2	2243	678	0.301	0.05	1.78	1000	0.1	0.0067	3.9965	0.001	3.5805	0.9	6.522	0.364		
M3Q1D-10	3.4	1367	1097	0.803	0.05	2.84	972.76	0.06	0.007	4.077	0.001	2.9297	0.72	6.683	0.329		
M3Q1D-11	2.4	1715	784	0.459	0.05	2.5	1015.23	0.07	0.0065	4.0142	0.001	3.1404	0.78	6.425	0.33		
M3Q1D-12	5.1	2835	1671	0.592	0.05	2.23	1035.2	0.09	0.0064	4.0122	0.001	3.3328	0.83	6.299	0.336		
M3Q1D-13	5.8	5819	1994	0.343	0.05	1.47	1025.64	0.04	0.0066	3.0451	0.001	2.6651	0.88	6.356	0.297		
M3Q1D-14	0.8	223	204	0.913	0.07	10.83	910.75	0.07	0.0103	11.2675	0.0011	3.0974	0.27	6.952	0.354	†	
M3Q1D-15	2.8	2814	952	0.339	0.05	1.79	1027.75	0.07	0.0065	3.6328	0.001	3.1619	0.87	6.352	0.328		
M3Q1D-16	3.4	2673	1163	0.434	0.05	2.16	1009.08	0.05	0.0065	3.5724	0.001	2.8436	0.8	6.469	0.313		

(continued)

Sample / grain	Concentrations (ppm) Pb	U	Th	Th/U	Isotope ratios $^{207}Pb/^{206}Pb$	2σ (%)	$^{238}U/^{206}Pb$	2σ (%)	$^{207}Pb/^{235}U$	2σ (%)	$^{206}Pb/^{238}U$	2σ (%)	Rho	Isotopic age (Ma) ^{207}Pb and ^{230}Th-corrected $^{206}Pb/^{238}U$ age	2σ abs.			
M3Q1D-17	1.2	399	409	1.029	0.05	5.16	946.07	0.06	0.0074	5.9438	0.0011	2.9567	0.5	6.842	0.339			
M3Q1D-18	2.3	1618	813	0.5	0.05	2.76	1035.2	0.07	0.0063	4.1472	0.001	3.0979	0.75	6.312	0.322			
M3Q1D-19	2.3	1849	794	0.43	0.05	2.7	1024.59	0.07	0.0065	4.1552	0.001	3.1565	0.76	6.37	0.328			
M3Q1D-20	2.6	427	886	2.062	0.05	4.57	996.02	0.06	0.0069	5.4122	0.001	2.8945	0.53	6.493	0.318			
M3Q1D-21	7.8	4213	2793	0.663	0.05	1.61	1006.04	0.04	0.0065	3.099	0.001	2.6459	0.85	6.482	0.301			
M3Q1D-22	1.6	707	592	0.835	0.05	4.11	1026.69	0.04	0.0064	4.8383	0.001	2.5448	0.53	6.347	0.289			
M3Q1D-23	1.4	1501	564	0.375	0.05	2.42	1048.22	0.04	0.0065	3.5723	0.001	2.6234	0.73	6.214	0.287			
M3Q1D-24	5.3	651	1870	2.824	0.07	5.59	994.04	0.09	0.0102	6.5498	0.001	3.4078	0.52	6.277	0.34	†		
M3Q1D-25	0.8	158	141	0.89	0.15	6.83	863.56	0.12	0.0236	7.8277	0.0012	3.8235	0.49	6.569	0.383	†		
M3Q1D-26	0.6	497	232	0.467	0.05	5.91	996.02	0.04	0.0068	6.4462	0.001	2.5772	0.4	6.532	0.299			
M3Q1D-27	0.7	456	279	0.611	0.05	5.84	1001	0.07	0.0072	6.5891	0.001	3.043	0.46	6.477	0.327			
M3Q1D-28	2.9	1654	1067	0.641	0.05	2.7	1017.29	0.06	0.0065	3.9781	0.001	2.924	0.74	6.408	0.316			
M3Q1D-29	8.5	1481	3319	2.216	0.05	2.55	1007.05	0.03	0.007	3.4829	0.001	2.3743	0.68	6.403	0.28			
M3Q1D-30	0.8	342	318	0.923	0.1	6.37	1340.48	0.09	0.0097	7.2217	0.0007	3.4055	0.47	4.584	0.248	†		
M3Q1D-31	0.5	377	232	0.611	0.06	7.06	1216.55	0.04	0.0062	7.534	0.0008	2.6289	0.35	5.321	0.246	†		
M3Q1D-32	7.2	630	2532	4.006	0.11	7.81	968.05	0.06	0.016	8.3113	0.001	2.8563	0.34	6.105	0.297	†		
M3Q1D-33	2.2	1617	889	0.548	0.05	2.32	1024.59	0.05	0.0065	3.5806	0.001	2.7283	0.76	6.367	0.301			
M3Q1D-34	1.7	1051	642	0.606	0.05	3.29	998	0.07	0.007	4.476	0.001	3.0382	0.68	6.505	0.328			
M3Q1D-35	1.1	654	429	0.652	0.05	4.51	1015.23	0.04	0.0065	5.2068	0.001	2.594	0.5	6.422	0.295			
M3Q1D-36	0.9	724	347	0.477	0.05	3.68	1009.08	0.03	0.0066	4.4068	0.001	2.4241	0.55	6.463	0.286			
M3Q1D-37	0.8	577	294	0.502	0.05	4.64	1006.04	0.03	0.0067	5.2547	0.001	2.474	0.47	6.477	0.29			
M3Q1D-38	3.9	3337	1460	0.433	0.05	1.74	1055.97	0.07	0.0062	3.5162	0.0009	3.0541	0.87	6.184	0.313			
M3Q1D-39	0.7	306	239	0.773	0.05	7.24	1015.23	0.06	0.0067	7.8355	0.001	2.9925	0.38	6.41	0.32			
M3Q1D-40	1.8	306	463	1.499	0.1	5.56	915.75	0.04	0.0153	6.1672	0.0011	2.6697	0.43	6.595	0.308	†		
M3Q1D-41	0.7	515	253	0.489	0.05	4.41	999	0.08	0.0065	5.4834	0.001	3.2631	0.6	6.539	0.344			
M3Q1D-42	3.6	3366	1240	0.366	0.05	1.82	1028.81	0.04	0.0064	3.1779	0.001	2.6061	0.82	6.349	0.292			
M3Q1D-43	2.7	1394	925	0.664	0.05	2.71	1010.1	0.06	0.0065	3.9808	0.001	2.914	0.73	6.455	0.317			
M3Q1D-44	2.1	1534	620	0.399	0.06	2.03	1016.26	0.04	0.0075	3.2949	0.001	2.595	0.79	6.359	0.292			
M3Q1D-45	4.4	2140	1496	0.689	0.05	2.17	995.02	0.05	0.0067	3.5597	0.001	2.8256	0.79	6.548	0.316			
M3Q1D-46	7.4	999	1370	1.36	0.05	1.83	548.85	0.06	0.0117	3.4803	0.0018	2.9597	0.85	11.801	0.585	†		
M3Q1D-47	1.8	920	553	0.594	0.05	2.94	968.05	0.06	0.0078	4.1925	0.001	2.9909	0.71	6.676	0.333			
M3Q1D-48	2.2	2601	752	0.284	0.05	1.75	1028.81	0.07	0.0062	3.6153	0.001	3.1637	0.88	6.363	0.329			
M3Q1D-49	2.2	2643	705	0.264	0.05	1.68	1036.27	0.07	0.0065	3.5273	0.001	3.0996	0.88	6.296	0.321			
M3Q1D-50	1.3	576	414	0.713	0.05	5.09	986.19	0.18	0.0067	6.7725	0.001	4.4689	0.66	6.604	0.427			
VC0503I3-1																		
M3Q3A-1	57	183	118	0.644	0.07	1.09	5.74	0.06	1.796	3.1795	0.1741	2.9877	0.94	1032.754	51.514	†	max. age	0.7
M3Q3A-2	0.6	241	184	0.759	0.05	7.83	914.91	0.08	0.0078	8.5029	0.0011	3.3125	0.39	7.079	0.376	†	±1s	-
M3Q3A-3	3.6	1553	1114	0.714	0.05	2.21	935.45	0.09	0.007	4.0816	0.0011	3.4307	0.84	6.965	0.378	†	±2s	-
M3Q3A-4	0.7	144	104	0.724	0.05	6.84	474.83	0.12	0.014	7.8077	0.0021	3.7724	0.48	13.602	0.785	†	MSWD	-
M3Q3A-5	1.2	441	343	0.78	0.05	5.09	925.93	0.07	0.0075	5.9723	0.0011	3.1254	0.52	7.008	0.359	†	n	-
M3Q3A-6	0.9	828	689	0.833	0.08	7.68	2743.48	0.06	0.004	8.2108	0.0004	2.9019	0.35	2.329	0.114	†		
M3Q3A-7	1	361	319	0.888	0.05	5.18	913.24	0.09	0.0079	6.1815	0.0011	3.3799	0.55	7.091	0.382	†		
M3Q3A-8	2.5	636	539	0.854	0.08	4.83	865.05	0.14	0.0128	6.3032	0.0012	4.0476	0.64	7.184	0.434	†		
M3Q3A-9	0	591	251	0.428	0.34	88.24	142857.1	6.63	0.0005	91.9353	0	25.7999	0.28	0.089	0.025	†		
M3Q3A-10	0.1	394	263	0.657	0.26	123.08	144927.5	11.13	0.0004	127.5322	0	33.3994	0.26	0.099	0.035	†		
M3Q3A-11	1.7	485	316	0.649	0.06	4.16	688.71	0.07	0.0132	5.1841	0.0015	3.0944	0.6	9.223	0.47	†		
M3Q3A-12	0.3	3054	1566	0.516	0.4	8.52	83194.68	0.25	0.0007	9.9715	0	5.1863	0.52	0.094	0.007	†		
M3Q3A-13	1.3	772	371	0.479	0.05	4.4	912.41	0.09	0.0071	5.5896	0.0011	3.45	0.62	7.149	0.39	†		
M3Q3A-14	0.6	139	146	1.041	0.06	9.93	788.64	0.16	0.0096	10.8026	0.0013	4.2602	0.39	8.136	0.509	†		
M3Q3A-15	4.6	1161	973	0.838	0.05	2.86	692.04	0.06	0.0097	4.0771	0.0014	2.9048	0.71	9.363	0.459	†		
M3Q3A-16	2	1729	1116	0.645	0.05	5.02	1818.18	0.07	0.004	5.9367	0.0006	3.1618	0.53	3.603	0.186	†		
M3Q3A-17	2.8	402	347	0.864	0.17	11.35	778.82	0.12	0.0309	11.9796	0.0013	3.8218	0.32	7.064	0.411	†		
M3Q3A-18	0.7	276	185	0.669	0.06	6.81	908.27	0.1	0.0084	7.6637	0.0011	3.5125	0.46	7.088	0.391	†		
M3Q3A-19	1.1	339	148	0.432	0.8	4.1	6172.84	1.26	0.0175	12.0295	0.0002	11.3078	0.94	0.044	0.006	†		
M3Q3A-20	0.9	299	252	0.837	0.05	5.24	906.62	0.11	0.0081	6.3917	0.0011	3.6553	0.57	7.114	0.402	†		
M3Q3A-21	0.9	523	244	0.463	0.05	4.38	899.28	0.1	0.0079	5.6453	0.0011	3.5625	0.63	7.208	0.401	†		
M3Q3A-22	1.2	125	122	0.967	0.19	6.33	653.59	0.12	0.0406	7.3979	0.0015	3.8297	0.52	8.099	0.472	†		

(continued)

Sample / grain	Concentrations (ppm) Pb	U	Th	Th/U	Isotope ratios $^{207}Pb/^{206}Pb$	2σ (%)	$^{238}U/^{206}Pb$	2σ (%)	$^{207}Pb/^{235}U$	2σ (%)	$^{206}Pb/^{238}U$	2σ (%)	Rho	Isotopic age (Ma) ^{207}Pb and ^{230}Th-corrected $^{206}Pb/^{238}U$ age	2σ abs.	
M3Q3A-23	1	526	298	0.564	0.05	4.6	910.75	0.15	0.0078	6.2339	0.0011	4.2049	0.67	7.119	0.442	†
M3Q3A-24	0.5	984	904	0.922	0.42	7.78	24330.9	0.42	0.0025	10.2414	0	6.6655	0.65	0.185	0.016	†
M3Q3A-25	1.7	431	527	1.223	0.06	6.99	909.09	0.09	0.0085	7.7887	0.0011	3.4421	0.44	7.067	0.385	†
M3Q3A-26	3	842	676	0.803	0.05	3.79	693.48	0.06	0.0099	4.7734	0.0014	2.9077	0.61	9.335	0.458	†
M3Q3A-27	1.5	777	406	0.522	0.06	4.8	918.27	0.12	0.0083	6.0978	0.0011	3.7627	0.62	7.025	0.405	†
M3Q3A-28	0	246	219	0.882	0.01	9700	169491.5	50.7	-0.0002	9700.2615	0	71.2174	0.01	0.128	0.094	†
M3Q3A-29	6.4	1248	1809	1.441	0.06	5.83	894.45	0.06	0.0094	6.5611	0.0011	3.003	0.46	7.134	0.357	†
M3Q3A-30	0.5	214	143	0.664	0.06	8.61	913.24	0.08	0.0086	9.1946	0.0011	3.2388	0.35	7.031	0.368	†
M3Q3A-31	0.9	331	252	0.762	0.06	7.57	919.96	0.06	0.0085	8.109	0.0011	2.9165	0.36	7	0.344	†
M3Q3A-32	0.1	1126	458	0.405	0.39	22.44	97087.38	1.61	0.0006	25.8357	0	12.7949	0.5	0.093	0.014	†
M3Q3A-33	0	361	264	0.727	0.93	79.58	163934.4	14.24	0.0006	88.082	0	37.7634	0.43	-0.016	-0.006	†
M3Q3A-34	1.8	371	412	1.102	0.08	5.69	851.06	0.08	0.0125	6.5206	0.0012	3.1763	0.49	7.35	0.38	†
M3Q3A-35	2.1	516	608	1.177	0.05	6.58	914.08	0.05	0.0079	7.1664	0.0011	2.8451	0.4	7.067	0.342	†
M3Q3A-36	0	318	155	0.488	0.81	72.85	144927.5	16.49	0.0009	83.4129	0	40.634	0.49	0.004	0.002	†
M3Q3A-37	1.2	219	287	1.325	0.05	8.28	805.15	0.05	0.0092	8.7261	0.0012	2.7473	0.31	8.008	0.38	†
M3Q3A-38	0.7	249	169	0.672	0.06	5.4	912.41	0.08	0.0095	6.3312	0.0011	3.3071	0.52	7.004	0.372	†
M3Q3A-39	0	133	62	0.463	1.01	78.22	44843.05	9.05	0.002	83.822	0	30.1181	0.36	-0.053	-0.017	†
M3Q3A-40	0	351	132	0.375	0.52	69.24	119047.6	11.13	0.0007	76.8728	0	33.3994	0.43	0.061	0.022	†
M3Q3A-41	0.8	596	371	0.619	0.05	6.81	1506.02	0.08	0.005	7.5258	0.0007	3.1963	0.42	4.32	0.225	†
M3Q3A-42	1.6	551	486	0.879	0.05	5.53	922.51	0.08	0.0079	6.3849	0.0011	3.1879	0.5	7.002	0.363	†
M3Q3A-43	1.2	613	409	0.667	0.05	5.14	1042.75	0.44	0.0065	8.5213	0.001	6.7976	0.8	6.24	0.549	†
M3Q3A-44	0.2	11250	5090	0.45	0.25	13.13	245098	0.22	0.0001	14.0128	0	4.8861	0.35	0.091	0.006	†
M3Q3A-45	2.3	413	655	1.585	0.05	5.03	846.74	0.06	0.0086	5.8508	0.0012	2.9818	0.51	7.608	0.379	†
M3Q3A-46	0.4	122	93	0.752	0.05	14.51	777	0.15	0.0093	15.1074	0.0013	4.2126	0.28	8.302	0.516	†
M3Q3A-47	12.1	1132	2811	2.478	0.05	2.89	661.81	0.03	0.0098	3.8115	0.0015	2.4823	0.65	9.75	0.437	†
M3Q3A-48	8.9	307	38	0.123	0.06	1.12	12.63	0.05	0.613	2.9656	0.0792	2.7449	0.93	491.294	23.313	†
M3Q3A-49	0.1	475	365	0.776	0.88	26.16	58823.53	5.84	0.0018	35.6396	0	24.2089	0.68	-0.011	-0.003	†
M3Q3A-50	0.4	153	110	0.718	0.06	8.31	894.45	0.09	0.0096	8.9592	0.0011	3.3374	0.37	7.134	0.381	†

2σ – 2σ standard error; w.m. = weighted mean age
† – excluded from age calculations

Table G.3 – (U–TH)/He analytical data for sample 005 & the Fish Canyon Tuff standard

Sample	Age (Ma)	Error (Ma)*	U (ppm)	Th (ppm)	147Sm (ppm)	[U]e**	Th/U	He (nmol/g)	mass (µg)	Ft***	ESR****		
005 – S 25.697°; W 66.180°													
zHP005-1	1.05	0.08	523.1	257.0	1.4	582.2	0.49	2.8	36.6	0.86	86.9	w.m. (Ma)	1.05
zHP005-2	1.03	0.08	573.3	250.0	1.1	630.8	0.44	3.0	21.1	0.84	75.4	±2s	0.06
zHP005-3	1.25	0.10	592.3	242.1	1.5	648.0	0.41	3.8	47.8	0.87	96.4	MSWD =	1.03
zHP005-4	1.04	0.08	690.5	219.1	1.4	740.9	0.32	3.6	28.8	0.86	86.7	n =	8
zHP005-5	0.93	0.07	201.7	85.6	1.4	221.4	0.42	1.0	47.6	0.88	104.1		
zHP005-6	1.06	0.08	463.2	304.0	1.3	533.2	0.66	2.6	24.9	0.84	76.5		
zHP005-7	1.09	0.09	613.0	383.3	1.3	701.2	0.63	3.4	18.4	0.83	72.4		
zHP005-8	1.06	0.08	566.8	280.4	1.4	631.4	0.49	3.0	17.5	0.83	70.7		
Fish canyon tuff													
zFCT-562	28.35	2.27	247.0	127.6	0.9	276.4	0.52	34.8	14.7	0.82	66.6		
zFCT-563	28.06	2.25	170.1	83.0	1.0	189.2	0.49	23.3	10.7	0.81	63.4		

*2sigma uncertainty based on 8% reproducibility, as deduced from measureed FCT zircon standard.
**[U]e is the effective uranium concentration.
***Ft is the alpha ejection coefficient, based on grain dimensions.
****ESR is equivalent spherical radius of the grains.
w.m. – Weighted mean age (Ma); MSWD - Mean square weighted deviation

Table G.4 – Summary of U–Pb zircon analytical data of volcanic ash samples using CAMECA IMS 1270 ion microprobe at UCLA.

Sample/ grain	Analysis date	$^{238}U/^{206}Pb$	$^{238}U/^{206}Pb$ $\pm1\sigma$	$^{207}Pb/^{206}Pb$	$^{207}Pb/^{206}Pb$ $\pm1\sigma$	Level of Concordia	$^{206}Pb/^{238}U$ age (Ma)	$^{206}Pb/^{238}U$ age $\pm1\sigma$ (Ma)	U (ppm)	U/ Th	$^{206}Pb^*$ (%)		Weighted average $^{206}Pb/^{238}U$ age $\pm2\sigma$ (Ma)	
CQ38 – S 27.115°; W 66.928°														
1	May-04	1777.5	110.3	0.0760	0.0096	0.16	3.51	0.23	661	1247	96.2		3.65	0.12
2	May-04	1848.1	101.8	0.0678	0.0090	-0.10	3.44	0.20	844	1130	97.2			MSWD = 0.83
4	May-04	1763.7	61.3	0.0806	0.0079	-0.35	3.53	0.13	1066	1653	95.6			
5	May-04	1777.5	55.6	0.0569	0.0057	0.30	3.65	0.12	1383	927	98.6			
6	May-04	1532.6	135.3	0.1213	0.0158	0.17	3.86	0.38	174	178	90.4			
7	May-04	1182.3	36.2	0.3191	0.0171	0.03	3.58	0.21	309	510	65.1			
8	May-04	1460.5	131.8	0.1392	0.0073	-0.20	3.93	0.41	755	1044	88.1			
9	May-04	1723.2	150.9	0.0661	0.0086	0.14	3.70	0.33	571	735	97.4			
10	May-04	1719.7	130.7	0.1079	0.0225	0.17	3.45	0.30	338	844	92.1			
13	May-04	1531.4	46.2	0.1090	0.0092	0.04	3.91	0.14	501	719	92.0			
CQ12 – S 27.218°; W 67.045°														
1	May-04	625.8	26.5	0.0642	0.0083	-0.47	10.10	0.45	309	435	97.7	†	8.74	0.53
3	May-04	619.2	16.1	0.0581	0.0035	0.00	10.31	0.34	1083	966	98.5	†		MSWD = 0.41
4	May-04	541.7	17.7	0.0826	0.0145	-0.35	11.42	0.45	333	208	95.3	†		
5	May-04	591.4	33.7	0.0588	0.0063	-0.03	10.79	0.63	396	285	98.4	†		
6	May-04	741.8	33.3	0.0663	0.0111	0.23	8.54	0.41	104	68	97.4			
7	May-04	525.8	12.7	0.1521	0.0064	-0.11	10.68	0.35	847	379	86.5	†		
8	May-04	505.1	18.1	0.0585	0.0045	0.01	12.60	0.46	426	558	98.4	†		
10	May-04	542.3	19.1	0.0570	0.0032	0.10	11.78	0.42	817	812	98.6	†		
11	May-04	540.2	12.8	0.0614	0.0050	-0.17	11.79	0.39	627	166	98.1	†		
12	May-04	547.0	15.4	0.0523	0.0014	-0.04	11.78	0.39	2327	774	99.2	†		
13	May-04	722.0	27.9	0.0562	0.0046	0.04	8.89	0.35	339	242	98.7			
14	May-04	465.1	9.5	0.0497	0.0039	-0.23	13.83	0.46	777	1073	99.6	†		
15	May-04	427.7	11.0	0.0531	0.0030	0.23	15.00	0.49	3313	2517	99.1	†		
16	May-04	530.2	14.6	0.0770	0.0040	-0.21	11.67	0.39	1628	4028	96.1	†		

1σ – 1σ standard error
† – excluded from age calculations
all ages relative to standard zircon AS3 (1099.1 Ma) and corrected for ^{230}Th disequilibrium using $D_{230} = 0.2$
* common Pb correction using Southern California anthropogenic $^{208}Pb/^{206}Pb = 0.8283$
U concentrations estimated from standard zircon 91500 (U = 81 ppm); uncertainty approx. 13% (rel.)
U/Th mass ratio from $^{208}Pb/^{206}Pb$ vs. Th/U for AS3 standard zircon

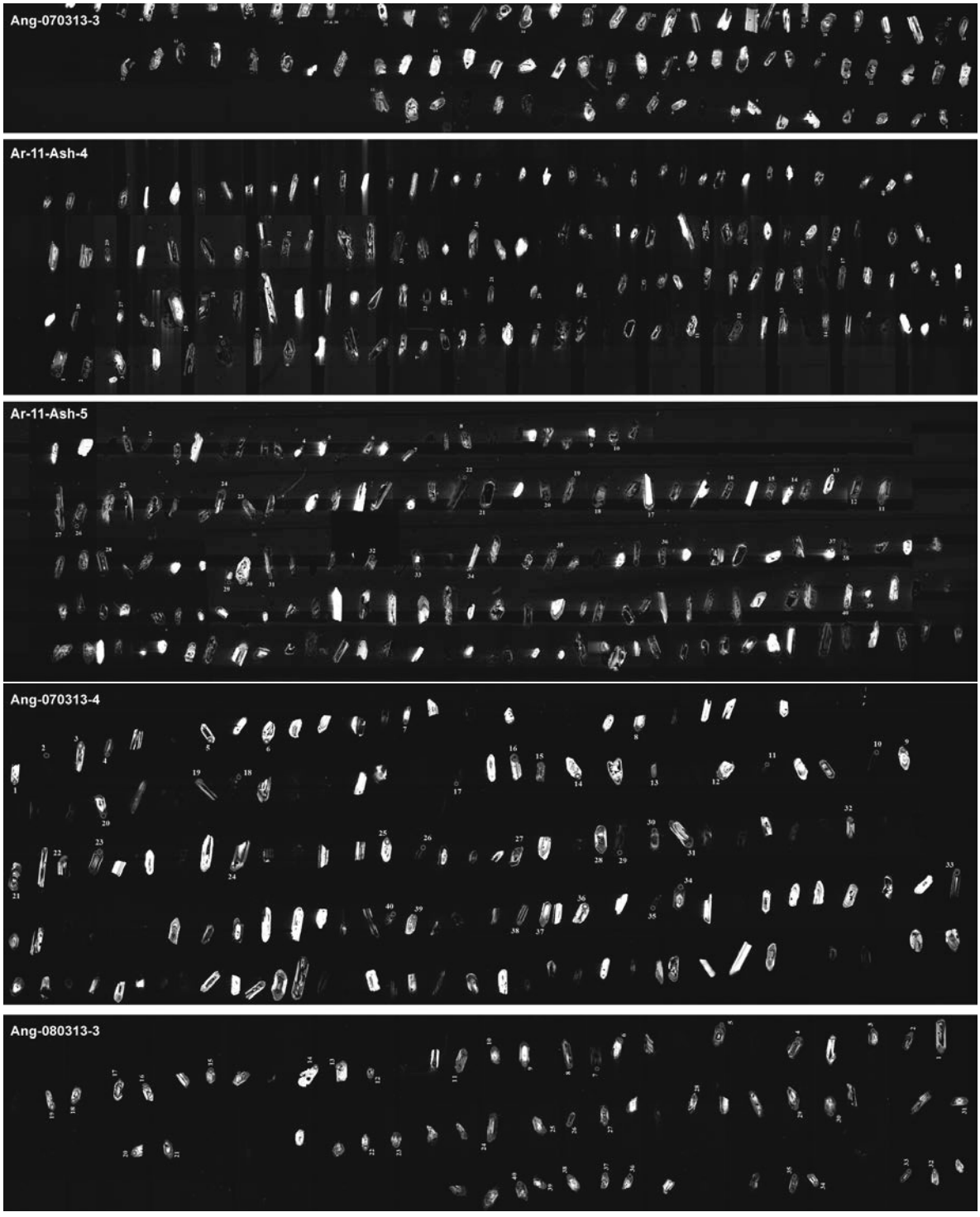

Figure G.1 – Cathodo-luminescence (CL) images of mounted zircons for four samples from the first analytical session using a FEI Q400 FEG scanning electron microscope at the University of California, Santa Barbara. CL images reveal simple concentric zonation for the majority of zircons. Circles indicate the location of individual U-Pb analyses using LA-ICPMS.

Figure G.2 – Cathodo-luminescence (CL) images of mounted zircons for four samples from the first analytical session using a FEI Q400 FEG scanning electron microscope at the University of California, Santa Barbara. CL images reveal simple concentric zonation for the majority of zircons. Circles indicate the location of individual U-Pb analyses using LA-ICPMS.

Appendix H

Hydrogen stable isotope results of volcanic glass & paleoaltimetry estimates

Table H.1 – Hydrogen stable isotope analysis of volcanic glass.

Name	Latitude (°)	Longitude (°)	Elevation (m)	Age (Ma)	2σ (Ma)	Method	References	δD_g (‰)	1σ (‰)	References	Stratigraphy
Angastaco basin											
Modern water	-	-	-	0.00	-	-	-	-64.5	8.0	Rohrmann *et al.* (2014)	Modern water
Vc-050313-1	-26.138000	-65.966950	1650	0.35	0.35	U-Pb zircon#	this study	-64.5	-	this study	Quaternary fill
005	-25.696986	-66.179650	1900	1.05	0.05	U-Th/He zircon	this study	-67.2	-	this study	Quaternary fill
Ang-070313-1	-25.764210	-65.988330	1731	1.87	0.03	U-Pb zircon*	this study	-83.1	-	this study	San Felipe
AT6-7-R	-25.670970	-66.029370	1925	3.28	0.21	U-Pb zircon	Bywater-Reyes *et al.* (2010)	-73.4	0.4	this study	San Felipe
AT3-11-R	-25.727320	-66.006720	1820	3.99	0.15	U-Pb zircon	Bywater-Reyes *et al.* (2010)	-71.7	2.4	this study	San Felipe
AT3-9-R	-25.727560	-66.007550	1820	4.04	0.26	U-Pb zircon	Bywater-Reyes *et al.* (2010)	-72.4	-	this study	San Felipe
Ar-11-Ash-5	-25.693400	-66.037020	1850	4.52	0.02	U-Pb zircon	this study	-91.8	-	this study	San Felipe
Ar-11-Ash-4	-25.678810	-66.050990	1862	4.60	0.08	U-Pb zircon*	this study	-80.8	-	this study	San Felipe
AT2-7-R	-25.729480	-66.019430	1855	4.81	0.17	U-Pb zircon	Bywater-Reyes *et al.* (2010)	-75.8	3.6	this study	San Felipe
AT2-2-R	-25.730920	-66.031650	1914	4.95	0.16	U-Pb zircon	Bywater-Reyes *et al.* (2010)	-75.2	-	this study	San Felipe
Ar-11-Ash-2/3	-25.686540	-66.054550	1822	5.12	0.04	U-Pb zircon	this study	-80.7	1.9	this study	San Felipe
AT4-3-R	-25.677160	-66.073110	1845	5.17	0.23	U-Pb zircon	Bywater-Reyes *et al.* (2010)	-88.0	-	this study	San Felipe
AI29	-25.673950	-66.071917	1900	5.27	0.28	U-Pb zircon	Coutand *et al.* (2006)	-94.8	-	this study	Palo Pintado
AT7-10-R	-25.674590	-66.077210	1840	5.98	0.32	U-Pb zircon	Bywater-Reyes *et al.* (2010)	-84.3	-	this study	Palo Pintado
Ang-070313-2	-25.681880	-66.079310	1825	6.43	0.04	U-Pb zircon	this study	-71.6	-	this study	Palo Pintado
Ang-070313-3	-25.681880	-66.079310	1825	6.37	0.08	U-Pb zircon*	this study	-74.7	-	this study	Palo Pintado
ASH1EB-R	-25.699541	-66.109571	1890	8.80	0.50	U-Pb zircon*	Carrapa *et al.* (2011)	-78.0	-	this study	Palo Pintado
AT3-9	-25.727620	-66.007620	1820	4.04	0.26	U-Pb zircon	Bywater-Reyes *et al.* (2010)	-74.8	4.0	Carrapa *et al.* (2014)	San Felipe
AT6-1	-25.674700	-66.038670	1880	4.61	0.16	U-Pb zircon	Bywater-Reyes *et al.* (2010)	-94.8	8.0	Carrapa *et al.* (2014)	San Felipe
AT2-7	-25.729480	-66.019430	1855	4.81	0.17	U-Pb zircon	Bywater-Reyes *et al.* (2010)	-73.4	3.0	Carrapa *et al.* (2014)	San Felipe
AT4-3	-25.677160	-66.073110	1845	5.17	0.23	U-Pb zircon	Bywater-Reyes *et al.* (2010)	-76.5	8.0	Carrapa *et al.* (2014)	San Felipe
AT7-10	-25.674590	-66.077210	1840	5.98	0.32	U-Pb zircon	Bywater-Reyes *et al.* (2010)	-85.3	1.0	Carrapa *et al.* (2014)	Palo Pintado
AT4-1	-	-	1820	6.90	0.30	U-Pb zircon	Carrapa *et al.* (2014)	-73.6	1.0	Carrapa *et al.* (2014)	Palo Pintado
AT1-1	-25.771110	-66.059590	1980	7.24	0.26	U-Pb zircon	Bywater-Reyes *et al.* (2010)	-75.0	2.0	Carrapa *et al.* (2014)	Palo Pintado
Southern basins											
Corral Quemado											
CQ38	-27.114800	-66.928283	2300	3.65	0.12	U-Pb zircon	this study	-88.3	-	this study	Corral Quemado Fm.
VV-1	-26.976380	-66.739490	2500	6.35	0.70	U-Pb zircon	Carrapa *et al.* (2014)	-74.6	1.0	Carrapa *et al.* (2014)	Andalhuala Fm.
CQ40	-27.094733	-66.855750	2360	7.70	0.10	40Ar/39Ar biotite	unpublished	-75.8	-	this study	Andalhuala Fm.
CQ12	-27.218150	-67.045017	2106	8.74	0.53	U-Pb zircon	this study	-75.9	-	this study	Chiquimil Fm.
Fiambalá basin											
001	-27.652996	-67.830339	2750	3.69	0.12	U-Pb zircon	Carrapa *et al.* (2008)	-76.0	-	this study	Punaschotter
074	-27.652996	-67.830339	2750	3.74	0.10	U-Pb zircon	Carrapa *et al.* (2008)	-89.7	-	this study	Punaschotter
003	-27.652996	-67.830339	2750	3.77	0.10	U-Pb zircon	Carrapa *et al.* (2008)	-83.2	-	this study	Punaschotter
FIA 840	-27.637400	-67.691600	1790	4.03	0.12	40Ar/39Ar oligoclas	Hynek (2011)	-67.6	-	this study	Guanchin Fm.
055	-27.684950	-67.820206	2215	5.23	0.30	U-Pb zircon	Carrapa *et al.* (2008)	-97.1	3.3	this study	Guanchin Fm.
J26-04	-27.324446	-67.865826	2575	5.91	0.22	U-Pb zircon	Carrapa *et al.* (2008)	-88.0	-	this study	Guanchin Fm.
Santa María basin & El Cajónn											
ENTR 909	-26.855200	-66.036600	2185	5.19	0.01	40Ar/39Ar sanidine	Hynek (2011)	-70.0	-	this study	Andalhuala Fm.
QJ4	-26.782833	-66.012400	2170	5.20	0.06	40Ar/39Ar biotite	unpublished	-77.0	-	this study	Andalhuala Fm.
QDJ 983	-26.781900	-66.014700	2134	5.27	0.01	40Ar/39Ar sanidine	Hynek (2011)	-86.3	-	this study	Andalhuala Fm.
T2-R	-26.989110	-66.266650	2220	5.50	0.90	Zr fission track	Strecker *et al.* (1989)	-96.9	-	this study	Playa del Zoro Fm.
Broken foreland											
Modern water	-	-	-	-	-	-	-	-67.0	11.0	Rohrmann *et al.* (2014)	-
Ash U	-25.106667	-65.163133	968	0.02	0.01	U-Th diseq.	Hain *et al.* (2011)	-76.8	-	this study	La Troja Fm.
Ash Q	-25.374417	-65.544600	1177	0.05	0.01	U-Th diseq.	Hain *et al.* (2011)	-77.6	-	this study	La Troja Fm.
AR14-ASH-1	-25.307980	-64.929360	775	7.39	0.03	U-Pb zircon	this study	-78.4	0.8	this study	Guanaco Fm.
Ash#2	-25.271000	-65.524570	1250	9.31	0.31	U-Pb zircon	Hain *et al.* (2011)	-75.0	-	this study	Guanaco Fm.
LVT-006	-25.596690	-65.592200	1170	14.40	0.60	U-Pb zircon	Carrapa *et al.* (2011)	-77.5	1.0	Carrapa *et al.* (2014)	Anta Fm.

(continued)

Name	Latitude (°)	Longitude (°)	Elevation (m)	Age (Ma)	2σ (Ma)	Method	References	δD_g (‰)	1σ (‰)	References	Region
Puna plateau between 25 and 28° S											
Modern water	-	-	-	0.00	-	-	-	-78.0	7.3	Rohrmann *et al.* (2014)	-
SL-117	-26.518370	-67.704200	3461	0.20	0.10	K/Ar feldspar	Kraemer *et al.* (1999)	-74.0	-	Quade *et al.* (2015)	Antofagasta Basin
Eastash2	-25.794000	-67.702000	3386	0.50	0.50	U-Pb zircon	Canavan *et al.* (2014)	-68.0	4.2	Canavan *et al.* (2014)	Antofalla Basin
ALB-tuff-1	-26.009783	-67.908800	3437	1.26	0.18	-	Schoenbohm & Carrapa (2009)	-94.0	1.0	Carrapa *et al.* (2014)	Antofalla Basin
1SJ3.7	-25.832000	-67.748000	3369	1.70	0.30	U-Pb zircon	Canavan *et al.* (2014)	-103.3	0.3	Canavan *et al.* (2014)	Antofalla Basin
1SJ44	-25.833000	-67.747000	3389	3.00	0.50	U-Pb zircon	Canavan *et al.* (2014)	-105.6	2.8	Canavan *et al.* (2014)	Antofalla Basin
Eastash1	-25.796000	-67.702000	3395	4.70	0.50	U-Pb zircon	Canavan *et al.* (2014)	-67.9	2.4	Canavan *et al.* (2014)	Antofalla Basin
PVN260	-26.764433	-67.219417	3663	7.77	0.40	-	Schoenbohm & Carrapa (2009)	-95.0	1.0	Carrapa *et al.* (2014)	Pastos Venturas
PVN226	-26.764100	-67.219950	3660	7.88	1.20	-	Schoenbohm & Carrapa (2009)	-84.0	1.0	Carrapa *et al.* (2014)	Pastos Venturas
PVN123	-26.762150	-67.222067	3643	9.90	0.20	-	Schoenbohm & Carrapa (2009)	-104.0	4.0	Carrapa *et al.* (2014)	Pastos Venturas
Vulcanash2	-25.644000	-67.851000	4383	10.40	0.20	U-Pb zircon	Canavan *et al.* (2014)	-95.4	1.1	Canavan *et al.* (2014)	Antofalla Basin
1AT8.3	-25.483000	-67.626000	3608	14.90	1.40	U-Pb zircon	Canavan *et al.* (2014)	-84.6	2.3	Canavan *et al.* (2014)	Antofalla Basin
Vulcanash5	-25.657000	-67.805000	3836	16.50	0.50	U-Pb zircon	Canavan *et al.* (2014)	-94.9	4.6	Canavan *et al.* (2014)	Antofalla Basin

*Age represents maximum age only, # Age and error represent possible range of deposition based on maximum depositional age of 0.7 Ma
Note: All samples were measured using TC/EA and Thermo-Finnigan MAT 253 stable-isotope mass spectrometer at Goethe University, Germany

Table H.2 – Paleoaltimetry results

Name	δD_{wc} (‰)	$\delta^{18}O_{wc}$ (‰)	Sample elevation (m)	Paleoelevation* (m)	-2σ (m)	+2σ (m)	Paleoelevation# (m)
Angastaco basin							
Modern water	-32.6	-2.8	-	-	-	-	-
Vc-050313-1	-32.6	-2.8	1650	1554	681	293	1845
005	-35.4	-3.2	1900	1712	754	332	2057
Ang-070313-1	-51.8	-5.2	1731	2518	1115	555	3178
AT6-7-R	-41.8	-4.0	1925	2054	910	422	2526
AT3-11-R	-40.0	-3.7	1820	1961	868	397	2398
AT3-9-R	-40.8	-3.8	1820	2002	886	408	2453
Ar-11-Ash-5	-60.8	-6.3	1850	2871	1262	664	3676
Ar-11-Ash-4	-49.4	-4.9	1862	2414	1069	524	3030
AT2-7-R	-44.3	-4.3	1855	2175	964	456	2694
AT2-2-R	-43.7	-4.2	1914	2147	952	448	2655
Ar-11-Ash-2/3	-49.3	-4.9	1822	2407	1067	522	3020
AT4-3-R	-56.9	-5.9	1845	2723	1201	618	3468
AI29	-63.9	-6.7	1900	2984	1307	700	3834
AT7-10-R	-53.0	-5.4	1840	2567	1135	570	3247
Ang-070313-2	-39.9	-3.7	1825	1958	867	396	2393
Ang-070313-3	-43.1	-4.1	1825	2117	939	440	2614
ASH1EB-R	-46.6	-4.6	1890	2284	1013	487	2847
AT3-9	-43.3	-4.2	1820	2126	943	442	2626
AT6-1	-64.0	-6.7	1880	2986	1308	700	3836
AT2-7	-41.8	-4.0	1855	2052	909	422	2523
AT4-3	-45.0	-4.4	1845	2208	979	465	2741
AT7-10	-54.1	-5.5	1840	2610	1154	583	3308
AT4-1	-42.0	-4.0	1820	2062	914	424	2537
AT1-1	-43.5	-4.2	1980	2136	947	445	2640
Statistics (min/mean/max)			1650/1850/1980	1550/2280/2990			1850/2840/3840
Southern basins							
Corral Quemado							
CQ38	-57.2	-5.9	2300	2735	1206	621	3484
VV-1	-43.1	-4.1	2500	2116	938	439	2613
CQ40	-44.2	-4.3	2360	2174	964	455	2693
CQ12	-44.4	-4.3	2106	2180	967	457	2702
Fiambalá basin							
001	-44.5	-4.3	2750	2187	970	459	2711
074	-58.7	-6.1	2750	2793	1230	639	3566
003	-51.9	-5.2	2750	2522	1116	557	3183
FIA 840	-35.8	-3.2	1790	1736	765	338	2090
055	-66.3	-7.0	2215	3065	1339	726	3945
J26-04	-56.9	-5.9	2575	2725	1202	618	3470
Santa María basin & El Cajón							
ENTR 909	-38.3	-3.5	2185	1872	827	373	2275
QJ4	-45.5	-4.4	2170	2236	992	473	2780
QDJ 983	-55.1	-5.6	2134	2653	1172	596	3368
T2-R	-66.1	-7.0	2220	3060	1337	724	3938
Statistics (min/mean/max)			1790/2340/2750	1740/2430/3070			2090/3060/3950
Broken foreland							
Ash U	-45.3	-4.4	968	2223	986	469	2762
Ash Q	-46.1	-4.5	1177	2263	1003	481	2817
AR14-ASH-1	-46.9	-4.6	775	2301	1020	492	2872
Ash2	-43.4	-4.2	1250	2135	946	444	2638
LVT-006	-46.0	-4.5	1170	2258	1001	479	2811
Statistics (min/mean/max)			780/1070/1250	2130/2240/2300			2640/2780/2870
Puna plateau between 25 and 28° S							
SL-117	-42.4	-4.0	3461	2084	923	430	2567
Eastash2	-36.2	-3.3	3386	1758	775	344	2120
ALB-tuff-1	-63.1	-6.6	3437	2954	1295	690	3792
1SJ3.7	-72.7	-7.8	3369	3273	1417	792	4224
1SJ44	-75.1	-8.1	3389	3345	1444	815	4316
Eastash1	-36.1	-3.3	3395	1752	773	343	2112
PVN260	-64.1	-6.8	3663	2991	1310	702	3843
PVN226	-52.8	-5.3	3660	2557	1131	567	3233
PVN123	-73.5	-7.9	3643	3296	1426	800	4254
Vulcanash2	-64.5	-6.8	4383	3006	1316	707	3863
1AT8.3	-53.4	-5.4	3608	2582	1142	575	3268
Vulcanash5	-64.0	-6.8	3836	2988	1308	701	3838
Statistics (min/mean/max)			3370/3600/4380	1750/2720/3340			2110/3450/4320

*Rohrmann *et al.* (2014); #Dettinger & Quade (2015)

Autorenerklärung

Hiermit erkläre ich, dass ich die vorliegende Doktorarbeit selbständig verfasst und keine anderen als die angegebenen Hilfsmittel benutzt habe. Die Stellen der Doktorarbeit, die anderen Quellen im Wortlaut oder dem Sinn nach entnommen wurden, sind durch Angaben der Herkunft kenntlich gemacht. Des Weiteren bestätige ich, dass die Arbeit an keiner anderen Hochschule eingereicht worden ist.

Potsdam, den 14. April 2015
Heiko Pingel